UNIVERSIDAD DE GRANADA

DEPARTAMENTO DE INGENIERÍA QUÍMICA
PROGRAMA DE DOCTORADO EN QUIMICA

DESARROLLO DE CATALIZADORES BASADOS EN g-C_3N_4 PARA SU APLICACIÓN EN FOTO-REACCIONES DE INTERÉS EN FASE LÍQUIDA

DEVELOPMENT OF g-C_3N_4-BASED CATALYSTS FOR THEIR APPLICATION IN PHOTO-REACTIONS OF INTEREST IN THE LIQUID PHASE

TESIS DOCTORAL

Presentada por

MARÍA ALEJANDRA QUINTANA LANCHEROS

Directores:
Mario Jesús Muñoz Batista
Rafael Rodríguez Solís

2024

UNIVERSIDAD DE GRANADA

TESIS DOCTORAL

DESARROLLO DE CATALIZADORES BASADOS EN g-C_3N_4 PARA SU APLICACIÓN EN FOTO-REACCIONES DE INTERÉS EN FASE LÍQUIDA.

DEVELOPMENT OF g-C_3N_4-BASED CATALYSTS FOR THEIR APPLICATION IN PHOTO-REACTIONS OF INTEREST IN THE LIQUID PHASE.

Memoria presentada para optar al título de Doctor en Química

MARÍA ALEJANDRA QUINTANA LANCHEROS

Departamento de Ingeniería Química

Granada, 2024

Editor: Universidad de Granada. Tesis Doctorales
Autor: María Alejandra Quintana Lancheros
ISBN: 978-84-1195-654-3
URI: https://hdl.handle.net/10481/102014

Autor: María Alejandra Quintana Lancheros
Ingeniera química por la Universidad de Bogotá Jorge Tadeo Lozano, Bogotá, Colombia.
Máster en ciencias y tecnologías químicas, KHEMIA por la Universidad de Granada, Granada, España.

A mis padres y hermana

AGRADECIMIENTOS

El desarrollo de esta tesis ha sido un proceso largo y arduo, en el que han surgido retos en diferentes escenarios de mi vida. No habría sido posible culminarlo sin el apoyo y guía de las personas que me acompañaron durante el proceso.

En primer lugar me gustaría agradecer a Mónica Calero de Hoces y Gabriel Blázquez García por permitirme formar parte del grupo de investigación Tecnologías de valorización de residuos y procesos catalíticos (RMN 152). No solo me brindaron los materiales e insumos necesarios para la realización del trabajo, sino que también me acogieron durante tantos años, ofreciéndome un ambiente de trabajo agradable y brindándome la oportunidad de desarrollar esta tesis en su equipo de trabajo.

Agradezco especialmente a mis directores de tesis, Mario Jesús Muñoz Batista y Rafael Rodríguez Solís, quienes a través de los años, me han proporcionado las herramientas necesarias para mi aprendizaje y han guiado mi camino de la mejor manera hacia el cumplimiento de los objetivos propuestos al inicio de esta experiencia. Su conocimiento y sus consejos fueron fundamentales para la realización de este trabajo. Valoro profundamente su disponibilidad en los momentos en que más los necesité y su ayuda oportuna para resolver los problemas que surgieron durante el camino. Además de ser unos excelentes profesionales, son excelentes personas que no solo han aportado en mi desarrollo académico, sino tambien en mi crecimiento personal.

Mis más sinceros agradecimientos a todos mis compañeros de laboratorio que me han acompañado en esta larga trayectoria: Inés, Marco, Maialen, Fran, Adil, Emilio, Javier, Sabrina, Sandra, Raziyeh, Guillermo, Alessandro, Ventura, Ledicia, Irene y Lourdes, quienes con sus consejos y apoyo han aportado a mi crecimiento profesional. Además de compartir conmigo largas jornadas de trabajo, desayunos, cumpleaños, risas, salidas, cenas y conversaciones agradables. No cabe duda que cada uno de estos momentos compartidos han hecho que este camino sea mucho mas ameno y enriquecedor en mi etapa predoctoral.

Un agradecimiento especial a mi pareja, Edgar, por estar siempre junto a mí, por compartir conmigo tantos logros a lo largo de los años y por ser un gran apoyo durante esta etapa de mi vida, llena de momentos inolvidables.

Quiero agradecer infinitamente a mi familia, que ha estado conmigo en los momentos mas difíciles, por ser aquellas personas que me impulsan a ser mejor cada dia, ser un pilar fundamental en distintas etapas de mi vida y por siempre creer en mí. A mi madre por mostrarme desde una edad temprana el mundo tan real y enseñarme a enfrentar los desafios con gran determinación, tal como ella lo ha hecho a lo largo

de su vida. A mi padre, quien a través de su sabiduría y disciplina, me ha enseñado a trabajar de manera constante por mis sueños y nunca rendirme por aquello que deseo. Y a mi hermana por estar siempre a mi lado brindándome consejos, palabras motivadoras y por escucharme constantemente en aquellos momentos donde mas lo necesitaba. Además de enseñarme tantas cosas fuera del ámbito en el que me desempeño.

A cada uno de mis amigos mas cercanos, Vane, Lau, Gabi, Sebas y Caro, con quienes he compartido gran parte de mi vida y emprendido un valioso camino de aprendizaje. Ellos, que a pesar de la distancia, han permanecido conmigo de una u otra forma.

A cada una de las personas que me ha acompañado durante esta etapa. ¡Muchas gracias!

“Nadie debe conocer su sentido mientras no hayan cumplido cien años."
(Gabriel Garcia Marquez, cien años de soledad)

“Por muchas cosas que se sepan, siempre habrá un número mayor de cosas por conocer.”
(Sonia Fernández Vidal, Quantic Love)

INDEX

RESUMEN....7
SUMMARY....13
CHAPTER 1. INTRODUCTION....17
1.1. INDUSTRIAL CHEMISTRY....19
1.1.1. Green chemistry....20
1.1.2. Aldehydes industry....21
1.2. PRODUCTION OF ALDEHYDES....23
1.2.1. Microbial synthesis....24
1.2.2. Biocatalysis....25
1.2.3. Chemical production of aldehydes....27
1.3. PHOTOCATALYSIS....29
1.3.1. Photocatalysts used....31
1.4. GRAPHITIC CARBON NITRIDE....33
1.4.1. Discovery....33
1.4.2. Structural Properties....34
1.4.3. Synthesis of graphitic carbon nitride....35
Thermal polymerization....36
Sol-gel method....37
Hydrothermal method....37
Microwave method....38
1.4.4. Nanostructure design....38
Top-down approach....38
Bottom-up method....39
1.4.5. g-C_3N_4 modifications....40
Elemental doping....40
Formation of g-C_3N_4 heterojunctions....43
Functionalization of g-C_3N_4....43

1.4.6. Applications 44
1.5. SELECTIVE OXIDATION OF ALCOHOLS 44
1.5.1. Oxidants used 45
1.5.2. Additives or solvents used 46
1.5.3. Catalysts used 47
1.6. BENZALDEHYDE PRODUCTION 48
1.6.1. Hydrolysis of benzyl chloride 48
1.6.2. Oxidation of toluene with air 49
1.6.3. Oxidation of benzyl alcohol to benzaldehyde 49
Precursor 49
Product 50
1.7. CINNAMALDEHYDE PRODUCTION 51
1.7.1. Perkin synthesis 52
1.7.2. Steam distillation 52
1.7.3. Oxidation of cinnamyl alcohol to cinnamaldehyde 52
Precursor 53
Product 54
1.8. REACTOR MODELING 55
1.8.1. Quantum efficiency 55
1.8.2. Modeling of the radiation field 56
Determination of the radiation flux emitted by the source 56
Evaluation of photon absorption 56
1.8.3. Radiative transfer 57
1.9. SPECIFIC OBJECTIVES 59
CHAPTER 2. EXPERIMENTAL SECTION 79
2.1. MATERIALS & CHEMICALS 81
2.2. CATALYSTS' SYNTHESIS AND CHARACTERIZATION 82
2.2.1. Catalyst synthesis 82
Impregnation method 82

Wet impregnation 83
Incipient wetness impregnation 83
Calcination 84
Synthesis of g-C_3N_4 85
Synthesis of boron-modified g-C_3N_4 85
Synthesis of Ru deposited onto g-C_3N_4 86
Synthesis of phosphorus-doped g-C_3N_4 86
Synthesis of sulfonic-tailored g-C_3N_4 87
2.2.2. Characterization and analysis techniques of catalysts 87
Thermogravimetric Analysis (TGA) 88
X-ray diffraction (XRD) 88
Fourier Transform Infrared Spectroscopy (FTIR) 90
X-ray Photoelectron Spectroscopy (XPS) 91
Scanning Transmission Electron Microscopy (STEM) 92
Electron Dispersed X-ray Analysis (EDX) 93
Elemental Analysis 93
Nitrogen adsorption isotherms 94
Diffuse Reflectance Spectroscopy (DRS) 96
Photoluminescence (PL) 98
Nuclear Magnetic Resonance (NMR) 99
2.3. EXPERIMENTAL SETUPS AND PROCEDURES 100
2.3.1. Experimental setup 100
2.3.2. Methods for aqueous analyses 101
High-performance liquid chromatography (HPLC) 101
Liquid chromatography coupled with electrospray ionization in positive mode and detection by quadrupole time-of-flight mass spectrometry (LC-ESI (+)-QTOF): 103
Total organic carbon (TOC) 104
2.3.3. Catalytic activity 104
Photolysis 104

Reaction yield 105
2.3.4. Reaction mechanism 105
Scavengers 105
2.3.5. Characterization of the radiation source 106
2.4. QUANTUM EFFICIENCY DETERMINATION 108
2.4.1. Volumetric rate of photon absorption 108
CHAPTER 3. PAPER ONE 121
3.1. INTRODUCTION 123
3.2. EXPERIMENTAL 125
3.2.2. Characterization of the solids 125
3.2.3. Photocatalytic production of benzaldehyde 126
3.3. RESULTS AND DISCUSSION 128
3.3.1. Characterization of the boron modified g-C_3N_4 128
3.3.2. Photocatalytic performance for the production of benzyl alcohol 135
3.4. CONCLUSIONS 140
CHAPTER 4. PAPER TWO 149
4.1. INTRODUCTION 151
4.2. EXPERIMENTAL SECTION 152
4.2.1. Materials and catalyst synthesis 152
4.2.2. Characterization of the catalysts 153
4.2.3. Photocatalytic experiments 154
4.3. RESULTS AND DISCUSSION 156
4.3.1. Characterization of the NaBCN-Ru photocatalysts 156
4.3.2. Photocatalytic production of benzaldehyde with NaBCN-Ru samples 163
4.3.3. Photocatalytic mechanism of BA oxidation with NaBCN-1Ru 166
4.4. CONCLUSIONS 169
CHAPTER 5. PAPER THREE 177

5.1. INTRODUCTION 179
5.2. EXPERIMENTAL SECTION 180
5.2.1. Materials and synthesis of the P-CN samples 180
5.2.2. Characterization of the P-CN samples 181
5.2.3. Photocatalytic tests of cinnamaldehyde production 182
5.3. RESULTS AND DISCUSSION 186
5.3.1. Characterization of the P-CN samples 186
5.3.2. Photocatalytic production of cinnamaldehyde with the P-CN samples 196
5.3.3. Photocatalytic mechanism and degradation pathway with P-CN-4% 198
5.4. CONCLUSIONS 204
CHAPTER 6. PAPER FOUR 219
6.1. INTRODUCTION 221
6.2. EXPERIMENTAL SECTION 223
6.2.1. Materials and catalyst preparation 223
6.2.2. Characterization of the catalysts 224
6.2.3. Photocatalytic production of benzaldehyde 225
6.3. RESULTS AND DISCUSSION 228
6.3.1. Characterization of the sulfonated carbon nitride 228
6.3.2. Photocatalytic oxidation of benzyl alcohol to benzaldehyde 238
6.4. CONCLUSIONS 243
CHAPTER 7. PAPER FIVE 257
7.1. INTRODUCTION 259
7.2. EXPERIMENTAL SECTION 260
7.2.1. Materials and synthesis of S-modified g-C_3N_4 260
7.2.2. Characterization of the S-modified g-C_3N_4 samples 261
7.2.3. Photocatalytic production of aldehydes 262
7.3. RESULTS 264
7.3.1. Characterization of the S-modified g-C3N4 samples 264

7.3.2. Photocatalytic activity in the production of aldehydes 273
7.4. CONCLUSIONS 283
CHAPTER 8. CONCLUSIONS 297

RESUMEN

La presente tesis doctoral se ha desarrollado dentro de la actividad investigadora del grupo VALORCAT, en el Departamento de Ingeniería Química de la Universidad de Granada. El trabajo realizado describe la preparación de distintos catalizadores basados en nitruro de carbono grafitico (g-C_3N_4) y su utilización en la síntesis de aldehídos aromáticos mediante tecnologías basadas en procesos fotocatalíticos. Los materiales obtenidos fueron modificados a partir de elementos metálicos y no metálicos (B, Ru, P y S).

Se estudiaron las propiedades estructurales, químicas, texturales y ópticas de los catalizadores obtenidos por medio de diversas técnicas de caracterización. Las propiedades fotocatalíticas de los materiales se evaluaron a partir de la conversión, selectividad y velocidad de reacción obtenidas durante la fotooxidación de alcoholes. Además, se realizó el modelado de la interacción radiación-catalizador y se determinaron los valores de rendimiento cuántico.

A continuación, se detalla el plan de trabajo llevado a cabo para la realización de la tesis doctoral.

El **Capítulo 1**, denominado ***Introducción y objetivos*** aborda la problemática de la contaminación ambiental generada por los procesos convencionales de producción de aldehídos, lo que sustenta el marco teórico para la elaboración de la presente tesis doctoral. A lo largo de este capítulo se destaca la importancia de los aldehídos aromáticos en el mercado mundial y los procesos comúnmente utilizados para su obtención. A partir de las debilidades encontradas en los procesos convencionales, se plantea el uso de procesos alternativos, como la tecnología fotocatalítica basada en algunos principios de la química verde. Por otra parte, se realiza una revisión de los diversos catalizadores usados en reacciones de oxidación, con un enfoque especial en el nitruro de carbono grafitico como catalizador potencial para este tipo de aplicaciones. También se definen algunos métodos de síntesis aplicados para mejorar las propiedades fotocatalíticas del nitruro de carbono grafitico. En la parte final de este capítulo, se resumen algunas características de los alcoholes y aldehídos utilizados

durante el desarrollo de la tesis. Por último, se presentan los objetivos que fundamentan este trabajo.

En el **Capítulo 2**, denominado ***Materiales y métodos*** se describen detalladamente los materiales, equipos, técnicas experimentales y procedimientos utilizados durante la investigación. Este capítulo comienza con la enumeración de reactivos y productos químicos utilizados en la parte experimental del trabajo. A continuación, se describen los métodos empleados para la preparación de los catalizadores de nitruro de carbono grafitico, así como las técnicas empleadas para su caracterización. Asimismo, se describe la configuración experimental utilizada para llevar a cabo la oxidación selectiva de alcoholes, se detallan los métodos y equipos usados para la evaluación de la actividad catalítica y el estudio del mecanismo reacción. Por otra parte, se explican las técnicas de caracterización empleadas para analizar las propiedades ópticas de la fuente de radiación. Finalmente se expone detalladamente el método usado para el cálculo de la tasa volumétrica de absorción de fotones y la eficiencia cuántica.

En el **Capítulo 3**, de título ***Enhanced boron modified graphitic carbon nitride for the selective photocatalytic production of benzaldehyde***, se utilizaron diversas fuentes de boro como el B elemental y $NaBH_4$ para modificar la estructura estratificada de g-C_3N_4, dando lugar a los materiales denominados BCN y NaBCN respectivamente, con el fin de inducir el dopado y la formación de defectos destinados a mejorar la actividad fotocatalítica. Los resultados de la caracterización por difracción de Rayos X y espectroscopía FTIR indicaron que las posiciones de C y N de g-C_3N_4 fueron remplazadas por B, obteniendo una estructura modificada en capas, en la que las unidades de tri-s-triazina se alteran. Por otra parte, la técnica espectroscopia de reflectancia difusa UV-visible indicó la disminución del *bandgap* en el siguiente orden CN>BCN>NaBCN, es decir que la muestra con mayor rango de absorción de luz fue NaBCN. Además, se encontró que la eficiencia cuántica máxima fue del 0,15% para NaBCN.

En el **Capítulo 4**, titulado ***Ruthenium deposited onto graphitic carbon modified with boron for the intensified photocatalytic production of benzaldehyde***, se ha modificado g-C_3N_4 con la incorporación de boro en la estructura polimérica con $NaBH_4$ (NaBCN)

y la deposición posterior de nanopartículas de rutenio (NaBCN-Ru). Se evaluó la proporción de Ru entre 0,5 y 4%. Los resultados sugieren que la modificación de la muestra CN original con B y Ru condujo a una disminución en las propiedades de la superficie, es decir, el volumen de poros y área específica. Por medio de espectroscopía fotoelectrónica de rayos X se pudo observar que la modificación con $NaBH_4$ creó defectos en la estructura, reduciendo la presencia de N ternario, creando enlaces B=N. En el caso de la muestra con 1% de Ru (NaBCN-1Ru), la presencia de B=C-N fue inferior al caso de NaBCN, probablemente debido a la reducción del rutenio para crear Ru^0. La incorporación de boro mejoró la selectividad hacia el benzaldehído debido a la mejor separación de cargas, tal y como sugirió la técnica de fotoluminiscencia. La deposición de Ru^0 mejoró la velocidad de reacción del alcohol, aunque afectó negativamente a la selectividad, seleccionándose la muestra que contenía 1% de Ru como óptima en términos de selectividad. Finalmente, se pudo observar que los valores de la tasa de foto-absorción promedio fueron similares entre todas las muestras modificadas.

El **Capítulo 5**, titulado ***Towards the photocatalytic production of cinnamaldehyde with phosphorous-tailored graphitic-like carbon nitride***, se centra en la mejora de la actividad fotocatalítica del g-C_3N_4 dopándolo con fósforo a partir de polifosfato de sodio (P-CN). Se realizaron diferentes niveles de dopaje de P (2–12% en peso). La caracterización realizada por difracción de Rayos X sugiere que el dopado no afectó significativamente al plano cristalográfico (002), lo que apunta a la falta de incorporación de P propiamente en el espacio entre las capas, lo cual se comprobó estimando el número de capas. El análisis elemental, espectroscopía fotoelectrónica de Rayos X y resonancia magnética nuclear sugirieron un ataque de P a las posiciones de C. Por medio de análisis elemental, se compararon las proporciones N/C antes y después del dopaje con P, comprobándose que el dopaje con P provocó un aumento de esta proporción. Además, los resultados de espectroscopía fotoelectrónica de Rayos X mostraron una disminución en el área de la contribución sp^2 N=CN, pasando del 71% en la muestra sin dopar al 59% en la muestra P-CN-4%, este hecho se confirmó adicionalmente con el aumento de la contribución del N ternario en la muestra dopada. Finalmente, el espectro ^{13}C de resonancia magnética nuclear señaló que el dopaje con P promovió la

disminución de carbono terciario, lo que sugiere una sustitución parcial de los átomos C ubicados en las posiciones internas de los anillos de tri-s-triazina por átomos de P.

En el **Capítulo 6**, denominado ***Sulfonic grafted graphitic-like carbon nitride for the improved photocatalytic production of benzaldehyde in water*** se funcionalizó la superficie de g-C_3N_4 con grupos sulfónicos (-SO_3H) usando diferentes dosis de ácido clorosulfónico.Estas muestras modificadas se evaluaron y aplicaron a la oxidación selectiva de alcohol bencílico (BA) a benzaldehído (BD). A través de las modificaciones con ácido clorosulfónico se pudo mejorar la oxidación hacia BD. Así, a medida que se incorporó azufre a la estructura, se mejoró la conversión y velocidad de reacción de BA. Por medio del difracción de Rayos X se pudo determinar que la inserción del grupo sulfónico crea defectos superficiales que generan tensión reticular y disminuyen la cristalinidad de la estructura inicial. Además, se calculó el tamaño de los cristalitos, y se pudo observar que el tamaño aumentó significativamente en un nivel alto de dopaje, lo cual pudo haberse producido debido a la presencia de grupos funcionales. El aumento del grado de sulfonación promovió la disminución gradual del pico (002), lo que evidenció el efecto de deslaminación química debido al ataque químico del ácido clorosulfónico. Finalmente, se optimizó la proporción óptima de grupos sulfónicos para el estudio de las especies oxidantes reactivas involucradas en el proceso fotocatalítico, sugiriendo que la especie con mayor contribución durante la oxidación de alcohol bencílico fue el radical superóxido, especialmente en términos de selectividad para la formación del aldehído.

En el **capitulo 7**, denominado ***Thiosulfate-tailored graphitic carbon nitride from different precursors for enhancing the photocatalytic production of aldehydes*** se modificó el nitruro de carbono grafítico con tiosulfato de sodio para mejorar el rendimiento fotocatalítico en la oxidación de alcoholes a aldehídos. El g-C_3N_4 fue obtenido a partir de diferentes compuestos químicos (urea, tiourea y melamina) con el objetivo de evaluar el impacto del precursor sobre la actividad catalítica. Los resultados mostraron que el g-C_3N_4 obtenido a partir de la urea (CNu) presentó una actividad fotocatalítica mejorada, además de dar lugar a propiedades texturales sobresalientes. Una vez identificado el precursor óptimo, se prepararon una serie de catalizadores con diferentes proporciones de $Na_2S_2O_3$, con el fin de

encontrar la concentracion ideal y se determinó que el catalizador SCNu-5% exhibía una cinética de reacción significativamente mejorada respecto a las otras proporciones, además de presentar propiedades ópticas superiores, como una reducción en el bandgap, una mejor absorción hacia el rango de la luz visible y un menor efecto de recombinación de cargas. En cuanto a la distribución de azufre en la estructura del g-C_3N_4, se observó que la mayor parte del azufre se ancló en la superficie del catalizador, lo que podría explicar el notable incremento de la actividad catalítica. Por otra parte, se evaluó la actividad del catalizador óptimo con diferentes alcoholes, y se determinó que este catalizador fue más selectivo en la producción de benzaldehído (selectividad, >100%), seguido del cinamaldehído (>23%) y la vainillina (~5%). Finalmente, el estudio del mecanismo de oxidación que interviene en la obtención del cinamaldehido sugirió una fuerte influencia de los huecos fotogenerados y del radical superóxido, siendo este último más selectivo en el proceso.

En el **Capítulo 8**, titulado ***Conclusiones***, se esquematizan las principales conclusiones generales obtenidas durante el desarrollo de la presente tesis. Se destaca el potencial uso de catalizadores de nitruro de carbono grafítico dopado con heteroátomos para su aplicación en la fotoxidación selectiva de alcoholes.

SUMMARY

This doctoral thesis was developed within the research activities of the VALORCAT group in the Department of Chemical Engineering at the University of Granada. The work describes the preparation of various catalysts based on graphitic carbon nitride (g-C_3N_4) and their use in the synthesis of aromatic aldehydes through photocatalytic process technologies. The obtained materials were modified with metallic and non-metallic elements (B, Ru, P, and S).

The structural, chemical, textural, and optical properties of the catalysts were studied using various characterization techniques. The photocatalytic properties of the materials were evaluated based on reaction rate, selectivity, and conversion rate obtained during the photooxidation of alcohols. Additionally, the interaction between radiation and catalyst was modeled, and quantum efficiency values were determined.

Next, the work plan carried out for the doctoral thesis is detailed.

Chapter 1, entitled ***Introduction and Objectives***, addresses the issue of environmental pollution generated by conventional aldehyde production processes, providing the theoretical framework for this doctoral thesis. This chapter highlights the importance of aromatic aldehydes in the global market and the commonly used processes for their production. Based on the weaknesses found in conventional processes, the use of alternatives such as photocatalytic technology based on some principles of green chemistry is proposed. Furthermore, a review of various catalysts used in oxidation reactions is conducted, focusing on graphitic carbon nitride as a potential catalyst for these applications. Some synthesis methods applied to improve the photocatalytic properties of graphitic carbon nitride are also defined. In the final part of the introduction, some characteristics of the alcohols and aldehydes used during the development of the thesis are summarized. Finally, the objectives that underpin this work are presented.

In **Chapter 2**, called ***Materials and Methods***, the materials, equipment, experimental techniques, and procedures used during the research are described in detail. This chapter begins with the enumeration of the reagents and chemical products used in the

experimental part of the work. Next, the methods employed for the preparation of the graphitic carbon nitride catalysts and the techniques used for their characterization are described. Additionally, the experimental configuration used to carry out the selective oxidation of alcohols is described. The methods and equipment used for evaluating catalytic activity and studying the reaction mechanism are detailed. Moreover, the characterization techniques used to analyze the optical properties of the radiation source are explained. Finally, the method used to calculate the volumetric photon absorption rate and quantum efficiency is detailed.

In **Chapter 3**, entitled ***Enhanced Boron-Modified Graphitic Carbon Nitride for the Selective Photocatalytic Production of Benzaldehyde***, various boron sources such as elemental B and $NaBH_4$ were used to modify the layered structure of g-C_3N_4, leading to the respectively labeled as BCN and NaBCN, to induce doping and defect formation aimed at improving photocatalytic activity. X Ray Diffraction and FTIR spectroscopy characterization results indicated that the C and N positions of g-C_3N_4 were replaced by B, obtaining a modified layered structure where the tri-s-triazine units are altered. Furthermore, the UV-visible Diffuse Reflectance Spectroscopy technique indicated a decrease in bandgap in the following order CN>BCN>NaBCN, meaning that the sample with the highest light absorption range was NaBCN. Additionally, the maximum quantum efficiency was found to be 0.15% for Na-BCN.

In **Chapter 4**, with the title ***Ruthenium Deposited onto Boron-Modified Graphitic Carbon for the Intensified Photocatalytic Production of Benzaldehyde,*** g-C_3N_4 was modified by incorporating boron into its polymeric structure using $NaBH_4$ (NaBCN) and subsequently depositing ruthenium nanoparticles (NaBCN-Ru). The Ru proportion was evaluated between 0.5 and 4%. The results suggest that modifying the original CN sample with B and Ru led to decreased surface properties, such as the specific surface area and pore volume. X-Ray Photoelectron Spectroscopy revealed that modification with $NaBH_4$ created defects in the structure, reducing the presence of ternary N and creating B=N bonds. In the sample with 1% Ru (NaBCN-1Ru), the presence of B=C-N was lower than in NaBCN, probably due to the reduction of ruthenium to create Ru^0. Boron incorporation improved selectivity towards benzaldehyde due to better charge separation, as

suggested by the photoluminescence technique. Ru^0 deposition improved the reaction rate of alcohol, though it negatively affected selectivity, with the 1% Ru sample being optimal in terms of selectivity. Finally, the average photo-absorption rate values and profiles for each modified sample were found to be similar.

Chapter 5, entitled ***Towards the Photocatalytic Production of Cinnamaldehyde with Phosphorous-Tailored Graphitic-Like Carbon Nitride***, focuses on enhancing the photocatalytic activity of g-C_3N_4 by doping it with phosphorus from sodium polyphosphate (P-CN). Different P doping levels (2-12% by weight) were conducted. X-ray diffraction characterization suggests that doping did not significantly affect the (002) crystallographic plane, indicating a lack of proper P incorporation between layers, which was verified by estimating the number of layers. Elemental analysis, X-ray photoelectron spectroscopy, and nuclear magnetic resonance suggested a possible attack of P on the C positions. Elemental analysis compared the N/C ratios before and after P doping, confirming that P doping increased this ratio. Furthermore, the X-ray photoelectron spectroscopy results showed a decrease in the area of the sp^2 N=CN contribution from 71% in the undoped sample to 59% in the P-CN-4% sample, which was confirmed by the increased contribution of ternary N in the doped sample. Finally, the ^{13}C nuclear magnetic resonance spectrum indicated that P doping promoted a decrease in bay sites, suggesting a partial substitution of C atoms located in the internal positions of tri-s-triazine rings by P atoms.

In **Chapter 6**, with the title ***Sulfonic Grafted Graphitic-Like Carbon Nitride for the Improved Photocatalytic Production of Benzaldehyde in Water,*** the surface of g-C_3N_4 was functionalized with sulfonic groups (-SO_3H) using different doses of chlorosulfonic acid (0.5 - 15 ml). These modified samples were evaluated and applied to the selective oxidation of benzyl alcohol (BA) to benzaldehyde (BD). Modifications with chlorosulfonic acid improved the oxidation to BD. As sulfur was incorporated into the structure, the conversion and reaction rate of BA were improved. X-ray diffraction determined that the insertion of the sulfonic group created surface defects that generated lattice strain and decreased the initial structure's crystallinity. Additionally, crystallite size was calculated, showing a significant increase at a high doping level, likely due to the presence of functional groups. The increased

degree of sulfonation gradually decreased the (002) peak, indicating the effect of chemical delamination due to the chemical attack of chlorosulfonic acid. Finally, the optimized sample with an optimum proportion of chlorosulfonic groups was selected for studying the reactive oxidant species involved during the photocatalytic process, suggesting that the superoxide radical was the species with the greatest contribution to alcohol oxidation, especially in terms of selectivity for aldehyde formation.

In **Chapter 7**, entitled ***Thiosulfate-tailored graphitic carbon nitride from different precursors for enhancing the photocatalytic production of aldehydes***, graphitic carbon nitride was modified with sodium thiosulfate as a sulfur source to improve the photocatalytic performance in the oxidation of alcohols to aldehydes. g-C3N4 was obtained from different chemical compounds (urea, thiourea and melamine) in order to evaluate the impact of the precursor on the catalytic activity. The results showed that g-C3N4 obtained from urea (CNu) presented an improved photocatalytic activity, in addition to obtaining outstanding textural properties. Once the optimal g-C3N4 was identified, a series of catalysts with different Na2S2O3 ratios were evaluated in order to find the ideal concentration. It was determined that the SCNu-5% catalyst exhibited significantly improved reaction kinetics compared to the other ratios, in addition to presenting superior optical properties, such as a reduction in the bandgap, better absorption towards the visible light range and a lower charge recombination effect. Regarding the sulfur distribution in the g-C3N4 structure, it was observed that most of the sulfur was anchored on the catalyst surface, which could explain the remarkable increase in catalytic activity. On the other hand, the activity of the optimal catalyst was evaluated with different alcohols, and it was determined that this catalyst was more selective in the production of benzaldehyde (selectivity, >100%), followed by cinnamaldehyde (>23%) and vanillin (~5%). Finally, the study of the oxidation mechanism involved in obtaining cinnamaldehyde suggested a strong influence of photogenerated holes and the superoxide radical, the latter being more selective in the process.

In **Chapter 8**, titled ***Conclusions***, the main general conclusions obtained during the development of this thesis are outlined. It highlights the potential use of heteroatom-doped graphitic carbon nitride catalysts for application in the selective photooxidation of alcohols.

CHAPTER 1. INTRODUCTION

This chapter begins with a brief description of the environmental problems generated by conventional processes for obtaining aldehydes of industrial interest. Then, the implementation of alternative technologies, such as photocatalysis, coupled to some of the principles of green chemistry, is proposed. The importance of photocatalysis and the factors involved in this process, including the catalyst and the radiation source, are described in detail. For this purpose, a brief investigation is made on the methodologies used for the modification and optimization of catalysts, and as a complement, the modeling of the catalyst-light interaction is explored to fully understand the process of selective photo-oxidation of alcohols to obtain aldehydes.

1.1. INDUSTRIAL CHEMISTRY

Society faces a transcendental challenge associated with the dizzying growth of the world population. According to the most recent statistics provided by the United Nations, in 2022, the population reached 8 billion people and it is estimated that by 2037 this number could increase to 9 billion [1]. This phenomenon of population growth has led to greater demand for goods and services over time, putting pressure on industries to increase their large-scale production.

The increase in production has caused an accelerated expansion of industries, far exceeding original projections. However, the development of various industrial activities has triggered a series of detrimental effects, among which the excessive generation of industrial waste stands out. This situation is exacerbated by the fact that most industrial activities depend on the massive use of various raw materials, particularly fossil fuels such as coal, oil, and gas, essential to power various industrial processes [2,3]. Fossil fuels, which have traditionally driven economic growth since the Industrial Revolution have also triggered diverse damages to ecosystems globally, altering the balance necessary for the existence of various forms of life [4]. According to scientific research, the widespread use of these fossil fuels represents more than 75% of global greenhouse gas emissions and almost 90% of all carbon dioxide emissions, generating devastating consequences for the environment and climate change [5].

This scenario underscores the urgent need to address the environmental impact of various industries, including the aldehyde industry. Aromatic aldehydes are valuable chemicals used as intermediates in the production of various consumer products. Traditionally, these substances are predominantly prepared by chemical synthesis, which enables the large-scale production of aldehydes at profitable prices. However, this conventional process has several significant drawbacks: (i) it relies mainly on raw materials derived from petroleum, such as benzene, toluene, and xylenes; (ii) it requires high energy consumption; (iii) it involves the use of highly toxic catalysts; (iv) it generates substantial quantities of waste, which are often not managed properly; and (v) it is generally a low-selectivity process, necessitating additional purification steps [6].

Alternative methods, such as extracting aldehydes from natural sources, have been explored to avoid the use of petroleum-derived raw materials. However, these methods face limitations, including high demand for natural products, price fluctuations due to climate variability, and extremely low production yields [7].

Given these major challenges, both the scientific community and industries are compelled to seek more sustainable alternatives. This necessity has given rise to green chemistry, a discipline focused on developing more sustainable processes that utilize renewable raw materials and minimize energy consumption. Photocatalysis is a promising technology in this field, as it adheres to many principles of green chemistry, utilizing sunlight or ultraviolet light to activate catalysts and drive desired reactions [7].

The development of effective photocatalytic processes involves several factors, with the choice of catalyst being paramount. The catalyst significantly influences the reaction's speed and selectivity and has a considerable environmental impact. In this work, graphitic carbon nitride (g-C_3N_4) has been selected as the base catalyst. This metal-free material is easy to synthesize from widely available precursors and offers several advantages over metallic photocatalysts, which can be excessively expensive, unstable, and environmentally toxic [8].

1.1.1. Green chemistry

The term green chemistry was introduced approximately 40 years ago by the Environmental Protection Agency (EPA), because of the environmental crisis caused by industrial chemistry practices of the 20th century, which left devastating consequences due to the intensive use of raw materials derived from fossil fuels and inadequate waste management, directly affecting ecosystems and the organisms that inhabit them. Green chemistry practices have been gradually implemented in large industries, constantly seeking methodologies to reduce the generation of hazardous waste and promote more sustainable practices [9,10].

Green chemistry is based on twelve principles focused on maintaining the level of development and well-being provided by modern chemistry while ensuring economic viability, environmental protection, and social benefit. The principles of green chemistry are listed below:

1. Prevent the formation of waste instead of treating or cleaning it after its formation.
2. Design processes that maximize the incorporation of substrates into the final product.
3. Design processes that generate and use substances of low or no toxicity.
4. Design chemical products while maintaining their effectiveness and low toxicity.
5. Avoid the use of highly polluting auxiliary substances and, if used, work in the most innocuous way.
6. Minimize energy expenditure using methods at ambient temperatures and pressures.
7. Use renewable raw materials as much as possible, whenever it is technically and economically viable.
8. Avoid unnecessary derivatization as much as possible.
9. Use catalysts, preferably selective and superior to stoichiometric reagents, and try to ensure that they are of natural origin as much as possible.
10. Design chemical products that at the end of their useful life do not represent a problem for the environment and are biodegradable.
11. Use analytical methodologies in the process to follow and control the process, avoiding the formation of harmful and dangerous substances.
12. Use safe chemical reagents to reduce and prevent chemical accidents.

This approach has been implemented in fields as important as catalysis, a currently useful discipline that has facilitated the obtaining of chemical products of industrial interest, including products such as aldehydes [11].

1.1.2. Aldehydes industry

Aldehydes are formed by carbonyl functional groups (C=O), characterized by a carbon atom bonded to oxygen via a double bond. Additionally, the carbonyl group is linked to a hydrogen atom and a substituent (R) by single bonds, resulting in a final R-CHO structure. The atomic arrangement of the aldehyde is characterized by presenting sp^2 hybridization with planar trigonal geometry, giving the carbonyl group

the ability to conduct a dipolar movement. The molecular arrangement plus the presence of resonant forms causes polarization or the appearance of partial charges that affect its reactivity, resulting in an electrophilic carbon atom susceptible to attack by a nucleophile [12,13].

This dipolar movement causes the polarization or appearance of partial charges that contribute to the high reactivity of the aldehyde, resulting in an electrophilic carbon atom, giving aldehydes a behavior like that of acids, making them prone to nucleophilic addition reactions [14]. Depending on the type of hydrocarbon radical attached to the functional group, aldehydes can be classified as aliphatic and aromatic, each exhibiting specific properties [13,15].

Particularly, aromatic aldehydes have a general structure expressed as R-CHO, where the R component represents a benzene nucleus or another aromatic ring attached to the aldehyde function. Aromatic and aliphatic aldehydes are distinguished from each other by the interaction between their carbon and hydrogen atoms, with a stronger interaction standing out in aromatic aldehydes thanks to their flat ring-shaped arrangement [14]. This type of aldehyde has a remarkable ease of forming bonds with various compounds. This synthetic versatility has aroused great interest in the chemical industry, allowing this type of compound to be used as intermediates in the preparation of products with high added value [16].

The aldehyde industry has experienced significant growth. Studies have shown that in 2022, the aldehyde market was valued at $6.3 billion, and it is projected to reach $8.5 billion by 2031, promising steady growth at a compound annual growth rate of 3.9% [17]. The remarkable growth of the aldehyde market is attributed to the presence of key players worldwide who have developed various marketing methodologies to take the market to new heights. Some of the techniques used in the market include mergers, acquisitions, agreements, and product launches, among other strategies. This has ultimately led to an increase in aldehyde sales in several end-use industries [18].

The aldehydes of greatest industrial interest include formaldehyde, cinnamaldehyde, acetaldehyde, tolualdehyde, furfural, benzaldehyde, butyraldehyde, propionaldehyde, among others. Primarily, formaldehyde is a significant revenue generator in the market, as it is widely used by resin manufacturers. It is also commonly employed in

medical applications to kill bacteria and microbes with high growth capacity. On the other hand, benzaldehyde is used in the production of a wide range of chemicals, such as acridine dyes and styrene, among others [18,19].

Aldehydes possess properties that enable them to play various roles within the industry, primarily being used as intermediates or raw materials in the production of medical disinfectants, dyes, plastic additives, fragrances in cosmetics, agrochemicals, pharmaceuticals, flavorings in food, and other specialized chemical materials [20].

Some aldehydes are found naturally in flavoring agents, such as benzaldehyde, which provides the smell and flavor of fresh almonds; cinnamaldehyde or cinnamon oil and vanillin flavoring agents in vanilla beans [21] Vanillin, for example, is an aromatic aldehyde used to provide the characteristic aroma and flavor of vanilla and is widely used in the food and pharmaceutical industries [22]. At an industrial level, this compound can be obtained in two ways. Firstly, artificially, meaning through the catalytic oxidation of lignin or petroleum derivatives as chemical sources. The second method involves obtaining it from natural sources by directly extracting essential oils from the vanilla orchid [23]. These two methods of obtaining mark a significant difference between them, as natural vanillin reaches market prices ranging from 1,200 to 4,000 dollars/kg, compared to 15 dollars/kg for artificial vanillin. Due to the high cost and limited supply, the production of natural vanillin is considerably lower, accounting for less than 1% of the 16,000 tons of vanilla sold annually [24]. The difference in prices perceived in the market has motivated the industry to lean towards the artificial production of various aromatic aldehydes of great interest; so, current, efforts have been focused on finding a process that offers greater versatility and sustainability, adapting to market demands and environmental considerations.

1.2. PRODUCTION OF ALDEHYDES

The production of aldehydes is an active and constantly evolving area of research. For several years, new methodologies have been developed and implemented to continuously improve existing processes. Choosing the appropriate method depends on several

factors, including availability and cost of raw materials, selectivity toward the desired product, and environmental sustainability. In this sense, some of the methods commonly used to obtain aldehydes will be described below.

1.2.1. Microbial synthesis

The functionality and prominent industrial use of aldehydes have driven the search for more environmentally friendly techniques, among which the synthesis of aldehydes through the microbial route stands out. This synthesis method consists of the joint use of microorganisms and various enzymes that can produce aldehydes from organic substrates. Microorganisms use diverse metabolic pathways to carry out the conversion to aldehydes, which may include fermentation, biochemical oxidation, and enzymatic synthesis, which vary depending on the characteristics of the microorganism and the substrate. The constant improvement of the process involves the use of different methods such as biotechnology, the application of advanced genetic and metabolic engineering techniques, as well as the integration of computational approaches. Obtaining aldehydes by microbial means is usually carried out from precursors such as alcohols or carboxylic acids, exposed to oxidation and reduction reactions correspondingly [25].

The route that uses the reduction of carboxylic acids is an option that has aroused great interest and has been studied in recent years. This is due to the ease that nature offers to find abundant reserves of carboxylic acids from renewable and non-renewable sources. When synthesized biologically, they can be found in various environments and can act as potential precursors of various aldehydes [25].

The reduction of carboxylic acids can be carried out through carboxylic acid reductases (CAR), which can reduce carboxylic acids to the corresponding aldehydes. CAR, with the help of Adenosine triphosphate (ATP), activates carboxylic acid substrates and reduces them to aldehydes through Nicotinamide Adenine Dinucleotide Phosphate (NADPH). Previously, work has been reported on fungi such as *Polystictus versicolor, Neurospora crassa* and bacteria such as *Nocardia asteroides, Nocardia sp, Escherichia Coli, Bacillus subtilis* and other microorganisms. Specifically, there are known studies in which *Bacillus subtilis* has effectively acted thanks to the activity of the enzyme phosphopantetheinyl transferase (PPTase), capable of catalyzing the

post-translational activation of carrier proteins, allowing the reductase activity to be increased 20 times [25]

A specific example of the application of microbial synthesis is the vanillin production process, which follows methodologies like those proposed by Li and Frost, which consists of the use of a modified strain of *E. Coli* to produce vanilla from glucose [26].

The microbial synthesis of vanillin and other aldehydes is commonly carried out by genetically modified microorganisms that can retain quantities of aldehyde inside. However, an inherent limitation lies in the fact that microbial hosts are usually invaded by aldehyde reductases (AR), enzymes that actively participate in the conversion of aldehydes into unwanted alcohols, obtaining low yields and selectivities in the process.

To address these complications, strain engineering is used, focused on modifying the *E. Coli* genome to eliminate endogenous AR activity, to avoid the formation of unwanted products. However, these modifications require extensive work, since the selection of the correct target genes to eliminate this activity is challenging due to the complexity of the genome, the lack of knowledge of the functions of many genes and the genetic variability since there are certain genes that they act differently in strains [27].

At a general level, microbial synthesis of aldehydes has been hindered by processes such as enzyme isolation and purification, the non-reusability of enzymes due to their inability to replicate, protein structure instability, and the high sensitivity of enzymes to severe reaction conditions, necessitating the implementation of temperature, pressure, and pH control in processes. This set of limitations results in high production costs, making this methodology less applicable on an industrial scale [27].

1.2.2. Biocatalysis

Biocatalysis, or enzymatic catalysis, has established itself as a line of interest within the field of catalysis, and has been the subject of intensive studies in recent years, positioning it as an ideal candidate for various chemical applications. This discipline uses different types of enzymes as intermediates, which act as catalysts in typical chemical reactions, performing the function of accelerating chemical reactions

and increasing selectivity to the product of interest. When used at laboratory scale, it usually offers fast kinetics and reactions are carried out under mild conditions, working within the framework of sustainability [28,29].

This line of catalysis focuses on the research, design, and evaluation of biocatalysts to make them more robust and allow reactions that are difficult to achieve by traditional chemical methods. It also aims to obtain pure compounds in one-step transformations, achieving transformations with simple starting materials. All this with the aim that the enzymes catalyze reactions that are regio and enantioselective.

Biocatalytic reactions can be carried out in two different environments, the first being developed by means of *in vivo* assays, where enzymes act inside a living organism, as happens in microbial synthesis. On the other hand, they can be developed by means of *in vitro* assays, where enzymes act outside a living organism, in turn acting on isolated cells, tissues, or organs under controlled conditions [29]. In this context, the obtaining of aldehydes employing *in vitro* biocatalysis, a methodology that traditionally employs two types of enzymes, the first of which is the production of aldehydes, which are:

Aldehydes can be obtained in an *in vitro* environment using isolated *Carboxylic acid reductases*, also known as aryl-aldehyde oxidoreductases, which are Mg^{2+} dependent enzymes capable of catalyzing the reduction of carboxylic acids to aldehydes through the action of ATP and the reducing capacity of NADPH. *In vitro* reduction involves fewer side reactions and simple optimization of reaction conditions [26]. Although this method has been used on numerous occasions, it also has several drawbacks. One of these is that reductases require post-translational modifications to be active; however, such modifications can be difficult to develop due to the structural complexity of the enzymes. Therefore, it becomes a difficult process to predict and control, which can hinder both the production and use of modified enzymes for industrial applications. Furthermore, this approach is overshadowed by the widespread strict use of additional co-substrates and co-factors, as cofactors such as NADPH and ATP are difficult to regenerate. In this case, it is suggested to perform co-factor regeneration in cells of living organisms (*in vivo*) since the continuous addition of co-factors implies high production costs [28,30,31].

Alcohol oxidase (AOX) enzymes are often isolated from different microorganisms and are used as oxidants for various types of primary alcohols. These immobilized enzymes allow faster reactions with short-chain alcohols. However, as the chain length increases, the solubility of the enzymes decreases, which significantly reduces their oxidative capacity [32]. On the other hand, there are other enzymes used to oxidize alcohols such as galactose oxidase, achieving a selective production of aldehydes in an O_2 environment. However, sometimes an excess of oxidation occurs leading to the synthesis of acids [32]

Some complications encountered in the oxidation method using immobilized AOX include their scarcity in nature and their reduced enzymatic activity at pH above 6, which limits their efficacy under extreme conditions [33].

Unlike systems implemented in living organisms, the use of the *in vitro* system brings advantages such as reduced toxicity to cells, reduced mass transfer problems, and less by-product generation. However, as highlighted above, challenges arise such as the addition of external cofactors, limited enzyme reusability, and low enzyme performance when exposed to different temperature and pH conditions [34]. To address the latter challenge, the potential of thermophilic enzymes has been explored. These enzymes operate at elevated temperatures, typically 50°C or higher, remaining active for long periods (up to 18 hours), and at an alkaline pH of ca. 9.5. Although this strategy provides the enzymes with the ability to operate under extreme conditions, some problems remain with the adaptation of this methodology, which poses difficulties for its successful application in industry [35].

1.2.3. Chemical production of aldehydes

There are two common ways of producing aldehydes by chemical routes, which are discussed below.

Alcohol oxidation reactions convert the -OH alcohol group into a carbonyl group (-CHO). This type of reaction is usually carried out using oxidizing agents such as osmium oxide (OsO_4), dimethyl sulfoxide (C_2H_6OS), potassium dichromate ($K_2Cr_2O_7$), or potassium permanganate ($KMnO_4$) in acidic or basic media to activate the oxidizing agent. Having the reaction been completed, the aldehyde is isolated

from the reaction medium by purification techniques such as extraction, distillation, or crystallization [36].

Although this process is widely used in industry, it still presents significant environmental challenges due to the use of highly toxic, expensive, and hazardous organic solvents and oxidants. In addition, some studies have reported the use of heavy metals, resulting in the generation of difficult-to-treat residues [37]. Conventional methods for the oxidation of alcohols also have limitations concerning the selectivity and the yield. In addition, some reactions require high oxygen pressures, and some catalysts need high temperatures to achieve efficient catalytic activity, resulting in long reaction times and high energy consumption [38]

Chemical reduction of carboxylic acids involves the use of reducing agents to convert the carboxylic acid functional group (-COOH) to an aldehyde group (-CHO). There are several routes to carry out this reaction, one of the most common being catalytic reduction with a reducing agent such as molecular hydrogen (H_2) in the presence of a metal catalyst, either palladium (Pd) or platinum (Pt). Although this is a widely used process, it has disadvantages such as high energy consumption, since high pressures are needed for the H_2 to produce an effective reaction, and high temperatures to activate the catalyst and increase the reaction rate [39]

Another method used is through reducing agents such as sodium borohydride ($NaBH_4$) or lithium aluminum borohydride ($LiAlH_4$), which can donate hydrides (H-) to the carbonyl group, completing the synthesis of the aldehyde. Although it is a widely used process, it has disadvantages such as limited selectivity due to excessive reduction caused by reducing agents that can result in the formation of undesired alcohols. Furthermore, several studies have indicated that the routes to aldehydes require acid chloride intermediates, reductive sulfidation of thiol esters, and stoichiometric amounts of the reducing agent, in addition to working at very low-temperature conditions (-30 to -40°C) [40].

The processes of microbial, biocatalytic, and chemical synthesis of aldehydes continue to present strong limitations due to their unsustainable nature. Faced with this problem, both industries and the scientific community have been forced to address various challenges related to the clean production of aldehydes, which has led to the

implementation of technologies and the adoption of responsible industrial practices aligned with the principles of green chemistry, whose objective is to promote the development of more sustainable chemical processes, minimize environmental impact and improve efficiency in the use of resources.

1.3. PHOTOCATALYSIS

The term "photocatalysis" was coined in 1911 when the German scientist Alexander Eibner investigated the effect of light irradiation on ZnO to decolorize Prussian blue. Since then, numerous studies have been conducted to understand the factors influencing photocatalyst activity and its application in various areas of chemistry [41]. However, it was not until the 1970s, amid the oil crisis, that researchers focused their investigations on the search for new alternative energy resources. From 1972 onwards, interest in photocatalysis increased exponentially with the discovery of photo-assisted electrochemical water splitting using TiO_2 as the working electrode and a platinum counter electrode, under the application of a chemical or electrochemical potential. This discovery marked the beginning of new perspectives for obtaining alternative energy resources [42]

Photocatalytic processes depend on four fundamental variables: light absorption, charge separation, charge migration to the surface, and charge recombination. Photocatalysis includes chemical processes that occur under irradiation and use semiconductor materials, which contain valence and conduction bands. The energy difference between these two bands is known as the bandgap (E_g), usually below 3 eV [43].

The photocatalysis process, illustrated in Fig. 1.1, begins with the activation of the semiconductor material or photocatalyst by the application of a light source, typically in the near ultraviolet radiation region, with an energy equal to or above the bandgap. This process generates charge carriers, such as photogenerated electrons (e^-) and holes (h^+) [44]. When the charge carriers are separated and transferred to the surface of the photocatalytic semiconductor, reactive oxygen species (ROS) are generated on the surface, which are of great interest due to their ability to react on the surface of the catalyst, triggering redox reactions and the degradation of various organic compounds [45]. Due to the discontinuous state between the semiconductor bands, e^- and h^+ can exist in the system for a very short time. Some holes directly

degrade or oxidize chemical compounds adsorbed on the semiconductors, while other holes are captured by water to generate highly reactive and strongly oxidizing ·OH radicals. On the other hand, e^- react with electron acceptor such as O_2, to generate $O_2^{\cdot-}$, H_2O^- and other ROS [46].

During photocatalysis, the charge recombination phenomenon limits the efficiency of the reaction. This process can occur both in the bulk and at the surface, where excited electrons tend to rapidly return to the valence band and recombine with holes, resulting in the deactivation of charge carriers through the release of absorbed energy. The recombination effect negatively interferes with the process by reducing the lifetime of the charge carriers, which are the main active species that trigger the desired photochemical reactions [47,48]. Therefore, to minimize the recombination it is a priority to use electron and hole scavengers or to resort to surface defect engineering. The latter option is considered the most viable. Not only does it involve the design and fabrication of catalysts with lower recombination capabilities, but it also leads to the production of more stable and efficient photocatalysts with improved chemical, physical, and optical properties. In addition, studies have shown that the use of oxygen in the reaction medium can prevent recombination of electron-hole pairs, while allowing the formation of superoxide radicals [49–51].

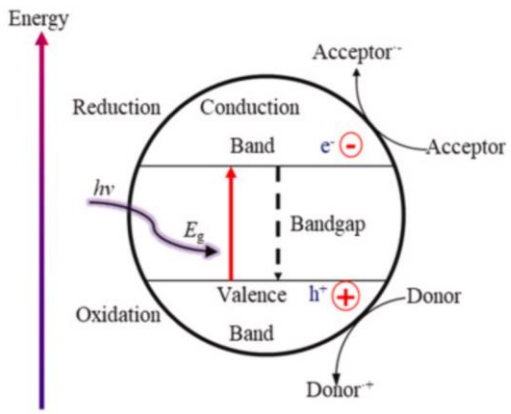

Fig. 1.1 *Photocatalysis process* [46].

Photocatalytic technology has been considered one of the most effective technologies for its ability to take advantage of the abundant availability of sunlight or artificial light [52]. It also stands out for the diverse qualities of its catalysts, characterized by excellent performance and selectivity, as well as high stability and capacity for regeneration and reuse. These characteristics, together with the ease of operation in mild conditions, make photocatalysis a highly efficient process that significantly reduces energy and economic costs in the long term, while maintaining an excellent sustainability ratio. As a result, this technology has become applicable in a wide range of processes [50,53].

Some of its applications are obtaining new energy sources or chemical fuels such as hydrogen, selective synthesis of organic compounds, and degradation of persistent organic or inorganic pollutants in wastewater such as herbicides, pesticides, and refractory dyes. It is also widely used in air treatment, CO_2 photoreduction and other environmental applications [52,54,55].

1.3.1. Photocatalysts used

Various photocatalysts have been investigated for several years, covering a wide range of semiconducting materials, from metal oxides such as ZrO_2, SiO_2, MnO_2, $BiVO_4$, Fe_2O_3, CeO_2, SnO_2, WO_3, Bi_2WO_6, etc., ferrite-based photocatalysts, organometallic frameworks (MOF), conjugated organic polymers as polytophene and covalent organic frameworks (COF), or sulfur compounds (CdS, MoS_2), among others. Materials such as metal sulfides and titanium dioxide (TiO_2) have been studied for their ability to interact with chemical compounds and catalyze redox reactions of interest [56]. Fig. 1.2 schematically presents the position of the valence and conduction bands that define the bandgap energy for different semiconductors, which can be expressed in eV or volts.

Metal sulfide semiconductors have been considered potential candidates for use in photocatalytic reactions, thanks to their narrow band gap, which allows them to efficiently absorb various light sources while the arrangement of their energy bands establishes them as materials with excellent catalytic performance and efficient charge separation capability. However, these catalysts are very unstable chemically, causing photo-corrosion after several cycles of use, as well as the lack of active sites, and tend to auto-oxidation [57].

On the other hand, TiO_2 has been the subject of massive study due to its ability to degrade harmful organic wastes [58]. TiO_2 stands out among other semiconductors due to its high photoactivity, affordability, non-toxic nature, and remarkable stability, which gives it a long lifetime when exposed to normal environmental conditions. In addition, it is relatively inexpensive if compared to other photocatalysts [59]. Despite these advantages, TiO_2 presents challenges related to its broad forbidden band, which reaches a value of 3.2 eV. This feature limits the activation outside the ultraviolet radiation range, which means that it can only be activated by light sources emitting wavelengths between 100 and 387 nm, which represent only 5% of the total solar spectrum [60]. In addition, the rapid charge recombination, and the limitation of working outside of ultraviolet radiation directly affect the selectivity and quantum efficiency of the catalyst. This is due to the ability to produce highly oxidizing hydroxyl radicals, which can pose problems in applications such as organic synthesis, where excessive ROS production can lead to over-oxidation processes. Finally, TiO_2 faces additional challenges due to its low affinity for hydrophobic organic compounds [61], resulting in low adsorption of contaminants, and, consequently, a decrease in its catalytic activity [62]

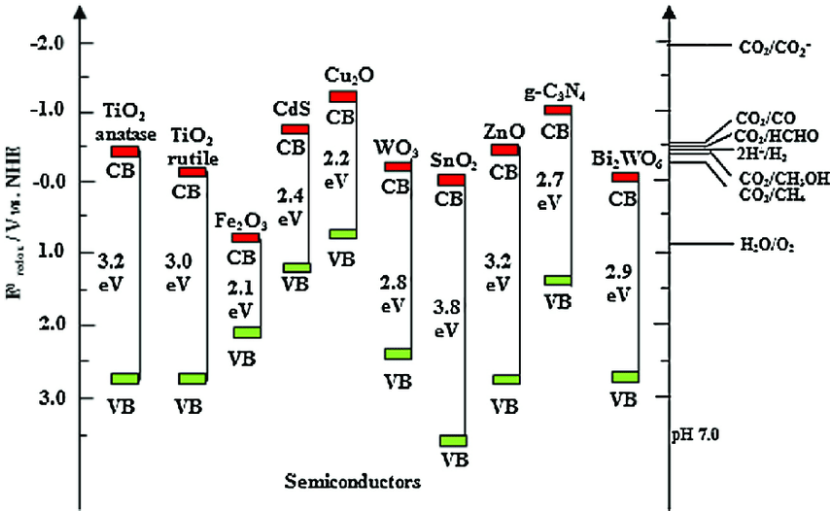

Fig. 1.2 *Relative positions of valance and conduction bands for some common photocatalysts* [63].

Like TiO_2, various semiconductors present similar challenges related to high synthesis costs, low catalytic performances, and the risk of heavy

metal contamination. For this reason, the design and development of catalysts with improved photocatalytic performance, higher charge separation efficiency, and better light absorption capacity to exploit the solar radiation spectrum have been widely studied for several years [64] To achieve these desired characteristics, several material modification techniques have been employed, such as morphological engineering, elemental doping, defect engineering, functionalization, and heterojunction construction, among others. In addition to focusing on catalyst modification, different techniques have been used, such as exploring the reaction mechanism and adjusting the reaction medium by adding alternative oxidants like peroxides, O_3, and persulfate [65].

In the search for more efficient semiconductors, new alternatives have emerged, among which various organic catalysts stand out, such as graphitic carbon nitride (CN or of g-C_3N_4), which is presented as a promising candidate because it is a metal-free material, leading to a significant reduction in the environmental footprint.

1.4. GRAPHITIC CARBON NITRIDE

1.4.1. Discovery

The discovery of g-C_3N_4 dates to 1834, when Jöns Jacob Berzelius and Justus von Liebig synthesized "melon" by pyrolyzing a mixture of ammonium chloride and potassium thiocyanate, obtaining a yellow, amorphous, insoluble powder. Although Liebig was unable to determine the exact structure of melon, he approximated its elemental composition, consisting of 3 carbon atoms for every 4 nitrogen atoms, with a stoichiometric ratio of (3:4) [66] At that time, it was predicted that g-C_3N_4 might possess an extraordinarily high hardness, like that of the diamond. In the 1990s an attempt was made to obtain this ordered solid but the intended goal was not achieved, the study took another direction and was focused on the synthesis of polymeric carbon nitrides (C_x,N_y, H_z), which exhibited excellent properties by incorporating nitrogen, carbon, and hydrogen into a single chemical structure [67].

Continuing this work, Liu and Cohen performed computational simulations of carbon nitride, demonstrating that it could exist in five different phases, with the graphitic phase being one of the most stable allotropes under ambient conditions [68].

A few years later, in 2007, Lotsch et al. experimentally discovered the exact chemical structure of melon, describing it as an infinite chain

of melamine (tri-s-triazine) monomers with NH bridges connected by hydrogen bonds in a zigzag geometry. It received the name polymeric carbon nitride (PCN) [69]

In 2009, Wang et al. pioneered the synthesis of high-quality g-C_3N_4 by thermal polymerization and published their first work using g-C_3N_4 as a photocatalyst for hydrogen water splitting under visible light [70]. This milestone marked an important point in the history of g-C_3N_4, as from this discovery studies exploring the potential of g-C_3N_4 as a photocatalytic material began to increase indiscriminately, resulting in the publication of more than ten thousand papers in the last ten years [70].

1.4.2. Structural Properties

Graphitic carbon nitride is a polymeric organic semiconductor characterized by a layered structure with interlayer distances decreasing from 0.335 to 0.315 nm, positioning it as a nitrogen-enriched analog of graphite. Solid-state NMR has determined that this compound exhibits a two-dimensional structure forming covalent bonds between nitrogen and carbon, organized in a flat hexagonal network as illustrated in Fig. 1.3 Additionally, the carbon and nitrogen atoms adopt sp^2 hybridization, leading to a trigonal planar geometry and the formation of delocalized π bonds, granting it excellent electrical conductivity and highly fascinating optical properties [71,72].

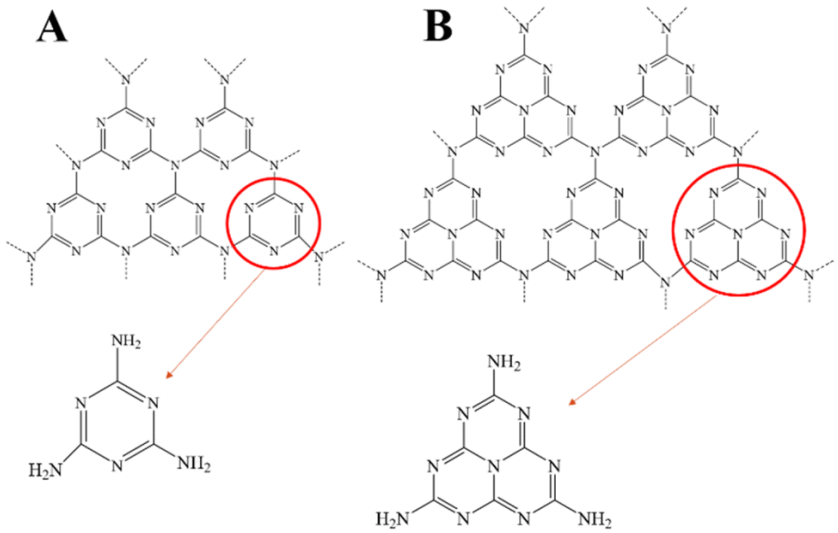

Fig. 1.3 *(a) g-C_3N_4 composed of s-triazine (C_3N_3) units, and (b) g-C_3N_4 composed of tri-s-triazine (C_6N_7) units*[73].

Each layer of graphitic carbon nitride is composed of either s-triazine (C_3N_3) or tri-s-triazine (C_6N_7) units Fig. 1.3, the latter being the most stable phase at room temperature. These units are linked together by tertiary amines, suggesting the presence of defects in the structure. The layers are held together by van der Waals forces, forming a porous three-dimensional graphitic structure, known as a honeycomb arrangement. This layered configuration provides a suitable surface for possible photocatalytic and adsorption reactions [74]. This material possesses the properties of an n-type semiconductor, with a moderate bandgap of 2.7 eV and suitable valence and conduction band potentials of +1.6 eV and -1.1 eV, respectively. Due to its bandgap and graphite-like planar shape, charge carriers can be transported across bands at wavelengths near 460 nm in the visible solar spectrum [75,76]. g-C_3N_4 has shown promise in oxidation processes due to its easy and cost-effective synthesis method using earth-abundant elements such as carbon and nitrogen. In addition, its unique electronic structure gives it excellent thermal stability, withstanding temperatures up to 600°C. Moreover, g-C_3N_4 also possesses high stability against mechanical and chemical resistance, it is biocompatible and shows resistance to extreme pH conditions. As a metal-free material, it does not decompose into toxic and harmful substances during use, making it environmentally friendly [77].

1.4.3. Synthesis of graphitic carbon nitride

The most common methods for synthesizing pure and modified g-C_3N_4 include thermal polymerization, sol-gel, hydrothermal, and microwave-assisted methods, see Fig. 1.4. These processes involve the use of different precursors, substrates, solvents, and atmospheres. Thermal polymerization is preferred as one of the most studied and adopted methods due to the ease it offers in the synthesis process [78].

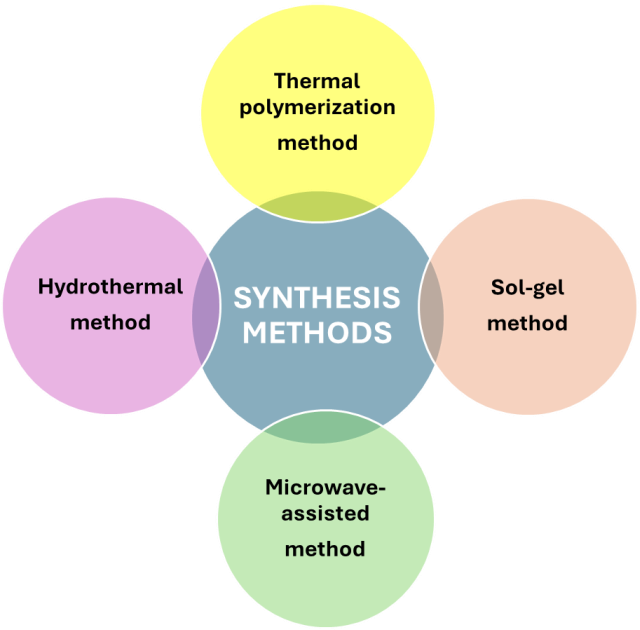

Fig. 1.4 *methods of g-C_3N_4 synthesis*

Thermal polymerization

Thermal polymerization is one of the frequently used methods and involves the thermal treatment of different nitrogen-rich organic precursors, as depicted in Fig. 1.5 This process consists of heating the precursor in a semi-closed vessel at a temperature of 500 to 650°C, with a heating rate ranging from 5 to 10°C/min for 2-4 hours, in an air or inert atmosphere. Under these conditions, thermal polymerization occurs, which is divided into two processes: polyaddition and polycondensation. Initially, the process starts with the polymerization of the precursors to give melamine (polyaddition process). The melamine is then condensed by loss of ammonia (polycondensation), which finally results in the formation of the polymer g-C_3N_4, a yellowish solid. In addition, crystalline graphitic carbon nitride can be synthesized, usually by adding a mixture of eutectic salts [79].

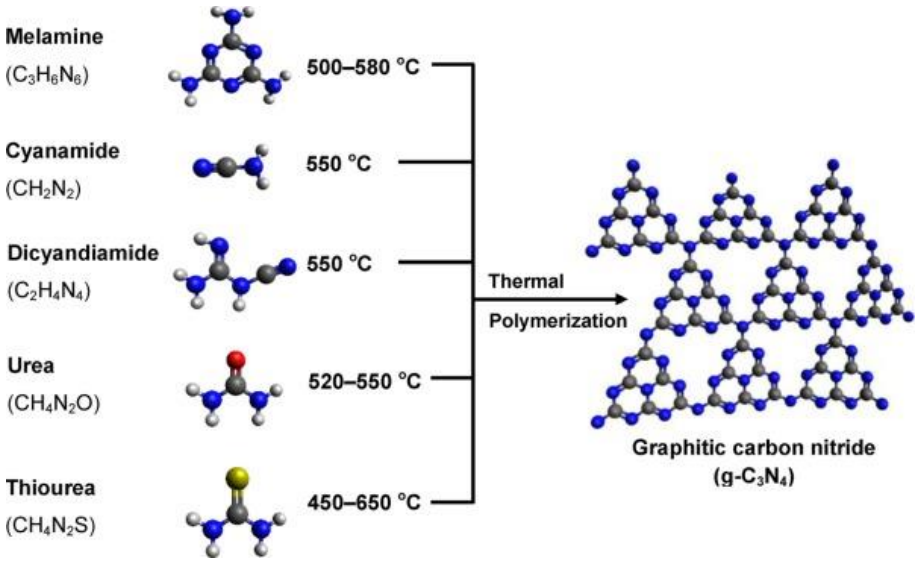

Fig. 1.5 *Formation of g-C_3N_4 through thermal polymerization*[80].

Sol-gel method

It is a wet chemical method and is commonly used for the preparation of nanomaterials. It is an ideal method due to its simple preparation, processing at room temperature and lower cost. The characteristic precursors are metal alkoxides and chlorides, which carry out hydrolysis and polycondensation reactions to form a colloid. Over time, when the colloidal particles are added, a gel is formed, which is usually taken to calcination processes. This method is particularly used to load metal nanoparticles on the catalytic surface, thus improving its properties. For example, Chang et al., synthesized a g-C_3N_4 /TiO_2 heterojunction, with improved properties such as its surface area and homogeneous size distribution after coupling TiO_2 with g-C_3N_4.[81].

Hydrothermal method

This method provides crystal formation and improved morphologies by controlling the surface chemistry by adjusting the sol composition, reaction temperatures and pressures. Furthermore, it is a method that offers facilities to dissolve or react poorly soluble species under usual conditions using various types of solvents and additives. This synthesis method can be carried out by means of simple equipment and an environmentally friendly process. For instance, Tian et al. prepared a Bi_2WO_6/g-C_3N_4 composite via a hydrothermal method for the

degradation of methyl orange. Chou et al. synthesized BiO_xI_y/g-C_3N_4 nanocomposite using a controlled hydrothermal method for the degradation of crystal violet under visible light irradiation [82]

Microwave method

The microwave-assisted method has been lately used for the preparation of g-C_3N_4. Compared to the previously described methods, this approach takes advantage of microwave radiation, since the homogeneous distribution of its waves allows for uniform heating and efficient energy transfer to the material. In addition, using a solvothermal pressurized, closed reaction system, allows a complete and accelerated reaction, ensuring a more homogeneous synthesis of the material, with fewer defects and decreased energy consumption. For example, Dai et al. synthesized g-C_3N_4 at a temperature of 180°C for only 30 min under microwave irradiation, resulting in a material with improved photocatalytic performance [83]

1.4.4. Nanostructure design

Nanostructure design is used to modify the morphology, texture, electronic structure, and surface of the catalyst in order to improve certain material properties, such as charge separation and optimization of catalytic performance. The design of various morphological nanostructures can be achieved by two different methods:

Top-down approach

To obtain 2D nanosheets, the g-C_3N_4 obtained from thermal polymerization is usually exfoliated by methods such as thermal, ultrasonic, and chemical exfoliation [84].

Thermal exfoliation is one of the simplest, most efficient, and environmentally friendly methods due to the absence of oxidizing acids and low energy consumption. This method is based on heating the g-C_3N_4 and water mixture and then subjecting the dispersed g-C_3N_4 to freezing for several hours to expand the water molecules, breaking the van der Waals interactions between the films [84].

Ultrasonic peeling uses ultrasonic waves combined with a suitable liquid solvent, such as glycerol, water, or isopropyl alcohol, to attack each g-C_3N_4 layer, dispersing them and specifically breaking the van der

Waals forces between the layers, resulting in the formation of nanosheets [85].

Chemical peeling involves the selective removal of layers of bulk material to obtain thin nanosheets. It requires the addition of strong acids such as sulfuric and nitric acids for approximately 24 hours. Then, to produce complete exfoliation, oxidizers such as sodium nitrate and potassium permanganate are added to achieve an atomically thick g-C_3N_4 layer. Finally, hydrogen peroxide is added to obtain g-C_3N_4 in the form of nanosheets [85].

Bottom-up method

This method consists of forming nanostructures from smaller units, such as atoms and molecules which are assembled to construct the desired nanoparticles, endowing the materials with specific properties not found in conventional materials. Among the most representative techniques of this approach are the following.

In *sequential self-assembly of molecules*, nanoparticles are obtained by the spontaneous organization of atoms, molecules, or particles without the need for external forces. This phenomenon occurs by interactions between the molecules themselves, which can be electrostatic, hydrophobic, hydrophilic, hydrogen bonding, etc. For example, Xiao et al. synthesized nanosheets using melamine and cyanuric acid by subjecting them to a hydrolysis process, followed by self-assembly into layered microrod precursors [86]. The presence of interlayer fields allows polar molecules such as ethanol and glycerol to mix, generating gaseous products that break the π-π interaction during the subsequent calcination process. These gaseous products are released in a way that creates numerous pores in the layers [79].

Template method encompasses several approaches, such as the rigid template method and the flexible template method. It is used to control the particle size of the material in order to obtain g-C_3N_4 nanometer structures and control the specific surface area and active sites. Generally, a template involves dispersing the precursor material to fill its pores, followed by various methods to process the precursors and shape the g-C_3N_4 according to the template. Finally, the template is removed using acids to obtain the material of interest.

Template-free method usually employs techniques such as hydrothermal processes, in which nanostructures are mainly designed by supramolecular self-assembly. This process is carried out by non-covalent bond connections, with hydrogen bonds being highly directional and significantly affecting the formation of supramolecular self-assemblies. Compared to template methods, template-free methods do not require hazardous agents such as hydrofluoric acid to remove the template [87].

1.4.5. g-C_3N_4 modifications

Despite the remarkable characteristics of g-C_3N_4, it is important to recognize some of its limitations that lead to low photocatalytic activity. These include its low specific surface area, lack of active sites, low electrical conductivity, and high charge carrier recombination rate, which have restricted its application to date.

For this reason, ongoing research is evaluating different approaches to modify the physicochemical properties of g-C_3N_4. These methods include doping, heterojunction formation, defect engineering and others chemical modifications, which have proven useful in altering the morphology, achieving different degrees of polymerization, improving the photoelectric properties, functionalizing the structure and chemical characteristics of g-C_3N_4 and improving its photocatalytic activity, and overall performance, broadening its range of applications [70,85,88]

Elemental doping

Elemental doping is a methodology used to improve the photocatalytic activity of various semiconductors, especially n-type semiconductors such as g-C_3N_4, characterized by having a particularly different energy band structure compared to metals and insulators, which limits their catalytic activity to the ultraviolet region. Elemental doping consists of adding metallic or non-metallic elements into the g-C_3N_4 lattice, modulating its electronic, optical, and other physicochemical properties. One of the most important modifications obtained by this technique is the adjustment of the g-C_3N_4 energy band structure, regulating the lowest unoccupied molecular orbital (LUMO) and the highest occupied molecular orbital (HOMO) [88].

g-C_3N_4 is an optimal material for tuning electronic properties because its layered structure facilitates homogeneous doping. In addition, the size of the dopant particles can be easily controlled by adjusting the

degree of exfoliation and the number of stacks. There is also a derivative technique known as co-doping, which pursues the same objective as elemental doping but incorporates two or more elements into the g-C_3N_4 structure [89].

Metal doping consists of the addition of metallic impurities in the g-C_3N_4, generating metal-N_x active sites. Generally, this addition can accelerate the charge transfer and decrease the bandgap size, improving the light absorption capability and reagent adsorption capacity [90]. Metal doping of NCs can be carried out by high-temperature condensation of single-molecule precursors or inorganic metal salts. Metals used for doping include transition metals, rare earth metals, alkali metals, and alkaline earth metals, including elements such as iron, zinc, ruthenium, cobalt, nickel, titanium, and copper [91].

Some studies have shown that metal doping contributes to the change of charge distribution on the g-C_3N_4 surface. As illustrated in Fig. 1.6, two different scenarios are observed. One in which donor levels are formed and the other in which acceptor levels are formed, which favors carrier mobility and enhances light absorption.

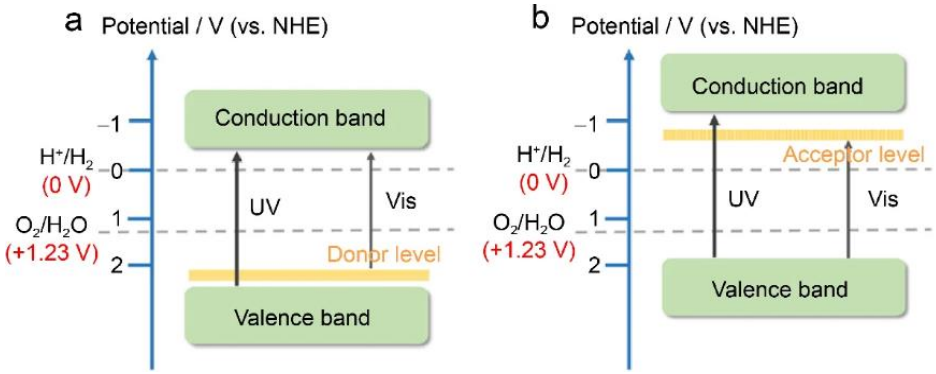

Fig. 1.6 *(a) formation of donor levels and (b) acceptor levels with metal doping*[89].

Alkali and alkaline earth metal ions, such as Mg^+, K^+, and Na^+, are of particular interest as dopant elements due to their low toxicity and cost, as well as their high electron-donating capacity. This contributes to enhancing the concentration of charge carriers and minimize the rate of charge recombination. The modifications produced by these metals lead to electron loss and delocalization, which directly affect the energy band structure of the catalyst. In addition, the lost electrons of these metals overlap with the top and bottom layers of the g-C_3N_4, creating interlayer

charge transfer channels that enhance the photogenerated charge separation and migration efficiency of the catalyst. In the case of Li and Na, the modifications occur in the N-plane voids due to their small atomic radii and weak metallic properties [87].

g-C_3N_4 catalysts doped with transition metals and rare earth metals exhibit a reduced bandgap and a red-shifted absorption edge. This is due to the strong interaction of metal ions with g-C_3N_4, which generates a metal-ligand charge transfer and significantly increases the absorption range of visible light. Especially in rare earth metals, the unoccupied 4s and 5s orbitals can act as electron capture centers, enhancing the catalytic activity of g-C_3N_4 [87].

Non-metallic doping has arisen due to the leaching problems of metal ions produced in metal doping. Some nonmetallic heteroatoms studied for g-C_3N_4 modification include oxygen, sulfur, phosphorus, boron, fluorine, iodine, and bromine, along with self-doping with elements such as carbon and nitrogen. These elements are introduced from various precursors and under different types of atmospheres [87,90].

Non-metallic elements usually possess high electronegativity and ionization energy, which favors the delocalization of conjugated π electrons and the formation of covalent bonds by accepting electrons from other compounds. This process leads to the formation of new impurity energy levels, modification of properties such as electron mobility and conductivity, resulting in higher redox yields of g-C_3N_4. Importantly, the use of a dopant with a lower electronegativity value than the substituted element and its homogeneous distribution within the g-C_3N_4 are key factors for effective bandgap-reducing doping [92]. For this reason, techniques have been developed to allow the controlled introduction of non-metallic atoms into the g-C_3N_4 structure, including ball milling, solvent heat, thermal oxidation, and chemical oxidation [87,93]. This doping method is frequently applied nowadays, as it has proven to be very beneficial due to its simple synthesis procedure, environmental friendliness, and abundant availability of elements in nature [94]. In addition, co-doping with two or more atoms has been employed as an excellent doping strategy. For example, in a study by Huang et al. co-doped g-C_3N_4 with phosphorus and oxygen was prepared, in which phosphorus atoms substituted for carbon sites, while oxygen atoms substituted for nitrogen sites, resulting in improved properties such as reduced bandgap, improved charge separation, and

specific surface area [93]. Similarly, Lui et al. performed a study on co-doping with phosphorus and sulfur, which favored the opening of new pathways for photogenerated electrons and holes, resulting in improved photocatalytic activity of g-C_3N_4 [91].

Formation of g-C_3N_4 heterojunctions

The formation of heterojunctions is achieved by modifying the covalent and non-covalent bonds between semiconductors. In the specific case of g-C_3N_4, most of the heterojunctions have been obtained by non-covalent bonds with other semiconductors. Some advantages provided by this technique can be translated into obtaining narrow bandgaps, spatial separation of charges, modification of energy levels, and improvement of the adsorption capacity of reagents, obtaining materials with excellent redox properties [95].

Functionalization of g-C_3N_4

For some time, efforts have been made to introduce functional groups, including oxygen-containing groups such as -O-, -OH, and -COOH, or urea group, to design high-efficiency g-C_3N_4-based systems [96]. For example, in the work of Cheng et al. sulfur-doped g-C_3N_4 was synthesized, and it was determined that sulfur atoms substituted for nitrogen atoms, contributing to the modification of the surface area and morphology of the material, which resulted in improved catalytic activity [75].The surface functionalization method has demonstrated its capability as a tool to create active anchor sites and tune the chemical and electronic properties of the g-C_3N_4. This strategy is based on two approaches, such as covalent and non-covalent interaction techniques [75].

The covalent interaction technique is carried out through covalent bonds between the g-C_3N_4 structure and the chemical modifier. They can be performed by oxidation/carboxylation, amination, sulfonation/phosphorylation, etc. In some cases, this approach allows the formation of defects in the material by altering the sp^2 structure of the material, undergoing significant changes in its electrical characteristics. However, these defects can benefit various applications, such as catalysis. When talking about covalent techniques, care must be taken, as irreversible alterations can be created [97,98].

Non-covalent interaction technique is an attractive approach due to its accessibility and ease of forming physical bonds and weak intermolecular interactions, such as van der Waals interactions, electrostatic interactions, π-π interactions, hydrogen bonds, etc. [99].

1.4.6. Applications

g-C_3N_4 possesses unique characteristics that make it an attractive material for a wide range of applications, including medical healthcare, food safety, and environmental applications. Due to its photocatalytic properties, g-C_3N_4 has been used in cancer cell treatment, drug delivery systems, wound healing, artificial enzyme development, bioimaging, and photodynamic therapy [98]. The high chemical stability, structural composition, and biocompatibility make g-C_3N_4 a potential candidate used as a detection system for toxins in food, such as aflatoxin, a highly toxic metabolite produced by certain fungi. In addition, this material is used as a raw material to construct antibacterial and functional packaging films for food preservation [100]. Lastly, g-C_3N_4 has been used mainly in photocatalysis and photoelectrochemistry to carry out photodegradation reactions of organic compounds in liquid and gas phases, hydrogen photo-production, CO_2 reduction, and organic synthesis of high value-added compounds [98,100].

1.5. SELECTIVE OXIDATION OF ALCOHOLS

The selective oxidation of alcohols to carbonyl compounds has become one of the most essential transformations in the organic synthesis of high value-added organic chemicals and intermediates for the pharmaceutical and food industries. Furthermore, it has emerged as an environmentally friendly alternative, which allows reactions to be carried out in water and under aerobic conditions. At present, this field accounts for about 30% of the total production of the modern chemical industry. Therefore, the partial aerobic oxidation of carbohydrates and alcohols has been intensively studied during the last decade [101].

For several years, industrial-scale oxidation processes have been developed that require the use of intermediates such as organic solvents, external additives, and metal oxidants, including chromates, permanganates, and organic peroxides in stoichiometric proportions. These processes tend to generate large amounts of waste, which poses several environmental challenges related to the minimization and proper

management of these wastes. In response to this problem, recent research has focused on the development of alternative methodologies capable of replacing conventional processes, promoting catalytic conversions aligned with sustainability [102].

1.5.1. Oxidants used

For years, interest has focused on the search for environmentally friendly oxidants with strong oxidative properties, considering peroxides such as tert-butyl hydroperoxide (TBHP) and hydrogen peroxide (H_2O_2) as options. Although they are powerful oxidants, they present problems when used industrially, mainly due to their high cost and the difficult storage and transport, since they are unsteady compounds. For this reason, oxygen has been explored as a promising alternative that changes the perspective of selective oxidation processes, since it is an abundant, low-cost resource with no associated pollution [103,104]

During the oxidation of organic compounds, reactive oxygen species (ROS) are generated in situ and are usually carried out at ambient temperature and pressure conditions [105]. ROS, also known as secondary oxidants, are derived from primary oxidants such as hydrogen peroxide (H_2O_2) or ozone (O_3), which act in combination with various technologies such as UV radiation, Fenton, photo-Fenton, photocatalysis, electrolysis, ultrasonic irradiation, and wet air oxidation, among others [106]. These reactive oxygen species are divided into radical and non-radical molecules. Free radicals are characterized by having one or more unpaired electrons in their outer orbital, which gives them high reactivity and the ability to indirectly oxidize various chemical compounds. This characteristic is very useful in applications such as water purification, where they degrade most persistent organic pollutants into simpler, less toxic, and biodegradable substances, such as CO_2, H_2O, inorganic ions, and mineralized salts. In addition, in recent years, ROS have demonstrated their usefulness in the synthesis of aromatic compounds of industrial interest, promising an efficient means to develop selective reactions that ensure minimal waste generation from the formation of secondary products [107].

In various chemical reactions, common ROS include hydroxyl radicals (·OH), singlet oxygen ($^1O_2$), superoxide anions ($O_2^{\cdot-}$), perhydroxyl radicals ($HO_2^{\cdot}$), peroxyl radicals (ROO·) and alkoxyl radicals (RO·). Among them, the ·OH radical stands out, especially for its ability

to oxidize soluble inorganic and organic substances by electron transfer, dehydrogenation, addition, and self-extinction. It is distinguished as one of the most active oxidants due to its high standard oxidation-reduction potential of 2.8 V [108]. This property makes it highly reactive and capable of participating in a wide variety of chemical processes. In addition, ·OH is considered an excellent radical due to its low toxicity and short half-life, although the latter property also poses challenges for the development of multistage processes, necessitating the continuous addition of external precursor agents to ensure the formation of sufficient ·OH for a complete reaction. Another limitation of ·OH is its low selectivity at the end of the process, which can lead to undesired overoxidation, posing a problem in systems requiring specific formation of high-purity products [109].

In addition to ·OH, other vital ROS are superoxide radicals and singlet oxygen, which, unlike ·OH, tend to have longer half-lives and moderate oxidation potentials, resulting in controlled and slightly selective oxidation reactions. Several studies have highlighted the functionality of lattice oxygen (O_L) derived from transition metal oxides present in catalysts, taking advantage of their role as moderate ROS directly oxidize organic matter. The use of O_L in chemical synthesis and biomass conversion offers important benefits, as selective oxidation of the organic substrate, preventing overoxidation, and often acting with fast reaction rates [110,111]

1.5.2. Additives or solvents used

The selective oxidation of alcohols usually requires the use of additives or solvents, such as alkaline chemicals and polar organic solvents that favor alcohol deprotonation and improve catalytic efficiency. Although these substances act positively in obtaining aldehydes, they present problems in terms of hazardous waste generation and significant industrial safety risks, due to the high flammability resulting from the mixture of these solvents with oxygen. For this reason, there is now a need to apply more environmentally friendly and safer additives or solvents [112]. In recent years, the use of aqueous solvents has been promoted to reinforce safe practices in the industry. Among these, water has stood out as an ideal environmentally friendly solvent, in line with sustainability principles.

1.5.3. Catalysts used

For several years, selective oxidation processes have been carried out using two types homogeneous and heterogeneous catalysts.

The homogeneous processes are characterized by catalysts based on organic ligands attached to metal groups, such as metal salts. Several studies have shown that homogeneous catalysts are highly beneficial due to the numerous options for ligand selection, in addition to containing modulable properties such as morphology and pore size, providing large specific surface area, dense and dispersed active sites that drive high catalytic activities [113–115]. However, despite possessing remarkable characteristics, these catalysts still face some challenges related to the use of metals and organic ligands that are expensive and highly polluting, along with the susceptibility of these ligands to oxidative self-degradation. In addition, difficult catalyst recovery, extreme reaction conditions and the need to apply additional bases or other additives have limited the applicability of these catalysts to promote the oxidation process. For this reason, there has been a growing interest in heterogeneous catalysts, which have shown great efficiency in the catalytic oxidation processes of alcohols [112,116].

The heterogeneous catalysts are mostly composed of active species, such as metal oxides, immobilized on catalytic supports. These materials are of great interest due to their ability to operate under relatively mild conditions and their reusability potential [117]Similarly, they can easily incorporate various metals into their structure and modify certain properties by adding active components to the porous materials, such as dispersion and stability. In addition, they are remarkably resistant to poisoning by substrates and by-products. These characteristics facilitate the optimization of reactions and contribute to lower final production costs [118,119]. Nonetheless, metallic catalysts face some limitations, such as leaching and the release of highly toxic residues. In response to this issue, research has focused on the use of non-metallic species, which not only can mitigate leaching but also generate less toxic residues [120]. After conducting various comparative studies between homogeneous and heterogeneous catalysts, it has been determined that heterogeneous catalysts are not only effective but also offer a sustainable and cost-effective alternative [121].

The selective oxidation of alcohols to the corresponding aldehydes illustrated in Fig. 1.7 has been carried out in recent years using metallic

catalysts, and the reaction mechanism can be summarized in several essential steps [122]:

1. Adsorption of the alcohol on the surface of the catalyst.
2. Bonding of the metal atom through a link with the -OH group of the alcohol, creating metal alkoxide and a metal hydride.
3. Removal of hydrogen by the metal through the β-hydride elimination process.
4. Desorption of the product of interest (aldehyde or ketone).
5. Regeneration of the active sites of the metals.

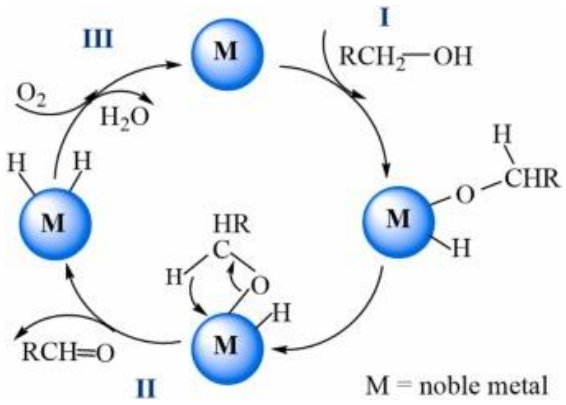

Fig. 1.7 *Oxidation of alcohol to the corresponding aldehyde over a noble metal* [122].

1.6. BENZALDEHYDE PRODUCTION

Benzaldehyde is obtained industrially through two processes, both involving a final stage of recovery and purification of the benzaldehyde by distillation. These processes are described as follows.

1.6.1. Hydrolysis of benzyl chloride

This process begins with the reaction between liquid toluene and chlorine gas which, mixed at temperatures between 100 and 200°C, produce benzyl chloride. The benzyl chloride produced undergoes hydrolysis in the presence of an acid or basic catalyst, resulting in a mixture of benzaldehyde and various by-products. Several studies have shown that acid hydrolysis generates yields of more than 90%. Although this process has been frequently used in industry, it still presents several problems, in particular high environmental pollution due to the generation of residual chlorine and toxic acid during the process, which raises significant doubts about its industrial application [123–125].

1.6.2. Oxidation of toluene with air

Toluene oxidation can be carried out in liquid or gas phase. Liquid phase oxidation is performed by mixing toluene and air or pure oxygen in the presence of a metal catalyst at temperatures between 110-170°C and adjusting the pressure to keep the reaction medium in a liquid state. This process has been considered one of the most successful industrial applications, reaching selectivities towards benzaldehyde ranging between 30-73%. On the other hand, gas-phase oxidation is carried out by mixing toluene with air and passing this mixture through a catalyst at temperatures between 350-650°C. In this process yields range from 20-60%. Although toluene oxidation is the method that produces most of the synthetic benzaldehyde worldwide, it also has several important disadvantages, such as the need to operate under extreme conditions and low yields caused by the high reactivity of benzaldehyde, which, when interacting with free radicals, tends to generate undesirable by-products [126–129]. For this reason, alternatives capable of overcoming these drawbacks are currently being sought. The production of benzaldehyde by oxidation of benzyl alcohol is an attractive option [125].

1.6.3. Oxidation of benzyl alcohol to benzaldehyde

The oxidation of benzyl alcohol to benzaldehyde has shown remarkable characteristics, such as the ease of controlling various process parameters, its energy efficiency and the achievement of high selectivities and yields. One of the particularities of this process is that it is still under constant development, with research focused on its optimization through the use of benign oxidants combined with catalysts that can be modified to improve its efficiency [130]. In addition, this synthesis route has been of vital importance in the industry mainly due to the use of benzyl alcohol as a precursor, which offers advantages such as high availability and low market costs [131].

Precursor

Benzyl alcohol is a monoaromatic alcohol whose chemical structure is shown in Table 1.1. It is characterized by a colorless liquid with a faint, slightly characteristic odor. This compound is found in natural sources, such as plants of the genus Allium, tea leaves, essential oils of jasmine and hyacinth, among others [132]. It has low volatility and toxicity and is also a widely used polar solvent, especially in polymer applications.

World consumption of benzyl alcohol is estimated at between 100 and 1,000 metric tons per year, with a market price ranging from $2,000 to $2,500 per ton [133].

Table 1.1 *Physicochemical properties of benzyl alcohol* [134].

Name	**Benzyl alcohol**
Synonyms	Benzenemethanol; α-hydroxytoluene; phenyl carbinol; phenylmethyl alcohol; α-toluenol
IUPAC name	Phenylmethanol
Formula	C_7H_8O
CAS number	100-51-6
Form	Liquid
Molecular weight (g/mol)	108.14
Density (g/cm^3)	1.045
Water Solubility (g/L)	40

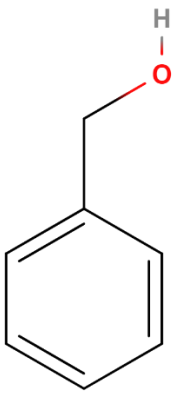

Benzyl alcohol is used to synthesize a variety of products for the flavors and fragrances industry, such as in the manufacture of cosmetics, fine fragrances, shampoos and toilet soaps. It also serves as an intermediate in the production of food products, being used as a food additive, preservative, in wines and beverages, both in free and bound form (bound to glycosides and/or phosphates) [135]. It is also used as a chemical intermediate in the manufacture of external analgesics, oral health medicines, household cleaning products, pesticides, inks, paints, adhesives, and hardening products (epoxy resins) [136], in addition to being an excellent pH regulator, solvent and/or viscosity reducing agent. It is also found naturally in fruits such as peaches, raspberries, blackberries and flowers such as petunia [136,137].

Product

Benzaldehyde is an organic chemical compound consisting of a benzene ring with an aldehyde substituent as shown in Table 1.2. It is characterized as the lightest aromatic aldehyde [138]. It is a colorless to pale yellow liquid with a strong fruity odor reminiscent of cherries and

bitter almonds. It is found naturally in the bark of stems, leaves, and seeds of plants such as almonds, cherries, peaches, and apples, and can also be found in various essential oils of bitter almonds, jackfruit, and Cananga [139]. The annual consumption of benzaldehyde is approximately 20 tons, and the price is around $260 per kg. In addition, it can be obtained from natural cinnamaldehyde, reaching up to 100 tons per year, and can be purchased for $110 [139].

Table 1.2 *Physicochemical properties of benzaldehyde* [140].

Name	**Benzaldehyde**	
Synonyms	Benzoic aldehyde; benzenecarbonal; phenylmethanal; benzenecarboxaldehyde	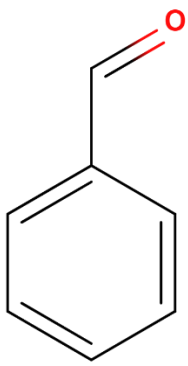
IUPAC name	Benzaldehyde	
Formula	C_7H_6O	
CAS number	100-52-7	
Form	Liquid	
Molecular weight (g/mol)	106.13	
Density (g/cm^3)	1.04	
Water Solubility (g/L)	3.3	

Benzaldehyde is the most useful aromatic aldehyde in the field of organic synthesis, as it contributes aroma and flavor to various products in the cosmetics industry, such as perfumes and soaps. Its importance also extends to the food industry, where it is used in the preparation of spices and flavors characteristic of almonds, cherries and walnuts. This compound is also widely used in the manufacture of flavoring agents [139,141]. Moreover, it serves as raw material in the synthesis of organic compounds such as pharmaceuticals, pesticides, fuels, repellents, lubricants, and dyes. It is also used as a solvent, additive for plastics and intermediate to produce other aldehydes, such as cinnamic, methylcinnamic, amylcinnamic, and hexylcinnamic aldehydes [142].

1.7. CINNAMALDEHYDE PRODUCTION

Cinnamaldehyde is usually obtained by two well-different routes.

1.7.1. Perkin synthesis

Perkin synthesis is one of the most widely used methods to synthesize cinnamaldehyde. In this process, compounds such as benzaldehyde and acetaldehyde interact in the presence of a polyethylene glycol ion-based resin catalyst. During the process, acetaldehyde is slowly added to benzaldehyde under alkaline conditions at a temperature ranging from 25-35°C, generating aldol condensation. At the end of the process, yields range from 75% to 85% [143]. However, this method presents some difficulties, particularly the generation of by-products, including cinnamaldehyde stereoisomers, which contribute to low yields, generation of polluting residues, and increased production costs due to additional purification processes. By the same token the industrial applicability of this method has become a challenge in the current context [144].

1.7.2. Steam distillation

One of the most commonly used methods to extract cinnamaldehyde from natural sources is steam distillation, which is used to directly extract the oil from cinnamon bark. This method consists of passing steam through the crushed cinnamon bark, facilitating the release of the essential oil containing a mixture of cinnamaldehyde and other compounds. Finally, the steam and oil mixture is separated by condensation and decantation, allowing the cinnamaldehyde-enriched essential oil to be collected. However, natural extraction requires large quantities of plant material to meet the global demand for cinnamaldehyde and longer extraction times, leading to higher energy consumption. These factors increase operating costs and may affect the economic viability of the process [145,146]. Alternatively, oxidation of cinnamyl alcohol could be considered an efficient way to produce cinnamaldehyde.

1.7.3. Oxidation of cinnamyl alcohol to cinnamaldehyde

The oxidation of cinnamyl alcohol to cinnamaldehyde is one of the most studied heterogeneously catalyzed oxidation reactions. In recent years, the study, synthesis, and application of various catalysts that have served as intermediates for the synthesis of cinnamaldehyde have been further studied, synthesized, and applied. In addition, efforts have

been made to improve the process using green oxidants such as molecular oxygen, following the principles of atomic economy and green chemistry practices [147]. One of the advantages of this method is that suitable catalysts can be operated under mild conditions, reducing the use of chemical solvents and the reliance on additional purification processes [148].

Precursor

Cinnamyl alcohol is an unsaturated aromatic organic compound whose structure is shown in Table 1.3. It occurs as a white crystalline solid with a characteristic sweet odor. Cinnamyl alcohol is present naturally in the leaves and inner bark of various trees of the genus *Cinnamomum*. It is present in balsams such as styrax and the resin of *Myroxylon pereirae*. Annual worldwide quantities of cinnamyl alcohol used industrially are estimated at 207 metric tons [149].

Table 1.3 *Physicochemical properties of cinnamyl alcohol*

Name	**Cinnamyl Alcohol**	
Synonyms	Cinnamyl alcohol; 3-phenyl-2-propen-1-ol; 2-propen-1-ol, 3-phenyl-; styryl carbinol; zimtalcohol	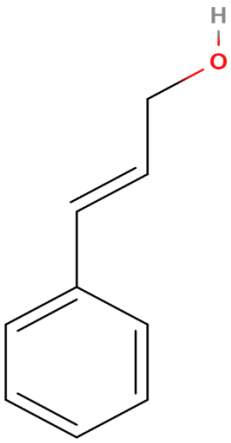
IUPAC name	(E)-3-fenilprop-2-en-1-ol	
Formula	$C_9H_{10}O$	
CAS number	104-54-1	
Physical form	Solid	
Molecular weight, (g/mol)	134.18	
Density, (g/cm^3)	1.044	
Water Solubility (g/L)	1.8	

Cinnamyl alcohol is a compound widely used in various industries. In the cosmetics sector, it serves as a raw material to produce aromatic oils, skin creams, shampoos, deodorants, and scented waters. In the food industry, it is used to flavor various products. Furthermore, it is often

used as a precursor for smart polymeric materials, such as cinnamyl acetate and cinnamyl methacrylate; the latter can be polymerized to create a double cross-linked product. In the pharmaceutical industry, cinnamyl alcohol is not only useful as a precursor for drugs to treat fungal infections and peripheral vascular conditions, but also in the synthesis of various advanced drugs such as dapoxetine and taxol [150].

Product

Cinnamaldehyde is an organic compound found naturally as trans-cinnamaldehyde. Its chemical structure, as shown in Table 1.4, consists of a phenyl group attached to an unsaturated aldehyde. It occurs as a yellow oily liquid with a cinnamon odor and sweet taste, characteristic of the natural trans (E) isomer. Known for its bioactive properties, cinnamaldehyde is found in cinnamon bark extract and other plants of the genus *Cinnamomum* [151,152]. The global cinnamaldehyde market was valued at $189 million in 2021 and is expected to reach $241.2 million by 2028 [153].

Table 1.4 *Physicochemical properties of cinnamaldehyde.*

Name	**Cinnamaldehyde**	
Synonyms	trans-Cinnamaldehyde, Cinnamic aldehyde, 3-Phenylacrylaldehyde, (E)-Cinnamaldehyde, Cinnamal	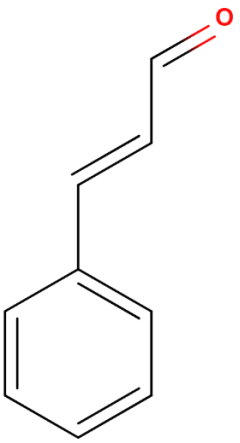
IUPAC name	(2E)-3-fenilprop-2-enal	
Formula	C_9H_8O	
CAS number	104-55-2	
Physical form	Liquid	
Molecular weight, (g/mol)	132.16	
Density, (g/cm^3)	1.041	
Water Solubility (g/L)	1.084	

Cinnamaldehyde is used to impart cinnamon flavor to a wide range of food products, such as chewing gum, ice cream, candies, beverages

and sweets. It has also been used as a flavoring agent in perfumes and cosmetic products, such as skin care treatments and hair growth products [154]. This compound can destroy fungal cells and inhibit the growth of bacteria, mycotoxins, and filamentous molds. These characteristics make it a valuable compound for the food preservation industry, being used in the construction of antimicrobial films that help maintain food quality and extend shelf life [155]. In addition, cinnamaldehyde is used as an intermediate for the synthesis of antiviral pharmaceuticals, such as HIV protease inhibitors [144]. Some of the challenges presented by this compound are its high volatility, instability, poor water solubility, irritant effect and its inability to reach target sites, which greatly limits its biological applications [151,156].

1.8. REACTOR MODELING

Despite much research in the photocatalysis field, the industrial application remains limited. This limitation is mainly due to the focus on the study and optimization of laboratory-scale photocatalysts, neglecting areas such as reactor design and construction [157].

Reactor modeling allows understanding the processes occurring inside the photocatalytic reactor from the beginning to the end of the reaction. This modeling must consider crucial parameters such as the distribution of radiant energy within the reaction space and the mass conservation equation of the compounds involved in the reaction, such as alcohols and aldehydes, as well as consider the various intermediate species that may arise during the photocatalytic process [158]. Achieving effective modeling and reactor design can not only improve the performance of photocatalysts, but also help identify obstacles that hinder the transition from R&D technology to actual practice [159]

1.8.1. Quantum efficiency

Photocatalytic efficiency is particularly influenced by three important elements: the photocatalyst, the photoreactor, and the light source. The interaction of these three elements is reflected in the differential quantum efficiency, calculated according to Eq. 1.1. This is defined as the ratio of the number of reacting molecules to the number of photons interacting with the catalyst, i.e. the photon absorption rate [160,161].

$$Q_E(\%) = \frac{r_{BA_0}\left(\text{mol}\cdot\text{m}^{-3}\cdot\text{s}^{-1}\right)}{e^{a,v}\left(\text{Einstein}\cdot\text{m}^{-3}\cdot\text{s}^{-1}\right)} \cdot 100 \tag{1.1}$$

where Q_E is the quantum efficiency, r_0 is the initial reaction rate, and $e^{\alpha,v}$ stands for the local volumetric rate of photon absorption (LVRPA).

1.8.2. Modeling of the radiation field

To determine the quantum efficiency, it is necessary to obtain the radiation flux emitted by the source and the quantification of the radiation absorption by the catalyst.

Determination of the radiation flux emitted by the source

There are several ways to determine the photon flux incident on the catalyst surface. Among them are those based on models that describe the distribution of light inside the reactors. In general, the existing light distribution models can be basically classified into two different types: linear source models and extensive source models [162].

In linear source models, the light source is assumed to be linear in shape, such as the linear source model with spherical emission (LSSE) and the linear source model with diffuse emission (LSDE), whereas, in extensive source models, the dimensions of the light source are considered, such as the extensive source model with volumetric emission (ESVE). Once the lamp emission model is defined, the radiation flux entering the reactor is defined analytically using the ray method, which allows for obtaining the spectral flux of radiant energy on the reactor [163].

Another alternative to obtain the radiation flux over the liquid-phase photocatalytic reactor is to use an experimental method of chemical actinometry, which consists of setting up a system used to measure the reaction rate of appearance or disappearance of a photochemically reacting compound with known kinetics and primary quantum yield. Once the reaction rate is known, the photon absorption rate can be calculated. Finally, there is a simpler way to measure the intensity of the light source and that is by means of a photometer or photodetector, which can also be a validation technique for more complex models [164].

Evaluation of photon absorption

It is essential to understand that the quantum yield depends on the operating conditions, such as temperature, reagent concentration, wavelength and local volumetric rate of photon absorption (LVRPA). The radiation field model is a fundamental part of modeling different types of

reactors, as it allows the determination of the local volumetric rate of photon absorption (LVRPA) for suspended systems, which is the number of photons absorbed per unit reactor volume and unit time at each location within the reaction space [165].

1.8.3. Radiative transfer

The radiative transfer allows to know the behavior of the light source within the heterogeneous dispersed system, where several fundamental phenomena are involved, such as elastic emission or scattering and absorption, as illustrated in Fig. 1.8. Scattering is presented as the redistribution of light in all directions, although normally with different intensities in different directions (anisotropic), depending on the characteristics of the particle. On the other hand, absorption depends on the local intensity of the light given by the modified electromagnetic field after light-particle interactions [166,167].

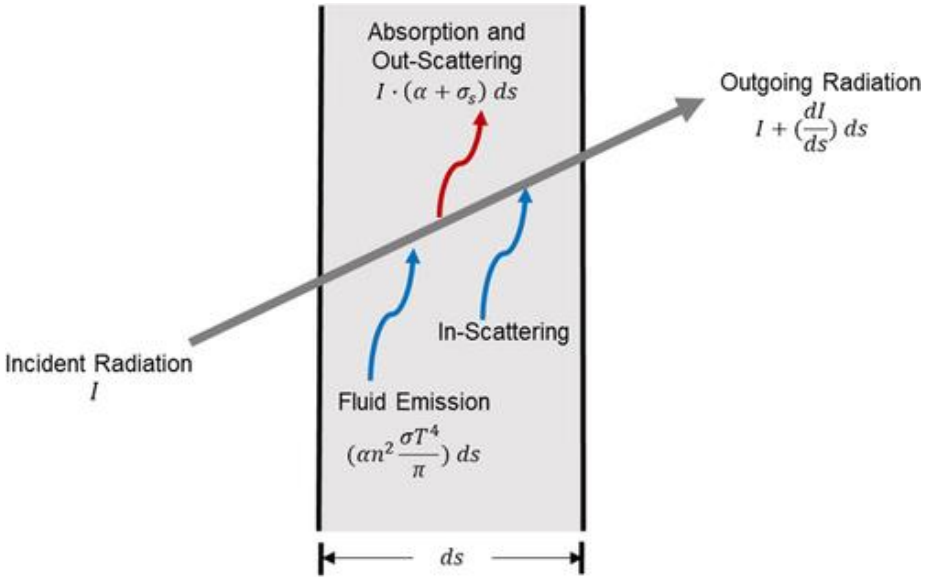

Fig. 1.8 *Process of radiative transfer for a control volume of a photoreactor* [166].

The simultaneous existence of these phenomena, based on the interaction of light and catalyst, makes the evaluation of the radiation field more complex. Therefore, the spatial and directional distribution of these phenomena has been systematically proposed by applying the radiative transfer equation (RTE) for the heterogeneous reactor as an approximation to the LVRPA [168].

$$\frac{dI_{\lambda,\underline{\Omega}}(\underline{x})}{ds} = -\kappa_\lambda(\underline{x})I_{\lambda,\underline{\Omega}}(\underline{x}) - \sigma_\lambda(\underline{x})I_{\lambda,\underline{\Omega}}(\underline{x}) + \frac{\sigma_\lambda(\underline{x})}{4\pi}\int_{\Omega'=4\pi} p(\underline{\Omega}' \rightarrow \underline{\Omega})\, I_{\lambda,\underline{\Omega}'} \quad (1.2)$$

where I_λ is the spectral radiation intensity, x represents x coordinate, s means the linear coordinate along the direction Ω , Ω represents solid angle, κ_λ is the spectral volumetric absorption coefficient, σ_λ represents spectral volumetric scattering coefficient and p ($\underline{\Omega}' \rightarrow \Omega$) means the phase function

To solve the equation, the optical parameters of the suspension are needed (κ_λ, σ_λ y p_λ). The Henyey-Greenstein function ($P_{HG,\lambda}$) was employed to calculate the phase function:

$$p(\underline{\Omega}' \rightarrow \underline{\Omega}) = \frac{1-g_\lambda^2}{(1+g_\lambda^2-2g_\lambda^2 u_0)^{3/2}} \quad (1.3)$$

where g_λ means the asymmetry factor (dimensionless) and u_0 is the cosine of the angle between the direction of the incident and scattered photons.

Rigorous and simplified numerical methods have been proposed to solve the RTE in systems with absorption and scattering. Numerical methods frequently used to calculate the LVRPA are known as the discrete ordinate, which allows solving problems in systems where scattering levels are high. In addition, the finite volume method and Monte Carlo simulation are used. These are useful to analyze the trajectory of many photons. With this information and using the appropriate mathematical and statistical model it is possible to obtain the distribution and profile of the photon absorption velocity [169].

1.9. SPECIFIC OBJECTIVES

The main objective of this thesis research is to develop catalytic systems based on g-C_3N_4, modified with metallic and non-metallic compounds, for application in the synthesis of organic compounds of high industrial value through photocatalytic processes. The specific objectives pursued are listed below:

1) To synthesize new photo-catalytic materials based on g-C_3N_4 through structural and surface modifications, using simple synthesis methods focused on reducing the use of complex equipment, toxic or hazardous substances, high energy consumption, and the generation of waste at the end of the process.

2) To fully characterize the synthesized materials to obtain relevant chemical, structural, morphological, electronic, and optical information, justifying the catalytic results and enabling the optimization of their catalytic properties.

3) To evaluate the catalytic properties of the new materials in the selective photooxidation of alcohols using a laboratory reactor and different operating and lighting conditions. Special attention is given to using water as a solvent, air as an oxidizing agent, and an appropriate light source for catalytic activity, operating at room temperature and atmospheric pressure.

4) To model the radiation-material interaction to determine photon absorption profiles and the photocatalytic performance under the operating conditions used.

REFERENCES

1. Población | Naciones Unidas Available online: https://www.un.org/es/global-issues/population (accessed on 29 June 2022).
2. Akhundi, A.; Badiei, A.; Ziarani, G.M.; Habibi-Yangjeh, A.; Muñoz-Batista, M.J.; Luque, R. Graphitic Carbon Nitride-Based Photocatalysts: Toward Efficient Organic Transformation for Value-Added Chemicals Production. Molecular Catalysis 2020, 488, 110902, doi:10.1016/J.MCAT.2020.110902.
3. Chen, S.; Wang, F.; Haroon, M. The Impact of Green Economic Recovery on Economic Growth and Ecological Footprint: A Case Study in Developing Countries of Asia. Resources Policy 2023, 85, 103955, doi:10.1016/J.RESOURPOL.2023.103955.
4. Shivanna, K.R. Climate Change and Its Impact on Biodiversity and Human Welfare. Proceedings of the Indian National Science Academy. Part A, Physical Sciences 2022, 88, 160, doi:10.1007/S43538-022-00073-6.
5. Nations, U. Causes and Effects of Climate Change | United Nations.
6. Giparakis, S.; Winkler, M.; Rudroff, F. Nature Stays Natural: Two Novel Chemo-Enzymatic One-Pot Cascades for the Synthesis of Fragrance and Flavor Aldehydes. Green Chemistry 2024, 26, 1338–1344, doi:10.1039/D3GC04191C.
7. Corberán, V.C.; Gómez-Avilés, A.; Martínez-González, S.; Ivanova, S.; Domínguez, M.I.; González-Pérez, M.E. Heterogeneous Selective Oxidation of Fatty Alcohols: Oxidation of 1-Tetradecanol as a Model Substrate. Catal Today 2014, 238, 49–53, doi:10.1016/J.CATTOD.2014.03.033.
8. Jiang, X.; Wang, W.; Wang, H.; He, Z.H.; Yang, Y.; Wang, K.; Liu, Z.T.; Han, B. Solvent-Free Aerobic Photocatalytic Oxidation of Alcohols to Aldehydes over ZnO/C3N4. Green Chemistry 2022, 24, 7652–7660, doi:10.1039/D2GC02293A.
9. de Marco, B.A.; Rechelo, B.S.; Tótoli, E.G.; Kogawa, A.C.; Salgado, H.R.N. Evolution of Green Chemistry and Its Multidimensional Impacts: A Review. Saudi Pharmaceutical Journal 2019, 27, 1–8, doi:10.1016/J.JSPS.2018.07.011.

10. Sheldon, R.A. The E Factor 25 Years on: The Rise of Green Chemistry and Sustainability. Green Chemistry 2017, 19, 18–43, doi:10.1039/C6GC02157C.
11. Aguilar, Q.J.G.F. " Síntesis Verde de Benzaldehído Por Oxidación de Estireno Mediante El Catalizador Cu-MOF-74 Obtenido Bajo Condiciones Sostenibles " Tesis Para Obtener El Grado de Maestro En Ciencias e Ingeniería Presenta : Q . José Gabriel Flores Aguilar Autónoma Metrop, Universidad Autónoma Metropolitana, 2017.
12. Vijayraghavan, S.; Saini, N. Aldehyde-Associated Mutagenesis—Current State of Knowledge. Chem Res Toxicol 2023, 36, 983–1001, doi:10.1021/ACS.CHEMRESTOX.3C00045/ASSET/IMAGES/LARGE/TX3C00045_0004.JPEG.
13. Lopachin, R.M.; Gavin, T. Molecular Mechanisms of Aldehyde: A Chemical. Chem Res Toxicol 2014, 27, 1081, doi:10.1021/TX5001046.
14. Meza, A.; Campbell, M.E.; Zmich, A.; Thein, S.A.; Grieger, A.M.; McGill, M.J.; Willoughby, P.H.; Buller, A.R. Efficient Chemoenzymatic Synthesis of α-Aryl Aldehydes as Intermediates in C-C Bond Forming Biocatalytic Cascades. ACS Catal 2022, 12, 10700–10710, doi:10.1021/ACSCATAL.2C02369/ASSET/IMAGES/LARGE/CS2C02369_0008.JPEG.
15. Paschke, A.S.; Selishchev, D.; Lyulyukin, M.; Kozlov, D. Selective Visible-Light-Induced Photooxidation of Benzylic Alcohols to Corresponding Carbonyl Compounds over Titanium Dioxide: A Study of the Structure-Reactivity Relationship. Molecular Catalysis 2022, 524, 112263, doi:10.1016/J.MCAT.2022.112263.
16. Zhao, H.; Caldora, H.P.; Turner, O.; Douglas, J.J.; Leonori, D. A Desaturative Approach for Aromatic Aldehyde Synthesis via Synergistic Enamine, Photoredox and Cobalt Triple Catalysis. Angewandte Chemie International Edition 2022, 61, e202201870, doi:10.1002/ANIE.202201870.
17. Aldehyde Market Size, Share | Growth Report 2031 Available online: https://straitsresearch.com/press-release/global-aldehyde-market-share (accessed on 5 March 2024).
18. Aldehyde Market Size, Share, Growth | Report, 2030 Available online: https://www.marketresearchfuture.com/reports/aldehyde-market-2356 (accessed on 5 March 2024).

19. Aldehydes Market Size, Demand, Share, Sales, Growth & Trend – FMI Available online: https://www.futuremarketinsights.com/reports/aldehydes-market (accessed on 5 March 2024).
20. Ribeaucourt, D.; Bissaro, B.; Lambert, F.; Lafond, M.; Berrin, J.G. Biocatalytic Oxidation of Fatty Alcohols into Aldehydes for the Flavors and Fragrances Industry. Biotechnol Adv 2022, 56, 107787, doi:10.1016/J.BIOTECHADV.2021.107787.
21. Aldehyde - Industrial Uses, Synthesis, Reactions | Britannica Available online: https://www.britannica.com/science/aldehyde/Other-carbonyl-compounds-of-industrial-use (accessed on 5 March 2024).
22. Fernandez, H.; Lorente, C. Antioxidant Properties of Vainillin during Photosensitizaed Oxidation of Biomolecules. Free Radic Biol Med 2023, 208, S121, doi:10.1016/J.FREERADBIOMED.2023.10.276.
23. Böhme, A.; Ulrich, N.; Schüürmann, G. Amino Chemoassay Profiling of Aromatic Aldehydes-Unraveling Drivers of Their Skin Sensitization Potency. Chem Res Toxicol 2023, 36, 1055–1070, doi:10.1021/ACS.CHEMRESTOX.3C00013/ASSET/IMAGES/LARGE/TX3C00013_0012.JPEG.
24. Kunjapur, A.M.; Tarasova, Y.; Prather, K.L.J. Synthesis and Accumulation of Aromatic Aldehydes in an Engineered Strain of Escherichia Coli. J Am Chem Soc 2014, 136, 11644–11654, doi:10.1021/JA506664A/SUPPL_FILE/JA506664A_SI_001.PDF.
25. Basri, R.S.; Rahman, R.N.Z.R.A.; Kamarudin, N.H.A.; Ali, M.S.M. Carboxylic Acid Reductases: Structure, Catalytic Requirements, and Applications in Biotechnology. Int J Biol Macromol 2023, 240, 124526, doi:10.1016/J.IJBIOMAC.2023.124526.
26. Kunjapur, A.M.; Prather, K.L.J. Microbial Engineering for Aldehyde Synthesis. Appl Environ Microbiol 2015, 81, 1892–1901, doi:10.1128/AEM.03319-14/ASSET/5A90D921-262C-48FB-B956-CA0256C02FC9/ASSETS/GRAPHIC/ZAM9991160960002.JPEG.
27. Rodriguez, G.M.; Atsumi, S. Toward Aldehyde and Alkane Production by Removing Aldehyde Reductase Activity in Escherichia Coli. Metab Eng 2014, 25, 227–237, doi:10.1016/J.YMBEN.2014.07.012.
28. Kazimírová, V.; Rebroš, M. Production of Aldehydes by Biocatalysis. Int J Mol Sci 2021, 22, 22, doi:10.3390/IJMS22094949.
29. France, S.P.; Hepworth, L.J.; Turner, N.J.; Flitsch, S.L. Constructing Biocatalytic Cascades: In Vitro and in Vivo

Approaches to de Novo Multi-Enzyme Pathways. ACS Catal 2017, 7, 710–724, doi:10.1021/ACSCATAL.6B02979/ASSET/IMAGES/LARGE/CS-2016-02979U_0018.JPEG.

30. Napora-Wijata, K.; Strohmeier, G.A.; Winkler, M. Biocatalytic Reduction of Carboxylic Acids. Biotechnol J 2014, 9, 822–843, doi:10.1002/BIOT.201400012.
31. Strohmeier, G.A.; Schwarz, A.; Andexer, J.N.; Winkler, M. Co-Factor Demand and Regeneration in the Enzymatic One-Step Reduction of Carboxylates to Aldehydes in Cell-Free Systems. J Biotechnol 2020, 307, 202–207, doi:10.1016/J.JBIOTEC.2019.10.016.
32. Dienys, G.; Jarmalavičius, S.; Budriene, S.; Čitavičius, D.; Sereikaite, J. Alcohol Oxidase from the Yeast Pichia Pastoris—a Potential Catalyst for Organic Synthesis. J Mol Catal B Enzym 2003, 21, 47–49, doi:10.1016/S1381-1177(02)00135-2.
33. Schober, L.; Dobiašová, H.; Jurkaš, V.; Parmeggiani, F.; Rudroff, F.; Winkler, M. Enzymatic Reactions towards Aldehydes: An Overview. Flavour Fragr J 2023, 38, 221–242, doi:10.1002/FFJ.3739.
34. Claassens, N.J.; Burgener, S.; Vögeli, B.; Erb, T.J.; Bar-Even, A. A Critical Comparison of Cellular and Cell-Free Bioproduction Systems. Curr Opin Biotechnol 2019, 60, 221–229, doi:10.1016/J.COPBIO.2019.05.003.
35. Wu, S.; Snajdrova, R.; Moore, J.C.; Baldenius, K.; Bornscheuer, U.T. Biocatalysis: Enzymatic Synthesis for Industrial Applications. Angewandte Chemie International Edition 2021, 60, 88–119, doi:10.1002/ANIE.202006648.
36. Ciriminna, R.; Pandarus, V.; Béland, F.; Xu, Y.J.; Pagliaro, M. Heterogeneously Catalyzed Alcohol Oxidation for the Fine Chemical Industry. Org Process Res Dev 2015, 19, 1554–1558, doi:10.1021/ACS.OPRD.5B00204/ASSET/IMAGES/LARGE/OP-2015-002047_0004.JPEG.
37. Akbari, A.; Amini, M.; Tarassoli, A.; Eftekhari-Sis, B.; Ghasemian, N.; Jabbari, E. Transition Metal Oxide Nanoparticles as Efficient Catalysts in Oxidation Reactions. Nano-Structures & Nano-Objects 2018, 14, 19–48, doi:10.1016/J.NANOSO.2018.01.006.
38. Qin, K.; Zang, D.; Wei, Y. Polyoxometalates Based Compounds for Green Synthesis of Aldehydes and Ketones. Chinese Chemical Letters 2023, 34, 107999, doi:10.1016/J.CCLET.2022.107999.

39. Liu, C.; Qin, Z.X.; Ji, C.L.; Hong, X.; Szostak, M. Highly-Chemoselective Step-down Reduction of Carboxylic Acids to Aromatic Hydrocarbons via Palladium Catalysis. Chem Sci 2019, 10, 5736–5742, doi:10.1039/C9SC00892F.
40. Butler, N.; Kunjapur, A.M. Carboxylic Acid Reductases in Metabolic Engineering. J Biotechnol 2020, 307, 1–14, doi:10.1016/J.JBIOTEC.2019.10.002.
41. Irshad, M.; Ain, Q. tul; Zaman, M.; Aslam, M.Z.; Kousar, N.; Asim, M.; Rafique, M.; Siraj, K.; Tabish, A.N.; Usman, M.; et al. Photocatalysis and Perovskite Oxide-Based Materials: A Remedy for a Clean and Sustainable Future. RSC Adv 2022, 12, 7009–7039, doi:10.1039/D1RA08185C.
42. Zhu, S.; Wang, D. Photocatalysis: Basic Principles, Diverse Forms of Implementations and Emerging Scientific Opportunities. Adv Energy Mater 2017, 7, 1700841, doi:10.1002/AENM.201700841.
43. Balapure, A.; Ray Dutta, J.; Ganesan, R. Recent Advances in Semiconductor Heterojunctions: A Detailed Review of the Fundamentals of Photocatalysis, Charge Transfer Mechanism and Materials. RSC Applied Interfaces 2024, 1, 43–69, doi:10.1039/D3LF00126A.
44. Ahmed, S.N.; Haider, W. Heterogeneous Photocatalysis and Its Potential Applications in Water and Wastewater Treatment: A Review. Nanotechnology 2018, 29, 342001, doi:10.1088/1361-6528/AAC6EA.
45. Ismael, M. Environmental Remediation and Sustainable Energy Generation via Photocatalytic Technology Using Rare Earth Metals Modified G-C3N4: A Review. J Alloys Compd 2023, 931, 167469, doi:10.1016/J.JALLCOM.2022.167469.
46. Zheng, J.; Zhang, P.; Li, X.; Ge, L.; Niu, J. Insight into Typical Photo-Assisted AOPs for the Degradation of Antibiotic Micropollutants: Mechanisms and Research Gaps. Chemosphere 2023, 343, 140211, doi:10.1016/J.CHEMOSPHERE.2023.140211.
47. Hureau, M.; Duplouy, L.; Andrade, P.H.M.; De Waele, V.; Moissette, A. Photoinduced Electron-Hole Recombination in Zeolites: Marcus Theory Applied to DCB@MFI Systems. J Photochem Photobiol A Chem 2024, 448, 115337, doi:10.1016/J.JPHOTOCHEM.2023.115337.
48. Rafiq, U.; Majid, K. Mitigating the Charge Recombination by the Targeted Synthesis of Ag2WO4/Bi2Fe4O9 Composite: The Facile Union of Orthorhombic Semiconductors towards Efficient

Photocatalysis. J Alloys Compd 2020, 842, 155876, doi:10.1016/J.JALLCOM.2020.155876.
49. Chong, M.N.; Jin, B.; Chow, C.W.K.; Saint, C. Recent Developments in Photocatalytic Water Treatment Technology: A Review. Water Res 2010, 44, 2997–3027, doi:10.1016/J.WATRES.2010.02.039.
50. Nagella, S.R.; Vijitha, R.; Ramesh Naidu, B.; Krishna Rao, K.S.V.; Ha, C.S.; Venkateswarlu, K. Benchmarking Recent Advances in Hydrogen Production Using G-C3N4-Based Photocatalysts. Nano Energy 2023, 111, 108402, doi:10.1016/J.NANOEN.2023.108402.
51. Bhatkhande, D.S.; Pangarkar, V.G.; Beenackers, A.A.C.M. Photocatalytic Degradation for Environmental Applications – a Review. Journal of Chemical Technology & Biotechnology 2002, 77, 102–116, doi:10.1002/JCTB.532.
52. Paul, R.; Warkad, I.R.; Arulkumar, S.; Parthiban, S.; Darji, H.R.; Naushad, M.; Kadam, R.G.; Gawande, M.B. Facile Synthesis of Nanostructured TiO2-SiO2 Powder for Selective Photocatalytic Oxidation of Alcohols to Carbonyl Compounds. Molecular Catalysis 2022, 530, 112566, doi:10.1016/J.MCAT.2022.112566.
53. Marzo, L.; Pagire, S.K.; Reiser, O.; König, B. Visible-Light Photocatalysis: Does It Make a Difference in Organic Synthesis? Angewandte Chemie International Edition 2018, 57, 10034–10072, doi:10.1002/ANIE.201709766.
54. Li, H.; Cheng, B.; Xu, J.; Yu, J.; Cao, S. Crystalline Carbon Nitrides for Photocatalysis. EES Catalysis 2024, 2, 411–447, doi:10.1039/D3EY00302G.
55. Valange, S.; Védrine, J.C. General and Prospective Views on Oxidation Reactions in Heterogeneous Catalysis. Catalysts 2018, Vol. 8, Page 483 2018, 8, 483, doi:10.3390/CATAL8100483.
56. Prasad, C.; Liu, Q.; Tang, H.; Yuvaraja, G.; Long, J.; Rammohan, A.; Zyryanov, G. V. An Overview of Graphene Oxide Supported Semiconductors Based Photocatalysts: Properties, Synthesis and Photocatalytic Applications. J Mol Liq 2020, 297, 111826, doi:10.1016/J.MOLLIQ.2019.111826.
57. Zhang, H.; Wang, Z.; Zhang, J.; Dai, K. Metal-Sulfide-Based Heterojunction Photocatalysts: Principles, Impact, Applications, and in-Situ Characterization. Chinese Journal of Catalysis 2023, 49, 42–67, doi:10.1016/S1872-2067(23)64444-4.
58. Rashid, R.; Shafiq, I.; Gilani, M.R.H.S.; Maaz, M.; Akhter, P.; Hussain, M.; Jeong, K.E.; Kwon, E.E.; Bae, S.; Park, Y.K. Advancements in TiO2-Based Photocatalysis for Environmental

Remediation: Strategies for Enhancing Visible-Light-Driven Activity. Chemosphere 2024, 349, 140703, doi:10.1016/J.CHEMOSPHERE.2023.140703.

59. Rengifo-Herrera, J.A.; Pulgarin, C. Why Five Decades of Massive Research on Heterogeneous Photocatalysis, Especially on TiO2, Has Not yet Driven to Water Disinfection and Detoxification Applications? Critical Review of Drawbacks and Challenges. Chemical Engineering Journal 2023, 477, 146875, doi:10.1016/J.CEJ.2023.146875.
60. Ramalingam, M.; Kamaraj, D.; Senthil Kumar, S.R.R.; Raghavi, R.; Rajalinggam, D. Development of Super-Hydrophobic Surface Using Tio2 to Reduce Adverse Effects of Environmental Pollutants on Buildings. Mater Today Proc 2023, doi:10.1016/J.MATPR.2023.07.331.
61. Ge, M.; Hu, Z.; Wei, J.; He, Q.; He, Z. Recent Advances in Persulfate-Assisted TiO2-Based Photocatalysis for Wastewater Treatment: Performances, Mechanism and Perspectives. J Alloys Compd 2021, 888, 161625, doi:10.1016/J.JALLCOM.2021.161625.
62. Alotaibi, M.A.; Alharthi, A.I.; Qahtan, T.F.; Alotibi, S.; Ali, I.; Bakht, M.A. Green Synthesis of Xanthene Derivatives through Visible Light-Driven Photocatalysis Using Blackberry Dye-Sensitized TiO2. J Alloys Compd 2024, 978, 173388, doi:10.1016/J.JALLCOM.2023.173388.
63. Ola, O.; Maroto-Valer, M.M. Review of Material Design and Reactor Engineering on TiO2 Photocatalysis for CO2 Reduction. Journal of Photochemistry and Photobiology C: Photochemistry Reviews 2015, 24, 16–42, doi:10.1016/J.JPHOTOCHEMREV.2015.06.001.
64. Jia, J.; Zhang, Q.; Li, K.; Zhang, Y.; Liu, E.; Li, X. Recent Advances on g–C3N4–Based Z-Scheme Photocatalysts: Structural Design and Photocatalytic Applications. Int J Hydrogen Energy 2023, 48, 196–231, doi:10.1016/J.IJHYDENE.2022.09.272.
65. Yu, Y.; Huang, H. Coupled Adsorption and Photocatalysis of G-C3N4 Based Composites: Material Synthesis, Mechanism, and Environmental Applications. Chemical Engineering Journal 2023, 453, 139755, doi:10.1016/J.CEJ.2022.139755.
66. Su, H.; Yin, H.; Wang, R.; Wang, Y.; Orbell, W.; Peng, Y.; Li, J. Atomic-Level Coordination Structures Meet Graphitic Carbon Nitride (g-C3N4) for Photocatalysis: Energy Conversion and Environmental Remediation. Applied Catalysis B: Environment and Energy 2024, 348, 123683, doi:10.1016/J.APCATB.2023.123683.

67. Wang, C.Y.; Maeda, K.; Chang, L.L.; Tung, K.L.; Hu, C. Synthesis and Applications of Carbon Nitride (CNx) Family with Different Carbon to Nitrogen Ratio. Carbon N Y 2022, 188, 482–491, doi:10.1016/J.CARBON.2021.12.027.
68. Priyanga, G.S.; Pransu, G.; Sampath, S. A Comprehensive Overview of the Graphitic-Carbon Nitride Computational Approach: From Basic Properties to a Wide Range of Applications. Chemical Physics Impact 2024, 8, 100408, doi:10.1016/J.CHPHI.2023.100408.
69. Budiarso, I.J.; Dabur, V.A.; Rachmantyo, R.; Judawisastra, H.; Hu De, C.; Wibowo, A. Carbon Nitride- and Graphene-Based Materials for the Photocatalytic Degradation of Emerging Water Pollutants. Mater Adv 2024, 5, 2668–2688, doi:10.1039/D3MA01078C.
70. Torres-Pinto, A.; Silva, C.G.; Faria, J.L.; Silva, A.M.T. The Effect of Precursor Selection on the Microwave-Assisted Synthesis of Graphitic Carbon Nitride. Catal Today 2023, 424, 113868, doi:10.1016/J.CATTOD.2022.08.010.
71. Thomas, S.A.; Pallavolu, M.R.; Khan, M.E.; Cherusseri, J. Graphitic Carbon Nitride (g-C3N4): Futuristic Material for Rechargeable Batteries. J Energy Storage 2023, 68, 107673, doi:10.1016/J.EST.2023.107673.
72. Ismael, M. A Review on Graphitic Carbon Nitride (g-C3N4) Based Nanocomposites: Synthesis, Categories, and Their Application in Photocatalysis. J Alloys Compd 2020, 846, 156446, doi:10.1016/J.JALLCOM.2020.156446.
73. Gu, Y.; Li, S.; Li, M.; Wang, X.; Liu, Y.; Shi, K.; Bai, X.; Yao, Q.; Wu, Z.; Yao, H. Recent Advances in G-C 3 N 4 -Based Photo-Enzyme Catalysts for Degrading Organic Pollutants. RSC Adv 2023, 13, 937–947, doi:10.1039/D2RA06994F.
74. Bhanderi, D.; Lakhani, P.; Modi, C.K. Graphitic Carbon Nitride (g-C3N4) as an Emerging Photocatalyst for Sustainable Environmental Applications: A Comprehensive Review. RSC Sustainability 2024, 2, 265–287, doi:10.1039/D3SU00382E.
75. Pourmadadi, M.; Rahmani, E.; Eshaghi, M.M.; Shamsabadipour, A.; Ghotekar, S.; Rahdar, A.; Romanholo Ferreira, L.F. Graphitic Carbon Nitride (g-C3N4) Synthesis Methods, Surface Functionalization, and Drug Delivery Applications: A Review. J Drug Deliv Sci Technol 2023, 79, 104001, doi:10.1016/J.JDDST.2022.104001.
76. Chen, L.; Maigbay, M.A.; Li, M.; Qiu, X. Synthesis and Modification Strategies of G-C3N4 Nanosheets for Photocatalytic Applications.

Advanced Powder Materials 2024, 3, 100150, doi:10.1016/J.APMATE.2023.100150.
77. Cao, S.; Low, J.; Yu, J.; Jaroniec, M. Polymeric Photocatalysts Based on Graphitic Carbon Nitride. Advanced Materials 2015, 27, 2150–2176, doi:10.1002/ADMA.201500033.
78. Nazir, A.; Huo, P.; Rasool, A.T. Recent Advances on Graphitic Carbon Nitride-Based S-Scheme Photocatalysts: Synthesis, Environmental Applications, and Challenges. J Organomet Chem 2024, 1004, 122951, doi:10.1016/J.JORGANCHEM.2023.122951.
79. Budiarso, I.J.; Dabur, V.A.; Rachmantyo, R.; Judawisastra, H.; Hu, C.; Wibowo, A. Carbon Nitride- and Graphene-Based Materials for the Photocatalytic Degradation of Emerging Water Pollutants. Mater Adv 2024, 5, 2668–2688, doi:10.1039/D3MA01078C.
80. Hayat, A.; Al-Sehemi, A.G.; El-Nasser, K.S.; Taha, T.A.; Al-Ghamdi, A.A.; Jawad Ali Shah Syed; Amin, M.A.; Ali, T.; Bashir, T.; Palamanit, A.; et al. Graphitic Carbon Nitride (g–C3N4)–Based Semiconductor as a Beneficial Candidate in Photocatalysis Diversity. Int J Hydrogen Energy 2022, 47, 5142–5191, doi:10.1016/J.IJHYDENE.2021.11.133.
81. Li, H.; Wang, L.; Liu, Y.; Lei, J.; Zhang, J. Mesoporous Graphitic Carbon Nitride Materials: Synthesis and Modifications. Research on Chemical Intermediates 2016, 42, 3979–3998, doi:10.1007/S11164-015-2294-9/FIGURES/17.
82. Ismael, M. A Review on Graphitic Carbon Nitride (g-C3N4) Based Nanocomposites: Synthesis, Categories, and Their Application in Photocatalysis. J Alloys Compd 2020, 846, 156446, doi:10.1016/J.JALLCOM.2020.156446.
83. Darkwah, W.K.; Ao, Y. Mini Review on the Structure and Properties (Photocatalysis), and Preparation Techniques of Graphitic Carbon Nitride Nano-Based Particle, and Its Applications. Nanoscale Research Letters 2018 13:1 2018, 13, 1–15, doi:10.1186/S11671-018-2702-3.
84. Jiang, X.; Li, X.; Liu, Y.; Zhai, H.; Wang, G. The Oxidative Thermal Exfoliation-Dependent Microstructure and Photocatalytic Performance of g-C3N4 Nanosheets. Diam Relat Mater 2024, 143, 110918, doi:10.1016/J.DIAMOND.2024.110918.
85. Joy, J.; George, E.; Poornima Vijayan, P.; Anas, S.; Thomas, S. An Overview of Synthesis, Morphology, and Versatile Applications of Nanostructured Graphitic Carbon Nitride (g-C3N4). Journal of Industrial and Engineering Chemistry 2024, 133, 74–89, doi:10.1016/J.JIEC.2023.12.016.

86. Rao, A.; Roy, S.; Jain, V.; Pillai, P.P. Nanoparticle Self-Assembly: From Design Principles to Complex Matter to Functional Materials. ACS Appl Mater Interfaces 2023, 15, 25248–25274, doi:10.1021/ACSAMI.2C05378/ASSET/IMAGES/MEDIUM/AM2C05378_0017.GIF.
87. Miao, Z.; Wu, G.; Wang, Q.; Yang, J.; Wang, Z.; Yan, P.; Sun, P.; Lei, Y.; Mo, Z.; Xu, H. Recent Advances in Graphitic Carbon Nitride-Based Photocatalysts for Solar-Driven Hydrogen Production. Materials Reports: Energy 2023, 3, 100235, doi:10.1016/J.MATRE.2023.100235.
88. Song, X.L.; Chen, L.; Gao, L.J.; Ren, J.T.; Yuan, Z.Y. Engineering G-C3N4 Based Materials for Advanced Photocatalysis: Recent Advances. Green Energy & Environment 2024, 9, 166–197, doi:10.1016/J.GEE.2022.12.005.
89. Yang, F.; Hu, P.; Yang, F.; Hua, X.J.; Chen, B.; Gao, L.; Wang, K.S. Photocatalytic Applications and Modification Methods of Two-Dimensional Nanomaterials: A Review. Tungsten 2023 6:1 2023, 6, 77–113, doi:10.1007/S42864-023-00229-X.
90. Xing, J.; Wang, N.; Li, X.; Wang, J.; Taiwaikuli, M.; Huang, X.; Wang, T.; Zhou, L.; Hao, H. Synthesis and Modifications of G-C3N4-Based Materials and Their Applications in Wastewater Pollutants Removal. J Environ Chem Eng 2022, 10, 108782, doi:10.1016/J.JECE.2022.108782.
91. Wang, J.; Wang, S. A Critical Review on Graphitic Carbon Nitride (g-C3N4)-Based Materials: Preparation, Modification and Environmental Application. Coord Chem Rev 2022, 453, 214338, doi:10.1016/J.CCR.2021.214338.
92. Patnaik, S.; Sahoo, D.P.; Parida, K. Recent Advances in Anion Doped G-C3N4 Photocatalysts: A Review. Carbon N Y 2021, 172, 682–711, doi:10.1016/J.CARBON.2020.10.073.
93. Wudil, Y.S.; Ahmad, U.F.; Gondal, M.A.; Al-Osta, M.A.; Almohammedi, A.; Sa'id, R.S.; Hrahsheh, F.; Haruna, K.; Mohamed, M.J.S. Tuning of Graphitic Carbon Nitride (g-C3N4) for Photocatalysis: A Critical Review. Arabian Journal of Chemistry 2023, 16, 104542, doi:10.1016/J.ARABJC.2023.104542.
94. Singh, R.; Chauhan, M.; Garg, P.; Sharma, B.; Attri, P.; Sharma, R.K.; Sharma, D.; Chaudhary, G.R. A Critical Review on Visible Light Active Graphitic Carbon Nitride (g-CN) Based Photocatalyst for Environment Remediation Application: A Sustainable Approach. J Clean Prod 2023, 427, 138855, doi:10.1016/J.JCLEPRO.2023.138855.

95. Zhang, X.; Li, C.; Dai, L.; Si, C.; Shen, Z.; Qiu, Z.; Wang, J. Graphite Carbon Nitride Photocatalytic Materials: A Roadmap to Modification for Current and Future Water Purification. J Environ Chem Eng 2023, 11, 110869, doi:10.1016/J.JECE.2023.110869.
96. Li, Y.; He, Z.; Liu, L.; Jiang, Y.; Ong, W.J.; Duan, Y.; Ho, W.; Dong, F. Inside-and-out Modification of Graphitic Carbon Nitride (g-C3N4) Photocatalysts via Defect Engineering for Energy and Environmental Science. Nano Energy 2023, 105, 108032, doi:10.1016/J.NANOEN.2022.108032.
97. Majdoub, M.; Anfar, Z.; Amedlous, A. Emerging Chemical Functionalization of G-C3N4: Covalent/Noncovalent Modifications and Applications. ACS Nano 2020, 14, 12390–12469, doi:10.1021/ACSNANO.0C06116/ASSET/IMAGES/MEDIUM/NN0C06116_0072.GIF.
98. Chen, M.; Sun, M.; Cao, X.; Wang, H.; Xia, L.; Jiang, W.; Huang, M.; He, L.; Zhao, X.; Zhou, Y. Progress in Preparation, Identification and Photocatalytic Application of Defective g-C3N4. Coord Chem Rev 2024, 510, 215849, doi:10.1016/J.CCR.2024.215849.
99. Bresolin, B.M.; Sgarbossa, P.; Bahnemann, D.W. Synthesis of Metal-Free Functionalized g-C3N4 Nanosheets for Enhanced Photocatalytic Activity. J Environ Chem Eng 2021, 9, 106389, doi:10.1016/J.JECE.2021.106389.
100. Akple, M.S.; Takyi, G.K.S.; Chimmikuttanda, S.P. Graphitic Carbon Nitride (g-C3N4) Based Materials: Current Application Trends in Health and Other Multidisciplinary Fields. Int Nano Lett 2023, 13, 223–234, doi:10.1007/S40089-023-00395-3/FIGURES/8.
101. Cerdan, K.; Ouyang, W.; Colmenares, J.C.; Muñoz-Batista, M.J.; Luque, R.; Balu, A.M. Facile Mechanochemical Modification of G-C3N4 for Selective Photo-Oxidation of Benzyl Alcohol. Chem Eng Sci 2019, 194, 78–84, doi:10.1016/J.CES.2018.04.001.
102. Chen, L.; Tang, J.; Song, L.N.; Chen, P.; He, J.; Au, C.T.; Yin, S.F. Heterogeneous Photocatalysis for Selective Oxidation of Alcohols and Hydrocarbons. Appl Catal B 2019, 242, 379–388, doi:10.1016/J.APCATB.2018.10.025.
103. Tang, D.; Lu, G.; Shen, Z.; Hu, Y.; Yao, L.; Li, B.; Zhao, G.; Peng, B.; Huang, X. A Review on Photo-, Electro- and Photoelectro-Catalytic Strategies for Selective Oxidation of Alcohols. Journal of Energy Chemistry 2023, 77, 80–118, doi:10.1016/J.JECHEM.2022.10.038.
104. Li, J.; Li, M.; Sun, H.; Ao, Z.; Wang, S.; Liu, S. Understanding of the Oxidation Behavior of Benzyl Alcohol by Peroxymonosulfate via

Carbon Nanotubes Activation. ACS Catal 2020, 10, 3516–3525, doi:10.1021/ACSCATAL.9B05273/ASSET/IMAGES/MEDIUM/CS9B05273_M010.GIF.

105. Brillas, E. A Review on the Photoelectro-Fenton Process as Efficient Electrochemical Advanced Oxidation for Wastewater Remediation. Treatment with UV Light, Sunlight, and Coupling with Conventional and Other Photo-Assisted Advanced Technologies. Chemosphere 2020, 250, 126198, doi:10.1016/J.CHEMOSPHERE.2020.126198.
106. Fajardo-Puerto, E.; Elmouwahidi, A.; Bailón-García, E.; Pérez-Cadenas, A.F.; Carrasco-Marín, F. From Fenton and ORR 2e−-Type Catalysts to Bifunctional Electrodes for Environmental Remediation Using the Electro-Fenton Process. Catalysts 2023, Vol. 13, Page 674 2023, 13, 674, doi:10.3390/CATAL13040674.
107. Averill-Bates, D. Reactive Oxygen Species and Cell Signaling. Review. Biochimica et Biophysica Acta (BBA) - Molecular Cell Research 2024, 1871, 119573, doi:10.1016/J.BBAMCR.2023.119573.
108. Wang, X.; Zhang, L. Kinetic Study of Hydroxyl Radical Formation in a Continuous Hydroxyl Generation System. RSC Adv 2018, 8, 40632–40638, doi:10.1039/C8RA08511K.
109. Wu, Y.; Huang, W.; Peng, D.; Huang, X.A.; Gu, J.; Wu, S.; Deng, T.; Liu, F. Synthesis of Dihydroquinolines as Scaffolds for Fluorescence Sensing of Hydroxyl Radical. Org Lett 2021, 23, 135–139, doi:10.1021/ACS.ORGLETT.0C03852/ASSET/IMAGES/LARGE/OL0C03852_0004.JPEG.
110. Antonopoulou, M.; Evgenidou, E.; Lambropoulou, D.; Konstantinou, I. A Review on Advanced Oxidation Processes for the Removal of Taste and Odor Compounds from Aqueous Media. Water Res 2014, 53, 215–234, doi:10.1016/J.WATRES.2014.01.028.
111. Wen, Y.; Yan, J.; Yang, B.; Zhuang, Z.; Yu, Y. Reactive Oxygen Species on Transition Metal-Based Catalysts for Sustainable Environmental Applications. J Mater Chem A Mater 2022, 10, 19184–19210, doi:10.1039/D2TA02188A.
112. An, G.; Zhang, X.; Zhang, C.; Gao, H.; Liu, S.; Qin, G.; Qi, H.; Kasemchainan, J.; Zhang, J.; Wang, G. Metal-Organic-Framework-Based Materials as Green Catalysts for Alcohol Oxidation. Chinese Journal of Catalysis 2023, 50, 126–174, doi:10.1016/S1872-2067(23)64451-1.

113. Álvarez, M.S.; Longo, M.A.; Rodríguez, A.; Deive, F.J. The Role of Deep Eutectic Solvents in Catalysis. A Vision on Their Contribution to Homogeneous, Heterogeneous and Electrocatalytic Processes. Journal of Industrial and Engineering Chemistry 2024, 132, 36–49, doi:10.1016/J.JIEC.2023.11.030.
114. Kakaei, K.; Esrafili, M.D.; Ehsani, A. Introduction to Catalysis. Interface Science and Technology 2019, 27, 1–21, doi:10.1016/B978-0-12-814523-4.00001-0.
115. Kumar, A.; Daw, P.; Milstein, D. Homogeneous Catalysis for Sustainable Energy: Hydrogen and Methanol Economies, Fuels from Biomass, and Related Topics. Chem Rev 2022, 122, 385–441, doi:10.1021/ACS.CHEMREV.1C00412/ASSET/IMAGES/MEDIUM/CR1C00412_0045.GIF.
116. Pelletier, J.D.A.; Basset, J.M. Catalysis by Design: Well-Defined Single-Site Heterogeneous Catalysts. Acc Chem Res 2016, 49, 664–677, doi:10.1021/ACS.ACCOUNTS.5B00518/ASSET/IMAGES/LARGE/AR-2015-00518R_0028.JPEG.
117. Najafishirtari, S.; Friedel Ortega, K.; Douthwaite, M.; Pattisson, S.; Hutchings, G.J.; Bondue, C.J.; Tschulik, K.; Waffel, D.; Peng, B.; Deitermann, M.; et al. A Perspective on Heterogeneous Catalysts for the Selective Oxidation of Alcohols. Chemistry – A European Journal 2021, 27, 16809–16833, doi:10.1002/CHEM.202102868.
118. Friend, C.M.; Xu, B. Heterogeneous Catalysis: A Central Science for a Sustainable Future. Acc Chem Res 2017, 50, 517–521, doi:10.1021/ACS.ACCOUNTS.6B00510/ASSET/IMAGES/LARGE/AR-2016-00510E_0003.JPEG.
119. Védrine, J.C. Heterogeneous Catalysis on Metal Oxides. Catalysts 2017, Vol. 7, Page 341 2017, 7, 341, doi:10.3390/CATAL7110341.
120. Chen, X.; Cheng, L.; Gu, J.; Yuan, H.; Chen, Y. Chemical Recycling of Plastic Wastes via Homogeneous Catalysis: A Review. Chemical Engineering Journal 2024, 479, 147853, doi:10.1016/J.CEJ.2023.147853.
121. Mitchell, S.; Martín, A.J.; Pérez-Ramírez, J. Transcending Scales in Catalysis for Sustainable Development. Nature Chemical Engineering 2024 1:1 2024, 1, 13–15, doi:10.1038/s44286-023-00005-1.
122. Yang, H.; Li, G.; Jiang, G.; Zhang, Z.; Hao, Z. Heterogeneous Selective Oxidation over Supported Metal Catalysts: From

Nanoparticles to Single Atoms. Appl Catal B 2023, 325, 122384, doi:10.1016/J.APCATB.2023.122384.
123. Losada, J.P.; Heckl, I.; Bertok, B.; Friedler, F.; Garcia-Ojeda, J.C.; Argoti, A. Process Network Synthesis for Benzaldehyde Production: P-Graph Approach. Chem Eng Trans 2015, 45, 1369–1374, doi:10.3303/CET1545229.
124. Mitran, G.; Neaţu, F.; Pavel, O.D.; Trandafir, M.M.; Florea, M. Behavior of Molybdenum–Vanadium Mixed Oxides in Selective Oxidation and Disproportionation of Toluene. Materials 2019, Vol. 12, Page 748 2019, 12, 748, doi:10.3390/MA12050748.
125. Zhan, G.; Hong, Y.; Lu, F.; Ibrahim, A.R.; Du, M.; Sun, D.; Huang, J.; Li, Q.; Li, J. Kinetics of Liquid Phase Oxidation of Benzyl Alcohol with Hydrogen Peroxide over Bio-Reduced Au/TS-1 Catalysts. J Mol Catal A Chem 2013, 366, 215–221, doi:10.1016/J.MOLCATA.2012.09.026.
126. Wu, X.; Deng, Z.; Yan, J.; Zhang, F.; Zhang, Z. Effect of Acetic Anhydride on the Oxidation of Toluene to Benzaldehyde with Metal/Bromide Catalysts. Ind Eng Chem Res 2014, 53, 14601–14606, doi:10.1021/IE502686U/ASSET/IMAGES/LARGE/IE-2014-02686U_0008.JPEG.
127. Morozov, R.S.; Golovin, M.S.; Uchaev, D.A.; Fakhrutdinov, A.N.; Gavrilyak, M. V.; Arkhipushkin, I.A.; Boronin, V.A.; Korshunov, V.M.; Podgornov, F. V.; Taydakov, I. V.; et al. Polytriazine Imide-LiCl Semiconductor for Highly Efficient Photooxidation of Benzyl Alcohol to Benzaldehyde. Journal of Chemical Sciences 2021, 133, 1–17, doi:10.1007/S12039-021-01999-Y/FIGURES/12.
128. Xu, S.; Wu, J.; Huang, P.; Lao, C.; Lai, H.; Wang, Y.; Wang, Z.; Zhong, G.; Fu, X.; Peng, F. Selective Catalytic Oxidation of Benzyl Alcohol to Benzaldehyde by Nitrates. Front Chem 2020, 8, 525060, doi:10.3389/FCHEM.2020.00151/BIBTEX.
129. Luo, J.; Yu, H.; Wang, H.; Wang, H.; Peng, F. Aerobic Oxidation of Benzyl Alcohol to Benzaldehyde Catalyzed by Carbon Nanotubes without Any Promoter. Chemical Engineering Journal 2014, 240, 434–442, doi:10.1016/J.CEJ.2013.11.093.
130. Tong, J.; Su, L.; Li, W.; Wang, W.; Ma, H.; Wang, Q. Hybrids of [C4mim]3+xPMo12−xVxO40: A New Catalyst for Oxidation of Benzyl Alcohol to Benzaldehyde in Water with Greatly Improved Performances. Polyhedron 2016, 115, 282–287, doi:10.1016/J.POLY.2016.05.024.
131. Nowicka, E.; Althahban, S.; Leah, T.D.; Shaw, G.; Morgan, D.; Kiely, C.J.; Roldan, A.; Hutchings, G.J. Benzyl Alcohol Oxidation

with Pd-Zn/TiO2: Computational and Experimental Studies. Sci Technol Adv Mater 2019, 20, 367, doi:10.1080/14686996.2019.1598237.
132. Pugh, S.; McKenna, R.; Halloum, I.; Nielsen, D.R. Engineering Escherichia Coli for Renewable Benzyl Alcohol Production. Metab Eng Commun 2015, 2, 39–45, doi:10.1016/J.METENO.2015.06.002.
133. Scognamiglio, J.; Jones, L.; Vitale, D.; Letizia, C.S.; Api, A.M. Fragrance Material Review on Benzyl Alcohol. Food and Chemical Toxicology 2012, 50, S140–S160, doi:10.1016/J.FCT.2011.10.013.
134. Alcohol Bencílico CAS 100-51-6 | 100987 Available online: https://www.merckmillipore.com/ES/es/product/Benzyl-alcohol,MDA_CHEM-100987 (accessed on 18 May 2024).
135. Younes, M.; Aquilina, G.; Castle, L.; Engel, K.H.; Fowler, P.; Fürst, P.; Gürtler, R.; Gundert-Remy, U.; Husøy, T.; Mennes, W.; et al. Re-Evaluation of Benzyl Alcohol (E 1519) as Food Additive. EFSA Journal 2019, 17, e05876, doi:10.2903/J.EFSA.2019.5876.
136. Johnson, W.; Bergfeld, W.F.; Belsito, D. V.; Hill, R.A.; Klaassen, C.D.; Liebler, D.C.; Marks, J.G.; Shank, R.C.; Slaga, T.J.; Snyder, P.W.; et al. Safety Assessment of Benzyl Alcohol, Benzoic Acid and Its Salts, and Benzyl Benzoate. Int J Toxicol 2017, 36, 5S-30S, doi:10.1177/1091581817728996/ASSET/IMAGES/10.1177_1091581817728996-IMG7.PNG.
137. Liu, L.; Zhu, Y.; Chen, Y.; Chen, H.; Fan, C.; Mo, Q.; Yuan, J. One-Pot Cascade Biotransformation for Efficient Synthesis of Benzyl Alcohol and Its Analogs. Chem Asian J 2020, 15, 1018–1021, doi:10.1002/ASIA.201901680.
138. Maurya, R.; Patel, H.; Bhatt, D.; Shakhreliya, S.; Gohil, N.; Bhattacharjee, G.; Lam, N.L.; Alzahrani, K.J.; Gyanchander, E.; Singh, V. Microbial Production of Natural Flavors and Fragrances. Recent Advances in Food Biotechnology 2022, 139–159, doi:10.1007/978-981-16-8125-7_7/TABLES/1.
139. Paula Dionísio, A.; Molina, G.; Souza de Carvalho, D.; dos Santos, R.; Bicas, J.L.; Pastore, G.M. Natural Flavourings from Biotechnology for Foods and Beverages. Natural Food Additives, Ingredients and Flavourings 2012, 231–259, doi:10.1533/9780857095725.1.231.
140. Benzaldehyde | C6H5CHO | CID 240 - PubChem Available online: https://pubchem.ncbi.nlm.nih.gov/compound/benzaldehyde#section=InChI (accessed on 18 May 2024).

141. Zhang, Z.; Hao, S.; Duan, X.; Wang, T.; Li, H.; Fan, G.; Zhao, Y.; Li, J. Photocatalytic Activity of CuBi2O4/WO3 p-n Heterojunction Photocatalysts in Benzyl Alcohol Oxidation to Benzaldehyde. J Alloys Compd 2023, 968, 172209, doi:10.1016/J.JALLCOM.2023.172209.
142. Gao, G.; Rong, R.; Zhang, Z.; Pan, B.; Sun, X.; Zhang, Q.; Zheng, G.; Xu, K.; Gao, L. Selective Oxidation of Benzyl Alcohol to Benzaldehyde over CoFe2O4 Nanocatalyst. Catal Commun 2023, 183, 106757, doi:10.1016/J.CATCOM.2023.106757.
143. Son, J.; Choi, I.H.; Lim, C.G.; Jang, J.H.; Bang, H.B.; Cha, J.W.; Jeon, E.J.; Sohn, M.G.; Yun, H.J.; Kim, S.C.; et al. Production of Cinnamaldehyde through Whole-Cell Bioconversion from Trans-Cinnamic Acid Using Engineered Corynebacterium Glutamicum. J Agric Food Chem 2022, 70, 2656–2663, doi:10.1021/ACS.JAFC.1C07398/SUPPL_FILE/JF1C07398_SI_001.PDF.
144. Bang, H.B.; Son, J.; Kim, S.C.; Jeong, K.J. Systematic Metabolic Engineering of Escherichia Coli for the Enhanced Production of Cinnamaldehyde. Metab Eng 2023, 76, 63–74, doi:10.1016/J.YMBEN.2023.01.006.
145. Bang, H.B.; Lee, Y.H.; Kim, S.C.; Sung, C.K.; Jeong, K.J. Metabolic Engineering of Escherichia Coli for the Production of Cinnamaldehyde. Microb Cell Fact 2016, 15, 1–12, doi:10.1186/S12934-016-0415-9/FIGURES/7.
146. Lee, H.G.; Jo, Y.; Ameer, K.; Kwon, J.H. Optimization of Green Extraction Methods for Cinnamic Acid and Cinnamaldehyde from Cinnamon (Cinnamomum Cassia) by Response Surface Methodology. Food Sci Biotechnol 2018, 27, 1607–1617, doi:10.1007/S10068-018-0441-Y/FIGURES/2.
147. Iqbal, Z.; Khan, M.S.; Khattak, R.; Iqbal, T.; Zekker, I.; Zahoor, M.; Hetta, H.F.; Batiha, G.E.S.; Alshammari, E.M. Selective Oxidation of Cinnamyl Alcohol to Cinnamaldehyde over Functionalized Multi-Walled Carbon Nanotubes Supported Silver-Cobalt Nanoparticles. Catalysts 2021, Vol. 11, Page 863 2021, 11, 863, doi:10.3390/CATAL11070863.
148. Waffel, D.; Alkan, B.; Fu, Q.; Chen, Y.T.; Schmidt, S.; Schulz, C.; Wiggers, H.; Muhler, M.; Peng, B. Towards Mechanistic Understanding of Liquid-Phase Cinnamyl Alcohol Oxidation with Tert-Butyl Hydroperoxide over Noble-Metal-Free LaCo1–XFexO3 Perovskites. Chempluschem 2019, 84, 1155–1163, doi:10.1002/CPLU.201900429.

149. Niklasson, I.B.; Delaine, T.; Islam, M.N.; Karlsson, R.; Luthman, K.; Karlberg, A.T. Cinnamyl Alcohol Oxidizes Rapidly upon Air Exposure. Contact Dermatitis 2013, 68, 129–138, doi:10.1111/COD.12009.
150. Klumbys, E.; Zebec, Z.; Weise, N.J.; Turner, N.J.; Scrutton, N.S. Bio-Derived Production of Cinnamyl Alcohol via a Three Step Biocatalytic Cascade and Metabolic Engineering. Green Chem 2019, 20, 658, doi:10.1039/C7GC03325G.
151. Ramasamy, M.; Lee, J.H.; Lee, J. Direct One-Pot Synthesis of Cinnamaldehyde Immobilized on Gold Nanoparticles and Their Antibiofilm Properties. Colloids Surf B Biointerfaces 2017, 160, 639–648, doi:10.1016/J.COLSURFB.2017.10.018.
152. Sharma, S.; Perera, K.Y.; Jaiswal, A.K.; Jaiswal, S. Natural Antimicrobials from Fruits and Plant Extract for Food Packaging and Preservation. Food Packaging and Preservation: Antimicrobial Materials and Technologies 2024, 133–152, doi:10.1016/B978-0-323-90044-7.00008-2.
153. Cinnamaldehyde Market | Size, Share, Price, Import, Export, Volume 2022 Forecast to 2029 Available online: https://www.24chemicalresearch.com/reports/129834/global-cinnamaldehyde-market-2022-2028-133 (accessed on 18 May 2024).
154. Shreaz, S.; Wani, W.A.; Behbehani, J.M.; Raja, V.; Irshad, M.; Karched, M.; Ali, I.; Siddiqi, W.A.; Hun, L.T. Cinnamaldehyde and Its Derivatives, a Novel Class of Antifungal Agents. Fitoterapia 2016, 112, 116–131, doi:10.1016/J.FITOTE.2016.05.016.
155. Doyle, A.A.; Stephens, J.C. A Review of Cinnamaldehyde and Its Derivatives as Antibacterial Agents. Fitoterapia 2019, 139, 104405, doi:10.1016/J.FITOTE.2019.104405.
156. Ji, M.; Sun, X.; Guo, X.; Zhu, W.; Wu, J.; Chen, L.; Wang, J.; Chen, M.; Cheng, C.; Zhang, Q. Green Synthesis, Characterization and in Vitro Release of Cinnamaldehyde/Sodium Alginate/Chitosan Nanoparticles. Food Hydrocoll 2019, 90, 515–522, doi:10.1016/J.FOODHYD.2018.12.027.
157. Visan, A.; Van Ommen, J.R.; Kreutzer, M.T.; Lammertink, R.G.H. Photocatalytic Reactor Design: Guidelines for Kinetic Investigation. Ind Eng Chem Res 2019, 58, 5349–5357, doi:10.1021/ACS.IECR.9B00381/ASSET/IMAGES/MEDIUM/IE-2019-003814_M030.GIF.
158. Ballari, M. de los M.; Satuf, M.L.; Alfano, O.M. Photocatalytic Reactor Modeling: Application to Advanced Oxidation Processes

for Chemical Pollution Abatement. Top Curr Chem 2019, 377, 1–37, doi:10.1007/S41061-019-0247-2/TABLES/6.
159. Wang, D.; Mueses, M.A.; Márquez, J.A.C.; Machuca-Martínez, F.; Grčić, I.; Peralta Muniz Moreira, R.; Li Puma, G. Engineering and Modeling Perspectives on Photocatalytic Reactors for Water Treatment. Water Res 2021, 202, 117421, doi:10.1016/J.WATRES.2021.117421.
160. De Lasa, H.; Rosales, B.S.; Moreira, J.; Valades-Pelayo, P. Efficiency Factors in Photocatalytic Reactors: Quantum Yield and Photochemical Thermodynamic Efficiency Factor. Chem Eng Technol 2016, 39, 51–65, doi:10.1002/CEAT.201500305.
161. Manassero, A.; Satuf, M.L.; Alfano, O.M. Photocatalytic Reactors with Suspended and Immobilized TiO2: Comparative Efficiency Evaluation. Chemical Engineering Journal 2017, 326, 29–36, doi:10.1016/J.CEJ.2017.05.087.
162. Quan, Y.; Pehkonen, S.O.; Ray, M.B. Evaluation of Three Different Lamp Emission Models Using Novel Application of Potassium Ferrioxalate Actinometry. Ind Eng Chem Res 2004, 43, 948–955, doi:10.1021/IE0304210/ASSET/IMAGES/LARGE/IE0304210F00011.JPEG.
163. Deng, B.; Peng, S.; Ye, K.; Zhao, B. Axisymmetric Radiation Intensity Model for Annular Reactors. AIChE Journal 2021, 67, e17331, doi:10.1002/AIC.17331.
164. Sundar, K.P.; Kanmani, S. Progression of Photocatalytic Reactors and It's Comparison: A Review. Chemical Engineering Research and Design 2020, 154, 135–150, doi:10.1016/J.CHERD.2019.11.035.
165. Kant, P.; Trinkies, L.L.; Gensior, N.; Fischer, D.; Rubin, M.; Alan Ozin, G.; Dittmeyer, R. Isophotonic Reactor for the Precise Determination of Quantum Yields in Gas, Liquid, and Multi-Phase Photoreactions. Chemical Engineering Journal 2023, 452, 139204, doi:10.1016/J.CEJ.2022.139204.
166. Barbosa, I.S.O.; Santos, R.J.; Dias, M.M.; Faria, J.L.; Silva, C.G. Radiation Models for Computational Fluid Dynamics Simulations of Photocatalytic Reactors. Chem Eng Technol 2023, 46, 1059–1077, doi:10.1002/CEAT.202200551.
167. Zhao, J.M.; Liu, L.H. Radiative Transfer Equation and Solutions. Handbook of Thermal Science and Engineering 2017, 1–46, doi:10.1007/978-3-319-32003-8_56-1.
168. Trujillo, F.J.; Safinski, T.; Adesina, A.A. Oxidative Photomineralization of Dichloroacetic Acid in an Externally-

Irradiated Rectangular Bubble Tank Reactor: Computational Fluid Dynamics Modeling and Experimental Verification Studies. Ind Eng Chem Res 2010, 49, 6722–6734, doi:10.1021/IE901364Z/ASSET/IMAGES/LARGE/IE-2009-01364Z_0019.JPEG.

169. Brucato, A.; Cassano, A.E.; Grisafi, F.; Montante, G.; Rizzuti, L.; Vella, G. Estimating Radiant Fields in Flat Heterogeneous Photoreactors by the Six-Flux Model. AIChE Journal 2006, 52, 3882–3890, doi:10.1002/AIC.10984.

CHAPTER 2. EXPERIMENTAL SECTION

This chapter summarizes the experimental content related to the work developed in this dissertation research. It describes the materials and methods used to synthesize the photocatalysts and briefly describes the physicochemical characterization techniques, equipment, and analysis methodologies. Finally, the reaction system used to synthesize aldehydes, the modeling of photocatalytic efficiencies, and the study of the kinetic spectrum carried out are detailed.

2.1. MATERIALS & CHEMICALS

In this investigation, the reagents and chemicals used were mainly of analytical or pure grade and were used as received. Table 2.1 summarizes the details of each of these products. It specifies the name, chemical formula, CAS number, commercial manufacturer, and purity of each material supplied by the laboratory.

Table 2.1 *Chemical substances used in this research.*

Name	Formula	CAS	Purity (%)
benzyl alcohol	C_7H_8O	100-51-6	>99%
benzaldehyde	C_7H_6O	100-52-7	>99%
benzoic acid	$C_7H_6O_2$	65-85-0	≥99.5%
cinnamyl alcohol	$C_9H_{10}O$	104-54-1	98%
cinnamaldehyde	C_9H_8O	14371-10-9	99%
acetonitrile	C_2H_3N	75-05-8	≥99.9%
methanol	CH_4O	67-56-1	≥99.9%
trifluoroacetic acid	$C_2HF_3O_2$	76-05-1	99%
sulfuric acid	H_2SO_4	7664-93-9	99.9%
melamine	$C_3H_6N_6$	108-78-1	99%
urea	NH_2CONH_2	57-13-6	99%
thiourea	NH_2CSNH_2	62-56-6	≥99.9%
sodium borohydride	$NaBH_4$	16940-66-2	>99%
ruthenium (iii) chloride	$RuCl_3$	14898-67-0	99.98%
sodium polyphosphate	$(NaPO_3)_n$	68915-31-1	65-70%
chlorosulfonic acid	$ClSO_3H$	7790-94-5	99 %
dichloromethane	CH_2Cl_2	75-09-2	99.8%,
sodium thiosulfate	$Na_2O_3S_2$	7772-98-7	99%
oxalic acid	$C_2H_2O_4$	144-62-7	98%
EDTA	$C_{10}H_{16}N_2O_8$	60-00-4	99.5%
tert-butyl alcohol	$C_4H_{10}O$	75-65-0	≥99.0%
p-benzoquinone	$C_6H_4O_2$	106-51-4	≥98%
TIRON	$C_6H_6Na_2O_9S_2$	270573-71-2	97%
L-histidine	$C_6H_9N_3O_2$	71-00-1	≥99%
2-hydroxytrephthalic acid	$C_8H_6O_5$	636-94-2	97%
terephthalic acid	$C_8H_6O_4$	100-21-0	98%
sodium hydroxide	NaOH	1310-73-2	97%
hydrochloric acid	HCl	7647-01-0	37%
iron (III) chloride	$FeCl_3$	7705-08-0	97%
Tungstosilicic acid hydrate	$H_4SiW_{12}O_{40}$	12027-43-9	≥99.9%
acetic acid	$C_2H_4O_2$	64-19-7	≥99.7%

2.2. CATALYSTS' SYNTHESIS AND CHARACTERIZATION

2.2.1. Catalyst synthesis

In this work, several catalysts were synthesized using g-C_3N_4 as support, using melamine as its precursor, as shown in Table 2.2, simple synthesis methods were employed, which mostly avoided the use of highly polluting chemical solvents and did not require extreme temperature and pressure conditions. Specifically, systems doped with boron, ruthenium, phosphorus and sulfur were studied, referred to in this document as (NaBCN, BCN), NaBCN-Ru, PCN, SCN and SCNu respectively.

Supported catalysts are characterized by having a modifying agent uniformly distributed on a support material. It is crucial that the modifying agent is correctly supported on the surface of the material, as the catalytic reaction takes place on the inner surface of the catalyst, i.e. inside its pores. To achieve a correct distribution of the modifying agent, the impregnation method, a simple and frequently used technique, was used.

Table 2.2 *Precursors and synthesis methods of catalysts.*

PHOTOCATALYST	DOPING PRECURSOR	SYNTHESIS METHOD
NaBCN	sodium borohydride	Two-step calcination
BCN	elemental boron	Two-step calcination
NaBCN-Ru	sodium borohydride, ruthenium chloride	Incipient moisture impregnation, two-step calcination
PCN	Sodium polyphosphate	Two-step calcination, wet impregnation
SCN	chlorosulfonic acid	Two-step calcination, wet impregnation
SCNu	sodium thiosulfate	Two-step calcination

Impregnation method

The impregnation method consists of adding a certain volume of the modifying agent precursor solution, usually a metal salt, to the catalytic support. The purpose of this process is to adsorb metal ions onto the support material. After adsorption, the drying and, if necessary, heat treatment process is carried out. This method offers several advantages,

as it is relatively cheap and simple, does not require complex synthesis steps or specialized equipment, and is therefore widely adopted in the production of catalysts in various industries [1]. There are two common methods of impregnation deposition depending on the volume of solution used, namely wet and incipient wet impregnation procedures.

Wet impregnation

In this method, the support is completely immersed in a volume of solution that exceeds the pore volume of the support, producing a fine suspension, see Fig. 2.1. After a certain time, the solid is separated by filtration and undergoes evaporative drying steps in which excess solvent is removed. Once the interaction of the precursors with the support has been achieved, the material is subjected to heat treatments, with possible additional oxidation or reduction treatments, to ensure that the modifying agent and its counterion are deposited on the surface of the catalytic support [2].

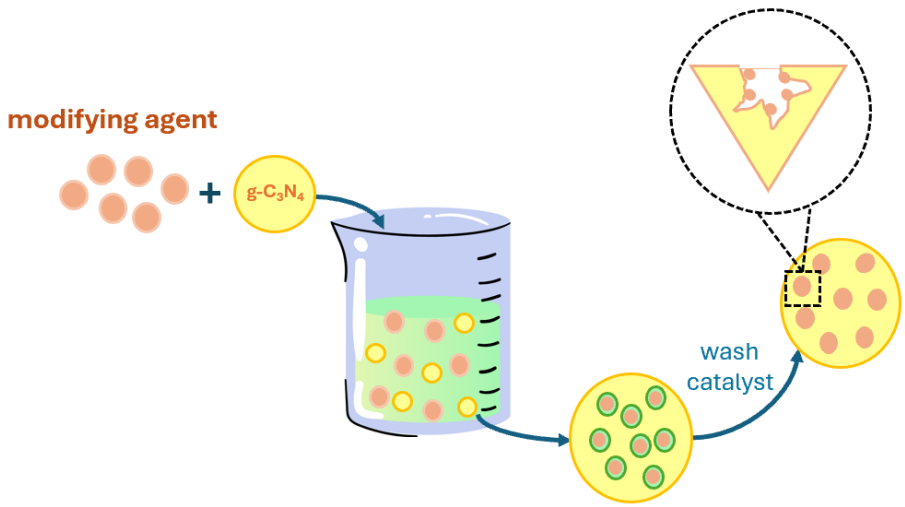

Fig. 2.1 *Wet impregnation method.*

Incipient wetness impregnation

This technique uses a solution volume equal to or slightly less than the pore volume of the substrate, see Fig. 2.2. To calculate the total volume of solution to be used, the wetting volume characteristic of each support is used. Thus, the solution volume is slowly added dropwise in a uniform manner to obtain a homogeneous distribution of the active component on the catalyst. Then, to produce catalysts with zero-valent metal particles anchored to the support, the impregnated and dried

powder is heat treated in an oxidizing or reducing environment. Precursor ligands are removed, either by decomposition or by reaction with gaseous molecules producing air/hydrogen. Any components that do not form gaseous products, such as alkali metals or their salts, remain in the final catalyst [2]. Unlike wet impregnation, in this case there is no excess liquid containing any precursor, so no additional filtration step is required. This can be a disadvantage, as the absence of filtration may mean that any counterions of the precursor salt of the active compound remain trapped in the dry catalyst, which in turn may require additional processing to remove these and other substances [1].

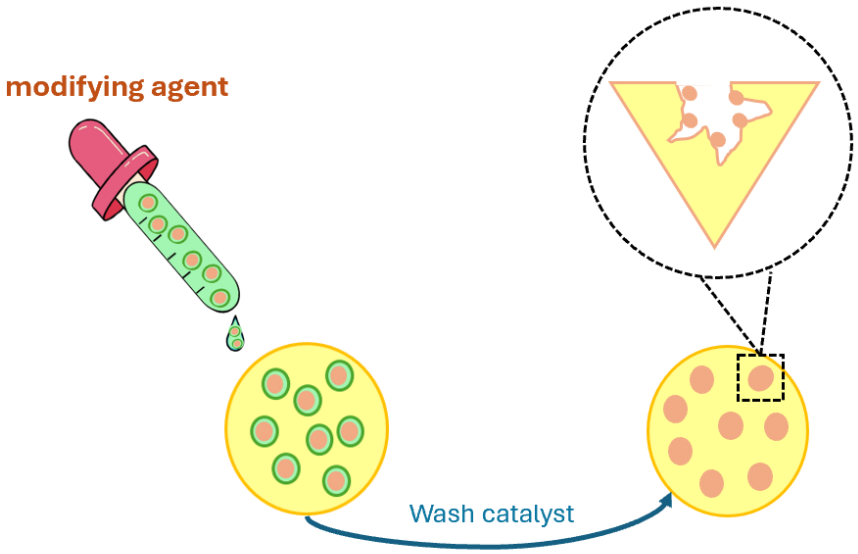

Fig. 2.2 *Incipient wetness impregnation method.*

Calcination

The calcination process is a thermal treatment performed on chemical compounds, in which the material is exposed to high temperatures in a modifiable atmosphere composed of air or in the presence of an inert gas, see Fig. 2.3. The objective of this process is to induce thermal decomposition reactions, eliminate volatile components or modify the physical or chemical state of the material. Normally, the temperatures used are kept below the melting point of the sample to be calcined.

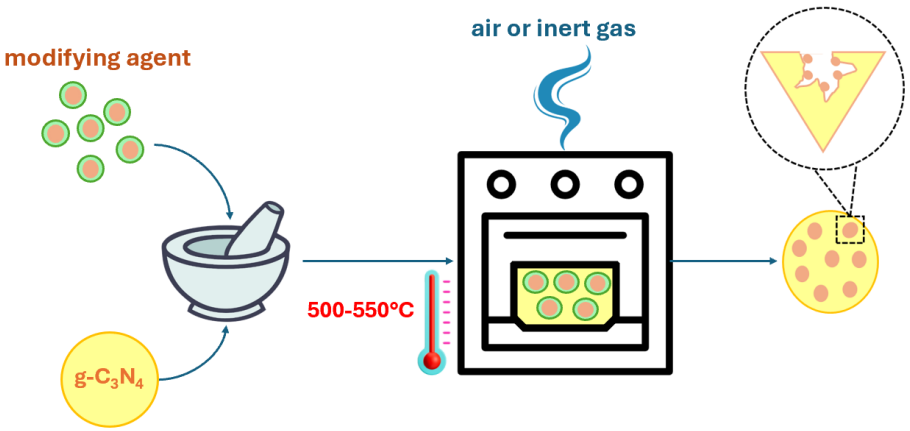

Fig. 2.3 *calcination method.*

Synthesis of g-C_3N_4

In this work, g-C_3N_4 was used as catalytic support for all the synthesized materials. This support was prepared by calcining 40 g of melamine, the precursor material. The material was subjected to a temperature between 500-550°C, with a heating rate of 10°C min^{-1} for 2 hours, under an inert atmosphere to undergo controlled decomposition, remove volatile compounds, and produce condensation and polymerization reactions between the remaining molecular units to obtain g-C_3N_4 with an organized network structure and more stable carbon-nitrogen bonds. As a result, a yellowish solid is obtained, washed, separated by filtration, and dried at 80°C.

Synthesis of boron-modified g-C_3N_4

1. In both cases, a total of 1.5 g of catalyst was prepared.
2. To prepare the NaBCN sample, $NaBH_4$ and CN were mixed in a ratio (1-2) and ground in a mortar.
3. In the case of the elemental boron-modified sample, the proportional amount of B was added to the 0.5 g of $NaBH_4$.
4. The prepared mixtures of NaBCN and BCN were calcined at a temperature of 450°C for 1 h with a heating rate of 10°C min^{-1} and a flow rate of 20 mL min^{-1} of N_2.
5. After cooling the resulting brown samples, they were washed several times with water and dried at 80°C overnight.
6. Finally, $NaBH_4$-modified CN was labeled NaBCN, and boron-modified CN as BCN.

Synthesis of Ru deposited onto g-C_3N_4

1. CN and $NaBH_4$ were mixed in equal proportions in a mortar, ensuring a homogeneous mixture.
2. The amount of water needed to wet 1 g of the CN- $NaBH_4$ mixture was calculated, resulting in a value of 0.59 mL g^{-1}. This value corresponds to the proportion used to obtain RuCN. This value corresponds to the ratio used for the impregnation by incipient wetting of all the samples.
3. Considering that 1.5 g of NaBCN with different percentages of ruthenium (0.5, 1, 2, and 4%) were synthesized, the desired amount of $RuCl_3$ was dissolved in 0.9 mL of MilliQ water.
4. The NaBCN solid mixture was transferred and dispersed evenly on the surface of a crucible. $RuCl_3$ solution was then added dropwise using a micropipette, obtaining a clay-like material after the deposition was completed.
5. The obtained material was dried for 2 hours and then ground to a powder.
6. The resulting powder was heated in a furnace at 450°C for 1 h, with a heating rate of 10°C min^{-1} and a nitrogen flow of 100 L h^{-1}.
7. The calcined material was cooled, washed, and dried.
8. The paste obtained was ground to a brown powder.

Synthesis of phosphorus-doped g-C_3N_4

1. Several suspensions of g-C_3N_4 were prepared in 20 mL of MilliQ water and uniformly dispersed by stirring for 10 min.
2. A certain amount of P (x = 2, 4, 8, and 12 wt.% to the amount of CN) as sodium phosphate was added to the g-C_3N_4 suspension and kept under magnetic stirring for 2 h at room temperature.
3. The above suspension was evaporated by heating at 100°C until all water was removed.
4. The paste obtained was subjected to heat treatment under a nitrogen atmosphere at 550°C with a heating rate of 10°C min^{-1} for 2 h.
5. The resulting solid was ground to a homogeneous brown powder.
6. The obtained samples were labeled as P-CN-x%, where x represents the percentage of P doping by weight.

Synthesis of sulfonic-tailored g-C_3N_4

1. Several suspensions with a concentration of 0.1 g mL^{-1} of g-C_3N_4 in 20 mL dichloromethane were prepared and uniformly dispersed by stirring for 10 min.
2. Subsequently, x volumes of chlorosulfonic acid were added dropwise according to the degree of sulfonation (x = 0.5, 1, 1.5, 2, 5, 7, 10, and 15 mL) to the g-C_3N_4 suspension and kept under magnetic stirring for 3 h at room temperature.
3. The resulting paste was washed several times with methanol to remove species not strongly adsorbed on the surface of the g-C_3N_4 component.
4. The washed solid was recovered by centrifugation.
5. Finally, the solid was dried at 80°C, yielding a light yellowish powder.
6. The final sample was labeled SCN-x, where x is the total volume of chlorosulfonic acid added.

2.2.2. Characterization and analysis techniques of catalysts

The synthesized photocatalysts were characterized by several techniques depending on the information required. Taken together, these techniques allow a comprehensive study of their structural, textural, morphological, and optical properties. Table 2.3 summarizes the techniques used and the type of information they provide in this report.

Table 2.3 *Chemical-physical characterization techniques used for the study of the synthesized catalysts.*

Method of analysis	Parameter
Thermogravimetric Analysis (TGA)	Thermal and oxidative stability
X-Ray Diffraction (XRD)	Crystalline phases, particle size, crystallite size, interlayer spacing
Fourier Transform InfraRed analysis (FTIR)	Functional groups present in the catalyst
X-Ray Photoelectron Spectroscopy (XPS)	Oxidation state and chemical composition of surface species
Scanning Transmission Electron Microscopy (STEM) with Energy Dispersive X-ray (EDX)	Distribution and homogeneity of phases, chemical composition, particle size
Elemental Analysis (EA)	Chemical composition

Nitrogen adsorption isotherm. BET area	Surface area, pore size, pore diameter, pore volume, pore distribution
Diffuse Reflectance Spectroscopy UV-vis (DRS-UV-vis)	Bandgap energy
Photoluminescence (PL)	Luminescence
Nuclear Magnetic Resonance (NMR)	Surface chemical environment

Thermogravimetric Analysis (TGA)

Thermogravimetric analysis (TGA) is a thermal analysis technique that measures the mass variation of a sample over time while the temperature is modified at a specific rate under a controlled atmosphere [3]. The information provided by this method allows to understand various physical phenomena such as absorption, adsorption, desorption, and phase changes, as well as chemical changes including chemisorption, thermal decomposition, and solid-gas reactions. Specifically, this analysis makes it possible to evaluate the thermal stability of a material at a given temperature and its oxidative stability, that is, the oxygen absorption capacity of the material [4,5].

Several factors affect the mass variation of the sample. For example, weight gain is typically attributed to adsorption or oxidation, while weight loss is typically associated with decomposition, desorption, dehydration, desolvation, or volatilization [5,6]. Additionally, TGA is commonly used to evaluate volatile or gaseous products lost during chemical reactions for samples such as nanomaterials, polymers, polymeric nanocomposites, fibers, paints, coatings, and films [6].

The thermal stability of the samples synthesized in this work was evaluated on a Perkin Elmer thermobalance (model STA 6000). A constant heating rate of 10 °C min^{-1} in an N_2 atmosphere (flow rate, 20 ml min^{-1}) was used from room temperature up to 450 °C.

X-ray diffraction (XRD)

Diffraction can be defined as a common property of all types of waves. This phenomenon occurs when X-ray waves pass through a slit or around an obstacle, and instead of moving in a straight line, they spread out, depending largely on the size of the slit or solid surface through which they pass.

The X-ray diffraction technique involves the use of electromagnetic radiation with a wavelength of 0.01 to 100 Å, generated in a cathode ray

tube. This technique directs a beam of monochromatic X-rays at the crystalline sample. Then the rays are diffracted and predictably enter the detector according to the ordered arrangement of the crystal atoms, generating patterns that can be analyzed to determine the crystal structure. This analytical technique provides information about the three-dimensional structure, chemical composition, and physical properties of crystalline materials [7]. Both constructive and destructive interferences are generated between the scattered rays during scattering.

The theoretical basis of the XRD technique is Bragg's law, which explains how X-rays scatter from a crystal composed of layers or atomic planes with a spacing distance d. According to Bragg's law, diffraction occurs when the incident X-rays are reflected from the planes of a crystal and combine constructively, see Fig. 2.4. The Bragg diffraction condition is met if the path length differences of the scattered rays are equal to an integer number of wavelengths [8]. The condition for this is described with the formula:

$$n\lambda = 2\,d\sin\theta \tag{2.1}$$

where, n is the diffraction order, λ represents the X-ray wavelength of the incident radiation Kα (λ =1,5406 Å), d refers to the distance between crystal planes and θ is the angle of incidence of X-rays in a crystalline structure.

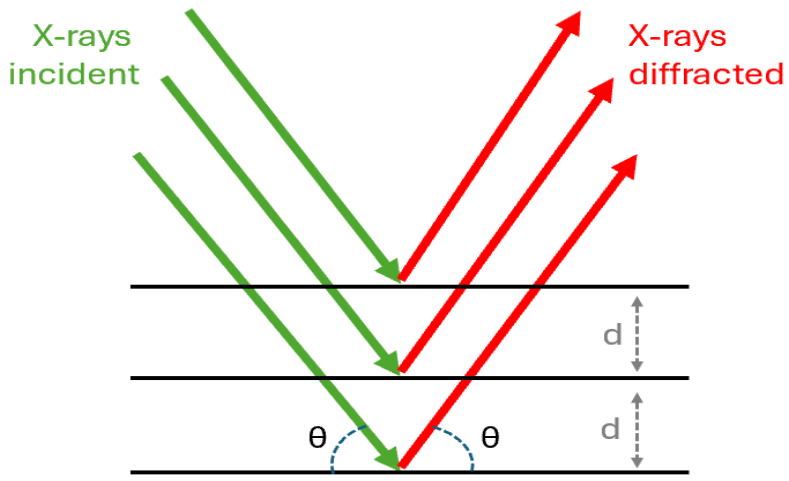

Fig. 2.4 *Bragg's Principle: X-rays incident and reflected make an angle θ symmetric to the normal crystal plane.*

When destructive interference occurs, Bragg's law is not fulfilled, and therefore, no peaks are formed in the diffraction pattern because the intensity of the X-rays is too low. However, by modifying the orientation of the material or detector, it can become a constructive interference capable of generating a peak. The diffraction patterns recorded by the detector can be used as a fingerprint that defines each crystalline solid material. Crystals are identified through various databases that provide information on the quantity, orientation, and distance between planes. The results are represented as the intensity of the detected X-rays versus 2θ [9].

In compounds such as g-C_3N_4, there is a characteristic XRD pattern represented by peaks at approximately 13.1° and 27.4°, each representing the in-plane structural packing and the interplanar stacking, respectively. When any modification is made to g-C_3N_4, it is common for the peaks to change in intensity, so the changes can be determined by Scherrer's formula [10]. The crystallite size 'd' of a material, expressed in units of nm, can be determined using the Scherrer equation for peak line broadening [11].

$$d = \frac{k\lambda}{\beta cos\theta} \tag{2.2}$$

where, k is the Scherrer constant and β represents width at half maximum (FWHM) [12].

In this study, the crystalline structure was studied by X-ray diffraction (XRD) on a Bruker D8 Discover diffractometer using a Cu Kα radiation source (λ = 1.5406 Å) and a Pilatus3R 100 KA detector within a 2θ range of 8-80° at a speed of 0.08°·min $^{-1}$. Match!®, QualX®, and the Crystal Open Database (COD) library were used to process the obtained diffractograms. The crystallite size was estimated by the Scherrer equation from the most intense peak, and the interlayer spacing was calculated from the peak with the highest intensity, i.e. plane (002). The $L_{crystallite}/d_{layer}$ ratio was used as an approximation to estimate the number of layers.

Fourier Transform Infrared Spectroscopy (FTIR)

This is a spectroscopic analysis technique that uses a part of the electromagnetic spectrum, using the whole infrared region with wavenumbers between 40 cm^{-1} and 14000 cm^{-1}, although it is now common to work in the mid-infrared region (400 cm^{-1} - 4000 cm^{-1}) [13]. The analysis begins when a continuous source emits infrared light over

a wide range of infrared wavelengths. The infrared light passes through an interferometer, modifying the light so that it splits into two beams. One beam is reflected by a fixed mirror and the other by a movable mirror and is then directed towards the sample, which absorbs part of the energy at a given wavenumber. The part of the energy that the sample passes through is received by a detector which converts the signal, known as an “interferogram”, into an absorbance spectrum using the mathematical method of the Fourier transform [14].

The FTIR technique is used to identify organic and inorganic materials by applying an infrared light source to the sample, which is absorbed at specific wavelengths depending on the chemical nature, bond vibrations within the molecules, and functional groups that make up the sample. Each material has a unique absorption pattern that can be considered its "molecular fingerprint", represented in an absorbance spectrum as intensity versus wavenumber [15].

The information provided by FTIR is used for both qualitative and quantitative analysis. Qualitative analysis can identify various chemical components, compare the sample spectra with standard spectra, and even detect trace impurities in the sample. Quantitative analysis, on the other hand, relates the absorption intensity to the concentration of the substance measured, i.e. it determines the purity of a chemical component in a sample, following the Lambert-Beer law [16].

This technique can be used on graphitic carbon nitride to analyze functional groups, checking for the presence of carbon-nitrogen bonds. Typically, peaks are found around 800 and 1500 cm^{-1} representing tri-s-triazine rings. Peaks between 1300 and 1600 cm^{-1} indicate the presence of C-N and C=N bonds, respectively. In addition, peaks around 3300-3400 cm^{-1} correspond to the deformation of the $-NH_2$ groups [10].

The FTIR analysis was performed on a Perkin-Elmer Spectrum65 device (Spectrum65 model) between 400 and 4000 cm^{-1}.

X-ray Photoelectron Spectroscopy (XPS)

X-ray photoelectron spectroscopy (XPS) is a sensitive quantitative spectroscopic technique for analyzing the surface chemistry of a material. The XPS technique is performed when high-energy photons such as X-rays from typical sources like Al Kα or Mg K (in the keV range) bombard the surface of solid material, causing a photoelectric effect that emits electrons from the first few layers of the surface. After the impact

is generated, the kinetic energy of the photoelectron E_k is measured, see Eq. 2.3 based on Einstein's law [17]:

$$E_k = h_v - E_b \quad (2.3)$$

where, h_v is the energy of the incident radiation and E_b represents the binding energy of the electron at a particular level.

The photoelectron peaks are named after the element and the orbital from which they are emitted, e.g. O_{1s}, which provides information about the electrons in the oxygen atom emitted from the 1s orbital. [18,19] This technique is widely used because of its excellent surface sensitivity and its ability to reveal qualitative and quantitative information about the chemical state, elemental composition, overall electronic structure, and density of electronic states of various solid samples, except for samples containing H and He. It has also been widely used for its ability to measure both the elements that make up the sample and the chemical environment to which it is bound [20].

This technique is used to analyze g-C_3N_4, providing information such as the ratio of carbon to nitrogen atoms. The structure of the compound can be determined thanks to the high resolution of the spectra of C_{1s} and N_{1s}. In structures such as CN, in the C_{1s} spectrum, binding energies close to 288 eV are often found, representing the bonding of one carbon to three nitrogen atoms. Other typical binding energies of CN in the N_{1s} region are around 398 and 399 eV, indicating the bonding of one carbon to two nitrogen atoms and the bonding of a trigonally bonded nitrogen atom to three carbon atoms, respectively [10].

The chemical composition of the surface was analyzed by X-ray photoelectron spectroscopy (XPS) on a Kratos AXIS UltraDLD device operating with an Al Kα X-ray source. The XPS spectra were referenced to the C_{1s} peak of the adventitious carbon at 284.6 eV. The deconvolution of the peaks was performed using XPSpeak 4.1® software, considering a Shirley background correction.

Scanning Transmission Electron Microscopy (STEM)

Scanning transmission electron microscopy (STEM) results from the combination of SEM and TEM, generating a transmission image using the scanning method. The high-resolution image obtained in STEM is similar to that obtained in TEM, allowing the complete characterization of the morphology and distribution of nanoparticles in a solid material. It is important to highlight that STEM has a wider range as the electron beam passes through the sample, being very useful for analyzing the

internal composition of the material. On the contrary, SEM only scans the surface of the sample, providing less information about it [21].

The measurement starts with the generation of a beam of light from an electron gun. Part of this electron beam is focused through a series of lenses onto a small sample area. These electrons interact with atoms in the sample, and some are transmitted to form a high-resolution image that provides information about the sample's morphology at the atomic level [22].

As explained above, this technique consists of imaging from the interaction of electrons with the sample. Therefore, STEM detectors are placed downstream of the sample to detect the electrons transmitted in the process. There are several detection methods coupled to STEM, such as high-angle annular dark-field detection (HAADF) being the most widely used. This method consists of collecting only the electrons scattered at a high angle, resulting in an image that is more sensitive to heavy elements than to light ones [23–25].

Electron Dispersed X-ray Analysis (EDX)

STEM can be coupled with various complementary techniques for element identification, such as energy-dispersive X-ray spectroscopy (EDX). This technique measures the energy and intensity of X-rays emitted by the sample resulting from the decomposition of the excited system. The measurements are represented as peaks corresponding to specific elements, which is useful for identifying the chemical composition of various samples through elemental mapping. The EDX detector also has a wide operating range as it can function at different tilt angles, maximizing X-ray collection [26,27].

Materials based on g-C_3N_4 were analyzed using scanning transmission electron microscopy and high-resolution scanning transmission electron microscopy (STEM and HR-STEM, respectively) to study the morphology and element composition distribution with high-angle annular dark-field (HAADF) detection and electron-dispersive X-ray microanalysis (EDX) on a Thermo Scientific™ Talos™ F200X (200 kV) device.

Elemental Analysis

Elemental analysis (EA), also known as organic elemental analysis or microelemental analysis, determines the elemental composition of a sample, either liquid or solid. Elemental analysis can be either qualitative, providing information on the elements present, or

quantitative, determining the amount of the chemical element in a sample [28] This analysis is important in organic chemistry, where the mass fraction of elements such as carbon, hydrogen, nitrogen and heteroatoms or halogens in a sample is determined. It is also considered a fundamental tool used as a complementary technique to determine the chemical structure and purity of a compound within the sample [29].

This technique commonly operates through the dynamic, controlled combustion of several samples in a reactor. By subjecting the samples to combustion in a column filled with an electronically temperature-controlled oxidizing-reducing catalytic bed, gases composed of elements such as C, H, and N, among others, are generated. These combustion products are directed to the analyzer, usually a simplified gas chromatograph, to determine the proportion of the elements in the original sample. Once the molecular weight of the compound is known, the result of the analysis is of great use in finding the molecular formula of the analyzed substance [29].

This type of analysis is used on materials such as g-C_3N_4 to determine their purity. This is done by comparing the theoretical ratio between the percentages of carbon and nitrogen, which is around 0.75, with the experimental ratio. If this ratio differs from the theoretical value, it indicates the presence of impurities in the prepared g-C_3N_4 [10]. The elemental composition, i.e. C, N, and H, was determined using a Thermo Scientific™ Flash 2000 analyzer and Leco Instruments TrueSpec® Micro CHNS.

Nitrogen adsorption isotherms

Gas adsorption is a useful methodology for characterizing a wide range of porous materials. These materials have an irregular surface structure, making direct measurement of surface area difficult. One technique commonly used to characterize such solids is physical nitrogen adsorption, which involves the physical adsorption of gas molecules on the solid surface through Van der Waals forces, as a function of the relative pressure of the contacting gas (N_2), at a constant temperature of 77 K [30].

Nitrogen adsorption occurs on the pore wall, which will adsorb gas molecules in successive layers until the pore is filled, reaching equilibrium between the adsorbed and gas-phase molecules. As depicted in Fig. 2.5, if the relative pressure increases, the pore adsorbs a new layer until filling. If the pore diameter is larger, more nitrogen layers will be needed, resulting in a higher P/P_0 [31,32].

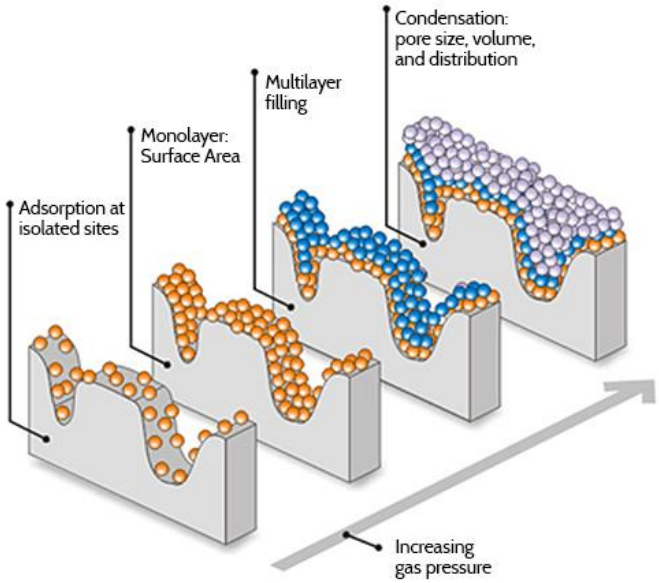

Fig. 2.5 *BET model of multilayer adsorption* [33].

Adsorption isotherms are represented by curves that provide insight into the behavior of an adsorbed particle during the adsorption process, i.e. the interaction between the particles and the surface and the surface characteristics. If the adsorbed particles correspond to those of a gas, their pressure is considered. The isotherm can be used to determine the specific surface area, the adsorbed volume at a given pressure, and the pore size distribution and pore shape of a porous solid material [32].

The calculation of the surface area of an adsorbent is commonly performed by the Brunauer, Emmett, and Teller (BET) method, which is a technique applicable in the equilibrium of gas-solid systems. The linear form of BET equation is expressed as follows:

$$\frac{P}{q_{e(}P_0 - P)} = \frac{1}{q_m C_{BET}} + \frac{(C_{BET} - 1)}{q_m C_{BET}} \frac{P}{P_0} \tag{2.4}$$

where, P_0 is the vapor saturation pressure, P represents equilibrium pressure, q_m refers to monolayer volume, q_e represents adsorbed volume at equilibrium pressure P, and C_{BET} is the constant indicative of the degree of adsorbate-adsorbent interaction.

The linear adjustment of $\frac{P}{q_{e(P_0-P)}}\ vs.\frac{P}{P_0}$, allows to calculate C_{BET} and q_m from the slope and intercept values, respectively [31]. Once the volume of the monolayer is known, the specific surface area (S_g) is determined by the following equation:

$$S_g = \frac{q_m\ N\ A_m}{V_{mol}} \tag{2.5}$$

where, N is Avogadro's number, A_m represents the area of the adsorbed molecule and V_{mol} is the volume of one mole of gas under normal conditions.

The Barrert, Joywner, and Halenda (BJH) method is used to calculate pore size distributions from experimental isotherms. This method is based on two fundamental assumptions: the first assumes that the pore geometry is cylindrical and the second that the amount adsorbed results from both physical adsorption on the pore walls and capillary condensation within the pores. This method is based on the Kelvin pore model, see Eq. 2.6, which is only applicable to mesopores and macropores [32,34]. The Kelvin equation or Young-Laplace equation relates the pressure to the radius of curvature of a liquid meniscus. The radius is obtained by the Kelvin equation:

$$r\left(\frac{P}{P_0}\right) = 0.416\ \left[\log\left(\frac{P}{P_0}\right)\right]^{-1} + t\left(\frac{P}{P_0}\right) + 0.3 \tag{2.6}$$

where, r is pore radius, P_0 refers to vapor saturation pressure and P is equilibrium pressure.

The N_2 adsorption-desorption isotherms at 77 K were performed on an ASAP 2020 (Micromeritics) and Sync 200 equipment from 3P Instruments©. The samples were degassed overnight at 150 °C under vacuum. The specific surface area was obtained by the Brunauer-Emmett-Teller (S_{BET}) method, and the total specific pore volume (V_T) was calculated from the adsorption of N_2 at P/P_0 ~0.99. The Barrett, Joyner, and Halenda (BJH) method was applied to analyze the and most frequent pore diameter.

Diffuse Reflectance Spectroscopy (DRS)

This analysis aims to measure the optical and/or scattering properties of radiation in the ultraviolet-visible range (190 - 800 nm) of a sample.

In addition, it is used to obtain information about the environment of metallic and organic species present in the material. The reflectance spectrometer consists of an ultraviolet light source, two double monochromators connected by an optical fiber, and a spectrometer connected to a computer [35].

Diffuse reflectance spectroscopy is carried out by irradiating the sample with a beam of light; only a small fraction of this light is reflected in two ways, through the phenomenon known as specular reflectance and diffuse reflectance, see Fig. 2.6. In this technique, both phenomena usually occur, as specular reflectance reflects light from outside the sample, providing little information about the composition of the sample. In the case of diffuse reflectance, the light penetrates the front surface of a substance, scatters within its volume, and exits through the front surface in all directions. The reflected light is measured with a spectrometer, generating relevant information about the optical properties of the catalyst [36–38].

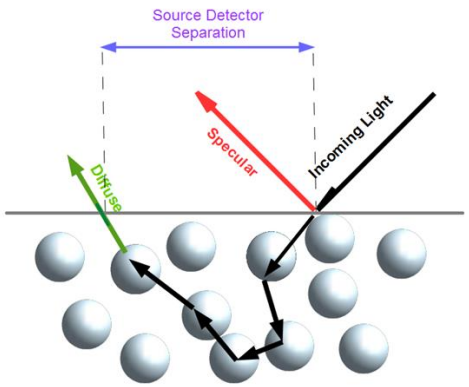

Fig. 2.6 *Specular and diffuse reflectance* [39]

The bandgap energy (E_g) is a fundamental characteristic of the electronic structure of semiconductor materials, which indicates the minimum energy necessary to provide electrical conductivity. A common procedure for determining the value of E_g involves the use of diffuse reflectance spectroscopy (DRS) in conjunction with the Tauc method, see Eq. 2.7, which is based on the relationship between E_g and the optical absorption coefficient.

$$(\propto hv)^{1/\gamma} = C(hv - Eg) \tag{2.7}$$

where $\propto$ is a coefficient of absorption, h refers to Planck's constant, v means photon's frequency, C is a proportionality constant, Eg represents the band gap energy, and the value of the exponent γ denotes the nature of the electron transition. This parameter takes the following values: direct allowed transitions, γ=1/2; direct forbidden transitions, γ=3/2; indirect allowed transition γ=2; indirect forbidden transition, γ=3. All catalysts used in this work are based on g-C_3N_4, thus they are considered indirect semiconductors, with γ=2 for all samples. When $\propto$ equals zero, hv takes the value of Eg. The value of hv, is calculated considering that $v = c/\lambda$, with c being the speed of light. Once the value of Eg is known, the Kubelka-Munk model is used, expressed by the following equation:

$$\mathrm{F(R_\infty)} = \frac{\mathrm{K}}{\mathrm{S}} = \frac{(1-\mathrm{R_\infty})^2}{2\mathrm{R_\infty}} \tag{2.8}$$

where, $\mathrm{R_\infty}$ is the reflectance of the sample with "infinite thickness"; K represents absorption coefficient and S refers scattering coefficient. Considering that $\mathrm{F(R_\infty)}$ is proportional to $\propto$, this value is replaced in Eq. 2.7, obtaining:

$$(\mathrm{F(R_\infty)}\, hv)^{1/\gamma} \tag{2.9}$$

Consequently, by representing $(\mathrm{F(R_\infty)}\, hv)^{1/\gamma}$ versus Eg and extrapolating the linear interval with a straight line, it is possible to obtain the value of E_g at the intersection with the x-axis. The value of E_g is found through the intersection of the linear fit of the region associated with the optical absorption edge and the hv axis.

The optical properties were measured using a Varian Cary 5E spectrophotometer in the UV-visible range. The Kubelka-Munk function, $F(R_\infty)$, was obtained from the reflectance spectra, and the band gap was estimated using the Tauc plot method considering indirect electronic transitions γ =2 [40–42].

Photoluminescence (PL)

Luminescence is the emission of light by a material due to various types of processes. Several processes can result in light generation at room temperature, including chemical reactions (chemiluminescence) or external stimuli such as electrical (electroluminescence) or light stimuli (photoluminescence) [43].

The non-destructive photoluminescence (PL) technique is used to characterize photocatalytic materials containing an electronic band

structure. The analysis begins when a sample is irradiated with a light source, initiating the photoexcitation process in which electrons in the valence band (VB) are promoted to the conduction band (CB), while holes are generated in the VB. During this process, some of the excited electrons in the CB tend to readily return to the VB and recombine with the holes, known as the charge carrier recombination phenomenon. During this process, a certain amount of chemical energy is released, which can be transformed into thermal or light energy. The luminous energy or fluorescence emitted by the sample is measured and a photoluminescence spectrum is obtained, which makes it possible to observe the absorption edge of different samples and the dependence of the spectrum on the relaxation time of the photo-generated electron-hole pairs. In photocatalytic processes, the catalyst is expected to generate the least amount of fluorescence, i.e. the material is expected to reduce its ability to recombine charge carriers. By reducing recombination, the photocatalytic performance is improved, resulting in more selective reactions [44].

The recombination rate of the photo-generated electrons was assessed by photoluminescence (PL) analysis using a Varian Cary Eclipse device, applying light with an excitation wavelength of 365 nm (2.5 nm slit) and monitoring the emission signal between 400 and 600 nm.

Nuclear Magnetic Resonance (NMR)

Nuclear magnetic resonance spectroscopy is a non-destructive technique that can be applied to any substance in liquid or solid-state containing nuclei with non-zero spin values (^{1}H, ^{2}H, ^{13}C, ^{15}N, and ^{31}P, among others). It consists of the absorption of selective radio frequencies by selected nuclei of a molecule while the sample is subjected to a strong magnetic field. After the nuclei absorb the energy and return to their ground state, signals are emitted which are detected and converted into a nuclear magnetic resonance spectrum [45].

This technique allows the characterization of solid materials, determining their structure and surface locations. In addition, it offers facilities as it can be performed in the presence of gases or liquids over a wide range of temperatures and pressures. Solid-state spectra tend to have much broader signals due to magnetic interactions between the spins of the nuclei. The interactions that produce the broadening include dipolar coupling, chemical shift anisotropy, and quadrupole interactions. These constraints have been solved by rapidly rotating the sample

around an axis at the magic angle θ = 54.7° concerning the direction of the external magnetic field (MAS) [46].

For example, NMR has been widely used to probe Brønsted acid sites by ^{1}H MAS NMR spectroscopy and Lewis's acid sites by adsorption of probe molecules. As a result of their interactions with the surface sites, the ^{1}H, ^{2}H, ^{13}C, ^{15}N, and ^{31}P nuclei of the hydroxyl groups and probe molecules change their NMR spectroscopic parameters in a characteristic way [47,48].

In this study, solid materials belonging to the PCN series were characterized by magic angle spinning nuclear magnetic resonance (MAS NMR), focusing on the chemical environment of C and P. The analyses were performed on a Bruker Advance 500 MHz NMR spectrometer equipped with a 4-mm cross-polarized (CP) MAS probe. For ^{13}C spectra, CP-MAS experiments were performed at 10 kHz. For the ^{31}P MAS, the experiments were performed at 12 kHz.

2.3. EXPERIMENTAL SETUPS AND PROCEDURES

2.3.1. Experimental setup

The evaluation of the photocatalysts was carried out in two types of photoreactors, see schematic in Fig. 2.7, both with a discontinuous type of annular configuration, in which a liquid solution circulates through the outer space while the radiation source is located in the center. The solution is recirculated to a stirring tank that includes a cooling system, maintaining the mixture at a constant temperature of 20°C. Excess air is constantly bubbled in the stirring tank to maintain an oxidizing environment and thus promote the selective oxidation reaction of the alcohol.

In all cases, before irradiation, an adsorption period of 30 minutes was carried out in the dark. This process consisted of mixing 350 mL of an aqueous alcohol solution whose concentration varies between 0.5-1.0 mM, with the solid catalyst at a dose of 0.5 g L^{-1}. After the adsorption period, the photocatalytic tests begin by loading the mixture into the reactor and irradiating it with a light source for 5 h. To analyze the behavior of the reagent and product, samples were collected every 30 minutes using an extraction system incorporated in the stirring tank and the suspended photocatalyst was removed using syringe filters (PVDF, 0.45 μm).

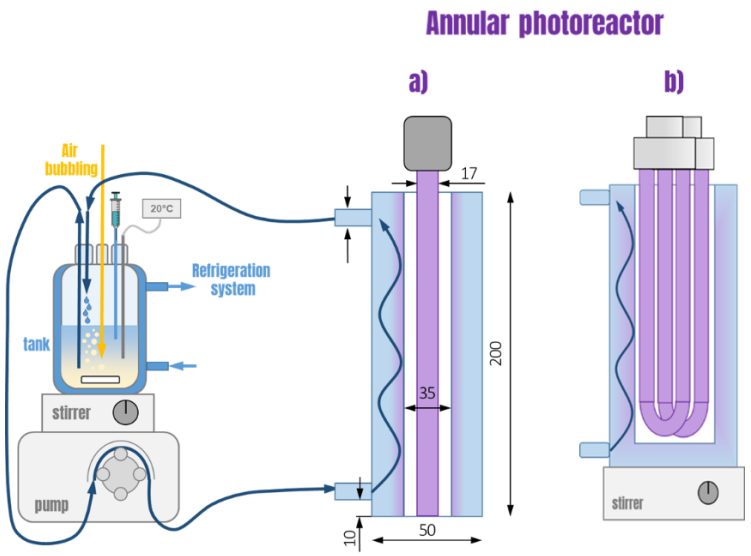

Fig. 2.7 *Experimental setup: a) cylindrical photoreactor with 304 stainless steel outer wall and tubular lamp, b) photoreactor with borosilicate glass outer wall and double lamp.*

The configuration 2.7(a) consists of a cylindrical photoreactor with a 304 stainless steel outer wall and a Pyrex glass inner cylinder. The mixture circulating through the outer wall of the reactor is kept unstirred. The irradiation source was a Sylvania® F11W T5 BL368 lamp, emitting at 365 nm, 11 W. This configuration was used in the reactions described in Chapter 3, which were carried out over 4 h. In addition, this configuration was also used in Chapter 5, with the difference that the activity was evaluated for 5 h under visible radiation using daylight from a commercial lamp (Sylvania® F6W/T5/54-765, emitting radiation >400 nm, 6 W). On the other hand, configuration 2.7(b) consists of a photoreactor with a borosilicate glass annular jacket equipped with two UVA lamps emitting at 365 nm (9 W each). The mixture circulating along the outer wall of the reactor is kept in agitation, which ensures that the catalyst remains in suspension during the 5 hours of the reaction. This configuration has been used to carry out the reactions described in Chapters 4, 5, and 6.

2.3.2. Methods for aqueous analyses

High-performance liquid chromatography (HPLC)

The behavior during the oxidation reaction was evaluated by high-performance liquid chromatography (HPLC) analysis, in which the concentration of both the alcohol and the aldehyde produced was

monitored over time. This technique involves a mobile or eluent phase, and a stationary phase, i.e. column consisting of solid particles based on silica, coated silica, or polymers that improve surface area and retention time. The analytical process begins when the sample enters the system and mixes with the mobile phase, then passes through the stationary phase under pressure exerted by a pump. As the mixture moves through the column, each component interacts differently with the stationary and mobile phases. The interaction of the sample with the stationary phase is defined by the nature of the stationary phase, by adsorption, partition, ion exchange, and size exclusion chromatography. When the sample leaves the column, it is directed to the detection and quantification module. Commonly used detectors are based on techniques such as UV-vis, fluorescence, refractive index, or mass spectrometry, which send a signal and translate it graphically into a chromatogram. The chromatogram represents the different compounds in the sample with distinct peaks, known by their retention times. These peaks can have different areas depending on the concentration of the compound in the mixture, making it a quantitative analysis technique that allows the concentration of a specific compound dissolved in a sample to be determined using a previously defined calibration curve [49,50].

The quality of the analytical method was determined by linearity, standard deviation, and limit of detection. To measure the precision of the measurements, the standard deviation was used, obtained by performing several tests to ensure the consistency of the results. The limit of detection (LOD), described by Eq. 2.9, where σ is the standard deviation and m is the slope found on the calibration curve, represents the smallest amount of analyte whose signal can be distinguished from the noise signal, i.e. the minimum concentration of the substance that can be reliably detected by the analytical method [51]:

$$LOD = \frac{3 \times \sigma}{m} \times 1000 \tag{2.9}$$

Ultraviolet-based detection is widely used in high-performance liquid chromatography because of its ease of operation, relative sensitivity, and cost-effectiveness compared to other methods. This detector measures the absorbance of UV-vis light at multiple wavelengths simultaneously [52]. Diode array detectors (UV-vis DADs), also known

as photodiode array detectors (UV-vis PADs), measure the absorbance of UV-vis light at multiple wavelengths simultaneously and are very sensitive, allowing the detection of compounds at low concentrations [53].

In the present investigation, the behavior of alcohols and aldehydes was analyzed using an HPLC coupled to a UV-vis detector. Two different instruments were used. The first instrument was a Shimadzu LC-10 equipped with a UV-visible DAD detection system, using a Kromasil C18 100 5C18 column (100 Å, 5 µm, 2.1 x 150 mm) as the stationary phase. The mobile phase was a mixture of methanol (2.5%), acetonitrile (27.5%), and 0.1% H_3PO_4 in ultrapure water (70%) pumped at 1.0 ml min^{-1}. Retention times were 3.7 minutes for benzyl alcohol and 6.4 minutes for benzaldehyde. The second used HPLC was the Waters™ HPLC Alliance e2695 coupled to a 2998 UV visible photodiode array (PDA) detector. The stationary phase consisted of a Zorbax Bonus-RP column (4.6 × 150 mm, 5 µm). The mobile phase was pumped at 1 mL min^{-1} and sample injection was performed under an isocratic mode with an injection volume of 50–90 µL. For the analysis of benzyl alcohol (BA) and benzaldehyde (BD), a mixture of 30% acetonitrile (A) and 70% acidified water (B, 0.1% v/v trifluoroacetic acid) was pumped, and quantification was performed at 215 nm for BA and 248 nm for BD. The same device was used to analyze cinnamyl alcohol (CA) and cinnamaldehyde (CD) with a mobile phase consisting of 40% (v/v) acetonitrile and 60% (v/v) ultrapure water acidified with 0.1% (v/v) trifluoroacetic acid. The injection volume was 50 µL. Quantification was performed at 240 nm for CA and 331 nm for CD. Finally, the presence of short-chain organic acids as oxidation end products was analyzed using a CoreGel 87H3 column (7.8 × 300 mm) under isocratic pumping of an acidified aqueous solution (H_2SO_4 4 mM) at 1 ml min^{-1} with detection at 210 nm.

Liquid chromatography coupled with electrospray ionization in positive mode and detection by quadrupole time-of-flight mass spectrometry (LC-ESI (+)-QTOF):

HPLC coupled with mass spectrometry detection (LC-MS) is a technique that offers high sensitivity and selectivity, making it ideal for analyses requiring higher precision, such as in the pharmaceutical industry. This equipment consists of a sampler, the HPLC system, the ionization source, and the mass spectrometer. The ionization source is crucial as it serves as the interface between the HPLC eluent and the

mass spectrometer. The ionization source operates at atmospheric pressure and high voltages, together with heat sources, to generate the ions analyzed by the system. Two common ionization systems are atmospheric pressure chemical ionization (APCI) and electrospray ionization (ESI), the latter being used in this research. ESI employs a high voltage field (3-5 kV) to nebulize the column effluent, resulting in the generation of small droplets containing individual ions that then enter the detector, which separates these ions. The detector is a hybrid system that combines a quadrupole mass spectrometer with a time-of-flight (TOF) mass spectrometer, providing a higher-resolution mass spectrum for each chromatographic peak eluted from the column [54,55].

In the present study, the transformation products during the photocatalytic oxidation of cinnamyl alcohol with P-CN were analyzed by liquid chromatography coupled with electrospray ionization in positive mode and detection by quadrupole time-of-flight mass spectrometry, LC-ESI(+)-QTOF. Chromatographic separation was carried out on a Waters™ Acquity UPLC ultra-high pressure, H-Class, equipped with PDA detection. Ionization was performed on a Waters Zspray™ and high-resolution mass spectrometry on a Waters QTOF Triwave®, model Synapt G2. Acquisition conditions were as follows: capillary voltage 3500 V, collision energy, X eV, m/z range from 50 to 1000. Transformation products were identified based on the MS spectra of the precursor using MassLynx software.

Total organic carbon (TOC)

Total organic carbon was measured with a Shimadzu® TOC-V_{CSH} analyzer. This technique is an indicator of the complete oxidation of the organic compounds present in a sample, converting all the carbon content to carbon dioxide. In the selective reaction of alcohols, this technique is used to determine whether there are highly oxidizing species capable of causing over-oxidation and affecting the selectivity towards the desired product.

2.3.3. Catalytic activity

Photolysis

Before carrying out any photocatalytic reaction, each reagent was subjected to photolysis tests. This test consists of irradiating each alcoholic solution in the absence of a catalyst to determine whether chemical decomposition occurs, i.e. whether aldehyde production

results solely from the transfer of light energy to the initial alcoholic sample [56]. The photolysis tests were carried out under the same conditions as the reactions contained in each chapter, with the only difference being that in no case was a solid catalyst added.

Reaction yield

The reaction yield was determined from parameters such as conversion, selectivity, and reaction rate, defined by (equations 2.10-2.12). The conversion indicates the fraction of the reagent consumed during the chemical reaction. Product selectivity refers to the ability of a chemical process to generate the desired product and the reaction rate indicates the variation of the concentration of the reactants with time. Each of these parameters can vary depending on the contact surface, temperature, and concentration of the reactants [57].

$$conversion = \frac{C_{ALC_0} - C_{ALC_f}}{C_{ALC_0}} \tag{2.10}$$

$$selectivity = \frac{C_{ALD_f}}{C_{ALC_0} - C_{ALC_f}} \tag{2.11}$$

$$r_0 = k\, C_{ALC_0} \tag{2.12}$$

were, C_{ALC_0} is the concentration of the initial alcohol, C_{ALC_f} represents the concentration of the alcohol at the end of the reaction, C_{ALD_f} means the final concentration of the aldehyde, r_0 is the initial reaction rate, k is the pseudo-first-order kinetic constant.

2.3.4. Reaction mechanism

Scavengers

To understand the reaction mechanism, scavengers or scavengers of chemical reactive species have been used. These species are commonly used in photocatalytic processes to qualitatively evaluate the main oxidative species involved. The scavengers react quickly and specifically with the radical, generating a stable species that does not interfere with the reaction, thus eliminating the effect of this radical in the reaction. In heterogeneous photocatalysis, various molecules are used as radical scavengers, for example, the action of the photo-generated holes is suppressed by adding oxalic acid (10 mM), or EDTA (1 mM), which are electron-donating species. For the inhibition of HO•, alcohols

such as methanol (10 mM) and tert-butyl alcohol (TBA, 10 mM) were used. To remove the action of the superoxide radicals, strategies such as the N_2 bubbling or the addition of specific scavengers such as p-benzoquinone (1 mM) and disodium 4,5-dihydroxybenzene-1,3-disulphonate (1 mM) have been used. Singlet oxygen role was tentatively studied by adding L-histidine (1 mM) as an inhibitor. Each of these species is added in excess, to ensure the capture of the radicals involved during the process. In all the scavenged assays, the pH was adjusted to the blank value with NaOH and/or HCl solutions [58].

The presence of the hydroxyl radical $HO^{\bullet}$ during the selective oxidation of alcohols is of special interest due to its high oxidative power. Controlling the concentration of these radicals allows directing the reaction toward the formation of specific products, minimizing the generation of unwanted products. Experiments to quantify the rate of generation of hydroxyl radicals were carried out in alkaline solutions containing non-fluorescent terephthalic acid (TA). The pH of the solutions was adjusted with NaOH to ensure complete dissolution of the TA. During the photocatalytic process, TA captures $HO^{\bullet}$ radicals by releasing fluorescent 2-hydroxy-terephthalic (2-HO-TA) acid, which undergoes emission at 425 nm when excited at a wavelength of 318 nm. The formation of 2-HO-TA the can be monitored over time as a direct indicator of the presence of $HO^{\bullet}$ radicals [59]. For this study, two tests were performed and compared with 2-HO-TPA (1 mM) in the presence and absence of cinnamyl alcohol. The analysis of 2-HO-TPA was performed on a Varian Cary fluorescence spectrometer with an excitation wavelength of 315 nm (2.5 nm slit) and emission spectra recorded between 360 and 600 nm (2.5 nm slit), with a maximum peak at 420 nm. The peak area correlated with the concentration of the 2-HO-TPA standard solution between 0.5 and 5 µM. The detection limit of 2-HO-TPA was estimated to be 0.21 mM.

2.3.5. Characterization of the radiation source

In photocatalytic reactions, light is considered as an intermediate capable of changing the course of the reaction. Therefore, it is necessary to study the interaction of light with photochemical systems. One of the techniques used to understand this behavior is chemical actinometry, a technique used to measure the amount of ultraviolet or visible radiation received by a sample. This technique consists of subjecting a chemical system containing a chromophore C to a light-

induced reaction at a certain wavelength whose quantum yield is precisely known; the amount of product formed or the decrease in the reactant is determined spectrophotometrically and correlated with the number of photons absorbed by the sample. Ferrioxalate is considered one of the most popular actinometers because it has high and constant quantum yields in the UV-vis region (250-500 nm). The chemical actinometry of ferrioxalate is based on the light-induced irreversible redox reaction of ferrioxalate, see equation 2.13-2.15, where Fe^{3+} is converted to Fe^{2+} and subsequently a reductive reaction takes place via CO_2, $CO_2^{-\cdot}$ radical anions [60,61].

$$[Fe^{III}(C_2O_4)_3]^{3-} + h\nu \rightarrow [Fe^{II}(C_2O_4)_2]^{2-} + (C_2O_4)^{-\cdot} \quad (2.13)$$

$$(C_2O_4)^{-\cdot} \rightarrow CO_2 + (CO_2)^{-\cdot} \quad (2.14)$$

$$[Fe^{III}(C_2O_4)_3]^{3-} + (CO_2)^{-\cdot} \rightarrow [Fe^{II}(C_2O_4)_2]^{2-} + (C_2O_4)^{2-} + CO_2 \quad (2.15)$$

However, this method presents some interferences, because it requires analytical procedures after irradiation to confirm the complete coloration of the Fe^{2+} complex, in addition to presenting possible sources of experimental errors. For this reason, in this work a modified system consisting of ferrioxalate-polyoxometalate has been used, in which the reduced polyoxometalate (blue color) is generated in situ and can be measured spectrophotometrically without any subsequent treatment. The reducing power of $(CO_2)^{-\cdot}$ can generate the reaction (Eq. 2.16) with a characteristic blue color [62].

$$POM\ (colorless) + (CO_2)^{-\cdot} \rightarrow POM^{-}(colored) + CO_2 \quad (2.16)$$

Actinometry tests were performed with 60 mM oxalic acid, 5 mM of $FeCl_3{\cdot}6H_2O$, and 1 mM of $H_4SiW_{12}O_{40}$. The pH of the solution was adjusted to 4.5 with the addition of HCl and NaOH to avoid possible self-decomposition of the polyoxometalate complex. It was considered that the rate of formation of POM^- follows zero-order kinetics according to:

$$C_{POM-} = I_0 \cdot \Phi_{POM^-,365nm} \cdot t \quad (2.17)$$

where, C_{POM^-} is the concentration of the POM^- formed, I_0 is the radiation intensity, and $\phi_{POM^-,365nm}$ is the quantum yield of the reaction at 365 nm. From the slope of the adjustment of the POM^- concentration with time, I_0 can be estimated, considering that, according to the literature, $\phi_{POM^-,365nm}$ =0.18 mol $Einstein^{-1}$ [62].

Alternatively, the intensity of the radiation can be measured by spectroradiometry. A spectroradiometer is a device used to measure spectral fluxes at different wavelengths within a specific range of the spectrum. Measuring the maximum emission of the light source at certain wavelengths, along with the optical characterization of the catalyst through DRS-UV-visible, which indicates the wavelengths at which the catalyst effectively absorbs light, are complementary studies of great interest for photocatalytic processes. The data provided by the spectroradiometer allow for adjusting the light source to maximize emission at wavelengths that the catalyst effectively absorbs. Alternatively, catalysts can be selected whose absorption spectrum matches the wavelengths emitted by the light source [63]. The joint study of these two properties can ensure efficiency in the photocatalytic reaction. In this study, the BLACK-Comet UV-visible spectroradiometer (StellarNet Inc., Florida, USA) was used, employing lamps that simulated daylight to ensure the activity of the photocatalyst in the visible region.

2.4. QUANTUM EFFICIENCY DETERMINATION

The quantum efficiency (QE) of alcohol photodegradation was quantified following the IUPAC recommendations, which define Q_E as the ratio between the number of molecules reacting via the reaction rate ($r_{ALC,0}$) and the number of photons interacting with the catalyst, i.e., the photon absorption rate ($e^{\alpha,v}$). The reaction rate is determined using Eq. 2.12, and the photon absorption rate is determined through the following procedure:

2.4.1. Volumetric rate of photon absorption

The average volumetric rate of photon absorption was obtained by solving the Radiative Transfer Equation (RTE) in the annular photo-reactor, available in Fig. 2.7 The RTE can be expressed as Eq. 2.18 assuming; (i) the emission radiation is negligible and (ii) steady state condition during the photocatalytic processes [64–66].

$$\frac{dI_{\lambda,\underline{\Omega}}(\underline{x})}{ds} = -\kappa_\lambda(\underline{x})I_{\lambda,\underline{\Omega}}(\underline{x}) - \sigma_\lambda(\underline{x})I_{\lambda,\underline{\Omega}}(\underline{x}) + \frac{\sigma_\lambda(\underline{x})}{4\pi}\int_{\Omega'=4\pi} p(\underline{\Omega}' \to \underline{\Omega})\, I_{\lambda,\underline{\Omega}'} \qquad (2.18)$$

To solve Eq. 2.18, it is first necessary to determine the optical properties of the photocatalyst suspensions. The spectral absorption coefficient (κ_λ), the spectral scattering coefficient (σ_λ), and the scattering phase, $p(\underline{\Omega}' \to \underline{\Omega})$ are required. Here, and according to previous studies

in similar catalysts, the Henyey and Greenstein phase function (Eq. 2.19) was adopted to calculate the scattering phase function [64,66].

$$p\left(\underline{\Omega}' \rightarrow \underline{\Omega}\right) = \frac{1-g_\lambda^2}{\left(1+g_\lambda^2-2g_\lambda^2 u_0\right)^{3/2}} \tag{2.19}$$

The optical properties were obtained by solving the RTE, which considers radiation absorption and scattering effect by the catalyst, by using the discrete ordinate method (DOM) in a rectangular spectrophotometer cell in combination with a nonlinear, multiparameter regression procedure (lsqnonlin, Algorithm: Trust-Region-Reflective Optimization). Before that, the extinction coefficient β_λ was obtained by applying a standard linear regression to the plots of β_λ versus catalyst concentration. Besides, considering that the cell can be represented as an infinite plane parallel medium with azimuthal symmetry, a one-dimensional, one-directional radiation transport model can be used to solve the RTE, see Fig. 2.8.

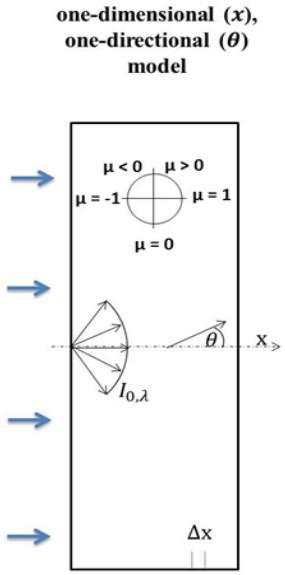

Fig. 2.8 *Schematic representation for the one-dimensional, one-directional radiation model of the cell used for the determination of the optical properties of the samples.*

Fig. 2.8 shows a schematic representation of the spectrophotometer cell and the corresponding RTE solution scheme where the net light intensity is presented by one angular-related variable ($\mu = \cos\theta$) at each point of the cell one-dimensional (x variable) representation. The fitting procedure renders the values of ω_λ (the albedo defined by Eq.

2.20) and g_λ (Eq. 2.21) parameters that minimize the differences between model predictions and experimental data of diffuse transmittance and reflectance measurements at the spectrophotometric cell for a set of catalyst concentrations, C, and in the wavelength range of the light source. Then, the volumetric scattering and absorption coefficients can be obtained as following:

$$\sigma_\lambda = \beta_\lambda \times \omega_\lambda \quad (2.20)$$

$$\kappa_\lambda = \beta_\lambda - \omega_\lambda \quad (2.21)$$

The extinction (β_λ), scattering (σ_λ) and absorption (κ_λ) coefficients, as well as the asymmetry factor g for all samples of the study are represented graphically.

Once the optical properties of the catalysts have been established, the evaluation of the radiation field inside the photoreactor can be carried out. The DOM tool was used to transform the integro-differential Eq. 2.18 into a system of algebraic equations that can be solved numerically. The reactor configuration requires the use of a cylindrical two-dimensional (r-z variables), two-directional (θ-ϕ variables) model of the photoreactor radiation field (Fig. 2.9A). The net radiation intensity at each r-z point of the reactor is now represented using a discretized spatial mesh having two angular-related coordinates (μ=cosθ, η=cosϕ). Fig. 2.9B displays the unitary (μ, η) pair, basal projections in a quadrant of the space around a $r - z$ point calculated using the so-called S16 method. The determination of the intensity at each point of the reactor require to divide the space in 4 quadrants as depicted in Fig. 2.9C and the measurement of the incident light intensity at the boundary (liquid surface) using chemical actinometry. According to the Duderstadt and Martin recommendation [67], and following the numerical procedure scheme, the finite difference method (DOM) was derived directly from the radiation balance for each mesh cell.

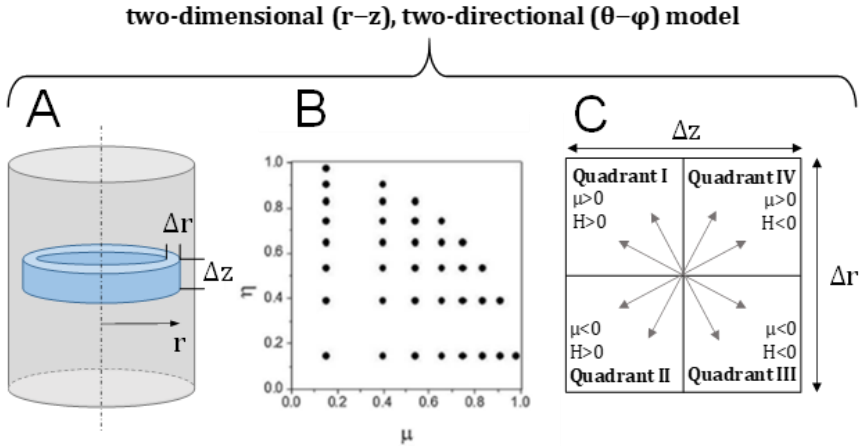

Fig. 2.9 *(A) Representation of the r and z spatial mesh discretization of the photoreactor, (B) Directional mesh for the Quadrant I and (C) representation of quadrants of directions as a function of the direction cosines (μ, η) respect to r and z-axis*

Using the DOM approach the central intensity at each cell ($I_m^{i,j}$) can be calculated from the previous ones starting from the appropriate boundary values ($I_m^{1\pm1/2,j}$; $I_m^{i,j\pm1/2}$) as well as one "auxiliary" one coming from the directional mesh ($I_{m-1/2}^{i,j}$) as:

$$I_m^{i,j} = |\mu_m|\left(A_{i+1/2,j} - A_{i-1/2,j}\right)D^{-1}I_m^{1\pm1/2,j} + 2|\eta_m|B_{i,j}D^{-1}I_m^{i,j\pm1/2} + \left(A_{i+1/2,j} - A_{i-1/2,j}\right)\cdot\left(\nu_{m+1/2} + \nu_{m-1/2}\right)D^{-1}W_m^{-1}I_{m-1/2}^{i,j} + \frac{\sigma_\lambda}{4\pi}\sum_{n=1}^{M} I_n^{i,j}P_{nm}W_nV_{i,j}\,D^{-1} \quad (2.22)$$

where, A is the area of the spatial cell parallel to the cylindrical axe, η means direction cosine, B represents the area of the spatial cell perpendicular to the cylindrical axe, ν is the effective area for angular fluxes, W means weight of direction cosines and V represents the volume. From eq. 2.2, some variables can be defined as:

$$D = |\mu_m|\left(A_{i+1/2,j} - A_{i-1/2,j}\right) + 2|\eta_m|B_{i,j} + \left(A_{i+1/2,j} - A_{i-1/2,j}\right)\cdot\left(\nu_{m+1/2} + \nu_{m-1/2}\right)W_m^{-1} + \kappa_\lambda V_{i,j} + \sigma_\lambda V_{i,j} \quad (2.23)$$

$$A_{i+1/2,j} = 2\pi r_{i+1/2}\Delta z_j \quad (2.24)$$

$$B_{i,j+1/2} = 2\pi\left(\frac{\left(r_{i+1/2}+r_{i-1/2}\right)}{2}\right)\Delta r_i \quad (2.25)$$

$$V_{i,j} = 2\pi\left(\frac{\left(r_{i+1/2}+r_{i-1/2}\right)}{2}\right)\Delta z_j\Delta r_i \quad (2.26)$$

The computational calculation at each quadrant begins from the corner of the spatial mesh in which two of the four boundary conditions can be applied. In this case, the boundary conditions are (i) known inlet radiation for quadrants I and II at r=0; and (ii) null reflection in the inner reactor wall surfaces. The directional mesh at each spatial cell is always calculated in ascending m values, selecting as m=1 the angular direction more parallel to the r-z plane in which $I_m^{i,j-1/2}$ is approximated to zero. With this extra condition and Eq. 2.27, the recursive Eq. 2.22 can be applied to the cell closer to the boundary conditions and so forth.

$$\nu_{m+1/2} - \nu_{m-1/2} = -\mu_m W_m \tag{2.27}$$

For each quadrant, the complete set of 6 intensities required for each spatial mesh cell is obtained by applying equations 2.28-2.30.

For the spatial mesh:

$$I_m^{i,j} = \frac{\left(I_m^{i-1/2,j} + I_m^{i+1/2,j}\right)}{2} \tag{2.28}$$

$$I_m^{i,j} = \frac{\left(I_m^{i,j-1/2} + I_m^{i,j+1/2}\right)}{2} \tag{2.29}$$

And for the directional mesh:

$$I_m^{i,j} = \frac{\left(I_{m-1/2}^{i,j} + I_{m+1/2}^{i,j}\right)}{2} \tag{2.30}$$

These equations consider linear intensity profiles inside each spatial mesh cell, an approximation that has increasing accuracy as the finite, delta r, and z elements go to zero.

Finally, once the intensities were obtained, the local volumetric rate of photon absorption ($e^{a,v}$) was calculated at each $r-z$ point of the reactor according to:

$$e^{a,v} = \int_{\lambda}^{\square} \kappa_{\lambda}(\underline{x}) \cdot \int_{\Omega=4\pi}^{\square} I_{\lambda,\underline{\Omega}}(\underline{x}) d\Omega \, d\lambda \tag{2.31}$$

REFERENCES

170. Su, H.; Yin, H.; Wang, R.; Wang, Y.; Orbell, W.; Peng, Y.; Li, J. Atomic-Level Coordination Structures Meet Graphitic Carbon Nitride (g-C3N4) for Photocatalysis: Energy Conversion and Environmental Remediation. Applied Catalysis B: Environment and Energy 2024, 348, 123683, doi:10.1016/J.APCATB.2023.123683.
171. Mehrabadi, B.A.T.; Eskandari, S.; Khan, U.; White, R.D.; Regalbuto, J.R. A Review of Preparation Methods for Supported Metal Catalysts. Advances in Catalysis 2017, 61, 1–35, doi:10.1016/BS.ACAT.2017.10.001.
172. Lázaro, I.A. A Comprehensive Thermogravimetric Analysis Multifaceted Method for the Exact Determination of the Composition of Multifunctional Metal-Organic Framework Materials. Eur J Inorg Chem 2020, 2020, 4284–4294, doi:10.1002/EJIC.202000656.
173. Loganathan, S.; Valapa, R.B.; Mishra, R.K.; Pugazhenthi, G.; Thomas, S. Thermogravimetric Analysis for Characterization of Nanomaterials. Thermal and Rheological Measurement Techniques for Nanomaterials Characterization 2017, 3, 67–108, doi:10.1016/B978-0-323-46139-9.00004-9.
174. Ng, H.M.; Saidi, N.M.; Omar, F.S.; Ramesh, K.; Ramesh, S.; Bashir, S. Thermogravimetric Analysis of Polymers. Encyclopedia of Polymer Science and Technology 2018, 1–29, doi:10.1002/0471440264.PST667.
175. Moseson, D.E.; Jordan, M.A.; Shah, D.D.; Corum, I.D.; Alvarenga, B.R.; Taylor, L.S. Application and Limitations of Thermogravimetric Analysis to Delineate the Hot Melt Extrusion Chemical Stability Processing Window. Int J Pharm 2020, 590, 119916, doi:10.1016/J.IJPHARM.2020.119916.
176. Baoping He, B. Two-Dimensional X-Ray Diffraction Available online: https://books.google.es/books?hl=es&lr=&id=G0JbDwAAQBAJ&oi=fnd&pg=PP2&dq=ray+x+diffraction+&ots=Kcoau3Irit&sig=n6sC0WyHl6oy4qk126m5-GYvU_k&redir_esc=y#v=onepage&q&f=false (accessed on 29 May 2024).
177. Ameh, E.S. A Review of Basic Crystallography and X-Ray Diffraction Applications. International Journal of Advanced

Manufacturing Technology 2019, 105, 3289–3302, doi:10.1007/S00170-019-04508-1/FIGURES/11.
178. Aparicio Ceja, M.E.; Carbajal Arizaga, G.G. Utilidad de La Difracción de Rayos x En Las Nanociencias Available online: https://www.scielo.org.mx/scielo.php?script=sci_arttext&pid=S2448-56912010000200062 (accessed on 29 May 2024).
179. Wang, J.; Wang, S. A Critical Review on Graphitic Carbon Nitride (g-C3N4)-Based Materials: Preparation, Modification and Environmental Application. Coord Chem Rev 2022, 453, 214338, doi:10.1016/J.CCR.2021.214338.
180. Hargreaves, J.S.J. Some Considerations Related to the Use of the Scherrer Equation in Powder X-Ray Diffraction as Applied to Heterogeneous Catalysts. Catalysis, Structure & Reactivity 2016, 2, 33–37, doi:10.1080/2055074X.2016.1252548.
181. Saleh, T.A. Structural Characterization of Hybrid Materials. Polymer Hybrid Materials and Nanocomposites 2021, 213–240, doi:10.1016/B978-0-12-813294-4.00005-4.
182. Khan, S.A.; Khan, S.B.; Khan, L.U.; Farooq, A.; Akhtar, K.; Asiri, A.M. Fourier Transform Infrared Spectroscopy: Fundamentals and Application in Functional Groups and Nanomaterials Characterization. Handbook of Materials Characterization 2018, 317–344, doi:10.1007/978-3-319-92955-2_9/FIGURES/13.
183. Zaera, F. New Advances in the Use of Infrared Absorption Spectroscopy for the Characterization of Heterogeneous Catalytic Reactions. Chem Soc Rev 2014, 43, 7624–7663, doi:10.1039/C3CS60374A.
184. Cherniienko, A.; Lesyk, R.; Zaprutko, L.; Pawełczyk, A. IR-EcoSpectra: Exploring Sustainable Ex Situ and in Situ FTIR Applications for Green Chemical and Pharmaceutical Analysis. J Pharm Anal 2024, doi:10.1016/J.JPHA.2024.02.005.
185. Hou, X.; Lv, S.; Chen, Z.; Xiao, F. Applications of Fourier Transform Infrared Spectroscopy Technologies on Asphalt Materials. Measurement 2018, 121, 304–316, doi:10.1016/J.MEASUREMENT.2018.03.001.
186. Venezia, A.M. X-Ray Photoelectron Spectroscopy (XPS) for Catalysts Characterization. Catal Today 2003, 77, 359–370, doi:10.1016/S0920-5861(02)00380-2.
187. Korin, E.; Froumin, N.; Cohen, S. Surface Analysis of Nanocomplexes by X-Ray Photoelectron Spectroscopy (XPS). ACS Biomater Sci Eng 2017, 3, 882–889,

doi:10.1021/ACSBIOMATERIALS.7B00040/SUPPL_FILE/AB7B00040_LIVESLIDES.MP4.
188. Krishna, D.N.G.; Philip, J. Review on Surface-Characterization Applications of X-Ray Photoelectron Spectroscopy (XPS): Recent Developments and Challenges. Applied Surface Science Advances 2022, 12, 100332, doi:10.1016/J.APSADV.2022.100332.
189. Stevie, F.A.; Donley, C.L. Introduction to X-Ray Photoelectron Spectroscopy. Journal of Vacuum Science & Technology A: Vacuum, Surfaces, and Films 2020, 38, 63204, doi:10.1116/6.0000412/1024200.
190. Ponce, A.; Mejía-Rosales, S.; José-Yacamán, M. Scanning Transmission Electron Microscopy Methods for the Analysis of Nanoparticles. Methods in Molecular Biology 2012, 906, 453–471, doi:10.1007/978-1-61779-953-2_37/FIGURES/20.
191. Nellist, P.D. Scanning Transmission Electron Microscopy. Springer Handbooks 2019, 49–99, doi:10.1007/978-3-030-00069-1_2/FIGURES/32.
192. Zhou, X.; Thompson, G.E. Electron and Photon Based Spatially Resolved Techniques. Reference Module in Materials Science and Materials Engineering 2017, doi:10.1016/B978-0-12-803581-8.10140-7.
193. Cha, E.; Chung, H.; Jang, J.; Lee, J.; Lee, E.; Ye, J.C. Low-Dose Sparse-View HAADF-STEM-EDX Tomography of Nanocrystals Using Unsupervised Deep Learning. ACS Nano 2022, 16, 10314–10326, doi:10.1021/ACSNANO.2C00168/ASSET/IMAGES/MEDIUM/NN2C00168_M025.GIF.
194. Recent Developments in STEM-Based Characterization of Energy Materials - 2023 - Wiley Analytical Science Available online: https://analyticalscience.wiley.com/content/article-do/recent-developments-stem-based-characterization-energy-materials (accessed on 29 May 2024).
195. Utama Kosasih, F.; Cacovich, S.; Divitini, G.; Ducati, C.; Kosasih, F.U.; Divitini, G.; Ducati, C.; Cacovich, S. Nanometric Chemical Analysis of Beam-Sensitive Materials: A Case Study of STEM-EDX on Perovskite Solar Cells. Small Methods 2021, 5, 2000835, doi:10.1002/SMTD.202000835.
196. Nellist, P.D. Scanning Transmission Electron Microscopy. Springer Handbooks 2019, 49–99, doi:10.1007/978-3-030-00069-1_2/FIGURES/32.

197. Zhu, J.; Jasper, S.; Zhang, X. Chemical Characterization of Electrospun Nanofibers. Electrospun Nanofibers 2017, 181–206, doi:10.1016/B978-0-08-100907-9.00008-8.
198. Frąckowiak, E.; Płatek-Mielczarek, A.; Piwek, J.; Fic, K. Advanced Characterization Techniques for Electrochemical Capacitors. Adv Inorg Chem 2022, 79, 151–207, doi:10.1016/BS.ADIOCH.2021.12.006.
199. Sing, K. The Use of Nitrogen Adsorption for the Characterisation of Porous Materials. Colloids Surf A Physicochem Eng Asp 2001, 187–188, 3–9, doi:10.1016/S0927-7757(01)00612-4.
200. Al-Ghouti, M.A.; Da'ana, D.A. Guidelines for the Use and Interpretation of Adsorption Isotherm Models: A Review. J Hazard Mater 2020, 393, 122383, doi:10.1016/J.JHAZMAT.2020.122383.
201. Jaroniec, M.; Kruk, M.; Sayari, A. Adsorption Methods for Characterization of Surface and Structural Properties of Mesoporous Molecular Sieves. Stud Surf Sci Catal 1998, 117, 325–332, doi:10.1016/S0167-2991(98)81008-2.
202. Área de Superficie - Micromeritics Available online: https://www.micromeritics.com/evaluacion-de-particulas/pruebas-analiticas/area-de-superficie/?lang=es (accessed on 29 May 2024).
203. Bardestani, R.; Patience, G.S.; Kaliaguine, S. Experimental Methods in Chemical Engineering: Specific Surface Area and Pore Size Distribution Measurements—BET, BJH, and DFT. Can J Chem Eng 2019, 97, 2781–2791, doi:10.1002/CJCE.23632.
204. Kausor, M. Al; Chakrabortty, D. Carbon Nitride Photocatalysts for Water Treatment and Purification. Nanostructured Carbon Nitrides for Sustainable Energy and Environmental Applications 2022, 137–174, doi:10.1016/B978-0-12-823961-2.00010-0.
205. Myrick, M.L.; English, C.M.; Kitzhaber, Z.B. A Brief Look at Optical Diffuse Reflection (ODR) Spectroscopy. Spectroscopy 2023, 31–36, doi:10.56530/SPECTROSCOPY.MJ8589F4.
206. Moy, A.J.; Tunnell, J.W. Diffuse Reflectance Spectroscopy and Imaging. Imaging in Dermatology 2016, 203–215, doi:10.1016/B978-0-12-802838-4.00017-0.
207. Ruvolo, E.; Chu, M.; Grossman, F.; Cole, C.; Kollias, N. Diffuse Reflectance Spectroscopy for Ultraviolet A Protection Factor Measurement: Correlation Studies between in Vitro and in Vivo Measurements. Photodermatol Photoimmunol Photomed 2009, 25, 298–304, doi:10.1111/J.1600-0781.2009.00469.X.

208. Colón-González, F.M. Analytical Method Development Using Quantum Laser Cascade Spectroscopy with Diffuse and Attenuated Total Reflectance for Determining Low Concentrations of Active Pharmaceutical Ingredients;
209. Mishra, V.; Warshi, M.K.; Sati, A.; Kumar, A.; Mishra, V.; Kumar, R.; Sagdeo, P.R. Investigation of Temperature-Dependent Optical Properties of TiO2 Using Diffuse Reflectance Spectroscopy. SN Appl Sci 2019, 1, 1–8, doi:10.1007/S42452-019-0253-6/FIGURES/9.
210. Landi, S.; Segundo, I.R.; Freitas, E.; Vasilevskiy, M.; Carneiro, J.; Tavares, C.J. Use and Misuse of the Kubelka-Munk Function to Obtain the Band Gap Energy from Diffuse Reflectance Measurements. Solid State Commun 2022, 341, 114573, doi:10.1016/J.SSC.2021.114573.
211. Tziourrou, P.; Vakros, J.; Karapanagioti, H.K. Using Diffuse Reflectance Spectroscopy (DRS) Technique for Studying Biofilm Formation on LDPE and PET Surfaces: Laboratory and Field Experiments. Environmental Science and Pollution Research 2020, 27, 12055–12064, doi:10.1007/S11356-020-07729-0/TABLES/2.
212. Bao, H.; Liu, Y.; Li, H.; Qi, W.; Sun, K. Luminescence of Carbon Quantum Dots and Their Application in Biochemistry. Heliyon 2023, 9, e20317, doi:10.1016/J.HELIYON.2023.E20317.
213. Lettieri, S.; Pavone, M.; Fioravanti, A.; Amato, L.S.; Maddalena, P. Charge Carrier Processes and Optical Properties in TiO2 and TiO2-Based Heterojunction Photocatalysts: A Review. Materials 2021, Vol. 14, Page 1645 2021, 14, 1645, doi:10.3390/MA14071645.
214. Garro Linck, L. Estudio y Caracterización de Sistemas Porosos Por Resonancia Magnética Nuclear. 2016.
215. Paul, G.; Bisio, C.; Braschi, I.; Cossi, M.; Gatti, G.; Gianotti, E.; Marchese, L. Combined Solid-State NMR, FT-IR and Computational Studies on Layered and Porous Materials. Chem Soc Rev 2018, 47, 5684–5739, doi:10.1039/C7CS00358G.
216. Jiang, Y.; Huang, J.; Dai, W.; Hunger, M. Solid-State Nuclear Magnetic Resonance Investigations of the Nature, Property, and Activity of Acid Sites on Solid Catalysts. Solid State Nucl Magn Reson 2011, 39, 116–141, doi:10.1016/J.SSNMR.2011.03.007.
217. Yi, X.; Ko, H.H.; Deng, F.; Liu, S. Bin; Zheng, A. Solid-State 31P NMR Mapping of Active Centers and Relevant Spatial Correlations

in Solid Acid Catalysts. Nature Protocols 2020 15:10 2020, 15, 3527–3555, doi:10.1038/s41596-020-0385-6.
218. Santos, S.A.O.; Félix, R.; Pais, A.C.S.; Rocha, S.M.; Silvestre, A.J.D. The Quest for Phenolic Compounds from Macroalgae: A Review of Extraction and Identification Methodologies. Biomolecules 2019, Vol. 9, Page 847 2019, 9, 847, doi:10.3390/BIOM9120847.
219. Nazim, T.; Lusina, A.; Cegłowski, M. Recent Developments in the Detection of Organic Contaminants Using Molecularly Imprinted Polymers Combined with Various Analytical Techniques. Polymers 2023, Vol. 15, Page 3868 2023, 15, 3868, doi:10.3390/POLYM15193868.
220. Miller, J.N. (James N.); Miller, J.C. (Jane C.; Miller, R.D. (Chemist) Statistics and Chemometrics for Analytical Chemistry. 292.
221. Santos, S.A.O.; Félix, R.; Pais, A.C.S.; Rocha, S.M.; Silvestre, A.J.D. The Quest for Phenolic Compounds from Macroalgae: A Review of Extraction and Identification Methodologies. Biomolecules 2019, Vol. 9, Page 847 2019, 9, 847, doi:10.3390/BIOM9120847.
222. UV vs Diode-Array (PDA) Detectors for (U)HPLC Available online: https://www.ssi.shimadzu.com/service-support/faq/liquid-chromatography/knowledge-base/uv-vs-pda-detectors/index.html (accessed on 29 May 2024).
223. Kruve, A.; Rebane, R.; Kipper, K.; Oldekop, M.L.; Evard, H.; Herodes, K.; Ravio, P.; Leito, I. Tutorial Review on Validation of Liquid Chromatography–Mass Spectrometry Methods: Part I. Anal Chim Acta 2015, 870, 29–44, doi:10.1016/J.ACA.2015.02.017.
224. Yoo, O.; Tang, E.K.Y.; Nguyen, M.N.; Salman, S.; Hua, A.J.; von Ungern Sternberg, B.S.; Lim, L.Y. HPLC-UV Assay of Tramadol and O-Desmethyltramadol in Human Plasma Containing Other Drugs Potentially Co-Administered to Participants in a Paediatric Population Pharmacokinetic Study. Journal of Chromatography B 2021, 1184, 122971, doi:10.1016/J.JCHROMB.2021.122971.
225. Um, M.; Fan, L.; Jones, O.A.H.; Roddick, F. A Comparative Study of Programs to Predict Direct Photolysis Rates in Wastewater Systems. Science of The Total Environment 2024, 912, 168921, doi:10.1016/J.SCITOTENV.2023.168921.
226. Towler, G.; Sinnott, R. Diseño En Ingeniería Química: Serie Ingeniería Química Coulson & Richardson. 2019, 1274.
227. Schneider, J.T.; Firak, D.S.; Ribeiro, R.R.; Peralta-Zamora, P. Use of Scavenger Agents in Heterogeneous Photocatalysis: Truths,

Half-Truths, and Misinterpretations. Physical Chemistry Chemical Physics 2020, 22, 15723–15733, doi:10.1039/D0CP02411B.
228. Balachandran, R.; Zhao, M.; Dong, B.; Brown, I.; Raghavan, S.; Keswani, M. Role of Ammonia and Carbonates in Scavenging Hydroxyl Radicals Generated during Megasonic Irradiation of Wafer Cleaning Solutions. Microelectron Eng 2014, 130, 82–86, doi:10.1016/J.MEE.2014.10.022.
229. Vandekerckhove, B.; Piens, N.; Metten, B.; Stevens, C. V.; Heugebaert, T.S.A. Practical Ferrioxalate Actinometry for the Determination of Photon Fluxes in Production-Oriented Photoflow Reactors. Org Process Res Dev 2022, 26, 2392–2402, doi:10.1021/ACS.OPRD.2C00079/SUPPL_FILE/OP2C00079_SI_002.XLSX.
230. Rabani, J.; Mamane, H.; Pousty, D.; Bolton, J.R. Practical Chemical Actinometry—A Review. Photochem Photobiol 2021, 97, 873–902, doi:10.1111/PHP.13429.
231. Lee, J.; Kim, J.; Choi, W. Ferrioxalate-Polyoxometalate System as a New Chemical Actinometer. Environ Sci Technol 2007, 41, 5433–5438, doi:10.1021/ES070474Z/ASSET/IMAGES/MEDIUM/ES070474ZE00009.GIF.
232. Gröbner, J.; Kouremeti, N. The Precision Solar Spectroradiometer (PSR) for Direct Solar Irradiance Measurements. Solar Energy 2019, 185, 199–210, doi:10.1016/J.SOLENER.2019.04.060.
233. Marugán, J.; Van Grieken, R.; Alfano, O.M.; Cassano, A.E. Optical and Physicochemical Properties of Silica-Supported TiO2 Photocatalysts. AIChE Journal 2006, 52, 2832–2843, doi:10.1002/AIC.10886.
234. Cassano, A.E.; Martín, C.A.; Brandi, R.J.; Alfano, O.M. Photoreactor Analysis and Design: Fundamentals and Applications. Ind Eng Chem Res 2002, 34, 2155–2201, doi:10.1021/IE00046A001.
235. Muñoz-Batista, M.J.; Ballari, M.M.; Kubacka, A.; Alfano, O.M.; Fernández-García, M. Braiding Kinetics and Spectroscopy in Photo-Catalysis: The Spectro-Kinetic Approach. Chem Soc Rev 2019, 48, 637–682, doi:10.1039/c8cs00108a.
236. Duderstadt, J.J.; Martin, W.R. Transport Theory; John Wiley & S: New York, 1979; ISBN 0-471-04492-X.

CHAPTER 3. PAPER ONE

Enhanced boron modified graphitic carbon nitride for the selective photocatalytic production of benzaldehyde

Separation and Purification Technology 298 (2022), 121613

https://doi.org/10.1016/j.seppur.2022.121613

M. Alejandra Quintana, Rafael R. Solís, M. Ángeles Martín-Lara, Gabriel Blázquez, F. Mónica Calero, Mario J. Muñoz-Batista

Abstract

Graphitic carbon nitride is a non-metal photocatalyst easily prepared from nitrogen organic compounds through green synthesis processes that do not require the use of solvents. This work proposes the use of boron to modify the layered g-C_3N_4 structure by incorporating B to induce defects aimed at the enhancement of the photocatalytic activity. Boron-modified graphitic carbon has been obtained using elemental B and $NaBH_4$ as precursors. The XRD and FTIR characterization results suggest that the C and N positions of g-C_3N_4 can be replaced by B, resulting in a layered modified structure in which the tri-s-triazine units are altered. The exchange of B atoms differed from the boron precursor according to the analysis of the chemical properties of the surface. Thus, the elemental B had a preference to exchange positions with N atoms, whereas the use of $NaBH_4$ led to the substitution of B into the C positions. This difference considerably affected the photocatalytic activity during the selective oxidation of benzyl alcohol. The sample modified with $NaBH_4$ led to the highest oxidation rate and selectivity linked to a lesser recombination effect than the other samples according to photoluminescence tests. This work provides evidence about the convenience of the selection of precursors during the modification of g-C_3N_4. The photon absorbance rate was determined for the estimation of the quantum yield. Although the photon absorbance rate was quite similar in all the cases, the different registered kinetics led to a maximum quantum efficiency of 0.15% for NaBCN.

Keywords: graphitic carbon nitride; boron; benzaldehyde; photocatalysis.

3.1. INTRODUCTION

Graphitic carbon nitride (g-C_3N_4) is a novel metal-free and non-toxic photocatalyst with promising optoelectronic properties in a wide range of photocatalytic applications [1]. It displays bandgap energy ca. 2.7 eV which allows better harvesting of the solar spectrum if compared to traditional TiO_2 [2]. g-C_3N_4 represents an environmentally friendly alternative since it is based on carbon, nitrogen, and hydrogen and can be easily prepared from nitrogen natural organic compounds such as melamine, urea, or cyanamide, among others [3,4]. The synthesis can be achieved by calcination under inert atmosphere or by hydrothermal treatment under pressure [5]. Analogously to graphene, pristine g-C_3N_4 is a polymeric monolayer of coupled tri-s-triazine (C_6N_7) rings connected by planar amino groups that can be tunable into different morphologies including nanosheets, nanotubes, or quantum dots [6]. Since it was first applied for water splitting [7], numerous applications have been proposed for diverse photocatalytic scenarios, including energy production [8], CO_2 conversion [9], organic transformations [10], water treatment [11], disinfection [3,12] or as sensor [6].

Several modifications have been proposed to enhance the activity of g-C_3N_4 [13]. Some examples of this improved photoactivity include the modification of the pristine structure aimed at the formation of nitrogen vacancies [14], modification of the layered structure with non-metal [15–18] and metal doping [16], the deposition of noble metal nanoparticles [19], anchoring of Na [20], the formation of hetero-structures based in photocatalytic metal oxides [2,15], Mxenes [21] or other organic semiconductors such as Metal Organic Frameworks [22]. Non-metal doping is an environmentally friendly alternative since it does not consider the use of expensive metals that could raise problems of metal leaching during photocatalytic performance. Diverse non-metal options are reported in the literature pursuing improved visible light absorption, increased carrier mobility, production of more active sites, and reduction of the recombination rate of photo-generated charges. The simplest modification of g-C_3N_4 includes the partial oxygenation of the g-C_3N_4 structure [23]; however, other non-metal atoms have been successfully incorporated into the structure such as boron [24–27], phosphorous [28], sulfur [29], or halides [30,31]. Boron is an interesting alternative to

modify the g-C_3N_4 structure due to the similar chemical properties of boron, carbon, and nitrogen which have raised the attention for a large range of applications owing to their outstanding features [32]. Boron can be exchanged by either carbon or nitrogen positions [33], leading to very interesting photoelectronic properties and defects in the structure.

The selective oxidation of alcohols is one of the most relevant and established transformations into added-value chemicals, i.e. aldehydes and ketones, in industrial catalysis. Currently, diverse technologies are already implemented such as thermo-catalysis, catalysis, and electrocatalysis [34–36]. Among them, photocatalysis is an emerging alternative that can help the migration of traditional technologies to other more respectful with the environment either due to their milder working conditions, the cost-efficient energy input compared with the traditional thermo-catalysis, or the reduction of consumed solvents [37].

This work reports the use of boron-modified graphitic carbon nitride as a novel metal-free photocatalyst for the selective oxidation of benzyl alcohol to the added-value benzaldehyde. Although g-C_3N_4 modified with boron has been reported using $NaBH_4$ in solid stated process for the photocatalytic production of O_2 [24] or H_2 [25], there is no information of the comparison efficiency with other precursors such as elemental boron. Moreover, these materials have not been tested in the photocatalytic production of aldehydes with industrial interest. For that reason, this work is focused in the use and comparison of two different boron precursors have been selected, elemental boron and sodium borohydride to generate defects that enhance the activity and selectivity toward the production of benzaldehyde from benzyl alcohol. A complete characterization including N_2 physisorption, XRD, XPS, FTIR, DRS UV-visible, and photoluminescence technique was applied to unveil the connection between the boron modified g-C_3N_4 and the photocatalytic activity observed. The use of $NaBH_4$ as the precursor, which promotes the exchange of B into carbon positions, led to the best results either reaction rate or selectivity. The photoelectronic characterization results suggested that, compared to the bare g-C_3N_4, the bandgap was reduced (from 2.72 to 2.28 eV) and the recombination effect considerably weakened. The selection of the suitable B precursor strongly impacts not only the structural changes but also the photoactivity response.

3.2. EXPERIMENTAL

3.2.1. Materials and catalysts synthesis

Analytical grade benzyl alcohol (>99%) and benzaldehyde (>99%) standards were used as received. HPLC grade acetonitrile and methanol were used for analytical purposes. Ultrapure water (18.2 MΩ·cm) from a Direct-Q®-UV system (Millipore®) was used in all the solutions preparation.

The graphitic carbon nitride (g-C_3N_4, CN) was prepared as previously reported in the literature from the pyrolyzation of melamine during 2 h at 550 ºC with a heating rate of 9 ºC·min^{-1} [27]. Next, the yellowish CN was washed with water and the higher particles were discharged by decantation. The suspended CN particles were filtered and dried at 80 ºC. The boron modified samples were prepared via calcination under an N_2 inert atmosphere [24]. Briefly, 1.0 g of CN and 0.4 g of $NaBH_4$ (>99%, Sigma-Aldrich®), were mixed and grounded in a mortar. The sample modified with elemental boron (>95%, Sigma-Aldrich®) was added as the equivalent B amount in the 0.5 g of $NaBH_4$. The mixed powder was calcined at 450 ºC for 1 h with a ramp of 10 ºC·min^{-1} with a gas flow rate of 20 mL N_2·min^{-1}. After cooling to room temperature, the resulting brownish samples were washed several times with water and dried at 80 ºC overnight. The boron modified CN with elemental boron was labeled as BCN whereas if $NaBH_4$ was used as the precursor, the sample was named NaBCN. Preliminary tests were carried out in a thermogravimetric balance to ensure the thermal stability of the samples at the selected temperature. Only a 4% mass loss was recorded.

3.2.2. Characterization of the solids

The thermal stability of the samples was evaluated in a Perkin Elmer (model STA 6000) thermobalance. A constant heating rate of 10 °C·min^{-1} was used under N_2 atmosphere (flow rate, 20 mL/min) from room temperature to 450 ºC. The crystalline structure was studied by X-Ray Diffraction (XRD) in a Bruker D8 Discover diffractometer w using a Cu Kα radiation source (λ = 1.5406 Å) and a Pilatus3R 100K-A detector within a 2q range of 8-80º at a rate of 0.08º·min^{-1}. The software *Match!*® and the Crystal Open Database (COD) library were used to process the diffractograms obtained. The stretching of the bonds in the structure was

studied by Fourier Transform InfraRed (FTIR) analysis, carried out in a Perkin-Elmer device (model Spectrum65) within 400-4000 cm^{-1}. The chemical composition of the surface was analyzed by X-ray Photoelectron Spectroscopy (XPS) in a Kratos AXIS UltraDLD device working with an X-ray source from Al Kα. The XPS spectra were referenced to the C1s peak of adventitious carbon to 284.6 eV. The software *XPSpeak 4.1*® was used for the deconvolution of the peaks, considering a Shirley background correction. Scan Transmission Electron Microscopy (STEM) was used to study the morphology and the distribution of element composition with High-Angle Annular Dark Field (HAADF) detection and Electron Disperse X-Ray (EDX) analysis in a Thermo Fisher Scientific TALOS F200X device. The elemental composition, i.e. C, N and H, was analyzed in a Thermo Scientific™, Flash 2000 device. The textural properties (surface area and pore volume) were determined from N_2 adsorption-desorption at 77 K performed in an ASAP 2020 equipment (Micromeritics). The specific surface area was obtained by the Brunauer-Emmett-Teller method (S_{BET}). The optical properties were obtained by Diffuse Reflectance Spectroscopy (DRS) in the UV-visible range in a Varian Cary 5E spectrophotometer. From the reflectance spectrum and the application of Tauc's plot method [38], the bandgap values were estimated. The recombination rate of the photogenerated electrons was assessed by photoluminescence (PL) analysis in a Varian Cary Eclipse device under an excitation wavelength of 365 nm.

3.2.3. Photocatalytic production of benzaldehyde

Photocatalytic reactions were carried out in a discontinuous type annular photoreactor, see scheme in Fig. 3.1, with the liquid mixture circulating through the jacked space and radiation source (Sylvania® F11W T5 BL368 lamp, emitting at 365 nm, 11 W) located in the center. To keep the temperature constant to 20 ºC, the mixture was recirculated to a stirring tank equipped with a jacketing system. Excess air was bubbled in this stirring tank to maintain an oxidizing environment which has been reported as beneficial for this reaction [39]. Every 30 min during 4 h of reaction, samples were extracted, and the photocatalyst was removed by centrifugation. Previous to irradiation, a 30 min adsorption step was carried out. Experiments were carried out by triplicate and the relative standard deviation error was minor to 5%. The

importance of photo-generated and radical species was assessed with scavenging experiments in the presence of methanol (10 mM), oxalic acid (10 mM) or N_2 bubbling following the same described procedure.

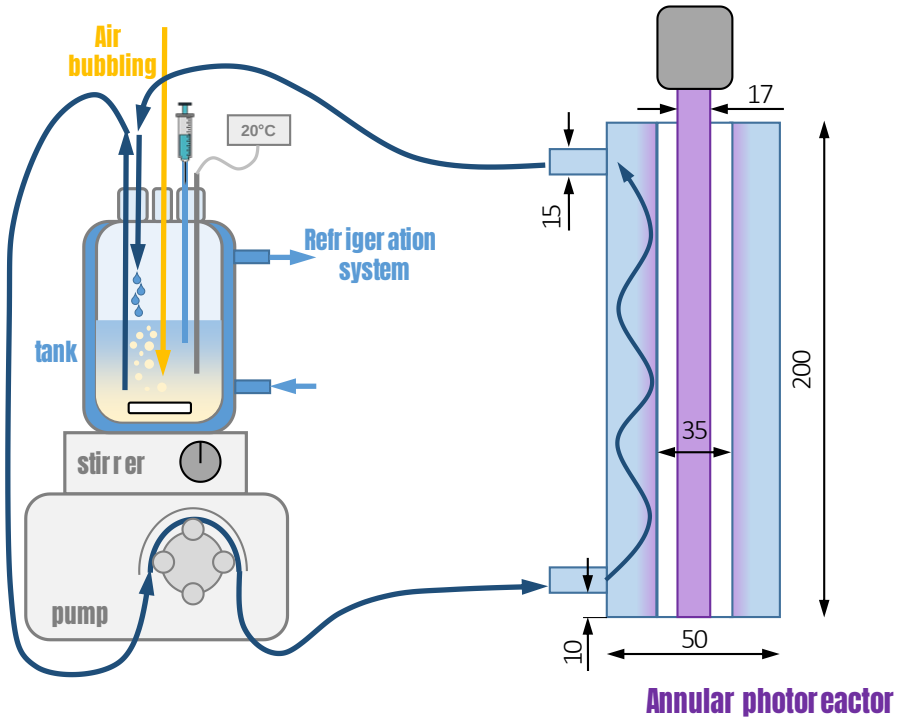

Fig. 3.1 *Experimental setup of the photoreaction system (dimensions expressed in mm). Experimental conditions: $V_{photorreactor}$=200 mL; V_{tank}=150 mL; T=20ºC*

The radiation intensity of the lamp was quantified by an in-situ chemical actinometry based on the photoreduction of the ferrioxalate combined with a polyoxometalate ($Na_2SiW_{12}O_6$) to monitor the temporal depletion of the ferrioxalate complex [40]. The experimental conditions included oxalic acid 60 mM, $FeCl_3$ 5 mM, and $SiW_{12}O_{40}^{4-}$ 1 mM. The pH was adjusted to 4.5 with HCl and NaOH to prevent self-decomposition of the polyoxometalate complex. Considering a quantum yield ϕ=0.18 mol·Einstein^{-1} [40] at 365 ± 10 nm during the photo-production of $SiW_{12}O_{40}^{5-}$, the radiation intensity value obtained was $I_0 = (2.2 \pm 0.1)\cdot10^{-4}$ Einstein L^{-1} min^{-1}.

The concentration of benzyl alcohol (BA) and benzaldehyde (BD) during the photoreaction was quantified by High-Performance Liquid Chromatography (HPLC) technique in a Shimadzu LC-10 device

coupled to DAD UV-visible detection. The stationary phase was a Kromasil C18 column 100 5C18 (100Å, 5 µm, 2.1×150 mm) and the mobile phase consisted of a constant elution grade of a mixture of methanol (2.5%), acetonitrile (27.5%), and 0.1% H_3PO_4 ultrapure water (70%) pumped at 1.0 mL min^{-1}. The BA (retention time, 3.7 min) was quantified at 215 nm and the BD (retention time, 6.4 min) at 248 nm. The limit of detection [41] was calculated as, respectively, 26 and 14 mM for BA and BD. The Total Organic Carbon (TOC) was analyzed in a Shimadzu® TOC-V_{CSH} analyzer.

The quantum efficiency (Q_E) was calculated according to the Eq. 3.1, according to the IUPAC recommendations [42–44], which defines the Q_E as the ratio of the number of molecules reacting, i.e. the reaction rate, by the number of photon which interact with the catalyst, i.e. the photon absorption rate [45]:

$$Q_E(\%) = \frac{r_{BA_0}\ (\mathrm{mol \cdot m^{-3} \cdot s^{-1}})}{e^{a,v}\ (\mathrm{Einstein \cdot m^{-3} \cdot s^{-1}})} \cdot 100 \qquad (3.1)$$

The initial BA degradation rate ($r_{BA,0}$) was determined from the slope of the temporal evolution of the C_{BA} extrapolating at the initial time, or after the reaction started in case of appreciating an inactivation period. To determine the photon absorption rate ($e^{a,v}$), the radiative transfer equation (RTE) was solved for the used reactor which needs as first step the determination of the optical properties of the catalytic suspensions. Detailed description of the mathematical procedure for both optical properties and photon rate estimations are provided in the supporting information.

3.3. RESULTS AND DISCUSSION

3.3.1. Characterization of the boron modified g-C_3N_4

The XRD technique was used to assess the changes in the graphitic carbon structure of CN after the incorporation of boron. Fig. 3.2A illustrates the registered XRD patterns for the CN, BCN, and NaBCN samples. As shown in this figure, the pristine sample, CN, presents two characteristic peaks reported in g-C_3N_4 samples, one located at 2q=13.4º, whose intensity is almost negligible, and a second intense peak at 27.3º which are assigned, respectively, to the (100) and (002)

planes [24]. The (100) plane refers to the in-plane of tri-s-triazine units that build the g-C_3N_4 sheet while the (002) plane, the most important and intense, results from the presence of interconnected layers. The almost negligible (100) peak in the CN sample suggests a lack of organized triazine units inside the sheet; nonetheless, the presence of an intense peak at 27.3º corroborates the formation of the layered structure. The incorporation of boron as elemental B led to a decrease of the (002) plane in the BCN sample, due to the increase of the disorder in the structure. The addition of $NaBH_4$ instead of elemental B contributed to the higher destruction of the interlayered structure giving to a lower peak.

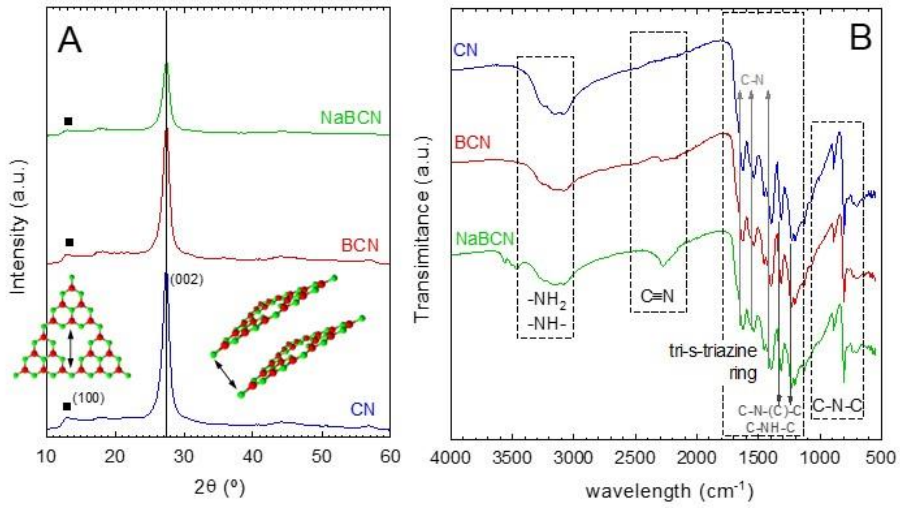

Fig. 3.2 *Changes in the XRD pattern (A) and FTIR spectra (B) of CN after B incorporation*

Fig. 3.2B depicts the FTIR spectra of CN, BCN, and NaBCN samples. There is a wide band within 3000-3500 cm^{-1} related to the vibration –NH_2 and –NH- groups. The incorporation of boron with the two precursors, elemental B, and $NaBH_4$, led to a slight depletion of this band as shown for BCN and NaBCN spectra. The CN sample also presents a peak located at ~810 cm^{-1} which is attributed to o the out-of-plane bonding vibration characteristics of triazine [24]. A decrease of this peak is observed after the incorporation of B with NaBCN. Moreover, a group of peaks between 900-1800 cm^{-1} is originated due to the stretching of the aromatic C-N heterocycles [24]. Concretely, the

intense peaks at 1620, 1530, and 1390 cm^{-1} can be assigned to the aromatic C-N stretching vibration [46,47]. The bands at 1310 and 1230 cm^{-1} correspond to the stretching vibration of C-N-(C)-C or C-NH-C bonds [46,47]. This group of peaks suffered soft modifications during the incorporation of boron, being the sample NaBCN the one giving less intensity for these peaks. A new peak at 2270 cm^{-1} emerged in the sample NaBCN. This peak corresponds to the asymmetric stretching vibration of the C≡N group that appears as a consequence of a thermal reaction between elemental B or $NaBH_4$ and g-C_3N_4 [24,25]. The presence of this C≡N group introduces nitrogen defects into the g-C_3N_4 structure. This peak appears in both boron-modified samples; however, the intensity acquired is higher in the NaBCN sample if compared to BCN. Summarizing, not great changes in FTIR footprint were appreciated rather the alteration on nitrogen defects. For that reason, a more sensitive superficial technique such as XPS was carried out.

The textural properties were assessed by N_2-physisorption analysis, see results in Table 3.1. The samples were macroporous with low specific surface area. The S_{BET} values slightly decreased with the boron incorporation, being the $NaBH_4$ the precursor that produced a greater modification.

Table 3.1 *Characterization of the CN, BCN, and NaBCN samples*

Sample	S_{BET} (m^2 g^{-1})	Surface atomic percentage (%) by XPS				Atomic N/C ratio		Bandgap (eV)
		C	N	O	B	XPS	Elemental analysis	
CN	13.0	49.4	46.7	3.9	-	0.94	1.54	2.72
BCN	11.5	51.3	28.3	9.4	11.0	0.55	1.50	2.53
NaBCN	3.7	38.9	19.0	21.5	10.2	0.49	1.31	2.28

The chemical changes on the surface of the samples after boron modification were studied by the XPS technique. Fig. 3.3 Changes in XPS spectra of N1s (left), C1s (center), and B1s (right) of CN after B incorporation provides a detailed analysis of the high-resolution C1s, N1s, and B1s regions. As observed, the incorporation of boron in the structure partially modifies the original C1s and N1s spectra of the bare

graphitic carbon nitride structure. It should be noted that as the B content was minor, the modifications displayed are a plausible suggestion of the bond changes. Moreover, an intense peak of B1s was registered in BCN and NaBCN samples, which proves the presence of boron after the synthesis. The spectra were deconvoluted according to the expected contributions reported in the literature. The N1s peak of CN can be explained as the sum of three contributions related to C_3–N (N_{3C}, 399.9 eV), N–C=N (N_{2C}, 398.4 eV), and N–H_x (401.0 eV) bonds [25–27,48]. The peak N_{3C}, considerably diminished in intensity, which provides evidence of a B attack to these points of s-triazine structure. Also, the peak related to -NH_x terminal defects decreased after B incorporation, suggesting the susceptibility to be attacked. As a consequence of the incorporation of boron in the structure, two extra contributions, B=N-C (399.0 eV) and N-(C_2)B (400.4 eV) appeared in the N1s network [27], which suggest the integration of B in the graphitic structure. The C1s region displayed major changes. The C1s peak of graphitic carbon nitride is commonly deconvoluted in sp^2 N=C-N (287.9 eV), sp^3 C-C/C-N (285.2 eV), and sp^2 C-C/C=C (284.4 eV) bonds [49]. The modification of the CN sample with boron intensively modified the carbon network. As the result of the formation of defects due to the boron presence, the contribution of the sp^2 N=C-N peak decreases, the contribution of sp^2 C-C/C-N defects raised, and the sp^2 C-C/C=C decreased in the NaBCN sample. The N/C ratios were, according to XPS analysis, highly modified being 0.94 (CN) > 0.55 (BCN) > 0.49 (NaBCN). The modification with boron led to a decrease of the N/C ratio, confirmed also elemental analysis technique (Table 3.1). In the case of elemental analysis, although the values are different due to the superficial character of XPS technique, the decrease tendency after the modification with boron was the similar and closer to the theoretical expected N/C=4/3 value of g-C_3N_4. This difference between techniques provides evidence of the incorporation of boron just at a surface level. According to the atomic percentages of elements in the surface, the pristine CN sample displays a very low amount of O. The two contributions detected in O1s peak were terminal -OH and C=O groups [50]. The global O percentage raises in the order NaBCN>BCN>CN probably also promoted by the oxidation of boron after contact with water in the washing steps. From the results, it can be deduced that boron alters the structure of bare CN not only by exchanging positions in the structure but also by generating terminal

oxygenated defects. The modification with boron using elemental boron or $NaBH_4$ as boron precursors led to very different B1s profiles. Due to the lower level of boron respect to the other elements, B1s spectrum can be used to deduce the boron bonding state in the structures. Up to four different contributions were identified, i.e. elemental boron (186.8 eV), NC_2-B (188.1), B-N (190.3 eV), and B related to oxides or hydroxides (191.9 eV) [27,51,52]. If elemental B was the precursor, the incorporation of B in the structure was placed as N-(C_2)B. Nonetheless, if $NaBH_4$ was used, the incorporation of boron as BN peak is predominant and the N-(C_2)B peak was minor. These results suggest that the nature of the B precursor could direct the positions in which B is going to be incorporated, which means elemental B prefer to attack C atoms while if $NaBH_4$ is used B is replaced in the N positions. Other secondary chemical states of B not meaning an exchange of this element into N or C positions of CN were also detected, i.e. elemental boron in BCN and boron oxide in NaBCN. The major presence of boron oxide in B1s spectrum would also contribute to explain the major content of oxygen in NaBCN sample. The XPS surface atomic composition is available in Table 3.1. Both boron modified samples, BCN and NaBCN presented very similar B incorporation yields in their structures, 11.0 and 10.2% respectively.

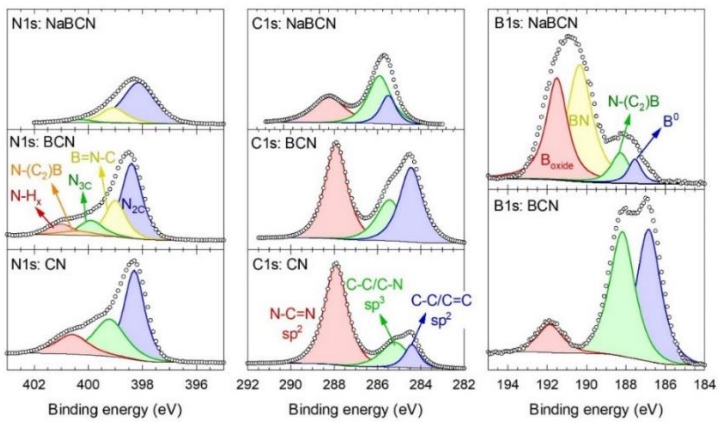

Fig. 3.3 *Changes in XPS spectra of N1s (left), C1s (center), and B1s (right) of CN after B incorporation*

The morphology and element distribution of NaBCN sample was analyzed by STEM and EDX mapping. The Fig. 3.4 STEM image and EDX

mapping of NaBCN sample shows an example the pictures obtained and the element mapping. The morphology displayed as layered flakes and the EDX mapping confirmed the presence of B, C and N. As observed in the individual mapping, B was uniformly distributed around the flake particle.

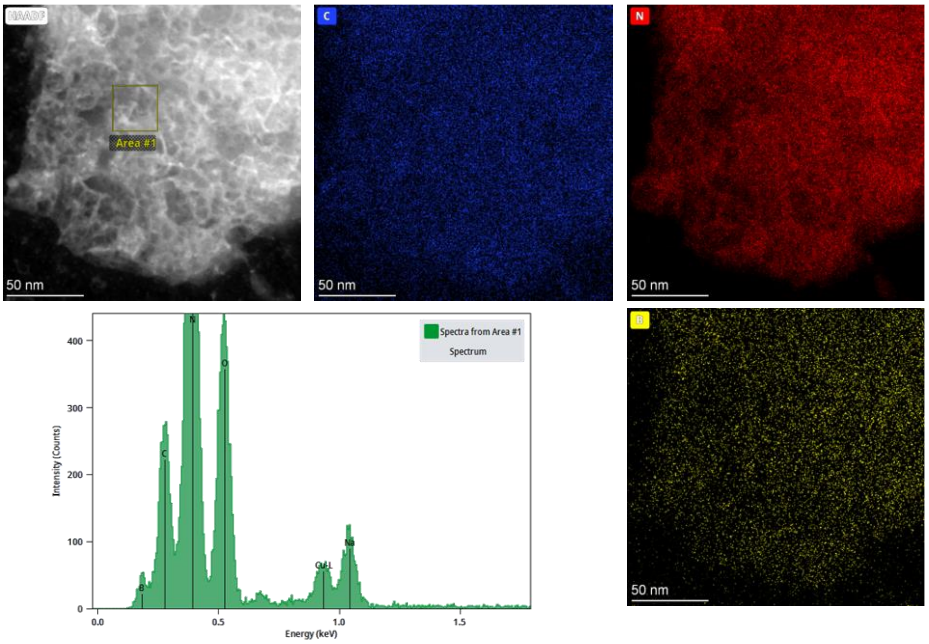

Fig. 3.4 *STEM image and EDX mapping of NaBCN sample*

Fig. 3.5A displays the UV-visible absorption spectra of the samples. As boron was incorporated in the structure, the edge of CN was red-shifted. The calculated bandgaps values, see Fig. 3.5B and Table 3.1 Characterization of the CN, BCN, and NaBCN samples, decreased from 2.72 eV in CN to 2.58 eV in BCN and 2.53 eV in NaBCN. Thus, the incorporation of boron in the structure of CN broadened the light absorption range by decreasing the bandgap value. Therefore, the boron-modified materials are expected to better harvest visible radiation; however, due to the monochromatic nature of the lamp used in the photo-reactor, the materials will only take advantage of the band gap reduction rather than the widening of the radiation absorptivity.

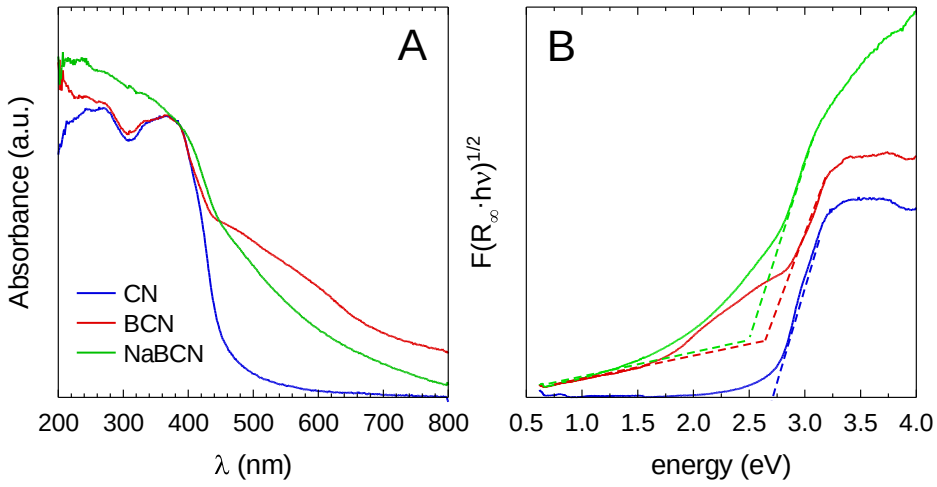

Fig. 3.5 *Changes in DRS-UV-visible spectra (A) and bandgap determination by Tauc's plot method (B) of CN after B incorporation*

Despite the fact of the differences register in the optical properties, the incorporation of boron in the structure seems not to have a significant influence in terms of the photon absorption rate. The boron-modified samples displayed similar behavior due to the net light emitted by the used UV lamp. In agreement with the UV-visible spectra, the increase of the light absorption level of the visible range was also detected when the properties of the catalytic suspension were determined. As depicted in Figure S3, the profiles of the related optical coefficients, i.e. the spectral absorption coefficient, the spectral scattering coefficient, and the scattering phase, show some differences. Nonetheless, these dissimilarities do not translate, as could be expected, into a significant modification of the rate of UV light photons absorbed by the materials, as presented in Fig. 3.6 Local volumetric rate of photon absorption of CN, BNC and NaBCN. As discussed later, the modification of the catalytic properties seems to be associated with an improvement in the load handling processes. This is also supported by the catalytic test under visible irradiation conditions (Sylvania® F6W T5 Daylight lamp, emitting over 420 nm), which shows negligible catalytic activity (data not included) under the same operating condition described in the experimental section.

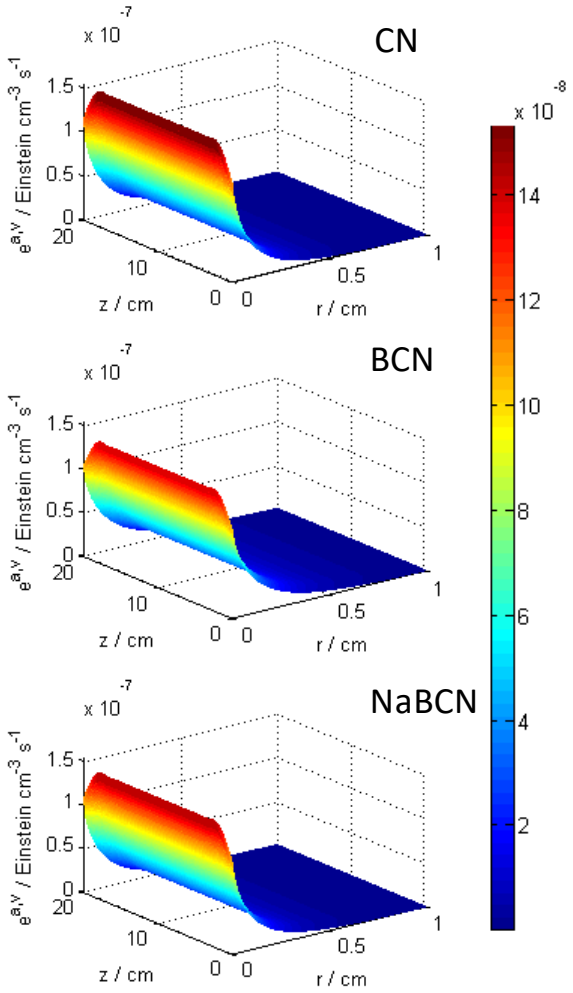

Fig. 3.6 *Local volumetric rate of photon absorption of CN, BNC and NaBCN.*

3.3.2. Photocatalytic performance for the production of benzyl alcohol

The graphitic carbon nitride and the boron modified samples were used as potential photocatalysts for the selective oxidation of benzyl alcohol to benzaldehyde. Fig. 3.7A shows the photocatalytic results in terms of initial reaction rates and selectivity towards benzaldehyde production. A preliminary test under irradiation and without photocatalyst proved the negligible contribution of photolysis of BA.

Adsorption of BA onto the samples was also discharged by carrying out 30 min of previous adsorption test before switching the lamp on. The BA conversion of the samples after 4 h, followed the order NaBCN (29 %), BCN (15 %) > CN (13 %). A pseudo-first order kinetics was registered except for the NaBCN sample which performed an initial inhibition step. The initial rate of benzyl alcohol removal ($r_{BA,0}$) did not significantly change if elemental boron was used as a modifier. Nevertheless, in terms of benzaldehyde production rate, the sample BCN performed a ~3-folded $r_{BD,0}$ value and therefore, an improved selectivity of BA to BD, i.e. ca. 30% for BCN and 12% for CN. If $NaBH_4$ was used as the boron precursor, enhanced reaction rates were registered. Regarding $r_{BA,0}$, NaBCN displayed a 3 times higher value; while for $r_{BD,0}$ photo-production the value was almost 16 times raised. The selectivity from BA to BD was also improved by a value of 36%. The BA oxidation has been reported to produce not only BD. The further oxidation of the aldehyde generates benzoic acid [53,54]. Moreover, benzyl benzoate has been reported after the reaction between oxidized product benzoic acid and reactant benzyl alcohol [55]. In some studies, certain mineralization degree has been reported [53]; however, it was not the case of this work since no significant changes of TOC were registered. The Q_E values of the BA disappearance were calculated from the rate of photon absorbance rate as described in Eq. 1. The NaBCN sample led to the highest value, Q_E = 0.153%; whereas the CN and BCN displayed very similar results, 0.048 and 0.046%, respectively. These results suggest that the defects created in the CN structure by B incorporation enhanced both the photo-activity and the selectivity of the photocatalysts toward the BD formation. Moreover, the sample NaBCN, in which B exchanges positions with C atoms as suggested by XPS analysis, resulted more reactive leading to higher $r_{BA,0}$ and $r_{BD,0}$ values. These photo-activity results are in good agreement with the recombination extent of the electron-hole pair. The PL technique, whose results are displayed in Fig. 3.7B, was used to compare the behavior of the three samples by comparing the intensity of the PL peak which is associated with a higher recombination rate. Hence, the sample CN, which was the most inefficient for BD production, led to the highest PL peak whose maximum was located at ~470 nm. The modification of the graphitic carbon nitride structure lead to enhanced solids whose PL peaks considerably decreased in the order CN>BCN>NaBCN. The B incorporation also decreases the wavelength

at which their maximum was located, ca. 460 nm. The intensity of the PL peak was correlated to the CN ratio, as shown in Fig. 3.7B. This figure depicts a linear correlation between both variables, which suggests that the creation of defects in the graphitic carbon nitride reduces the recombination effect, the reason why the photocatalytic activity was increased.

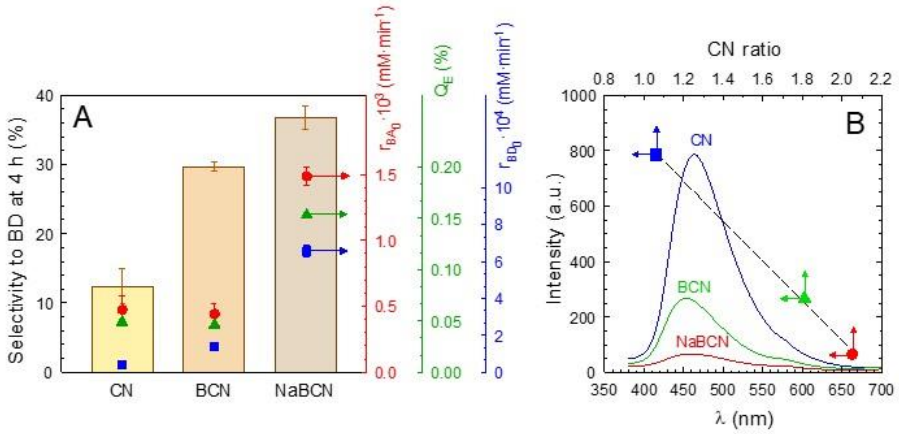

Fig. 3.7 *Changes in the photocatalytic performance in aqueous solution (A), PL spectra (B) of CN after B incorporation, and correlation between maximum PL value and CN ratio (B). Experimental conditions: V=350 mL, T=20ºC, $C_{BA,0}$=0.7 mM; C_{CAT}=0.5 g L^{-1}.*

The photocatalytic oxidation of benzyl alcohol to benzaldehyde is frequently carried out in the presence of organic solvents as reaction media instead of the aqueous solution to rise the selectivity of the reaction [39,53]. Among others, acetonitrile is commonly used to ensure a more selective environment of the reaction, decreasing the rate of the formation of powerful oxidants such as $HO^{\bullet}$, leading therefore the reaction toward other more selective reactive species such as $O_2^{\bullet-}$ [56]. Moreover, the beneficial effect of using acetonitrile is related to the larger amount of O_2 dissolved if compared to water [57]. After the light excitation, electrons are generated and migrate to the conduction band of the catalyst and migrate to the surface of the catalyst they react with adsorbed O_2 to form $O_2^{\bullet}$. $O_2^{\bullet-}$ abstracts proton from the BA to form the BD [55]. In the valence band, if water molecules, if present, could be oxidized by holes to $HO^{\bullet}$, that may contribute to the further oxidation of BD into other species that can lead complete oxidation to CO_2 [54], which was not observed in this study. Although the selectivity could be

compromised, the use of water as the solvent is highly desired from the ecological, economical, and safety points of view. For that reason, some tests were carried out to assess the influence of acetonitrile as solvent at different acetonitrile: water ratios in the most active solid sample that means NaBCN. The results of the initial reaction rates and the selectivity towards benzaldehyde production are depicted in Fig. 3.8. The addition of acetonitrile negatively impacted the reaction rates, either the degradation of BA or the formation of BD due to the scavenger effect of the organic solvent with hydroxyl radical which promotes further reaction of BD. Despite this effect, the selectivity was considerably raised if 20% of acetonitrile was added, ca. 82%. Higher proportions of ACN resulted detrimental for the selectivity of BA to BD. Although the selectivity is undoubtedly raised with a 20% of ACN, the use of water can be justified based on a higher reaction rate and greener conditions.

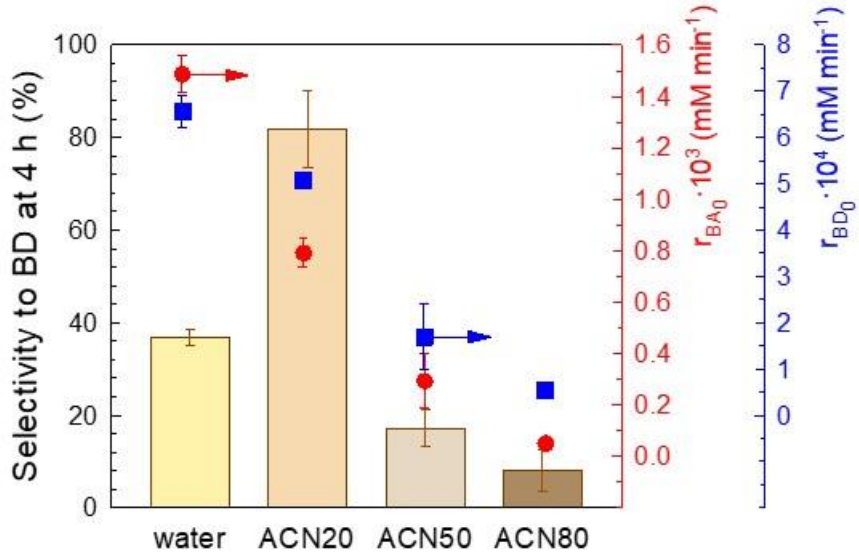

Fig. 3.8 *Influence of acetonitrile (ACN) in the photocatalytic performance of NaBCN. Experimental conditions: V=350 mL, T=20ºC, $C_{BA,0}$=0.7 mM; C_{CAT}=0.5 g L^{-1}.*

Some tests in aqueous solution were carried out to assess the relative importance of common oxidant species in the photocatalytic process and investigate the role played by superoxide radicals. Methanol was used as a potential scavenger of hydroxyl radicals [58], oxalic acid as a photo-generating hole trapping agent [59], and the impact played by O_2 was evaluated by replacing it with an inert

atmosphere by bubbling N_2 [60]. The results are depicted in Fig. 3.9. The presence of methanol slightly modified the BA profile registered for the blank test; however, better and faster production of BD was monitored, i.e. selectivity of 56% vs 30% of the blank test, suggesting the importance of hydroxyl radical, not high in the degradation rate of BD but negative for the production of BD. The bubbling of N_2 replacing O_2 led to a half reduction of BA conversion, denoting the importance of superoxide radicals in the photocatalytic conversion process. More interesting were the results obtained in the presence of oxalic acid which accelerated the degradation of BA, reaching 100% of conversion after 4 hours. The profile monitored for BD, in this case, reached a maximum within 60-90 min, although the selectivity was gradually decreasing due to the high BA converted, i.e. 63-23% in this BA maximum production peak. In this case, oxalic acid act as a hole trapping agent, enhancing the photo-generation of charges which would explain the enhanced BA degradation rate. It has been reported that the photocatalytic decomposition of oxalate might happen simultaneously with the transfer of electrons from this compound to the valence band of the photocatalyst [59].

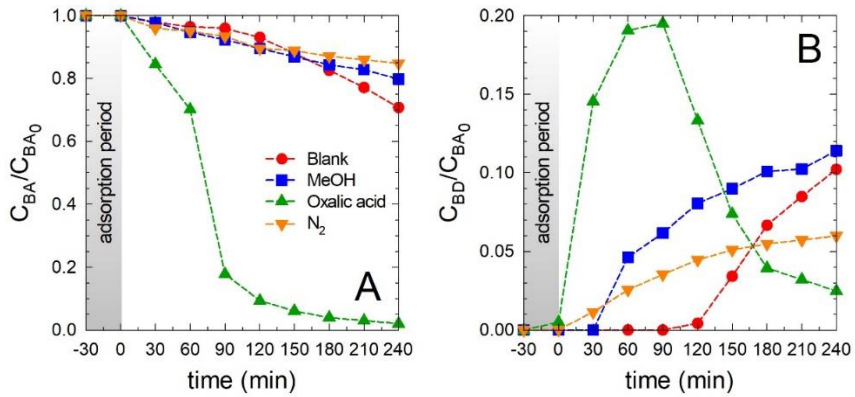

Fig. 3.9 *Time course of benzyl alcohol (A) and benzaldehyde (B) concentrations during the photocatalytic oxidation with NaBCN in the presence of scavengers. Experimental conditions: V=350 mL, T=20ºC, C_{BA},0=0.7 mM; C_{CAT}=0.5 g L^{-1}; $C_{scavenger}$= 10 mM*

The stability of the NaBCN sample after being used was studied by analyzing the solid properties during after being used in aqueous solution, (Fig. 3.10). The XRD and FTIR changes were analyzed and compared to the fresh sample. The FTIR spectrum of reused NaBCN

displayed fewer intensity peaks but still provided the footprint characteristic of graphitic carbon nitride structure. The band related to the vibration $–NH_2$ and –NH- groups which was poorly defined in the boron modified sample due to the presence of boron, was even more diffuse after the reuse. The new peak at 2270 cm^{-1} emerged in the sample NaBCN associated to the C≡N group was still well defined in the reused sample. The peaks corresponding to the tri-s-triazine (heptazine) ring were considerable weakened although still perceptible. The peak attributed to o the out-of-plane bonding vibration characteristics of triazine (~810 cm^{-1}) was well defined but at lesser intensity. Regarding the changes in XRD pattern after the reused, it is observed that definition of the (002) peak corresponding to the presence of interconnected layers.

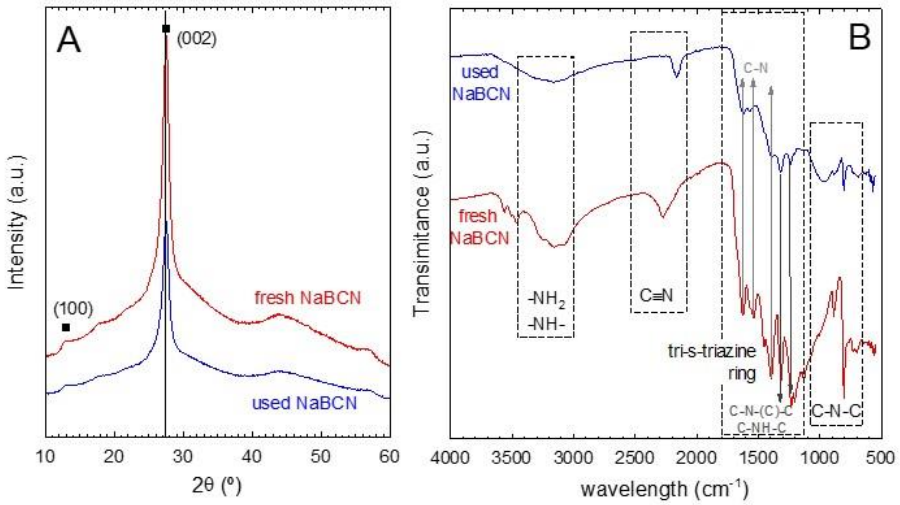

Fig. 3.10 *Changes in the XRD pattern (A) and FTIR spectra (B) of NaBCN after reuse*

3.4. CONCLUSIONS

The modification of graphitic carbon nitride with boron is a powerful strategy for the enhancement of photocatalytic activity. Moreover, the nature of the boron precursor results also in the high relevance of the chemical properties and, therefore, affects the photocatalytic activity of benzyl alcohol oxidation. The characterization results suggest that elemental boron favors the exchange of boron atoms by nitrogen whereas $NaBH_4$ prefers the exchange into carbon positions. Although

both boron sources improved the activity of the solid, the use of $NaBH_4$ resulted in the highest oxidation rate of benzyl alcohol and selectivity to benzaldehyde. A direct correlation between the recombination rate and the number of defects in the structure was observed in PL analysis. The use of acetonitrile as solvent was explored to raise the selectivity. This organic decreased the activity of the solid but addressed the reaction to the formation of benzaldehyde. A proportion of 20% of acetonitrile raised the selectivity to over 80% from 39% observed for water. However, higher proportions of acetonitrile resulted in detrimental selectivity, below the value observed for water. This contribution includes a deep analysis of the light-matter interaction from a strict determination of the quantum yield values of the materials. Although the variation of the photon absorption of the samples showed a relatively low influence to compare the catalytic properties, the determination of the quantum efficiency values has tremendous significance for the comparison of the results of this work with future reports of selective oxidation reactions of alcohols as the measured activity is normalized by the light absorbed by the material. Furthermore, the determination of photon absorption paves the way for intrinsic kinetic studies, which may be the basis for scaling-up efficient catalytic systems for this application.

REFERENCES

1. Akhundi, A.; Badiei, A.; Ziarani, G.M.; Habibi-Yangjeh, A.; Muñoz-Batista, M.J.; Luque, R. Graphitic Carbon Nitride-Based Photocatalysts: Toward Efficient Organic Transformation for Value-Added Chemicals Production. Molecular Catalysis 2020, 488, 110902, doi:10.1016/J.MCAT.2020.110902.
2. Zhao, Z.; Sun, Y.; Dong, F. Graphitic Carbon Nitride Based Nanocomposites: A Review. Nanoscale 2014, 7, 15–37, doi:10.1039/C4NR03008G.
3. Zhang, C.; Li, Y.; Shuai, D.; Shen, Y.; Xiong, W.; Wang, L. Graphitic Carbon Nitride (g-C3N4)-Based Photocatalysts for Water Disinfection and Microbial Control: A Review. Chemosphere 2019, 214, 462–479, doi:10.1016/J.CHEMOSPHERE.2018.09.137.
4. Yadav, A.A.; Kang, S.W.; Hunge, Y.M. Photocatalytic Degradation of Rhodamine B Using Graphitic Carbon Nitride Photocatalyst. Journal of Materials Science: Materials in Electronics 2021, 32, 15577–15585, doi:10.1007/S10854-021-06106-Y.
5. Cheng, J.; Hu, Z.; Lv, K.; Wu, X.; Li, Q.; Li, Y.; Li, X.; Sun, J. Drastic Promoting the Visible Photoreactivity of Layered Carbon Nitride by Polymerization of Dicyandiamide at High Pressure. Appl Catal B 2018, 232, 330–339, doi:10.1016/J.APCATB.2018.03.066.
6. Xavier, M.M.; Nair, P.R.; Mathew, S. Emerging Trends in Sensors Based on Carbon Nitride Materials. Analyst 2019, 144, 1475–1491, doi:10.1039/C8AN02110D.
7. Wang, X.; Maeda, K.; Thomas, A.; Takanabe, K.; Xin, G.; Carlsson, J.M.; Domen, K.; Antonietti, M. A Metal-Free Polymeric Photocatalyst for Hydrogen Production from Water under Visible Light. Nat Mater 2008, 8, 76–80, doi:10.1038/nmat2317.
8. Hao, Q.; Jia, G.; Wei, W.; Vinu, A.; Wang, Y.; Arandiyan, H.; Ni, B.J. Graphitic Carbon Nitride with Different Dimensionalities for Energy and Environmental Applications. Nano Res 2019, 13, 18–37, doi:10.1007/S12274-019-2589-Z.
9. Akhundi, A.; Habibi-Yangjeh, A.; Abitorabi, M.; Rahim Pouran, S. Review on Photocatalytic Conversion of Carbon Dioxide to Value-Added Compounds and Renewable Fuels by Graphitic Carbon Nitride-Based Photocatalysts. Catalysis Reviews 2019, 61, 595–628, doi:10.1080/01614940.2019.1654224.
10. Long, B.; Ding, Z.; Wang, X. Carbon Nitride for the Selective Oxidation of Aromatic Alcohols in Water under Visible Light.

ChemSusChem 2013, 6, 2074–2078, doi:10.1002/CSSC.201300360.

11. Huo, X.; Yi, H.; Fu, Y.; An, Z.; Qin, L.; Liu, X.; Li, B.; Liu, S.; Li, L.; Zhang, M.; et al. Porous Graphitic Carbon Nitride Nanomaterials for Water Treatment. Environ Sci Nano 2021, 8, 1835–1862, doi:10.1039/D1EN00171J.
12. Xu, J.; Wang, Z.; Zhu, Y. Enhanced Visible-Light-Driven Photocatalytic Disinfection Performance and Organic Pollutant Degradation Activity of Porous g-C 3 N 4 Nanosheets. ACS Appl Mater Interfaces 2017, 9, 27727–27735, doi:10.1021/acsami.7b07657.
13. Li, Y.; Gu, M.; Zhang, X.; Fan, J.; Lv, K.; Carabineiro, S.A.C.; Dong, F. 2D G-C3N4 for Advancement of Photo-Generated Carrier Dynamics: Status and Challenges. Materials Today 2020, 41, 270–303, doi:10.1016/J.MATTOD.2020.09.004.
14. Li, Y.; Gu, M.; Zhang, M.; Zhang, X.; Lv, K.; Liu, Y.; Ho, W.; Dong, F. C3N4 with Engineered Three Coordinated (N3C) Nitrogen Vacancy Boosts the Production of 1O2 for Efficient and Stable NO Photo-Oxidation. Chemical Engineering Journal 2020, 389, 124421, doi:10.1016/J.CEJ.2020.124421.
15. Zhou, L.; Zhang, H.; Sun, H.; Liu, S.; Tade, M.O.; Wang, S.; Jin, W. Recent Advances in Non-Metal Modification of Graphitic Carbon Nitride for Photocatalysis: A Historic Review. Catal Sci Technol 2016, 6, 7002–7023, doi:10.1039/C6CY01195K.
16. Hasija, V.; Raizada, P.; Sudhaik, A.; Sharma, K.; Kumar, A.; Singh, P.; Jonnalagadda, S.B.; Thakur, V.K. Recent Advances in Noble Metal Free Doped Graphitic Carbon Nitride Based Nanohybrids for Photocatalysis of Organic Contaminants in Water: A Review. Appl Mater Today 2019, 15, 494–524, doi:10.1016/J.APMT.2019.04.003.
17. Starukh, H.; Praus, P. Doping of Graphitic Carbon Nitride with Non-Metal Elements and Its Applications in Photocatalysis. Catalysts 2020, Vol. 10, Page 1119 2020, 10, 1119, doi:10.3390/CATAL10101119.
18. Ong, W.J.; Tan, L.L.; Ng, Y.H.; Yong, S.T.; Chai, S.P. Graphitic Carbon Nitride (g-C3N4)-Based Photocatalysts for Artificial Photosynthesis and Environmental Remediation: Are We a Step Closer to Achieving Sustainability? Chem Rev 2016, 116, 7159–7329, doi:10.1021/ACS.CHEMREV.6B00075.
19. Kavitha, R.; Nithya, P.M.; Girish Kumar, S. Noble Metal Deposited Graphitic Carbon Nitride Based Heterojunction Photocatalysts.

Appl Surf Sci 2020, 508, 145142, doi:10.1016/J.APSUSC.2019.145142.

20. Li, X.; Hu, Z.; Li, Q.; Lei, M.; Fan, J.; Carabineiro, S.A.C.; Liu, Y.; Lv, K. Three in One: Atomically Dispersed Na Boosting the Photoreactivity of Carbon Nitride towards NO Oxidation. Chemical Communications 2020, 56, 14195–14198, doi:10.1039/D0CC05948J.
21. Yang, C.; Tan, Q.; Li, Q.; Zhou, J.; Fan, J.; Li, B.; Sun, J.; Lv, K. 2D/2D Ti3C2 MXene/g-C3N4 Nanosheets Heterojunction for High Efficient CO2 Reduction Photocatalyst: Dual Effects of Urea. Appl Catal B 2020, 268, 118738, doi:10.1016/J.APCATB.2020.118738.
22. Muelas-Ramos, V.; Sampaio, M.J.; Silva, C.G.; Bedia, J.; Rodriguez, J.J.; Faria, J.L.; Belver, C. Degradation of Diclofenac in Water under LED Irradiation Using Combined G-C3N4/NH2-MIL-125 Photocatalysts. J Hazard Mater 2021, 416, 126199, doi:10.1016/J.JHAZMAT.2021.126199.
23. Guo, S.N.; Zhu, Y.; Yan, Y.Y.; Min, Y.L.; Fan, J.C.; Xu, Q.J. Holey Structured Graphitic Carbon Nitride Thin Sheets with Edge Oxygen Doping via Photo-Fenton Reaction with Enhanced Photocatalytic Activity. Appl Catal B 2016, 185, 315–321, doi:10.1016/J.APCATB.2015.11.030.
24. Zhao, D.; Dong, C.-L.; Wang, B.; Chen, C.; Huang, Y.-C.; Diao, Z.; Li, S.; Guo, L.; Shen, S.; Zhao, D.; et al. Synergy of Dopants and Defects in Graphitic Carbon Nitride with Exceptionally Modulated Band Structures for Efficient Photocatalytic Oxygen Evolution. Advanced Materials 2019, 31, 1903545, doi:10.1002/ADMA.201903545.
25. Wen, Y.; Qu, D.; An, L.; Gao, X.; Jiang, W.; Wu, D.; Yang, D.; Sun, Z. Defective G-C3N4 Prepared by the NaBH4 Reduction for High-Performance H2 Production. ACS Sustain Chem Eng 2019, 7, 2343–2349, doi:10.1021/ACSSUSCHEMENG.8B05124.
26. Xu, H.; Wu, Z.; Wang, Y.; Lin, C. Enhanced Visible-Light Photocatalytic Activity from Graphene-like Boron Nitride Anchored on Graphitic Carbon Nitride Sheets. J Mater Sci 2017, 52, 9477–9490, doi:10.1007/S10853-017-1167-6.
27. Caudillo-Flores, U.; Rodríguez-Padrón, D.; Muñoz-Batista, M.J.; Kubacka, A.; Luque, R.; Fernández-García, M. Facile Synthesis of B/g-C3N4 Composite Materials for the Continuous-Flow Selective Photo-Production of Acetone. Green Chemistry 2020, 22, 4975–4984, doi:10.1039/D0GC01326A.

28. Zhu, Y.P.; Ren, T.Z.; Yuan, Z.Y. Mesoporous Phosphorus-Doped g-C3N4 Nanostructured Flowers with Superior Photocatalytic Hydrogen Evolution Performance. ACS Appl Mater Interfaces 2015, 7, 16850–16856, doi:10.1021/ACSAMI.5B04947.
29. Wang, K.; Li, Q.; Liu, B.; Cheng, B.; Ho, W.; Yu, J. Sulfur-Doped g-C3N4 with Enhanced Photocatalytic CO2-Reduction Performance. Appl Catal B 2015, 176–177, 44–52, doi:10.1016/J.APCATB.2015.03.045.
30. Zhang, G.; Zhang, M.; Ye, X.; Qiu, X.; Lin, S.; Wang, X.; Zhang, G.; Zhang, M.; Ye, X.; Qiu, X.; et al. Iodine Modified Carbon Nitride Semiconductors as Visible Light Photocatalysts for Hydrogen Evolution. Advanced Materials 2014, 26, 805–809, doi:10.1002/ADMA.201303611.
31. Wang, Y.; Di, Y.; Antonietti, M.; Li, H.; Chen, X.; Wang, X. Excellent Visible-Light Photocatalysis of Fluorinated Polymeric Carbon Nitride Solids. Chemistry of Materials 2010, 22, 5119–5121, doi:10.1021/CM1019102.
32. Rao, C.N.R.; Gopalakrishnan, K. Borocarbonitrides, BxCyNz: Synthesis, Characterization, and Properties with Potential Applications. ACS Appl Mater Interfaces 2016, 9, 19478–19494, doi:10.1021/ACSAMI.6B08401.
33. Bahadur, R.; Singh, G.; Bando, Y.; Vinu, A. Advanced Porous Borocarbonitride Nanoarchitectonics: Their Structural Designs and Applications. Carbon N Y 2022, 190, 142–169, doi:10.1016/J.CARBON.2022.01.013.
34. Mateo, D.; Cerrillo, J.L.; Durini, S.; Gascon, J. Fundamentals and Applications of Photo-Thermal Catalysis. Chem Soc Rev 2021, 50, 2173–2210, doi:10.1039/D0CS00357C.
35. Najafishirtari, S.; Friedel Ortega, K.; Douthwaite, M.; Pattisson, S.; Hutchings, G.J.; Bondue, C.J.; Tschulik, K.; Waffel, D.; Peng, B.; Deitermann, M.; et al. A Perspective on Heterogeneous Catalysts for the Selective Oxidation of Alcohols. Chemistry – A European Journal 2021, 27, 16809–16833, doi:10.1002/CHEM.202102868.
36. Zhao, X.; Liu, Q.; Li, Q.; Chen, L.; Mao, L.; Wang, H.; Chen, S. Two-Dimensional Electrocatalysts for Alcohol Oxidation: A Critical Review. Chemical Engineering Journal 2020, 400, 125744, doi:10.1016/J.CEJ.2020.125744.
37. Nair, V.; Muñoz-Batista, M.J.; Fernández-García, M.; Luque, R.; Colmenares, J.C. Thermo-Photocatalysis: Environmental and Energy Applications. ChemSusChem 2019, 12, 2098–2116, doi:10.1002/CSSC.201900175.

38. Makuła, P.; Pacia, M.; Macyk, W. How to Correctly Determine the Band Gap Energy of Modified Semiconductor Photocatalysts Based on UV-Vis Spectra. Journal of Physical Chemistry Letters 2018, 9, 6814–6817.
39. Duarte, H.A.A.; Luggren, P.J.J.; Zelin, J.; Sad, M.E.E.; Díez, V.K.K.; Di Cosimo, J.I.I. Selective Aerobic Oxidation of Benzyl Alcohol on Inexpensive and Reusable ZnO/MnCO3 Catalyst. Catal Today 2021, doi:10.1016/J.CATTOD.2021.10.013.
40. Lee, J.; Kim, J.; Choi, W. Ferrioxalate-Polyoxometalate System as a New Chemical Actinometer. Environ Sci Technol 2007, 41, 5433–5438, doi:10.1021/ES070474Z.
41. Miller, J.N.; Miller, J.C.; Miller, R.D. Statistics and Chemometrics for Analytical Chemistry; Seventh ed.; Pearson Education Limited: Harlow (United Kingdom), 2018; ISBN 978-1-292-18671-9.
42. Serpone, N. Relative Photonic Efficiencies and Quantum Yields in Heterogeneous Photocatalysis. J Photochem Photobiol A Chem 1997, 104, 1–12, doi:10.1016/S1010-6030(96)04538-8.
43. Li Puma, G.; Brucato, A. Dimensionless Analysis of Slurry Photocatalytic Reactors Using Two-Flux and Six-Flux Radiation Absorption–Scattering Models. Catal Today 2007, 122, 78–90, doi:10.1016/J.CATTOD.2007.01.027.
44. Alfano, O.M.; Bahnemann, D.; Cassano, A.E.; Dillert, R.; Goslich, R. Photocatalysis in Water Environments Using Artificial and Solar Light. Catal Today 2000, 58, 199–230, doi:10.1016/S0920-5861(00)00252-2.
45. Muñoz-Batista, M.J.; Kubacka, A.; Fontelles-Carceller, O.; Tudela, D.; Fernández-García, M. Surface CuO, Bi2O3, and CeO2 Species Supported in TiO2-Anatase: Study of Interface Effects in Toluene Photodegradation Quantum Efficiency. ACS Appl Mater Interfaces 2016, 8, 13934–13945, doi:10.1021/ACSAMI.6B03081.
46. Kim, M.; Hwang, S.; Yu, J.S. Novel Ordered Nanoporous Graphitic C3N4 as a Support for Pt–Ru Anode Catalyst in Direct Methanol Fuel Cell. J Mater Chem 2007, 17, 1656–1659, doi:10.1039/B702213A.
47. Sunasee, S.; Leong, K.H.; Wong, K.T.; Lee, G.; Pichiah, S.; Nah, I.W.; Jeon, B.H.; Yoon, Y.; Jang, M. Sonophotocatalytic Degradation of Bisphenol A and Its Intermediates with Graphitic Carbon Nitride. Environmental Science and Pollution Research 2019, 26, 1082–1093, doi:10.1007/S11356-017-8729-7.
48. Wang, X.; Liu, B.; Xiao, X.; Wang, S.; Huang, W. Boron Dopant Simultaneously Achieving Nanostructure Control and Electronic

Structure Tuning of Graphitic Carbon Nitride with Enhanced Photocatalytic Activity. J Mater Chem C Mater 2021, 9, 14876–14884, doi:10.1039/D1TC04142H.

49. Wen, Y.; Qu, D.; An, L.; Gao, X.; Jiang, W.; Wu, D.; Yang, D.; Sun, Z. Defective G-C3N4 Prepared by the NaBH4 Reduction for High-Performance H2 Production. ACS Sustain Chem Eng 2019, 7, 2343–2349, doi:10.1021/ACSSUSCHEMENG.8B05124.
50. She, X.; Wu, J.; Zhong, J.; Xu, H.; Yang, Y.; Vajtai, R.; Lou, J.; Liu, Y.; Du, D.; Li, H.; et al. Oxygenated Monolayer Carbon Nitride for Excellent Photocatalytic Hydrogen Evolution and External Quantum Efficiency. Nano Energy 2016, 27, 138–146, doi:10.1016/J.NANOEN.2016.06.042.
51. Watanabe, M.O.; Itoh, S.; Mizushima, K.; Sasaki, T. Bonding Characterization of BC2N Thin Films. Appl Phys Lett 1998, 68, 2962, doi:10.1063/1.116369.
52. Dinescu, M.; Perrone, A.; Caricato, A.P.; Mirenghi, L.; Gerardi, C.; Ghica, C.; Frunza, L. Boron Carbon Nitride Films Deposited by Sequential Pulses Laser Deposition. Appl Surf Sci 1998, 127–129, 692–696, doi:10.1016/S0169-4332(97)00727-7.
53. Lima, M.J.; Tavares, P.B.; Silva, A.M.T.; Silva, C.G.; Faria, J.L. Selective Photocatalytic Oxidation of Benzyl Alcohol to Benzaldehyde by Using Metal-Loaded g-C3N4 Photocatalysts. Catal Today 2017, 287, 70–77, doi:10.1016/J.CATTOD.2016.11.023.
54. Lima, M.J.; Silva, A.M.T.; Silva, C.G.; Faria, J.L. Graphitic Carbon Nitride Modified by Thermal, Chemical and Mechanical Processes as Metal-Free Photocatalyst for the Selective Synthesis of Benzaldehyde from Benzyl Alcohol. J Catal 2017, 353, 44–53, doi:10.1016/J.JCAT.2017.06.030.
55. Samanta, S.; Khilari, S.; Pradhan, D.; Srivastava, R. An Efficient, Visible Light Driven, Selective Oxidation of Aromatic Alcohols and Amines with O2 Using BiVO4/g-C3N4 Nanocomposite: A Systematic and Comprehensive Study toward the Development of a Photocatalytic p. ACS Sustain Chem Eng 2017, 5, 2562–2577, doi:10.1021/ACSSUSCHEMENG.6B02902.
56. Magdziarz, A.; Colmenares, J.C.; Chernyayeva, O.; Lisovytskiy, D.; Grzonka, J.; Kurzydłowski, K.; Freindl, K.; Korecki, J. Insight into the Synthesis Procedure of Fe3+/TiO2-Based Photocatalyst Applied in the Selective Photo-Oxidation of Benzyl Alcohol under Sun-Imitating Lamp. Ultrason Sonochem 2017, 38, 189–196, doi:10.1016/J.ULTSONCH.2017.03.012.

57. Tripathy, J.; Loget, G.; Altomare, M.; Schmuki, P. Polydopamine-Coated TiO2 Nanotubes for Selective Photocatalytic Oxidation of Benzyl Alcohol to Benzaldehyde under Visible Light. J Nanosci Nanotechnol 2016, 16, 5353–5358, doi:10.1166/JNN.2016.12595.
58. Pelaez, M.; Falaras, P.; Likodimos, V.; O'Shea, K.; de la Cruz, A.A.; Dunlop, P.S.M.; Byrne, J.A.; Dionysiou, D.D. Use of Selected Scavengers for the Determination of NF-TiO2 Reactive Oxygen Species during the Degradation of Microcystin-LR under Visible Light Irradiation. J Mol Catal A Chem 2016, 425, 183–189, doi:10.1016/j.molcata.2016.09.035.
59. Schneider, J.T.; Firak, D.S.; Ribeiro, R.R.; Peralta-Zamora, P. Use of Scavenger Agents in Heterogeneous Photocatalysis: Truths, Half-Truths, and Misinterpretations. Physical Chemistry Chemical Physics 2020, 22, 15723–15733, doi:10.1039/d0cp02411b.
60. Palominos, R.; Freer, J.; Mondaca, M.A.; Mansilla, H.D. Evidence for Hole Participation during the Photocatalytic Oxidation of the Antibiotic Flumequine. J Photochem Photobiol A Chem 2008, 193, 139–145, doi:10.1016/J.JPHOTOCHEM.2007.06.017.

CHAPTER 4. PAPER TWO

Ruthenium deposited onto graphitic carbon modified with boron for the intensified photocatalytic production of benzaldehyde

Catalysis Today 423 (2023) 114266

https://doi.org/10.1016/j.cattod.2023.114266

Rafael R. Solís, M. Alejandra Quintana, Gabriel Blázquez, Mónica Calero, Mario J. Muñoz-Batista

Abstract

The selective oxidation of added-value aromatic alcohols into aldehydes of high interest via photocatalysis has been postulated as a green and competitive oxidative reaction at mild conditions. This work is focused on the design of a tertiary graphitic carbon nitride (g-C_3N_4) based photocatalysts competitive for the photocatalytic production of benzaldehyde in an aqueous solution. The polymeric g-C_3N_4 has been modified in an easy one-pot green synthesis scheme, with the incorporation of boron in the polymeric structure and the deposition of ruthenium nanoparticles. The Ru ratio within 0.5-4% was assessed. The photocatalysts were fully characterized (XRD, FTIR, XPS, N_2 isotherms, DRS-UV-visible, PL) and the photocatalytic activity was assessed in the oxidation of benzyl alcohol to benzaldehyde in an aqueous solution. The incorporation of boron enhanced the selectivity towards benzaldehyde due to enhanced separation charges suggested by the photoluminescence technique; whereas ruthenium improved the reaction rate of the alcohol, affecting negatively the selectivity though. The sample containing 1% of Ru was selected as the optimum in terms of selectivity. The relative contribution of the involved reactive oxidant species was assessed by chemical scavenger tests, highlighting the contribution of the photo-generated holes followed by $O_2^{\bullet-}$. The analysis of the band's alignment of the g-C_3N_4 before the modification with boron and ruthenium supports the enhancement by rising the redox potential of the holes released in the valence band.

Keywords: graphitic carbon nitride, boron, ruthenium, benzaldehyde, photocatalysis

4.1. INTRODUCTION

Aromatic aldehydes are organic substances bearing an aromatic ring and a formyl substituent. These organic substances are of paramount interest since are used in the industry of dyes, fragrances, and flavoring in the food industry or as pharmaceutical precursors. Benzaldehyde (C_6H_5CHO) has paramount relevance in organic synthesis as a raw material, for instance, it is widely used to flavor almonds, as an additive in personal care products, and in dye manufacturing, as an additive due to its antibacterial or antifungal properties. At large scale, benzaldehyde is synthesized from the hydrolysis of benzal chloride or the air oxidation of toluene. The current industrial process of benzaldehyde manufacturing involves the oxidation of toluene, either in the vapor or liquid phases. Nonetheless, the procedure requires rather high temperatures and pressures, leading to low yields due to the formation of by-products [1]. Milder conditions can be obtained if catalysts are used in the oxidation process [2].

Photocatalysis emerges as an environmentally friendly alternative for the production of aldehydes of high interest under a greener approach, at mild temperature and pressure conditions, without requiring additional solvents as other technological alternatives [3]. Furthermore, the use of semiconductors active under radiation sources of low-energy such and renewable as sunlight or UVA potentiates the interest in this alternative. Titanium dioxide has been largely researched in the photocatalysis field due to its potential semiconductor properties; however, photoexcitation is limited to the UV region and inefficient separation of photogenerated charges [4]. As a consequence of the effort paid in the development of new potential semiconductors, graphitic carbon nitride (g-C_3N_4) appeared as a promising alternative with a lower bandgap (2.7 eV) if compared to the benchmark titania polymorphs due to the improved absorption in the visible region and tunable structure to improve the electronic and optical properties [5,6]. The graphitic g-C_3N_4 is built by aromatic nitrogen-containing heteroatoms scaffolded with tris-s-triazine units which are interconnected via tertiary amines, with a unique delocalized stacking of C_3N_4 layers and high electronic conductivity. Among the diverse applications in the field of photocatalysis, g-C_3N_4 has been studied as a candidate for the photocatalytic production of benzaldehyde [7–9]. The energy of valence and conduction bands

compromises an alignment that promotes the reduction of O_2 into superoxide radical but is unable to generate hydroxyl radical, which launches the unselective oxidation of alcohols [10]. The tunable structure of g-C_3N_4 has been proven effective to develop imperfections which leads to the enhance the harvesting of radiation and improves the separation of photogenerated charges via non-metal doping [11,12]. Among them, the modification with boron has been demonstrated to raise the selectivity of benzaldehyde formation from benzyl alcohol oxidation [13]. Furthermore, the deposition of low amounts of noble metals such as Au, Pd, Pt, Ag, Ir, Rh, or Ru onto the g-C_3N_4 supports the improvement of the reaction rate, upgrading the separation charges [14–18]. The presence of metal nanoparticles can act as electron sinks to capture photoinduced electrons from the conduction band of g-C_3N_4 [19].

This work develops the preparation of a ternary-modified g-C_3N_4 photocatalyst in a one-pot-step synthesis scheme applied for the photocatalytic oxidation of benzyl alcohol to benzaldehyde. Two modifications have been included in the structure of g-C_3N_4 simultaneously; firstly, with boron modification aimed at the enhancement of benzaldehyde selectivity; and secondly, Ru deposition for the raise of the conversion of benzyl alcohol. Different boron-modified g-C_3N_4 samples under Ru loading within 0.5-4% (at. wt) were prepared and characterized with XRD, FTIR, N_2 isotherms, DRS-UV-visible and photoluminescence techniques. The activity towards benzyl alcohol oxidation was tested, assessing the alcohol conversion and selectivity to the aldehyde production to optimize the metal loading. The oxidation mechanism in terms of the reactive oxidant species involved in the process was accomplished for the optimized Ru content in terms of benzaldehyde selectivity.

4.2. EXPERIMENTAL SECTION

4.2.1. Materials and catalyst synthesis

The chemicals used were analytical grade at least, acquired from Merck®, and used as received. HPLC-quality acetonitrile was used as a mobile phase in chromatographic analysis. Ultrapure water (18.2 MΩ·cm) from a Direct-Q®-UV device (Millipore®) was used for the preparation of all the solutions.

The graphitic carbon nitride (g-C_3N_4, CN) was synthesized from pyrolysis of melamine (rate 10 ºC·min^{-1}, holding temperature 500 ºC, 2h). As a result, a yellowish solid was obtained. This solid was suspended in water to discharge those particles that are not successfully suspended in the solution. The suspended particles were collected by filtration and dried at 80 ºC. The boron-modified CN was prepared by pyrolysis under an N_2 atmosphere as described in a previous study. CN and $NaBH_4$ were mixed at the same mass ratio and grounded in a mortar. The mixed powder was next calcined at 450 °C (ramp 10 °C min^{-1}, 1 h). The resulting brownish material (NaBCN) was cooled down to room temperature, washed several times with water, and dried at 80 °C. The NaBCN samples with ruthenium deposited were prepared following a similar procedure in which $NaBH_4$ played a double role, as both boron precursor and reduction agent. Thus, CN and $NaBH_4$ were mixed at equal mass ratios in a mortar. Next, a desired amount of ruthenium was added as $RuCl_3$, and dissolved in 0.9 mL of water. This volume was estimated to carry out an incipient wetness impregnation method over 1.5 g of solid NaBCN. The ruthenium solution was dropwise added to the mixed powder wetting all the solid particles. Next, the wet solid was calcined at 450 ºC (heating rate, 10 °C min^{-1}, 1 h). The resulting solid was cooled down, washed, and dried as done with the NaBCN blank sample. The samples containing ruthenium were labeled as NaBCN-xRu where x stands for the atomic ruthenium to mass percentage in the sample.

4.2.2. Characterization of the catalysts

The crystalline structure was analyzed using powder X-Ray Diffraction (XRD) in a Bruker D8 Discover device working with a Cu Kα radiation source (λ = 1.5406 Å), equipped with a detector Pilatus3R 100 K-A registering within a 2θ range of 6-80° at a rate of 0.04° min^{-1}. The software QualX® and the Crystal Open Database (COD) were used for the identification of the crystal phases in the obtained diffractograms.

The structure was further studied by the stretching of the bonds by Fourier Transform InfraRed (FTIR) analysis, displayed in a Perkin-Elmer model Spectrum65 device within 400–4000 cm^{-1}.

The surface porous properties were assessed by N_2 adsorption–desorption at 77 K performed in a Sync 200 equipment from 3P Instruments©. Samples were degassed overnight at 150 ºC under a

vacuum. The specific surface area was obtained by the Brunauer-Emmett-Teller method (S_{BET}), and the total specific pore volume (V_T) was calculated from the N_2 uptake at p/p_0~0.99. The Barrett, Joyner, and Halenda method (BJH) was applied to analyze the average (4V/A) and most frequent (dV/dD) pore diameter.

X-ray Photoelectron Spectroscopy (XPS) was applied for the study of the elemental composition present at the surface of the materials in a Kratos AXIS UltraDLD device working with an X-ray source from Al Kα. The spectra were referenced to the C1s peak of adventitious carbon to 284.6 eV. The software XPSpeak 4.1® was used for the deconvolution of the peaks, considering a Shirley background correction.

The optical properties were assessed through Diffuse Reflectance Spectroscopy (DRS) in the UV-visible region in a Varian Cary 5E spectrophotometer. The Kubelka-Munk Function, $F(R_\infty)$, was obtained from the reflectance spectra, and the bandgap was estimated from the Tauc plot method considering indirect electron transitions [20]. The recombination rate of the photo-generated electrons was assessed by photoluminescence (PL) analysis in a Varian Cary Eclipse device under an excitation wavelength of 365 nm.

4.2.3. Photocatalytic experiments

The NaBCN-Ru catalysts were tested for the selective photocatalytic oxidation of benzyl alcohol to benzaldehyde in a borosilicate glass annular jacketed photoreactor equipped with two UVA lamps emitting at 365 nm (9 W each). Detailed information on the experimental setup can be found in a previous work [21]. The lamps were centered in the inner space and the aqueous solution with the slurry catalyst was circulating by the jacketing space. The slurry was constantly pumped from an auxiliary jacketed tank, cooled with water to 20 ºC, in which the catalyst was kept suspended through magnetic stirring in the bottom. To ensure O_2 saturation, the air was bubbled in the auxiliary tank. The radiation reaching the liquid phase was quantified by an in situ chemical actinometry, based on the photo-reduction of ferrioxalate complex combined with a polyoxometalate salt ($Na_2SiW_{12}O_6$) to monitor the temporal abatement of the ferrioxalate complex into CO_2 [22]. The actinometry tests were carried out with oxalic acid 60 mM, $FeCl_3 \cdot 6\ H_2O$ 5 mM, and $H_4SiW_{12}O_{40}$ 1 mM. The pH of the solution was adjusted to 4.5 with the addition of diluted 0.1 M HCl and NaOH to avoid the

plausible auto-decomposition of the polyoxometalate complex. Taking into account the quantum yield value during the photo-production of $(SiW_{12}O_{40})^{5-}$ (ϕ = 0.18 mol·Einstein^{-1} at 365 ± 10 nm) [22], the radiation intensity value estimated was $I_0 = (3.5 \pm 0.2)\times10^{-4}$ Einstein $L^{-1}\cdot min^{-1}$.

The photocatalytic tests of benzaldehyde production started by loading the aqueous solution of benzyl alcohol 0.5 mM. After, the photocatalyst was added at a dose of 0.5 g·L^{-1} in the auxiliary tank until homogeneously dispersed the solid in the reaction system. Before the irradiation, an adsorption step of 30 min was displayed in the darkness. Next, the lamps were switched on, and samples were regularly extracted for analysis. The photocatalyst was removed from the extracted samples by syringe filters (PVDF, 0.45 μm).

The concentration of the aromatic alcohols and their aldehydes was quantified by High-Pressure Liquid Chromatography (HPLC) in an HPLC Alliance e2695 from Waters™ coupled to a 2998 photodiode array UV-visible detector. The stationary phase consisted of a Zorbax Bonus-RP column (4.6×150 mm, 5 μm). The mobile phase, pumped at 1 mL min^{-1}, was fed under an isocratic program with 90 μL of sample injection. For the analysis of benzyl alcohol (BA) and benzaldehyde (BD), a mixture of 30% acetonitrile (A) and 70% acidified water (B, 0.1% v/v trifluoroacetic acid) was pumped, conducting the quantification at 215 for BA and 248 for BD.

The temporal evolution of BA abatement was adjusted to a pseudo-first order kinetics, and the observed constant (k_{BA}) was calculated as a mere tool of comparison between the performances of the NaBCN-Ru samples. Also, the selectivity (S) as calculated from the BD profiles, and an average value during the whole period tested was calculated as follows:

$$S_{average} = \frac{\int S(t)dt}{(t-0)} \tag{4.1}$$

The quantum efficiency (Q_E) of BA photo-degradation was quantified, following the IUPAC recommendations [23–25], which defines the Q_E as the ratio of the number of molecules reacting through the reaction rate ($r_{BA,0}$), by the number of the photon which interacts with the catalyst, i.e. the photon absorption rate ($e^{\alpha,v}$) [26]:

$$Q_E = \frac{r_{BA}\left(mol\ m^{-3}\ s^{-1}\right)}{e^{\alpha,v}\ (Einstein\ m^{-3}\ s^{-1})} \tag{4.2}$$

where $r_{BA,0}$ was estimated from the slope of the temporal evolution of the C_{BA} with the tangent at the initial reaction time. The determination of the photon absorption rate ($e^{\alpha,v}$), and the radiative transfer equation (RTE) was solved considering the geometry of the used photoreactor [21]. Firstly, the determination of the optical properties of the catalytic suspensions is required. Detailed description of the mathematical procedure for both optical properties and photon rate estimations are provided in previous works [13,21].

The contribution to the BA oxidation by the reactive species generated during the photocatalytic process was assessed by adding different chemical scavengers. The influence of superoxide radical was investigated with N_2 bubbling, or the addition of p-benzoquinone (pBQ, 1 mM) or disodium 4,5-dihydroxybenzene-1,3-disulfonate (tiron, 1 mM). The contribution of hydroxyl radicals was assessed by adding tert-butyl alcohol (TBA, 10 mM) while photo-generated holes were suppressed under the presence of oxalic acid (OA, 10 mM). These assays were conducted following the same procedure as the blank test and adjusting to the same initial pH value (pH=9±0.5).

4.3. RESULTS AND DISCUSSION

4.3.1. Characterization of the NaBCN-Ru photocatalysts

Fig. 4.1 A depicts the changes registered in the crystalline structure of the CN after boron modification and Ru deposition. The XRD pattern of the CN sample displayed the two main characteristic peaks generated as a consequence of the polycondensation of melamine to generate the tris-s-triazine units [27]. The main peak, located at around ~27º, reports the (002) plane defined by the interplanar aromatic layers from π-π* interactions of the heptazine rings. A secondary peak, much less intense, placed at ~13º, is attributed to the (100) plane, whose presence is reported by the intralayer spacing of the heptazine rings. The incorporation of boron in the CN structure led to a considerable decrease in both XRD peaks due to the partial loss of crystallinity in the structure [28], as shown in the pattern for NaBCN. The Ru deposition in the presence of $NaBH_4$ led to NaBCN-Ru samples, which led to the complete removal of the intralayer heptazine (100) facet, suggesting a

high distortion of the in-plane aromatic structure [29]. The Ru doping in the CN structure has been reported in the literature at low Ru loadings, which explains the deformation of the crystalline in-plane of the heptazine rings given to the disappearance of the (100) facet in their XRD pattern [16,29]. Moreover, the interplanar (002) peak considerably diminished its intensity, probably due to the partial loading of ruthenium, as already reported in the literature for other Ru modifications of CN materials [30,31]. A Rietveld refinement of the XRD patterns led to detect the presence of halite, NaCl (COD 00-900-8678), in all the samples containing Ru, as a consequence of the reaction between chloride and sodium, respectively contained in Ru and boron precursors, $RuCl_3$ and $NaBH_4$. Furthermore, the sample with the highest content of Ru, namely NaBCN-4Ru, also displayed the presence of tricalconite, $Na_6[B_4O_5(OH)_4]_3{\cdot}8H_2O$ (COD 00-900-2675). However, no metallic Ru peaks were identified, probably due to the low intensity they may appear [30–32], especially taking into account the possible overlapping problems with NaCl and tricalconite.

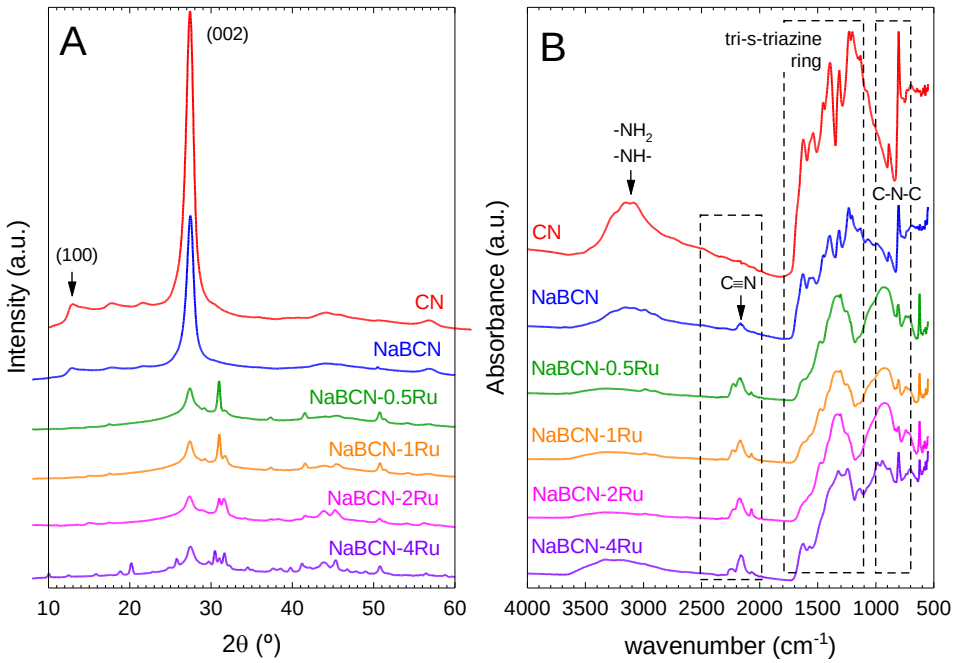

Fig. 4.1*XRD patterns (A) and FTIR spectra (B) of NaBCN-Ru samples.*

The structural modification of the CN structure with both B and Ru incorporation was further analyzed by FTIR, see Fig. 4.1B. The distortion of the intraplanar heptazine rings with Ru insertion can be corroborated in the FTIR footprint of NaBCN-Ru samples. The peals were smoothed, with an important loss of their definition. The CN sample displayed well-defined broadband at 3000-3500 cm^{-1}, attributable to -NH_2 and -NH- groups [33]. Also, the CN spectrum showed a peak at ~ 810 cm^{-1}, reported by the out-of-plane bonding vibration characteristics of the condensed triazine units [34]. The modification with boron of the graphitic structure of the carbon nitride led to a great depletion of this band. A group of peaks within 900 and 1800 cm^{-1} defined by the vibration of the aromatic C-N rings of the heptazine units were fully registered in the CN sample [35]. The intense peaks at 1620, 1530, and 1390 cm^{-1} can be assigned to the aromatic C-N stretching vibration, whereas the peaks at 1310 and 1230 cm^{-1} appear due to the stretching vibration of C-N-(C)-C or C-NH-C bonds, respectively [36,37]. The modification with boron considerably modified the intensity of these peaks, but still, the characteristic footprint registered in the pristine CN was recognized in the NaBCN sample. However, the further addition of Ru particles erased the defined pattern peaks of the heptazine units.

The textural properties of samples were analyzed by N_2 adsorption-desorption isotherms at 77 K. The isotherms are depicted in Fig. 4.2 and the main characterization results are shown in Table 4.1. The N_2 physisorption isotherms in the samples described the typical type IV pattern behavior with H3 hysteresis loops [38–40], characteristic of mesoporous with aggregates of plate-loke particles [41]. The BET surface area of all the samples was below 10 m^2 g^{-1}, typical reported values for graphitic carbon nitride prepared from the polymerization of melamine [42]. A slight mesoporosity was registered in the hysteresis loops with an average pore size of around 3 nm. The modification of the original CN sample either with B and Ru led to a decrease in the surface properties, i.e. BET area pore volume.

Table 4.1 *Textural and optical properties of the NaBCN-Ru samples*

Sample	S_{BET} ($m^2\ g^{-1}$)	V_T ($cm^3\ g^{-1}$)	$D_{average}$ (nm)	$D_{frequent}$ (nm)	E_{BG} (eV)	E_{VB} (eV)
CN	9.1	0.050	30.2	3.5	2.7	1.0
NaBCN	4.0	0.018	13.2	2.9	2.6	1.3
NaBCN-0.5Ru	3.1	0.014	11.9	3.5	2.4	-
NaBCN-1Ru	2.9	0.012	11.9	3.5	2.3	1.9
NaBCN-2Ru	2.8	0.014	10.6	2.9	2.0	-
NaBCN-4Ru	2.5	0.017	9.2	3.9	2.6	-

S_{BET}: total specific surface area by BET method; V_T: total pore volume; $D_{average}$ and $D_{frequent}$: average and most frequent pore diameter by BJH method, respectively; E_{BG}: bandgap by Tauc plot method; E_{VB}: valence band energy by XPS.

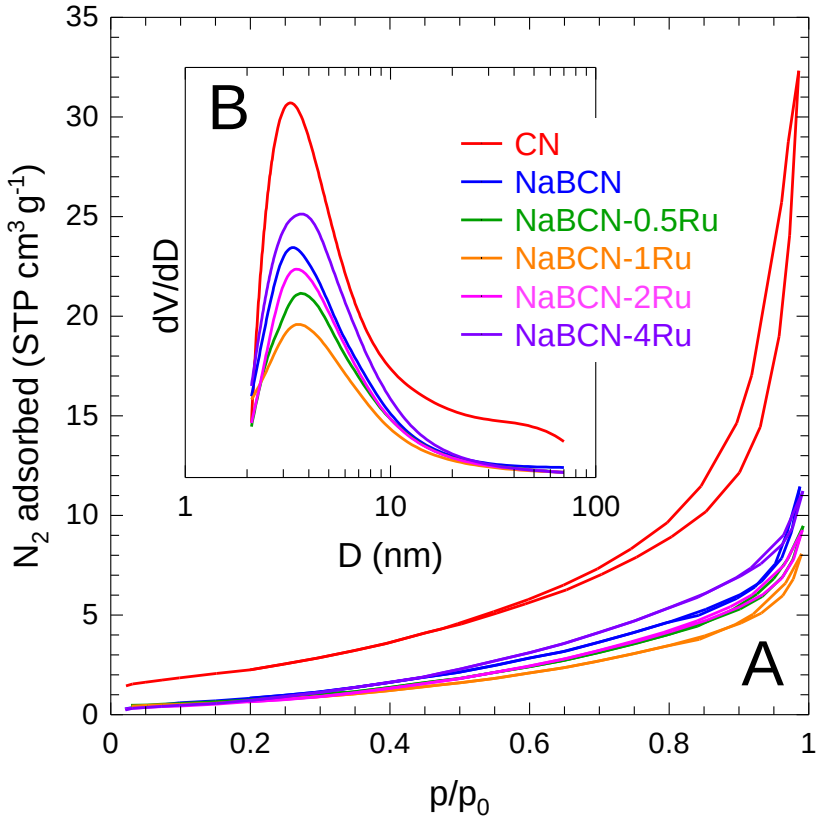

Fig. 4.2 *N_2 adsorption-desorption isotherms (A) and BJH pore size distribution (B) of NaBCN-Ru samples*

The chemical nature of the surface of CN, NaBCN, and NaBCN-4Ru samples was assessed by the XPS technique. The high-resolution XPS

spectra of C1s, N1s, B1s, and Ru3p are depicted in Fig. 4.3 High-resolution XPS spectra of N1s, C1s, and B1s and Ru3p regions of CN, NaBCN, and NaBCN-4Ru samples. As illustrated, the incorporation of B and Ru highly modifies the XPS spectra due to the structural changes incorporated. The spectra were deconvoluted following the contributions reported in the literature for graphitic carbon materials. The C1s peak of g-C_3N_4 is commonly deconvoluted in sp^2 N=C-N (287.9 eV), sp^3 C-C/C-N (285.2 eV), and sp^2 C-C/C=C (284.4 eV) bonds [43]. The sample CN displayed a major contribution of sp^2 carbon in the form of N=C-N bonds. The bonds attributable to sp^3 C-C/C-N or sp^2 C-C/C=C raised their relative contribution with the modification with boron as shown in NaBCN and NaBCN-4Ru samples. Moreover, a secondary peak regarding $Ru3d_{3/2}$ appeared at an energy of ~280 eV [44]. The Ru3d core levels overlap the C1s region, making difficult the analysis of Ru species by exclusive analysis of Ru3d. For that reason, the Ru3p level, equally accessible as Ru3d, was analyzed for the study of the oxidation state of Ru. The peaks in Ru3p were successfully assignable to Ru $3p_{3/2}$ (484.0 eV) and $3p_{1/2}$ (461.1 eV) of metallic Ru^0 [44–47]. The N bonds were analyzed in the N1s region, considering the following contributions C_3–N (N_{3C}, 399.9 eV), N–C=N (N_{2C}, 398.4 eV), and N–H_x (401.0 eV) and B=N-C (399.0 eV) [28,43,48,49]. The CN samples presented a high contribution of N contained in the aromatic rings (N_{2C}) and tertiary N (N_{3C}), and a small proportion of terminal NH_x was observed. The NaBCN samples displayed the three contributions; nonetheless, the sample NaBCN-1Ru only showed a peak located at ~192 eV. The modification con $NaBH_4$ created defects in the structure, reducing the N_{3C} creating B=N-C bonds. In the case of NaBCN-1Ru, the presence of B=C-N was inferior to the case of NaBCN, probably due to the reduction of ruthenium to create Ru^0. The B1s peak was deconvoluted in three contributions elemental boron (186.8 eV), B-N (190.3 eV), and B related to oxides or hydroxides (191.9 eV) [49–51]. While the three oxidation states of B are envisaged in the NaBCN sample, when adding the ruthenium precursor to the synthesis, the contribution of BN was not registered.

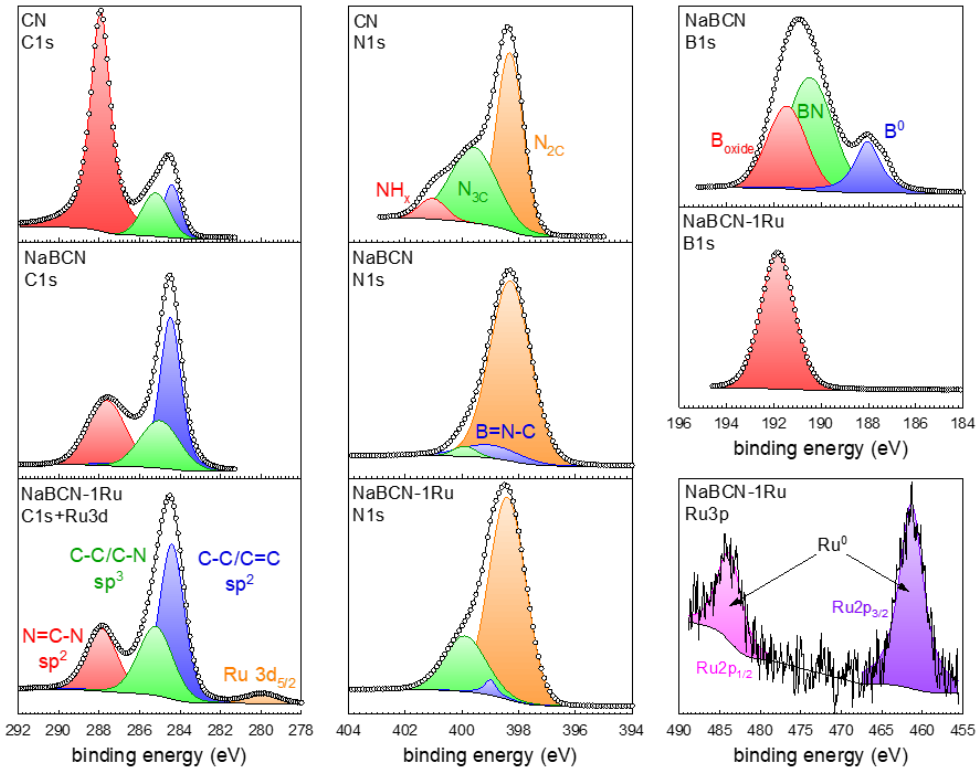

Fig. 4.3 *High-resolution XPS spectra of N1s, C1s, and B1s and Ru3p regions of CN, NaBCN, and NaBCN-4Ru samples.*

The optical properties were assessed by the DRS-UV-visible technique. The CN sample displayed radiation absorption in the UV region with a sharp decrease of over 400 nm. The absorption peak around 300–400 nm has been associated in previous works with π–π* transitions in the conjugated ring systems heptazine units [52]. The absorbance of the NaBCN sample was red-shifted improving the absorption in the visible region [13]. The addition of ruthenium enlarged the absorption in the visible region, as depicted in the spectra of Fig. 4.4A. The Kubelka-Munk function is depicted in Fig. 4.4B for the determination of the bandgap energy (see values in Table 4.1). The bandgap of CN (2.7 eV) was reduced after boron modification in NaBCN (2.6 eV) and further decreased up to 2.0 eV after Ru addition.

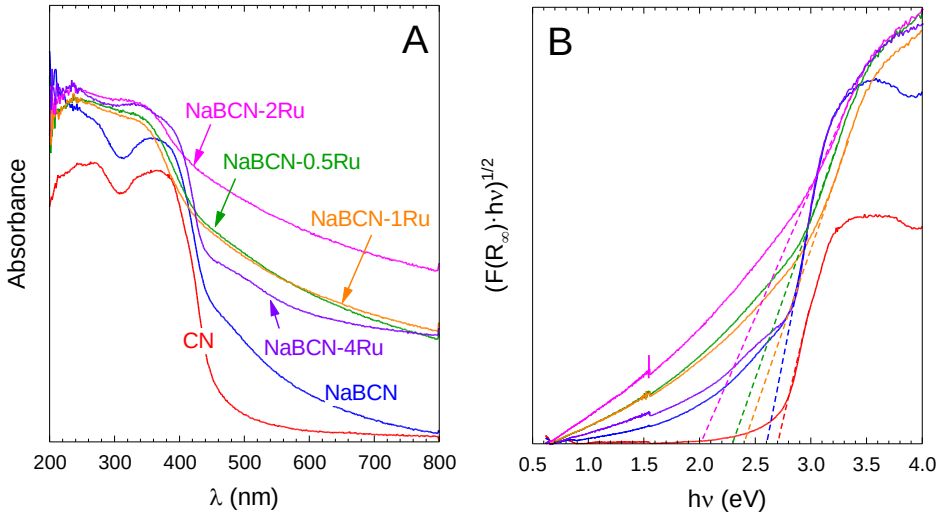

Fig. 4.4 *Absorption DRS-UV-visible spectra (A) and Tauc plot method for the bandgap determination (B) of NaBCN-Ru samples*

Fig. 4.5 illustrates the local volumetric rate of photon absorption with the radial distance for the different samples. Although optical differences regarding the absorption of radiation were registered in the visible region, at the emitting wavelength of the lamp used, i.e. 365 nm, the differences between the samples were minor. For that reason, the photo absorption rate values (average) and the profiles for each sample are quite similar.

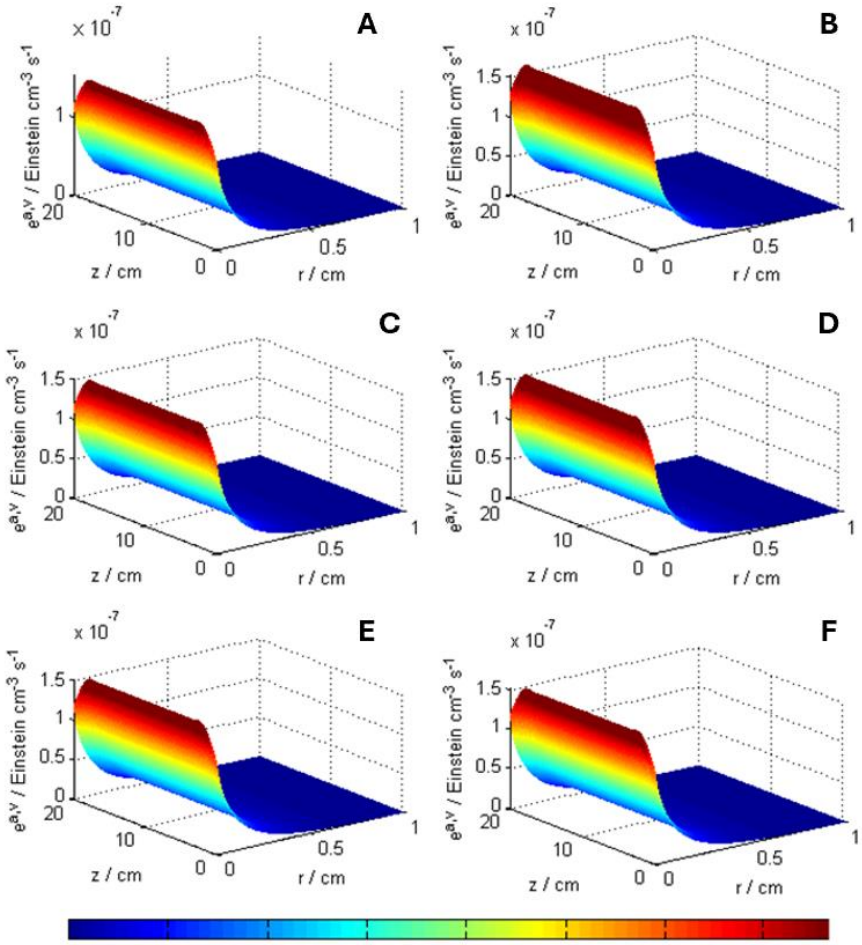

Fig. 4.5 *Local volumetric rate of photon absorption of CN (A), NaBCN (B), and Ru containing samples: (C) NaBCN-0.5Ru, (D) NaBCN-1Ru, (E) NaBCN-2Ru and (F) NaBCN-4Ru.*

4.3.2. Photocatalytic production of benzaldehyde with NaBCN-Ru samples

The influence of ruthenium presence on the activity of the photocatalysts was assessed in the selective oxidation of benzyl alcohol to benzaldehyde. Fig. 4.6 depicts the temporal evolution of the remaining concentration of BA and the efficiency of BD production. Also, the observed pseudo-first order rate constant of BA disappearance (k_{BA})

and the average selectivity of BD formation for each catalyst is summarized in Table 4.2 and Fig. 4.6

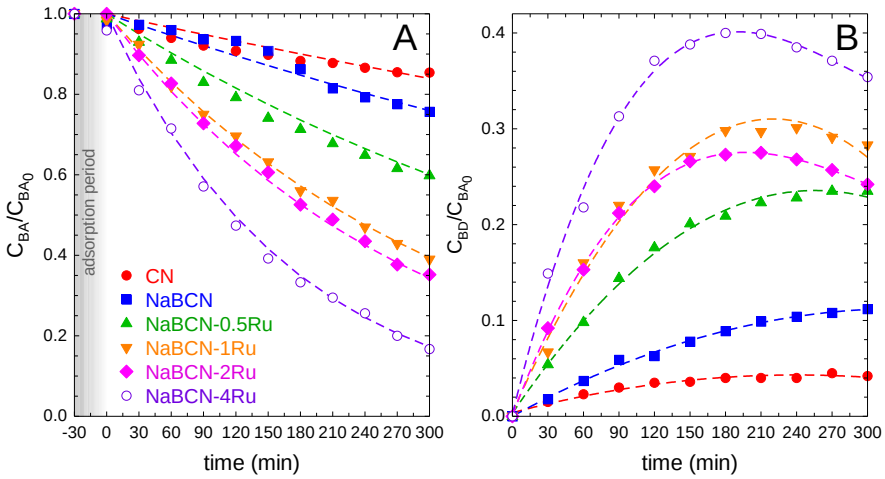

Fig. 4.6 *Photocatalytic production of benzaldehyde with NaBCN-Ru samples at different Ru ratios. Temporal normalized concentration of benzyl alcohol (A) and benzaldehyde (B). Experimental conditions: V= 350 mL, T=20ºC, $C_{BA,0}$= 0.5 mM; C_{CAT}=0.5 g L^{-1}; pH=9.5±0.2.*

Table 4.2 *Kinetic parameters of the photocatalytic production of benzaldehyde with NaBCN-Ru samples*

Sample	$r_{BA,0}\cdot10^3$ (mM min^{-1})	Q_E (%)	k_{BA} (h^{-1})	BA conversion at 3 h (%)	Average BD selectivity (%)
CN	0.243	0.03	0.035	14.6	33.0
NaBCN	0.405	0.04	0.055	24.3	65.5
NaBCN-0.5Ru	0.867	0.09	0.102	40.2	69.8
NaBCN-1Ru	1.267	0.13	0.186	61.0	67.5
NaBCN-2Ru	1.367	0.14	0.214	64.8	62.7
NaBCN-4Ru	2.375	0.24	0.351	83.3	57.3

The CN sample displayed roughly 15% conversion of BA which only was oriented in a 33% BD formation. The modification with $NaBH_4$, i.e. the sample NaBCN, raised the BA conversion to 24% and the selectivity to BD. The deposition of Ru particles onto the NaBCN drastically enhanced the photocatalytic activity, improving the kinetics of BA gradually as the Ru amount increases. As depicted in Fig. 4.7A, the k_{Obs} value was 1.8-6.3-folded depending on the Ru amount incorporated, ranging from 0.5-4.0%. The presence of noble metal particles contributes to enhancing the separation of the photogenerated charge

as reported in the literature for diverse semiconductors. In this case, Ru acts as an electron sink after the photo-activation of NaBCN, minimizing the undesirable recombination effect. The quantum efficiency shown in Table 4.2 follows a similar trend to the k_{Obs}, as the photon absorption rate calculated is very similar in each case (see Fig. 4.5). The presence of Ru enhanced the Q_E value by folding within 3-8 times depending on the Ru load.

An analysis by photoluminescence of the samples provided support to this theory. The emission PL spectrum of CN, see Fig. 4.7B, has a well-defined peak at 455 nm, whose intensity was quite diminished by the modification with $NaBH_4$. The incorporation of boron in the structure has been reported as an effective way to create structural defects that enhance the electronic separation of the photo-generated charges [13,28,48]. Besides, the further Ru deposition eliminated any emitted PL photon, leading to plain PL spectra which suggests an enhanced reduction of the recombination effect due to the improved electrical conductivity and electronic migration of charges [16,17,45]. The photogenerated electrons are expected to migrate from g-C_3N_4 to interfacial Ru due to its affinity to capture electrons acting as a sink which inhibits the recombination effect [45].

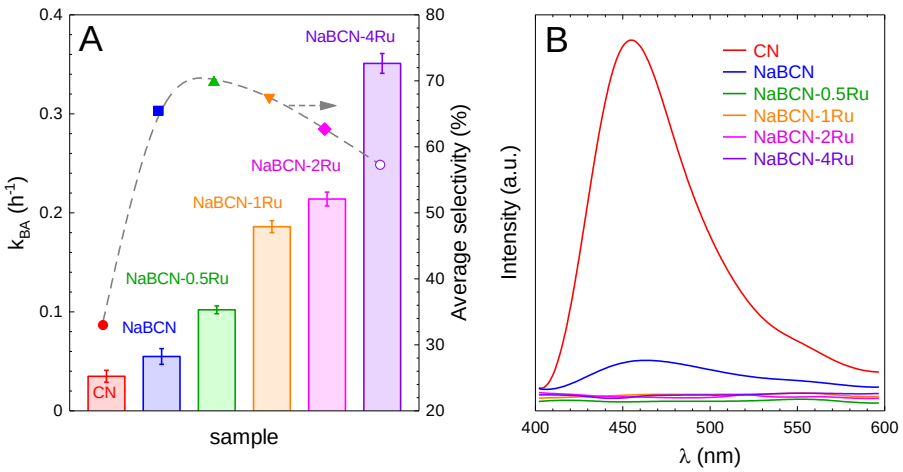

Fig. 4.7 *(A) Pseudo-first order rate constant of BA depletion (k_{BA}) and average selectivity to BD production of NaBCN-Ru samples. (B) PL spectra of the NaBCN-Ru photocatalysts.*

Regarding the selectivity, see Fig. 4.7A, the presence of Ru does not exert a positive effect except at a very low concentration, NaBCN-0.5Ru,

with a slight improvement if compared to the NaBCN sample, 69.8 vs 65.5%. A further raise of Ru decreases the selectivity value. There is, therefore, a confronted effect between selectivity and activity. Considering the results obtained, and the objective of minimization of the noble metal content, 1% of Ru content was selected as the optimum in a compromise of high activity and selectivity. The NaBCN-1Ru sample was selected for further study.

4.3.3. Photocatalytic mechanism of BA oxidation with NaBCN-1Ru

The relative influence of the different reactive oxidant species (ROS) involved in the photocatalytic activation of NaBCN-1Ru was tentatively by a chemical scavenger study [53]. Fig. 4.8A shows the temporal evolution of BA depletion registered in the blank test and the presence of the selected scavengers, whereas Fig. 4.8B depicts the pseudo-first order rate constant in each case. The impact of superoxide radical ($O_2^{\bullet-}$) was studied by replacing the air bubbling with N_2, with the addition of para-benzoquinone (p-BQ) or tiron. The formation of $O_2^{\bullet-}$ takes place by the reduction of dissolved O_2 adsorbed in the surface of the photocatalyst with the photogenerated electrons. The removal of O_2 by replacement with N_2 led to a 44% decrease in the k_{BA} compared to the blank. The use of p-BQ is widely extended in the scavengers' studies in photocatalytic processes [54], due to the affinity of this substance with $O_2^{\bullet-}$ ($k_{p\text{-}BQ,O2^{\bullet-}}=1\times10^9$ M^{-1} s^{-1} [55]). The addition of p-BQ decreased the k_{BA} considerably, i.e. 81%. Nonetheless, p-BQ can also trap $HO^{\bullet}$ ($k_{p\text{-}BQ,HO^{\bullet}}=6.6\times10^9$ M^{-1} s^{-1} [56]) and be photolyzed under UVA radiation. It has been reported that the photo-reduction of quinones in aqueous systems yields the formation of $HO^{\bullet}$ and semiquinone radicals which makes difficult the interpretation of the results [57]. Moreover, the use of p-BQ hides risks due to plausible interactions with the targeted to be converted into substances easily photolyzed [58]. For these reasons, alternative scavengers should be considered before any definitive conclusion. Tiron has been reported as a reliable alternative due to the higher reactivity with superoxide radical, $k_{tiron,O2^{\bullet-}}=5\times10^9$ M^{-1} s^{-1} [59], compared to the kinetics of the reaction towards $HO^{\bullet}$, $k_{tiron,HO^{\bullet}}=1.0\times10^9$ M^{-1} s^{-1} [60]. The presence of tiron reduced the k_{BA} to a 36% extent. Taking these results into account, it can be concluded that the oxidation

of BA is influenced by $O_2^{\bullet-}$, but not exclusively. The contribution of $HO^{\bullet}$ was evaluated by the addition of TBA, second-order rate constant $k_{TBA,HO^{\bullet}}=6.2\times10^8$ M^{-1} s^{-1} [61]. The effect of TBA was low, with only an 18% of reduction in the k_{BA} for the blank test, so the contribution of $HO^{\bullet}$ radical can be expected to play a minor role. Finally, the influence of the photogenerated holes was assessed by the presence of oxalic acid [62]. The oxalate anion after being adsorbed onto the surface of the photocatalyst is oxidized by the holes to release CO_2 [41]. Although oxalate anions also can react with $HO^{\bullet}$, the kinetics is slow $k_{Oxalate,HO^{\bullet}}=1.5\times10^7$ M^{-1} s^{-1} [63]. Under the presence of oxalic acid, the k_{BA} was reduced by 64% concerning the blank test, being, therefore, the most relevant species in the process. In summary, the importance of the ROS involved in the process of BA oxidation was: $h^+ > O_2^{\bullet-} >> HO^{\bullet}$. Other studies involving TiO_2 have identified the importance of holes [64] and superoxide [58] in the process of benzaldehyde production.

Fig. 4.8B also includes the average selectivity of benzaldehyde production in the presence of the selected scavengers. In the presence of superoxide radical scavengers, i.e. N_2, p-BQ, and tiron, the selectivity was slightly improved if compared to the blank test. The presence of $HO^{\bullet}$ has been demonstrated to be an unselective route of oxidation [58]. In this sense, the addition of TBA did not affect the selectivity of the process, due to the low impact of $HO^{\bullet}$ in the process. In the case of the suppression of the holes, the selectivity decreased. This fact provides evidence of the higher selectivity of the holes to the formation of benzaldehyde if compared to the superoxide radical.

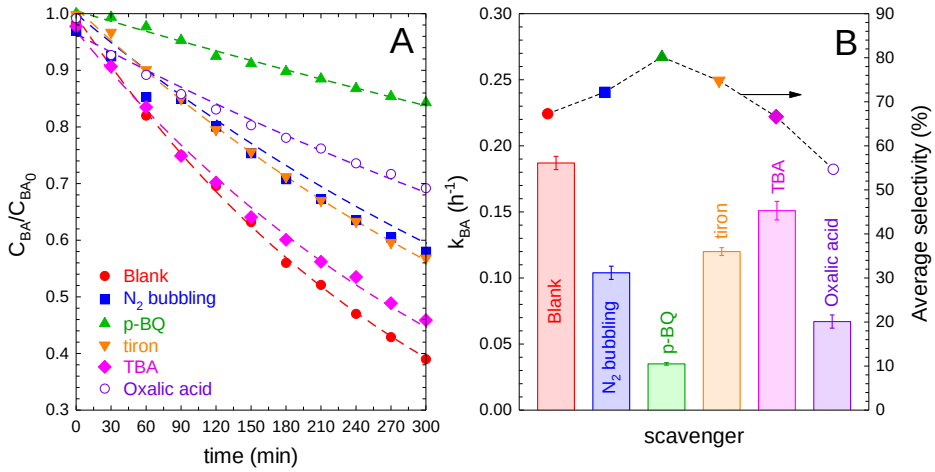

Fig. 4.8 *Photocatalytic production of benzaldehyde with NaBNC-1Ru in the presence of scavengers. Temporal normalized concentration of benzyl alcohol (A), pseudo-first order rate constant of BA depletion, and average BD selectivity (B). Experimental conditions: V=350 mL, T=20ºC, $C_{BA,0}$=0.5 mM; C_{CAT}=0.5 g L^{-1}; $C_{scavenger}$=1 mM (p-BQ and tiron) or 10 mM (TBA and oxalic acid); pH=9.5±0.5*

Considering the results obtained in the scavengers' studies and data obtained by XPS at low energies, a mechanism based on the bands' alignment is proposed (Fig. 4.9). As aforementioned, modification of CN with B did not display any substantial change in the bandgap value; however, a decrease from 2.6 eV (NaBCN) to 2.3 eV (NaBCN-1Ru) was observed with Ru incorporation. Fig. 4.9A depicts the XPS spectra at low energies for the evaluation of the minimum valence band energy of NaBCN (1.3 eV) and NaBCN-1Ru (1.9 eV). Obtained energy values are relative to the Fermi level of each material, however, may suggest a stabilization of the valence band with the deposition of Ru at small proportions on a well-defined CN-B active support. The deposition of Ru is expected to make the photogenerated holes possess higher redox potential (see Fig. 4.9B), supporting the evidence observed in the scavengers' tests, which displayed a higher impact on the oxidation of the alcohol.

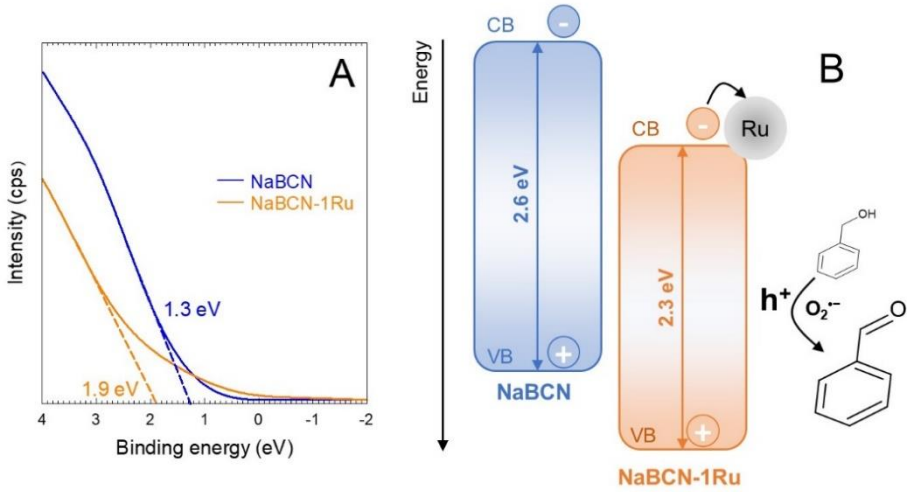

Fig. 4.9 *Determination of the valence band energy by XPS (A) and proposal of the relative band's alignment (B) of NaBCN and NaBCN-1Ru photocatalysts.*

4.4. CONCLUSIONS

The modification of the polymeric structure of graphitic carbon nitride results in an efficient strategy to tune the activity of the resulting semiconductor and the selectivity to the oxidation of benzyl alcohol to benzaldehyde in an aqueous solution. This works provides a one-step synthesis route for modification of the g-C_3N_4 structure with boron doping and Ru^0 deposition. The creation of defects on the graphitic structure via B modification enhanced the selectivity towards benzaldehyde due to the improved separation of the photogenerated charges as the photoluminescence response suggested. The deposition of Ru^0 considerably improved the degradation rate of the alcohol since it acts as an electron sink; however, the rise of Ru content rises the conversion unselectively, i.e. decreasing the selectivity of benzaldehyde. A metal proportion of around 1% reached a compromise between both effects. The photo-generated holes followed by the superoxide radical demonstrated to be the main reactive oxidant species involved in the oxidation process. The holes impacted to a higher extent in the selectivity of the process. The estimated valence band energies of the modified graphitic carbon nitride with B and Ru deposition suggest an increase in the redox energy for the valence band with ruthenium deposition, enlarging the oxidative potential of the photo-generated holes.

REFERENCES

1. Satrio, J.A.B.; Doraiswamy, L.K. Production of Benzaldehyde: A Case Study in a Possible Industrial Application of Phase-Transfer Catalysis. Chemical Engineering Journal 2001, 82, 43–56, doi:10.1016/S1385-8947(00)00351-X.
2. Ghahremani, M.; Ciriminna, R.; Pandarus, V.; Scurria, A.; La Parola, V.; Giordano, F.; Avellone, G.; Béland, F.; Karimi, B.; Pagliaro, M. Green and Direct Synthesis of Benzaldehyde and Benzyl Benzoate in One Pot. ACS Sustain Chem Eng 2018, 6, 15441–15446, doi:10.1021/ACSSUSCHEMENG.8B03893.
3. Akhundi, A.; Badiei, A.; Ziarani, G.M.; Habibi-Yangjeh, A.; Muñoz-Batista, M.J.; Luque, R. Graphitic Carbon Nitride-Based Photocatalysts: Toward Efficient Organic Transformation for Value-Added Chemicals Production. Molecular Catalysis 2020, 488, 110902, doi:10.1016/J.MCAT.2020.110902.
4. Loeb, S.K.; Álvarez, P.J.J.; Brame, J.A.; Cates, E.L.; Choi, W.; Crittenden, J.; Dionysiou, D.D.; Li, Q.; Li-Puma, G.; Quan, X.; et al. The Technology Horizon for Photocatalytic Water Treatment: Sunrise or Sunset? Environ Sci Technol 2019, 53, 2937–2947, doi:10.1021/acs.est.8b05041.
5. Zhao, Z.; Sun, Y.; Dong, F. Graphitic Carbon Nitride Based Nanocomposites: A Review. Nanoscale 2014, 7, 15–37, doi:10.1039/C4NR03008G.
6. Zhou, L.; Zhang, H.; Sun, H.; Liu, S.; Tade, M.O.; Wang, S.; Jin, W. Recent Advances in Non-Metal Modification of Graphitic Carbon Nitride for Photocatalysis: A Historic Review. Catal Sci Technol 2016, 6, 7002–7023, doi:10.1039/C6CY01195K.
7. Cerdan, K.; Ouyang, W.; Colmenares, J.C.; Muñoz-Batista, M.J.; Luque, R.; Balu, A.M. Facile Mechanochemical Modification of G-C3N4 for Selective Photo-Oxidation of Benzyl Alcohol. Chem Eng Sci 2019, 194, 78–84, doi:10.1016/J.CES.2018.04.001.
8. Lima, M.J.; Sampaio, M.J.; Silva, C.G.; Silva, A.M.T.; Faria, J.L. Magnetically Recoverable Fe3O4/g-C3N4 Composite for Photocatalytic Production of Benzaldehyde under UV-LED Radiation. Catal Today 2019, 328, 293–299, doi:10.1016/J.CATTOD.2018.11.018.
9. Wang, Y.; Wang, X.; Antonietti, M. Polymeric Graphitic Carbon Nitride as a Heterogeneous Organocatalyst: From Photochemistry to Multipurpose Catalysis to Sustainable Chemistry. Angewandte Chemie 2012, 51, 68–89, doi:10.1002/ANIE.201101182.

10. Marcì, G.; García-López, E.I.; Palmisano, L. Polymeric Carbon Nitride (C3N4) as Heterogeneous Photocatalyst for Selective Oxidation of Alcohols to Aldehydes. Catal Today 2018, 315, 126–137, doi:10.1016/J.CATTOD.2018.03.038.
11. Starukh, H.; Praus, P. Doping of Graphitic Carbon Nitride with Non-Metal Elements and Its Applications in Photocatalysis. Catalysts 2020, 10, 1119, doi:10.3390/CATAL10101119.
12. Jiang, L.; Yuan, X.; Pan, Y.; Liang, J.; Zeng, G.; Wu, Z.; Wang, H. Doping of Graphitic Carbon Nitride for Photocatalysis: A Reveiw. Appl Catal B 2017, 217, 388–406.
13. Quintana, M.A.; Solís, R.R.; Ángeles Martín-Lara, M.; Blázquez, G.; Mónica Calero, F.; Muñoz-Batista, M.J. Enhanced Boron Modified Graphitic Carbon Nitride for the Selective Photocatalytic Production of Benzaldehyde. Sep Purif Technol 2022, 298, 121613, doi:10.1016/J.SEPPUR.2022.121613.
14. Li, W.; Chu, X.S.; Wang, F.; Dang, Y.Y.; Liu, X.Y.; Wang, X.C.; Wang, C.Y. Enhanced Cocatalyst-Support Interaction and Promoted Electron Transfer of 3D Porous g-C3N4/GO-M (Au, Pd, Pt) Composite Catalysts for Hydrogen Evolution. Appl Catal B 2021, 288, 120034, doi:10.1016/J.APCATB.2021.120034.
15. Shimoyama, Y.; Koga, K.; Tabe, H.; Yamada, Y.; Kon, Y.; Hong, D. RuO2 Nanoparticle-Embedded Graphitic Carbon Nitride for Efficient Photocatalytic H2 Evolution. ACS Appl Nano Mater 2021, 4, 11700–11708, doi:10.1021/ACSANM.1C02301.
16. Mori, K.; Osaka, R.; Naka, K.; Tatsumi, D.; Yamashita, H. Ultra-Low Loading of Ru Clusters over Graphitic Carbon Nitride: A Drastic Enhancement in Photocatalytic Hydrogen Evolution Activity. ChemCatChem 2019, 11, 1963–1969, doi:10.1002/CCTC.201900073.
17. Yu, Z.; Li, Y.; Torres-Pinto, A.; LaGrow, A.P.; Diaconescu, V.M.; Simonelli, L.; Sampaio, M.J.; Bondarchuk, O.; Amorim, I.; Araujo, A.; et al. Single-Atom Ir and Ru Anchored on Graphitic Carbon Nitride for Efficient and Stable Electrocatalytic/Photocatalytic Hydrogen Evolution. Appl Catal B 2022, 310, 121318, doi:10.1016/J.APCATB.2022.121318.
18. Lima, M.J.; Tavares, P.B.; Silva, A.M.T.; Silva, C.G.; Faria, J.L. Selective Photocatalytic Oxidation of Benzyl Alcohol to Benzaldehyde by Using Metal-Loaded g-C3N4 Photocatalysts. Catal Today 2017, 287, 70–77, doi:10.1016/J.CATTOD.2016.11.023.

19. Cao, S.; Low, J.; Yu, J.; Jaroniec, M. Polymeric Photocatalysts Based on Graphitic Carbon Nitride. Advanced Materials 2015, 27, 2150–2176, doi:10.1002/ADMA.201500033.
20. Makuła, P.; Pacia, M.; Macyk, W. How to Correctly Determine the Band Gap Energy of Modified Semiconductor Photocatalysts Based on UV-Vis Spectra. Journal of Physical Chemistry Letters 2018, 9, 6814–6817.
21. Solís, R.R.; Quintana, M.A.; Martín-Lara, M.Á.; Pérez, A.; Calero, M.; Muñoz-Batista, M.J. Boosted Activity of G-C3N4/UiO-66-NH2 Heterostructures for the Photocatalytic Degradation of Contaminants in Water. Int J Mol Sci 2022, 23, 12871, doi:10.3390/IJMS232112871/S1.
22. Lee, J.; Kim, J.; Choi, W. Ferrioxalate-Polyoxometalate System as a New Chemical Actinometer. Environ Sci Technol 2007, 41, 5433–5438, doi:10.1021/ES070474Z.
23. Serpone, N. Relative Photonic Efficiencies and Quantum Yields in Heterogeneous Photocatalysis. J Photochem Photobiol A Chem 1997, 104, 1–12, doi:10.1016/S1010-6030(96)04538-8.
24. Li Puma, G.; Brucato, A. Dimensionless Analysis of Slurry Photocatalytic Reactors Using Two-Flux and Six-Flux Radiation Absorption–Scattering Models. Catal Today 2007, 122, 78–90, doi:10.1016/J.CATTOD.2007.01.027.
25. Alfano, O.M.; Bahnemann, D.; Cassano, A.E.; Dillert, R.; Goslich, R. Photocatalysis in Water Environments Using Artificial and Solar Light. Catal Today 2000, 58, 199–230, doi:10.1016/S0920-5861(00)00252-2.
26. Muñoz-Batista, M.J.; Kubacka, A.; Fontelles-Carceller, O.; Tudela, D.; Fernández-García, M. Surface CuO, Bi2O3, and CeO2 Species Supported in TiO2-Anatase: Study of Interface Effects in Toluene Photodegradation Quantum Efficiency. ACS Appl Mater Interfaces 2016, 8, 13934–13945, doi:10.1021/ACSAMI.6B03081.
27. Fina, F.; Callear, S.K.; Carins, G.M.; Irvine, J.T.S. Structural Investigation of Graphitic Carbon Nitride via XRD and Neutron Diffraction. Chemistry of Materials 2015, 27, 2612–2618, doi:10.1021/ACS.CHEMMATER.5B00411.
28. Wang, X.; Liu, B.; Xiao, X.; Wang, S.; Huang, W. Boron Dopant Simultaneously Achieving Nanostructure Control and Electronic Structure Tuning of Graphitic Carbon Nitride with Enhanced Photocatalytic Activity. J Mater Chem C Mater 2021, 9, 14876–14884, doi:10.1039/D1TC04142H.

29. Yan, Y.; Yang, Q.; Shang, Q.; Ai, J.; Yang, X.; Wang, D.; Liao, G. Ru Doped Graphitic Carbon Nitride Mediated Peroxymonosulfate Activation for Diclofenac Degradation via Singlet Oxygen. Chemical Engineering Journal 2022, 430, 133174, doi:10.1016/J.CEJ.2021.133174.
30. Rajkumar, C.; Kim, H. Interface Engineering of Ruthenium-Supported Sulfur-Doped Graphitic Carbon Nitride for Ultrasensitive Electrochemical Determination of Riboflavin. J Taiwan Inst Chem Eng 2022, 138, 104470, doi:10.1016/J.JTICE.2022.104470.
31. Sharma, P.; Sasson, Y. A Photoactive Catalyst Ru-g-C3N4 for Hydrogen Transfer Reaction of Aldehydes and Ketones. Green Chemistry 2017, 19, 844–852, doi:10.1039/C6GC02949C.
32. Ma, Z.; Zhao, S.; Xiong, X.; Hu, B.; Song, C. Effect of Graphitic Carbon Nitride on the Electronic and Catalytic Properties of Ru Nanoparticles for Ammonia Synthesis. Catal Letters 2016, 146, 2324–2329, doi:10.1007/s10562-016-1862-y.
33. Yan, S.C.; Li, Z.S.; Zou, Z.G. Photodegradation Performance of G-C3N4 Fabricated by Directly Heating Melamine. Langmuir 2009, 25, 10397–10401, doi:10.1021/LA900923Z.
34. Bojdys, M.J.; Müller, J.O.; Antonietti, M.; Thomas, A. Ionothermal Synthesis of Crystalline, Condensed, Graphitic Carbon Nitride. Chemistry – A European Journal 2008, 14, 8177–8182, doi:10.1002/CHEM.200800190.
35. Zhao, D.; Dong, C.-L.; Wang, B.; Chen, C.; Huang, Y.-C.; Diao, Z.; Li, S.; Guo, L.; Shen, S.; Zhao, D.; et al. Synergy of Dopants and Defects in Graphitic Carbon Nitride with Exceptionally Modulated Band Structures for Efficient Photocatalytic Oxygen Evolution. Advanced Materials 2019, 31, 1903545, doi:10.1002/ADMA.201903545.
36. Kim, M.; Hwang, S.; Yu, J.S. Novel Ordered Nanoporous Graphitic C3N4 as a Support for Pt–Ru Anode Catalyst in Direct Methanol Fuel Cell. J Mater Chem 2007, 17, 1656–1659, doi:10.1039/B702213A.
37. Sunasee, S.; Leong, K.H.; Wong, K.T.; Lee, G.; Pichiah, S.; Nah, I.W.; Jeon, B.H.; Yoon, Y.; Jang, M. Sonophotocatalytic Degradation of Bisphenol A and Its Intermediates with Graphitic Carbon Nitride. Environmental Science and Pollution Research 2019, 26, 1082–1093, doi:10.1007/S11356-017-8729-7.
38. Sing, K.S.W.; Williams, R.T. Physisorption Hysteresis Loops and the Characterization of Nanoporous Materials. Adsorption Science

and Technology 2016, 22, 773–782, doi:10.1260/0263617053499032.

39. Sing, K.S.W.; Everett, D.H.; Haul, R.A.W.; Moscou, L.; Pierotti, R.A.; Rouquerol, J.; Siemieniewska, T. Reporting Physisorption Data for Gas/Solid Systems with Special Reference to the Determination of Surface Area and Porosity. Pure and Applied Chemistry 1985, 57, 603–619, doi:10.1351/PAC198557040603.
40. Thommes, M.; Kaneko, K.; Neimark, A. V.; Olivier, J.P.; Rodríguez-Reinoso, F.; Rouquerol, J.; Sing, K.S.W.W. Physisorption of Gases, with Special Reference to the Evaluation of Surface Area and Pore Size Distribution (IUPAC Technical Report). Pure and Applied Chemistry 2015, 87, 1051–1069.
41. Babu, P.; Mohanty, S.; Naik, B.; Parida, K. Synergistic Effects of Boron and Sulfur Co-Doping into Graphitic Carbon Nitride Framework for Enhanced Photocatalytic Activity in Visible Light Driven Hydrogen Generation. Applied Energy Materials 2018, 1, 5936–5947, doi:10.1021/acsaem.8b00956.
42. Cai, H.; Han, D.; Wang, X.; Cheng, X.; Liu, J.; Jia, L.; Ding, Y.; Liu, S.; Fan, X. High Specific Surface Area Defective G-C3N4 Nanosheets with Enhanced Photocatalytic Activity Prepared by Using Glyoxylic Acid Mediated Melamine. Mater Chem Phys 2020, 256, 123755, doi:10.1016/J.MATCHEMPHYS.2020.123755.
43. Wen, Y.; Qu, D.; An, L.; Gao, X.; Jiang, W.; Wu, D.; Yang, D.; Sun, Z. Defective G-C3N4 Prepared by the NaBH4 Reduction for High-Performance H2 Production. ACS Sustain Chem Eng 2019, 7, 2343–2349, doi:10.1021/ACSSUSCHEMENG.8B05124.
44. Morgan, D.J. Resolving Ruthenium: XPS Studies of Common Ruthenium Materials. Surface and Interface Analysis 2015, 47, 1072–1079, doi:10.1002/SIA.5852.
45. Yang, Q.; Wang, T.; Zheng, Z.; Xing, B.; Li, C.; Li, B. Constructing Interfacial Active Sites in Ru/g-C3N4−x Photocatalyst for Boosting H2 Evolution Coupled with Selective Benzyl-Alcohol Oxidation. Appl Catal B 2022, 315, 121575, doi:10.1016/J.APCATB.2022.121575.
46. Zhang, M.; Chen, J.; Li, H.; Cai, P.; Li, Y.; Wen, Z. Ru-RuO2/CNT Hybrids as High-Activity PH-Universal Electrocatalysts for Water Splitting within 0.73 V in an Asymmetric-Electrolyte Electrolyzer. Nano Energy 2019, 61, 576–583, doi:10.1016/J.NANOEN.2019.04.050.
47. Li, W.; Wei, Z.; Wang, B.; Liu, Y.; Song, H.; Tang, Z.; Yang, B.; Lu, S. Carbon Quantum Dots Enhanced the Activity for the Hydrogen

Evolution Reaction in Ruthenium-Based Electrocatalysts. Mater Chem Front 2019, 4, 277–284, doi:10.1039/C9QM00618D.

48. Xu, H.; Wu, Z.; Wang, Y.; Lin, C. Enhanced Visible-Light Photocatalytic Activity from Graphene-like Boron Nitride Anchored on Graphitic Carbon Nitride Sheets. J Mater Sci 2017, 52, 9477–9490, doi:10.1007/S10853-017-1167-6.
49. Caudillo-Flores, U.; Rodríguez-Padrón, D.; Muñoz-Batista, M.J.; Kubacka, A.; Luque, R.; Fernández-García, M. Facile Synthesis of B/g-C3N4 Composite Materials for the Continuous-Flow Selective Photo-Production of Acetone. Green Chemistry 2020, 22, 4975–4984, doi:10.1039/D0GC01326A.
50. Dinescu, M.; Perrone, A.; Caricato, A.P.; Mirenghi, L.; Gerardi, C.; Ghica, C.; Frunza, L. Boron Carbon Nitride Films Deposited by Sequential Pulses Laser Deposition. Appl Surf Sci 1998, 127–129, 692–696, doi:10.1016/S0169-4332(97)00727-7.
51. Watanabe, M.O.; Itoh, S.; Mizushima, K.; Sasaki, T. Bonding Characterization of BC2N Thin Films. Appl Phys Lett 1998, 68, 2962, doi:10.1063/1.116369.
52. You, R.; Dou, H.; Chen, L.; Zheng, S.; Zhang, Y. Graphitic Carbon Nitride with S and O Codoping for Enhanced Visible Light Photocatalytic Performance. RSC Adv 2017, 7, 15842–15850, doi:10.1039/C7RA01036B.
53. Rodríguez, E.M.; Márquez, G.; Tena, M.; Álvarez, P.M.; Beltrán, F.J. Determination of Main Species Involved in the First Steps of TiO2 Photocatalytic Degradation of Organics with the Use of Scavengers: The Case of Ofloxacin. Appl Catal B 2015, 178, 44–53, doi:10.1016/j.apcatb.2014.11.002.
54. Pelaez, M.; Falaras, P.; Likodimos, V.; O'Shea, K.; de la Cruz, A.A.; Dunlop, P.S.M.; Byrne, J.A.; Dionysiou, D.D. Use of Selected Scavengers for the Determination of NF-TiO2 Reactive Oxygen Species during the Degradation of Microcystin-LR under Visible Light Irradiation. J Mol Catal A Chem 2016, 425, 183–189, doi:10.1016/j.molcata.2016.09.035.
55. Bielski, B.H.J.; Cabelli, D.E.; Arudi, R.L.; Ross, A.B. Reactivity of HO2/O−2 Radicals in Aqueous Solution. J Phys Chem Ref Data 1985, 14, 1041–1100, doi:10.1063/1.555739.
56. Nien Schuchmann, M.; Bothe, E.; von Sonntag, J.; von Sonntag, C. Reaction of OH Radicals with Benzoquinone in Aqueous Solutions. A Pulse Radiolysis Study. Journal of the Chemical Society, Perkin Transactions 2 1998, 791–796, doi:10.1039/A708772A.

57. Schneider, J.T.; Firak, D.S.; Ribeiro, R.R.; Peralta-Zamora, P. Use of Scavenger Agents in Heterogeneous Photocatalysis: Truths, Half-Truths, and Misinterpretations. Physical Chemistry Chemical Physics 2020, 22, 15723–15733, doi:10.1039/d0cp02411b.
58. Giannakoudakis, D.A.; Qayyum, A.; Barczak, M.; Colmenares-Quintero, R.F.; Borowski, P.; Triantafyllidis, K.; Colmenares, J.C. Mechanistic and Kinetic Studies of Benzyl Alcohol Photocatalytic Oxidation by Nanostructured Titanium (Hydro)Oxides: Do We Know the Entire Story? Appl Catal B 2023, 320, 121939, doi:10.1016/J.APCATB.2022.121939.
59. Greenstock, C.L.; Miller, R.W. The Oxidation of Tiron by Superoxide Anion. Kinetics of the Reaction in Aqueous Solution and in Chloroplasts. Biochim Biophys Acta 1975, 396, 11–16, doi:10.1016/0005-2728(75)90184-X.
60. Bors, W.; Saran, M.; Michel, C. Pulse-Radiolytic Investigations of Catechols and Catecholamines II. Reactions of Tiron with Oxygen Radical Species. BBA - General Subjects 1979, 582, 537–542, doi:10.1016/0304-4165(79)90145-4.
61. Alam, M.S.; Rao, B.S.M.; Janata, E. ·OH Reactions with Aliphatic Alcohols: Evaluation of Kinetics by Direct Optical Absorption Measurement. A Pulse Radiolysis Study. Radiation Physics and Chemistry 2003, 67, 723–728, doi:10.1016/S0969-806X(03)00310-4.
62. Shah, B.R.; Patel, U.D. Mechanistic Aspects of Photocatalytic Degradation of Lindane by TiO2 in the Presence of Oxalic Acid and EDTA as Hole-Scavengers. J Environ Chem Eng 2021, 9, 105458, doi:10.1016/J.JECE.2021.105458.
63. Ershov, B.G.; Janata, E.; Alam, M.S.; Gordeev, A. V. A Pulse Radiolysis Study of the Reactions of the Hydrated Electron and Hydroxyl Radical with the Oxalate Ion in Neutral Aqueous Solution. High Energy Chemistry 2008, 42, 1–6, doi:10.1134/s0018143908010013.
64. Zhao, L.; Zhang, B.; Xiao, X.; Gu, F.L.; Zhang, R.Q. Roles of the Active Species Involved in the Photocatalytic Oxidation of Benzyl Alcohol into Benzaldehyde on TiO2 under UV Light: Experimental and DFT Studies. J Mol Catal A Chem 2016, 420, 82–87, doi:10.1016/J.MOLCATA.2016.03.012.

CHAPTER 5. PAPER THREE

Towards the photocatalytic production of cinnamaldehyde with phosphorous-tailored graphitic-like carbon nitride

Applied Catalysis A: General 674 (2024) 119607
https://doi.org/10.1016/j.apcata.2024.119607
María Alejandra Quintana, Alba Picón, María Ángeles Martín-Lara, Mónica Calero, Mario J. Muñoz-Batista, Rafael R. Solís

Abstract

Photocatalysis has emerged as an environmentally friendly technology to develop selective reactions such as the oxidation of alcohol to aldehydes. Graphitic carbon nitride (CN) is a metal-free polymeric structure easily photoactivated under radiation. This work focuses on the enhancement of the photocatalytic activity of bare CN by doping it with phosphorous (P-CN) under a one-pot synthesis basis. Different doping levels of P (2-12 wt.) have been explored and the samples were fully characterized by XRD, FTIR, N_2 physisorption, elemental analysis, XPS, DRS-UV-visible, and photoluminescence. A better activity and enhanced selectivity were observed in the P-CN samples if compared to the undoped CN in the oxidation of cinnamyl alcohol to cinnamaldehyde in aqueous solution. The presence of P was demonstrated to contribute to a better delocalization of photo-generated charges. Moreover, the reactivity and selectivity of the CN and P-CN samples were analyzed in water-acetonitrile mixtures, appreciating a better selectivity in the presence of acetonitrile to the detriment of the conversion of the cinnamyl alcohol. The photocatalytic oxidation mechanism over P-CN in aqueous media has been tentatively proposed based on the influence of the reactive oxidative species generated in the process by chemical scavenger tests. They suggested the contribution of superoxide radicals with more selectivity than the photo-generated holes, the second reactive species of importance in the overall oxidation scheme. The contribution of hydroxyl radicals was discharged since its presence was negligible in the probe tests based on the formation of 2-hydroxy-terephthalic acid.

Keywords: graphitic carbon nitride; phosphorous; photocatalysis; cinnamaldehyde

5.1. INTRODUCTION

The oxidation of alcohols to aldehydes is one of the most important reactions in organic chemistry oriented to the high-scale production of added-value organics, as happens in the pharmaceutical industry. Cinnamaldehyde is one example of these substances, widely used in cosmetics [1], as a food additive [2,3] taking advantage of its antibacterial and antifungal activity [4], or as an ingredient of natural formulas for insecticides [5]. The synthesis of cinnamaldehyde at an industrial scale has been successfully carried out under catalytic oxidation with O_2 with noble metals such as Pd [6] or Pt [7]. Diverse techniques are subsequently implemented to purify the components of the mixture of the reaction, also carried out when obtaining form essential oil of cinnamon [8]. Among the available techniques, the most popular include hydrodistillation [9], steam distillation [10], microwave-assisted hydrodistillation [11], sonodistillation [12], or column chromatographic techniques [13].

Recently, the oxidation of alcohols to aldehydes through photocatalysis has emerged as an environmentally friendly alternative to traditional routes due to the mild pressure and temperature conditions [14–16]. Moreover, photocatalysis can be triggered with solar radiation which justifies the sustainability of the radiation consumption. The selectivity of the photocatalytic oxidation of alcohols to aldehydes has been reported to reach the highest values in the presence of an inert organic solvent, acetonitrile being the most popular [16]. Nonetheless, the disposal of organic solvents is an issue of major concern from an environmental point of view. The development of these reactions in water may solve this problem; however, the presence of water can trigger the production of unselective hydroxyl radicals, contributing to poor selectivity control [17,18]. This drawback can be addressed with a proper catalyst design. In this sense, graphitic carbon nitride (g-C_3N_4) has shown a competitive bandgap alignment for this purpose since the energy of the conduction band enables the formation of photogenerated electrons with enough energy to release the reduction of adsorbent O_2 molecules to superoxide radical. However, due to the energetic value of the valence band, the potential of the photogenerated holes in the valence band is not enough to oxidize H_2O molecules to release the formation of hydroxyl radicals [14]. The use of g-C_3N_4 has been

demonstrated as a sustainable photocatalyst for the photoproduction of added-value chemicals [19]. The doping of the polymeric structure of g-C_3N_4 with non-metal elements has been used as an efficient strategy to boost the activity and/or modulate the selectivity of certain reactions [20,21]. Among the different elements used as dopant agents, the effects of phosphorous doping in g-C_3N_4 applied to the photoproduction of organic substances are the least researched to date. The doping of g-C_3N_4 with $NH_4(H_2PO_4)$ has been reported as efficient in raising the selectivity to the detriment of the precursor conversion during the photoproduction of aldehydes from the oxidation of benzyl alcohol, 4-methoxy benzyl alcohol, or piperonyl alcohol [22]. In other work, g-C_3N_4 was doped with H_3PO_4, and Pd nanoparticles were also deposited on the surface. Both modifications enabled to reach a high yield of aldehydes production from their benzyl alcohol derivatives, using acetonitrile as solvent and H_2O_2 as an oxidant agent [23].

This work reports the study of P doping onto g-C_3N_4, using sodium polyphosphate as a dopant agent, for the photocatalytic production of cinnamaldehyde in an aqueous solution. Different P doping dosages have been investigated within 2-12% (wt.). The crystalline, morphological, textural, and optical properties were characterized by diverse techniques such as XRD, FTIR, N_2 physisorption, XPS, elemental analysis, DRS-UV-visible, and photoluminescence. The behavior in terms of conversion and selectivity during the oxidation of cinnamyl alcohol to cinnamaldehyde has been investigated in an aqueous solution. The undoped and the P-doped samples with the best selectivity were selected to investigate the effect of acetonitrile as the solvent, in acetonitrile-water mixtures. Finally, the tentative mechanism of oxidation species involved in the process was assessed by using chemical scavengers to assess the effects of superoxide radical (N_2, p-benzoquinone), hydroxyl radical (tertbutyl alcohol), and photogenerated holes (oxalic acid).

5.2. EXPERIMENTAL SECTION

5.2.1. Materials and synthesis of the P-CN samples

All the chemicals used were analytical grade, purchased from Merck®, and used as received. For liquid chromatographic analyses, HPLC-grade acetonitrile was used as a mobile phase. Ultrapure water

(18.2 MΩ cm) from a Direct-Q®-UV device (Millipore®) was used for the preparation of all the solutions.

The bare graphitic carbon nitride (CN) was prepared by thermal polymerization of melamine (>99%), under an N_2 atmosphere (100 mL min^{-1}) at 550°C (heating rate, 10°C min^{-1}) for 1 h. The P-doping of graphitic carbon nitride samples (P-CN) was carried out in a second post-treatment step [24], as illustrated in Fig. 5.1 A certain amount of P (2-12% wt. concerning the CN quantity) was added as sodium polyphosphate (65-70% P_2O_5 basis) to 20 mL of ultrapure water and kept under stirring for 2 hours. The suspension was thereafter subjected to evaporation by heating at 100°C until the complete removal of water. The powder was next treated thermally under N_2 atmosphere (100 mL min^{-1}) at 550°C (heating rate, 10°C min^{-1}) during 2 h. The resulting brownish powder was ground in a mortar. The samples were labeled as P-CN-X% where X means the doping P percentage (wt.).

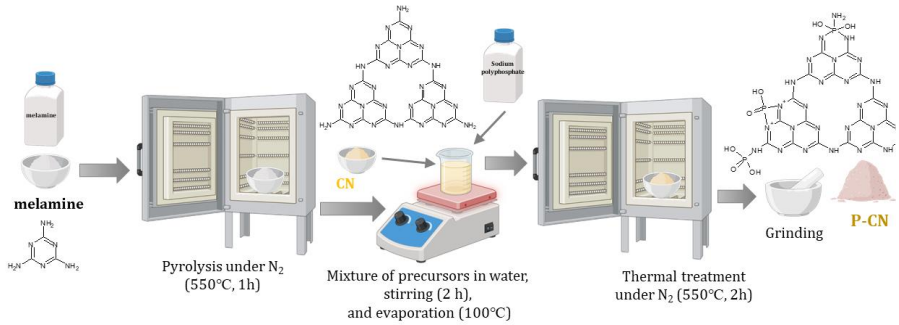

Fig. 5.1*Schematic representation of the synthesis steps of CN and P-CN samples.*

5.2.2. Characterization of the P-CN samples

The crystallinity was analyzed by X-ray diffraction in a Bruker D8 Discover device working with a Pilatus 3R 100K-A detector using Cu Kα radiation (1.5406 Å). The diffractograms were registered within a 2θ range of 5–65° at a rate of 0.034° min^{-1}. The freeware QualX® [25] and the Crystal Open Database (COD) were used for the processing of the diffractograms. The crystallite size was estimated by Scherrer's equation from the most intense peak and the interlayer spacing was calculated from the maximum of the (002) peak. The relation $L_{crystal}/d_{layer}$ was used as a rough approximation of the number of layers estimation [26].

The structural properties were studied by Fourier Transform InfraRed (FTIR) spectroscopy equipped with Attenuated Total Reflectance. The FTIR spectra were recorded in Perkin-Elmer equipment, model Spectrum65, within 400–4000 cm^{-1}.

The elemental composition was analyzed in a TrueSpec® Micro CHNS analyzer from Leco instruments. The chemistry of the surface was analyzed by X-ray Photoelectron Spectroscopy (XPS) in a Kratos AXIS UltraDLD device equipped with an X-ray source from Al Kα. The registered spectra were corrected to C_{1s} peak of adventitious carbon as referenced, ascribed to 284.6 eV. The treatment of the data and the deconvolution of the spectra were carried out with the software XPSpeak 4.1®, applying a Shirley background correction for the baseline definition. The chemical environment of C and P was further studied by solid state Magic Angle Spinning (MAS) Nuclear Magnetic Resonance (NMR) in a Bruker Advance NMR spectrometer of 500 MHz equipped with a 4 mm Cross-Polarization (CP) MAS detector. In the case of ^{13}C spectra, CP-MAS experiments were conducted at 10 kHz. For ^{31}P the MAS, tests were carried out at 12 kHz.

The morphology and element distribution in the nanoparticles were studied by High Resolution Scanning Transmission Electron Microscopy (HR-STEM) imaging in a Thermo Scientific™ Talos™ F200X (200 kV) equipped with High-angle annular dark-field imaging (HAADF) detector and Energy Dispersive X-Ray spectroscopy (EDX) microanalysis.

The optical absorption and reflection of the samples were studied by Diffuse Reflectance Spectroscopy (DRS) in the UV–visible region using a Varian Cary 5E spectrophotometer. The bandgap value was estimated from the Kubelka-Munk Function, e.g. $F(R_\infty)$, applying the Tauc plot method assuming indirect electron transitions in the semiconductors [27,28]. The photoluminescence (PL) technique was used for the analysis of the recombination rate of the samples. The PL spectra were obtained in a Varian Cary fluorescence spectrometer under an excitation wavelength of 365 nm (slit 2.5 nm) and monitored the emission signal within 400-600 nm (slit 2.5 nm).

5.2.3. Photocatalytic tests of cinnamaldehyde production

The photocatalytic activity of the prepared samples was evaluated in the selective oxidation of cinnamyl alcohol (CA) to cinnamaldehyde

(CD). The tests were carried out in a photoreactor equipped with two UVA lamps emitting at 365 nm (9 W each). The lamps were placed in the inner space of an annular photoreactor in whose inner space was circulating the aqueous solution with the suspended catalyst. An auxiliary jacketed tank contained the solution of cinnamyl alcohol with the catalyst and was pumped and recirculated to the photoreactor. The temperature was controlled to 20°C by cooling with water in the jacketed space of the auxiliary tank. A detailed scheme of the setup is available in previous work [29]. Alternatively, lamps simulating daylight radiation were used to test the activity of the photocatalyst in the visible region (Philips). The spectrum was characterized with the help of a BLACK-Comet UV–visible spectroradiometer (StellarNet Inc., Florida, USA). Air was bubbled in the auxiliary tank to ensure O_2 saturation. The photocatalytic reaction started with the loading of 350 mL of CA 1 mM to the auxiliary tank and the catalyst at a dose of 0.5 g L^{-1} until a homogeneous slurry was obtained which was pumped into the annular space of the photoreactor. Before the irradiation, a 30-minute adsorption step was carried out in the darkness. Then, the laps were switched on and samples were carried out regularly. The photocatalyst was removed by syringe filters (Millex PVDF, 0.45 µm).

The concentration of cinnamyl alcohol and cinnamaldehyde was determined by High-Pressure Liquid Chromatography (HPLC) coupled with photodiode array detection (PDA). An Alliance e2695 HPLC system from Waters™, coupled to a 2998 photodiode array detector. The stationary phase used for the separation of CA and CD was a Zorbax Bonus-RP column (5 µm, 4.6x150 mm). The mobile phase, pumped at 1 mL min^{-1} under the isocratic mode, consists of a mixture of 40% (v/v) acetonitrile and 60% (v/v) ultrapure water acidified with 0.1% (v/v) of trifluoroacetic acid. The injection volume was 50 µL. The quantification was carried out at 240 nm for CA and 331 for CD.

The temporal evolution of CA depletion was fitted to a pseudo-first order kinetics, and the observed constant (k_{CA}) was used as a mere comparison tool among the prepared catalysts. The selectivity towards cinnamaldehyde was calculated from the CD and CA profiles, and an average value (S_{CD}) during the whole period tested was calculated. The quantum efficiency (Q_E) of CA photo-degradation was estimated, following the IUPAC's recommendations [30–32] which defines the Q_E as the ratio of the number of molecules reacting through the reaction

rate ($r_{CA,0}$), by the photon absorption rate (LVRPA, $e^{\alpha,v}$), i.e. the number of the photons interacting with the catalyst [33]:

$$Q_E = \frac{r_{CA_0}(\text{mol m}^{-3}\ \text{s}^{-1})}{e^{\alpha,v}(\text{Einstein m}^{-3}\ \text{s}^{-1})} \quad (1)$$

where $r_{CA,0}$ was estimated from the pseudo-first order kinetics ($r_{CA,0}=k_{CA}\cdot C_{CA,0}$). The determination of the photon absorption rate ($e^{\alpha,v}$), and the radiative transfer equation (RTE) was solved considering the geometry of the used photoreactor [29]. The optical properties were determined by the DRS-UV-visible of the catalytic suspensions. Detailed descriptions of the mathematical procedure for both optical properties and photon rate estimations are provided in previous works [29,34]. Fig. 5.2 provides the LVRPA profiles for the different P-CN samples and the undoped CN reference.

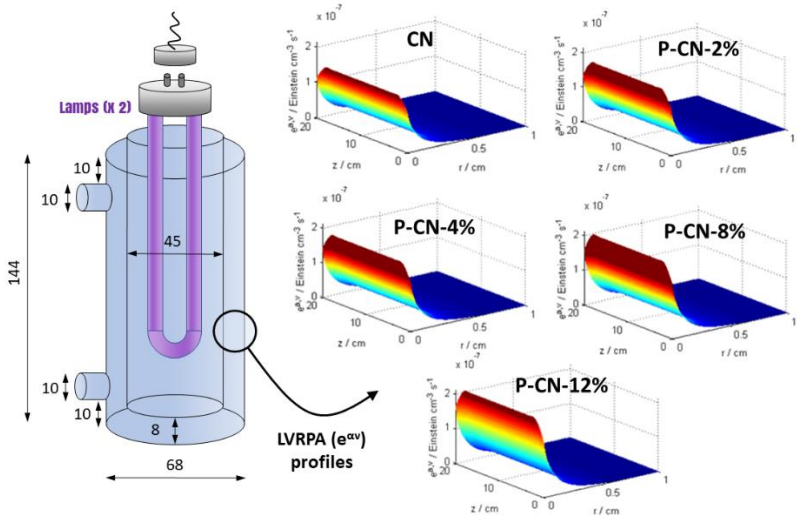

Fig. 5.2 *Local Volume Rate of Photon Absorption (LVRPA, $e^{\alpha,v}$) in the annular space of the photoreactor (left image, dimensions in mm) for the different P-CN samples.*

The behavior under visible radiation was conducted using a daylight simulated radiation with a commercial lamp (Sylvania® F6W/T5/54-765, emitting radiation >400nm, 6W) in a modified reaction system in which the lamp was inserted in a tubular photoreactor, see details in a previous work [34].

The contribution of the oxidative species involved in the oxidation of cinnamyl alcohol during the photocatalytic process was studied by the addition of chemical scavengers [35–37]. The role played by superoxide radical was evaluated by adding p-benzoquinone (p-BZQ, 1 mM), disodium 4,5-dihydroxy-1,3-benzenedisulfonate (tiron, 1 mM) or

bubbling N_2, the contribution of hydroxyl radicals by adding tert-butyl alcohol (TBA, 10 mM), the role played by the photo-generated holes was suppressed under the presence of oxalic acid (10 mM) or ethylenediaminetetraacetic acid (EDTA, 1 mM), and the influence of single oxygen was assessed by adding L-histidine (1 mM). These assays were conducted following the same procedure described before, but by adding the scavenger to the solution the pH was adjusted to the value of the blank test under the addition NaOH and/or HCl solutions 1M. The role played by the $HO^{\bullet}$ was additionally assessed by an indirect probe method based on terephthalic acid (TPA) [38,39]. Non-fluorescent terephthalic acid traps $HO^{\bullet}$ releasing the formation of the fluorescent 2-hydroxy-terephthalic acid (2-HO-TPA), which can be monitored over time as an indirect indicator of the $HO^{\bullet}$ present in the solution. Two tests with 2-HO-TPA (1 mM) in the presence and absence of cinnamyl alcohol were carried out and compared [40]. The analysis of 2-HO-TPA was conducted in a Varian Cary fluorescence spectrometer with an excitation wavelength of 315 nm (slit 2.5 nm) and the emission spectra recorded within 360-600 nm (slit 2.5 nm), whose maximum peak was located at 420 nm. The peak area was correlated with the concentration of the standard 2-HO-TPA solution within 0.5 and 5 μM. The limit of detection of 2-HO-TPA was estimated at 0.21 mM.

The transformation products during the photocatalytic oxidation of cinnamyl alcohol with P-CN were identified by liquid chromatography coupled to electrospray ionization under positive mode and mass spectrometry detection with a quadrupole time-of-flight, LC-ESI(+)-QTOF. The chromatographic separation was carried out in an ultra-high-pressure Acquity UPLC, H Class of Waters™, equipped with PDA detection. The ionization was carried out in a Zspray™ from Waters and the high-resolution mass spectrometry in a QTOF Triwave® Waters™, Synapt G2 model. The acquisition conditions were as follows: 3500 V capillary voltage, collision energy, X eV, m/z range from 50 to 1000. The identification of the transformation products was carried out based on MS spectra of precursor using the software MassLynx.

5.3. RESULTS AND DISCUSSION

5.3.1. Characterization of the P-CN samples

Fig. 5.3 depicts the structural modifications suffered by the graphitic carbon nitride sample before and after doping with sodium polyphosphate. Fig. 5.3A depicts the XRD patterns of bare CN and P-doped samples at two P loadings. The graphitic carbon nitride structure reports two crystalline peaks. The condensation of the precursor, i.e. melamine, conducts the formation of tris-s-triazine units distributed in plates of a certain number of layers [41,42]. As a consequence, a main and intensive peak located at 27° is described, corresponding to the (002) plane which appears due to the interplanar aromatic layers from π-π* interactions of the heptazine rings [43]. The polymerization temperature is linked to the sharpness of this peak and, the number of layers, within 22-31 at condensation temperatures of 500 and 600 °C, respectively, under air atmosphere [44]. A secondary peak, barely defined, placed at ca. 13° is defined by the (100) plane, a consequence of the intralayer spacing of the heptazine rings [45].

The modification of the g-C_3N_4 structure leads to considerable modification of the (002) peak, as a consequence of the alteration of the number of layers attached to the structure. For that reason, the decrease of the (002) peak is frequently analyzed as the degree of modification of the layered structure [46]. Thus, doping with a low P dose, i.e. P-CN-4%, depicts a decrease of the (002) peak, suggesting a considerable modification of the layered interactions, probably due to the incorporation of phosphate groups. Some previous works have reported a migration of the (002) peak to lower values, suggesting the incorporation of phosphate groups into the interlayers of the graphitic carbon structure, following a sandwich structure [47]. However, probably due to the post-treatment doping scheme followed in this work, it was not the case. The location of (002) of CN and P-CN-4% was roughly the same, around 27.4°, which provides evidence of a lack of modification of the layer spacing, discharging the incorporation of P between layers since the interlayer space slightly decreased (see Table 5.1). Accordingly, P is expected to be incorporated in the external faces of the plates or the heptazine rings. A further rise of P amount destroyed the layered nature of CN, as depicted for P-CN-12%, defining a crystalline structure of phosphate-based nitrogen organic compounds

that were not possible to identify due to the complexity of plausible generated species.

The doping with phosphate also led to considerable changes in the FTIR spectra as displayed in Fig. 5.3B. The absorption characteristics of P-CN samples are similar to those of CN, suggesting that the structure of g-C_3N_4 has not been changed after P doping, at least at P doses below X%. At high P doping, some changes in the fingerprint of FTIR spectra are envisaged. A wide band located within 3000-3300 cm^{-1} due to the vibration of terminal N–H and O–H stretching, which can be associated with the primary amine (-NH_2) and water molecules adsorbed on the surface of the material [48], is defined in the undoped CN sample. The increase in P dose led to a considerable decrease in this band, suggesting that P incorporation affected the terminal -NH_x groups. The aromatic tri-s-triazine rings lead to different peaks. Thus, the secondary nitrogen (N_{2C}) and tertiary nitrogen (N_{3C}) were conducted to well-defined peaks located at 1225 and 1312 cm^{-1}, respectively [49]. Moreover, the peaks located at 1391, 1450, 1537, and 1622 cm^{-1} can be attributed to the aromatic C-N vibration [42,50,51]. A strong peak at 811 cm^{-1} appears due to the out-plane vibration of the heptazine rings [49]. The presence of P led to the decrease and definition of the above-mentioned peaks of the bare CN sample. Significantly, the P doping contributed to an exfoliation effect of graphitic layers, corroborated by a considerable decrease in the out-of-plane vibration peak at 811 cm^{-1} [52]. When doping with over 8% of P, some new peaks appeared as a consequence of the significant amount of P in the structure. At 1271 cm^{-1} appears a peak that can be attributed to the stretching vibration mode of the P=O bond [53]. A plausible bonding as P=N was not reflected in the FTIR spectra, as no peaks centered at around 1336 and 1430 cm^{-1} were observed [53]. Additionally, the peak detected at 1094 cm^{-1} could be interpreted as the P^{+}-O- vibration in phosphate esters, in polyphosphate chain P-O-P [54,55]. The N-P vibration usually conducts to an FTIR peak centered at 700 cm^{-1} [54,56,57] which is consistent with the peak located at 701 cm^{-1} registered in this work at high P dosages. In brief, the above analysis suggests that P was successfully introduced in the g-C_3N_4 structure without changing the original framework at low doping doses, contributing just to an exfoliation effect and a plausible bonding of P groups to the N atoms.

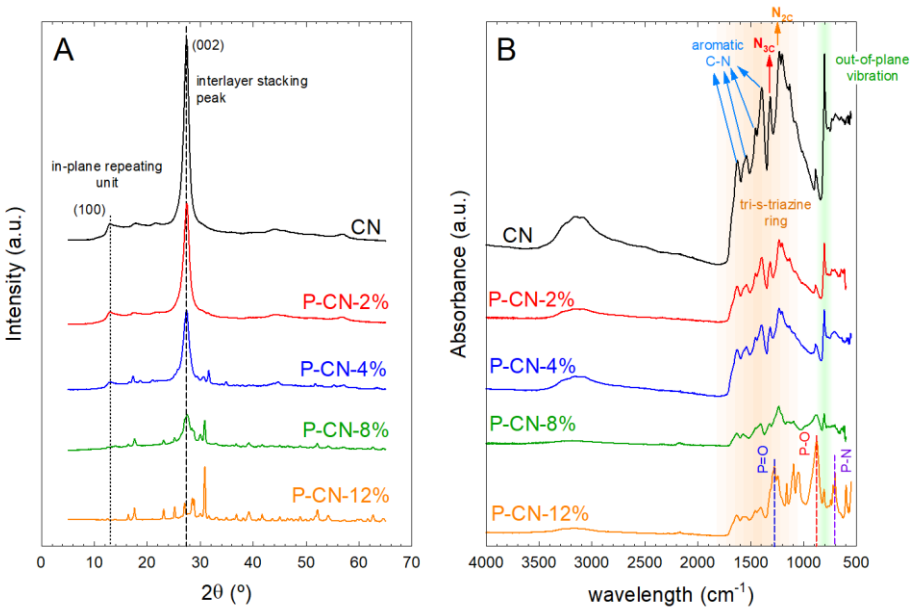

Fig. 5.3 *XRD diffractograms (A) and FTIR spectra (B) of the P-CN samples.*

Table 5.1 *Crystal and textural properties, elemental composition, and optical properties of P-CN samples.*

Sample	$L_{crystal}$ (nm)	d_{layer} (Å)	n	S_{BET} ($m^2\ g^{-1}$)	V_T ($cm^3\ g^{-1}$)	N_{EA} (wt. %)	C_{EA} (wt. %)	N/C_{EA} (at.)	O_{XPS} (wt. %)	P_{XPS} (wt. %)	E_{BG} (eV)
CN	5.77	3.250	18	9.1	0.050	60.8	35.1	1.485	4.8	-	2.7
P-CN-2%	7.37	3.245	22	8.4	0.035	53.0	30.6	1.499	8.8	1.78	2.6
P-CN-4%	7.62	3.250	29	4.2	0.018	50.4	28.7	1.505	8.2	4.04	2.6
P-CN-8%	6.62	3.236	-	8.7	0.047	36.9	19.6	1.600	16.3	7.84	2.5
P-CN-12%	19.45	3.131	-	6.6	0.027	12.3	6.7	1.574	24.3	10.6	2.0

$L_{crystal}$, crystallite size from the (002) peak by Scherrer's equation; d_{layer}, interlayer spacing from the (002) peak; n, number of layers; S_{BET}, specific total surface area obtained from the BET method; V_T, total pore volume obtained from the N_2 uptake at p/p_0~0.99; C and N composition from elemental analysis (EA); N/C_{EA}, the atomic N/C ratio by elemental analysis; O and P content from XPS analysis; and E_{BG}, bandgap energy estimated from the Tauc plot method.

The surface chemistry of the doped CN with sodium polyphosphate was analyzed by XPS. The sample with the optimum photocatalytic behavior, i.e. P-CN-4%, was selected for the evaluation of the chemical interaction type with carbon nitride. The XPS spectra are illustrated in

Fig. 5.4. The C_{1s} peak of g-C_3N_4 is traditionally deconvoluted in three main contributions, i.e. a peak of sp^2 bonds representative of N=C-N bonds (287.7 eV), a peak of sp^3 carbon in C-C/C-N bonds (285.6 eV), and a peak of sp^2 carbon bonds of C-C/C=C (284.4 eV) [34,58]. From the C_{1s} spectrum, the sp^2 N=C-N contribution counts as 59% of the whole area. In our previous works of the undoped sample [34,59], that means the CN sample, the sp^2 carbon of N=C-N considerably outlines the other two contributions, being 71% of the area contribution. The P doping forced a considerable decrease in this contribution, suggesting a plausible attack of P to the C positions and replacement as reported in the literature [60–62]. The diminishing contribution of the aromatic N=C-N could be considered the first evidence of P attacking C positions. The N_{1s} region of graphitic carbon nitride can be interpreted as the contribution of three bonds, namely tertiary N from $(C)_3$–N rings (N_{3C}, 399.9 eV), sp^2-bonded in the form of N–C=N (N_{2C}, 398.4 eV), and terminal -NH_x groups (400.8 eV) [44,63–66]. The N_{2C} and terminal -NH_x contributions in the P-CN-4% sample are lower in importance to the N_{3C} peak if compared to the bare CN blank reported in our previous works [34,59]. This evidence could be interpreted as a second fact of P replacing with C atoms, leading to a higher proportion of N_{3C}. The high-resolution peak P_{2p} spectrum has been deconvoluted in three plausible contributions: P–C, P–N, and P-O bonding at 132.6 eV, 133.7 eV, and 135.0 eV, respectively, according to the literature [67]. As portrayed in Fig. 5.4, the deconvolution led to a majority contribution of P-N although the contribution of P-O was lower but considerable. However, the contribution of P-C was negligible. The presence of the P-N bond suggests the anchorage of phosphate to nitrogen, either due to the reaction with terminal amino groups [68–70], supported by the decrease of the -NH_x stretching band in FTIR, or by the replacement of C in triazine rings atoms [62,71,72]. It has been reported a large nitrophilicity by P atoms, which provide stable P-N polymers. However, the larger bond length of P-N (150-170 pm) if compared to C-N in carbon nitride (135 pm) compromises the planar structure of P-CN [68]. Moreover, due to the possibility of coordination of P with O, the presence of P-O cannot be discharged. The presence of P-O binging may be linked to some terminal hydroxyl groups. The superficial quantification of P in P-CN-4% revealed a 4.04% (wt.) of P. The XPS analysis also revealed the presence of Na in the structure. From the results of the Na_{1s} spectrum

(results not shown), a plausible coordination of Na^+ with N atoms into the interstitial heptazine rings can be deduced. It has been reported that the calcination process in the presence of sodium tripolyphosphate promotes this coordination due to the strong ability of N atoms with lone-pair electrons towards metal ions [24], triggered by the lower electronegativity of N if compared to O. Finally, the doping with P increased the oxygen content, from 4.8% (wt.) of the bare CN to 8.2% (wt.) of P-CN-4%. In the O_{1s} region, the main peak observed originated from the sum of two plausible contributions located at 533 and 531 eV, assigned to, respectively, terminal -HO [73] and O^{2-} of phosphate environment [74] or C=O [73]. Surface O content, see Table 5.1, was raised with the increase of P doping, which suggests the binding of P to O, as discussed previously.

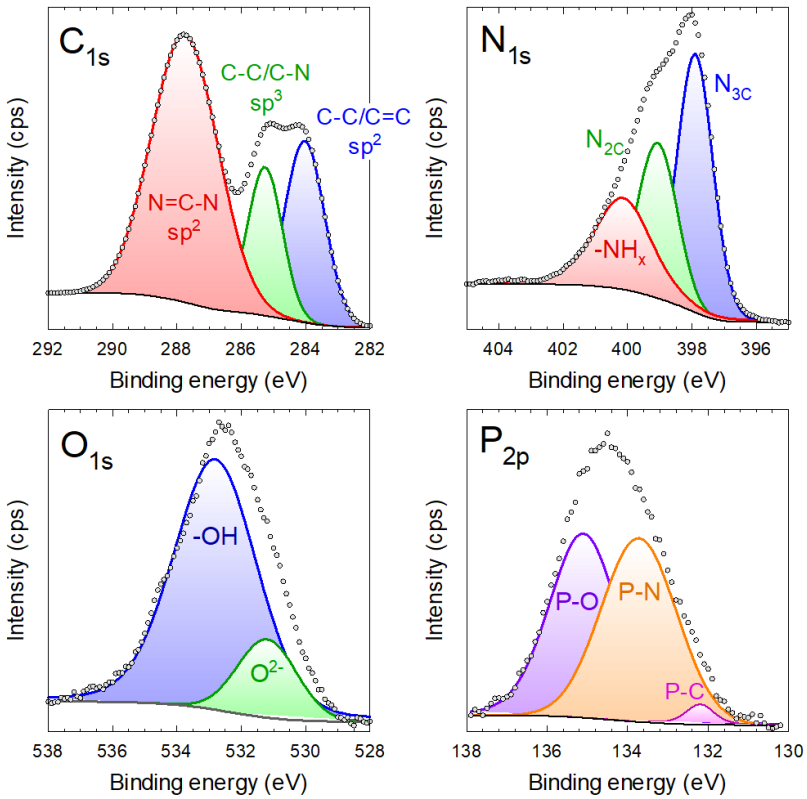

Fig. 5.4 *XPS spectra of high-resolution elements (C, N, O, and P) of P-CN-4% sample.*

Solid-state ^{13}C and ^{31}P MAS NMR were carried out to verify the changes in the chemical environment of C and P of g-C_3N_4 after doping. As illustrated in Fig. 5.5, the ^{13}C NMR spectrum was modified after the incorporation of P in the graphitic framework. Both spectra depicted two well-defined signals at ~154 and ~162 ppm, which can be attributed respectively to the bay site of C_3N corresponding to internal C atoms in tri-s-triazine rings, and the corner site C_2N-NHx atoms attributable to those C atoms connected next to bridging -NH_x [75–77]. There was no appreciated signal a 149 ppm, assignable to cyanuric groups, -C≡N [75]. According to the ^{13}C spectra of unmodified CN, the two contributions display a very similar intensity, being the corner contribution slightly higher. The P-CN-4% displayed a quite similar ^{13}C spectrum, revealing, therefore, a well-preserved framework. However, the doping with P promoted the decrease of the contribution of the bay sites, which means the peak located at ~154 ppm diminished its intensity, providing evidence of partial substitution of P atoms in the corner bay C of the g-C_3N_4 skeleton. The ^{31}P MAS NMR spectrum of P-CN-4%, see Fig. 5.5, described a broad peak due to the low P amount and the presence of multiple P-containing species [76]. The signals at roughly −10 and −20 ppm may be associated with the chemical environment of corner and bay phosphorus sites, respectively, whereas a signal at around 0 ppm can be ascribed to P-O at some edge terminal positions [78,79]. Taking this information into account, the ^{31}P spectra of P-CN-4% were deconvoluted in three contributions, obtaining deconvoluted peaks centered at -2.2 ppm for P-O, -10.6 ppm for corner, and -22.2 ppm for bay positions. Therefore, similar conclusions to XPS are withdrawn. The insertion of P in the g-C_3N_4 takes place by replacing C positions, either at bay or corner sites [68], including also the formation of P-O bindings, ascribed to the presence of hydroxyl groups.

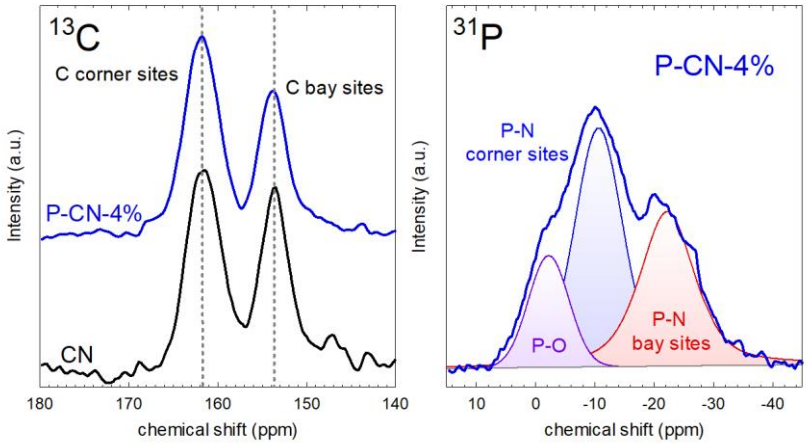

Fig. 5.5 *^{13}C CP-MAS NMR spectra of CN and P-CN-4% and ^{31}P MAS NMR spectrum of P-CN-4%*

Elemental analysis was carried out to compare the N/C ratios before and after doping with P, see results in Table 5.1. The unmodified CN displayed a value N/C=1.485 (at.) which is close to the theoretical value of N/C=4/3 expected for g-C_3N_4. The doping with P led to an increase in this ratio: 1.499 (P-CN-2%), 1.505 (P-CN-4%), 1.600 (P-CN-8%), and 1.574 (P-CN-12%). This tendency provides alternative evidence of a partial replacement of C by P. From bare CN to P-CN-8%, it is observed an increase of N/C ratio, with a waned value describing a minimum before further rise of P doping as observed with P-CN-12%. This replacement can be attributed, especially at low concentrations of P, to the substitution of corner or bay C positions as already reported in the literature with similar materials [61].

In summary, according to the global results of FTIR, XPS, and elemental analysis, it can be hypothesized that P is exchanged by C atoms in the graphitic structure [61]. Two points of attack have been reported in the literature, i.e. bay and corner carbon [80,81]. Moreover, phosphate can also be linked to N atoms, i.e. at the edge or building a bridge [69]. Among all these possibilities, the substitution of C seems to be preferential, although the positions at margins and defects of the CN structure are also plausible as phosphoramide or phosphorimide moieties [61].

The morphology and distribution of P were observed by STEM technique coupled with EDX analysis. Fig. 5.6 depicts some pictures of the P-CN-4% samples. The images show the presence of laminar

particles that can be aggregated in bigger associations of up to 500 nm. EDX microanalysis led to the elements imaging, i.e. C, N, and P. The EDX spectra of two selected areas are also provided, recording the existence of P in the sample. The mapping images showed random and almost uniform distribution of P dispersion. It should be noticed that the intensity of P mapping was much lesser intense than the corresponding for C and N due to the low content of P onto P-CN-4%, i.e. roughly 4%.

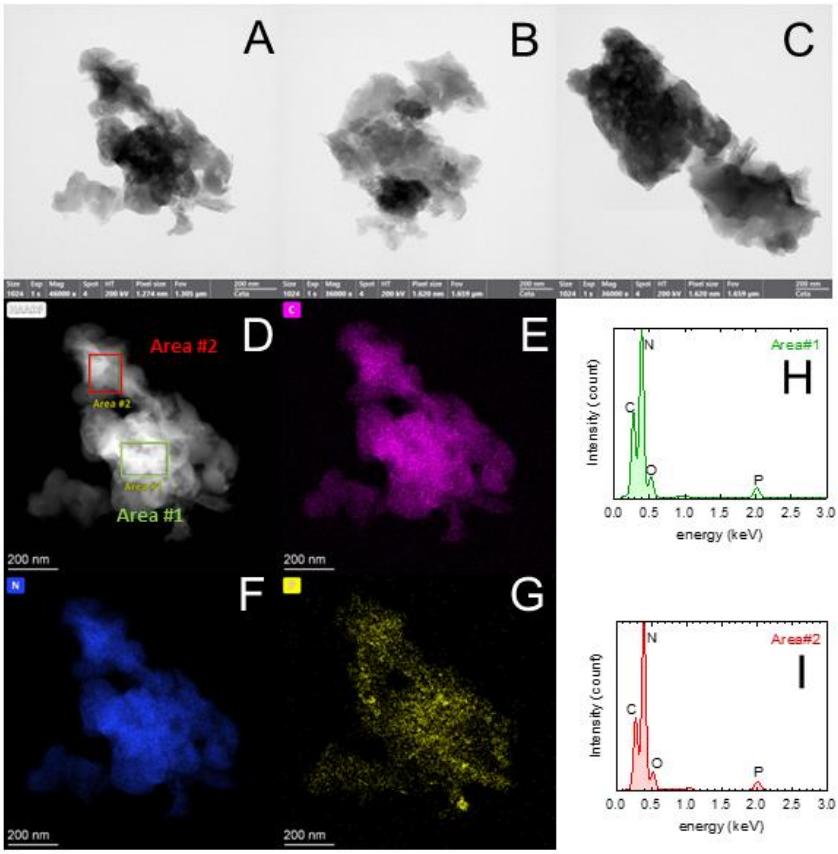

Fig. 5.6 *HR-STEM micrographs and EDX analysis of P-CN-4% sample. TEM images (A-B), HAADF image (D) and their element mapping of C (E), N (F) and P (G), and EDX spectra of two selected areas of HAADF image (D).*

The optical properties were assessed by DRS-UV-visible. Fig. 5.7A depicts the absorption spectra of the samples. Moreover, the spectra of the emitted radiation by the lamps is also included. In general terms, an intensive absorption enhancement in the UV and visible light regions is observed after P doping, and the band gap was narrowed as the P precursor amount was raised. The bare CN displayed a strong decay of

absorbance after 420 nm and a bandgap value (see Fig. 5.7B) of roughly 2.7 eV. The P-doping enhanced the absorbance in the visible region with a partial red-shifted of the absorption spectra and conferred to the material a characteristic brownish color [82]. The P-CN samples showed an important decrease in the absorbance at 420 nm, which diminished the rate of the absorbance decay afterward. This enables the material to absorb in the visible region, which is very limited for CN, enlarged as the amount of the doping P was increased. This extended absorbance up to 800 nm has been previously reported in the literature using different P precursor and synthesis strategies, such as phosphoric acid [82], phosphonic acid [82], hexachloro-tricyclophosphazene [69], or natural P sources like phytic acid [81]. Moreover, the bandgap was narrowed from 2.7 eV of bare CN to 2.5 eV (P-CN-4%) and 2.0 eV (P-CN-12%). Previous works have reported similar behavior by P tuning of g-C_3N_4, further confirmed by DFT calculations [83]. The reason for the red-shifted absorption edge has been attributed to the 3p stated of P located at the bottom of the conduction band in the g-C_3N_4, which contributes to a stabilization of the conduction band in lower energies and therefore a decrease of the bandgap [84–86].

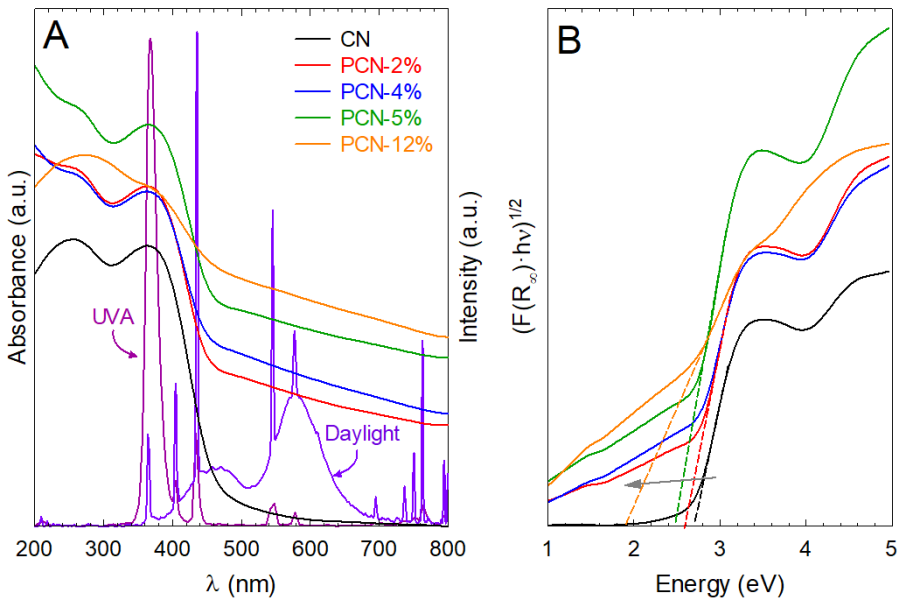

Fig. 5.7 *UV-visible absorption spectra of the P-CN samples and the emitting radiation spectra of the UVA and daylight lamps used (A) and bandgap determination of P-CN samples (B).*

Fig. 5.8 illustrates the photoluminescence (PL) spectra of the samples after excitation at 365 nm, the wavelength of the radiation used in the photocatalytic tests. The intensity of the PL peak can be associated with the recombination rate of the photogenerated charges, an undesirable effect for the photocatalytic process. A low-intensity PL signal implies a lower recombination rate of photoinduced electrons and holes; that means, a higher photocatalytic activity [87]. The PL spectrum of undoped CN shows a peak with a maximum centered at 458 nm. The PL spectra of the doped samples show that the doping of the P in the graphitic carbon nitride led to a dramatic decrease in the PL peak. Doping doses over 4% of P were conducted to negligible PL response, providing evidence of efficient separation of charges due to the presence of defects in the structure after doping, restraining the recombination rate of electron-hole pairs after P-doping. This effect has also been reported in previous works [82,88,89] and ascribed to the promoted electron delocalization on surface terminal sites after doping and structural advantages of P-CN, such as the interconnected nanosheets, as deduced from the higher crystal size, that can greatly curtail the charge migration [69].

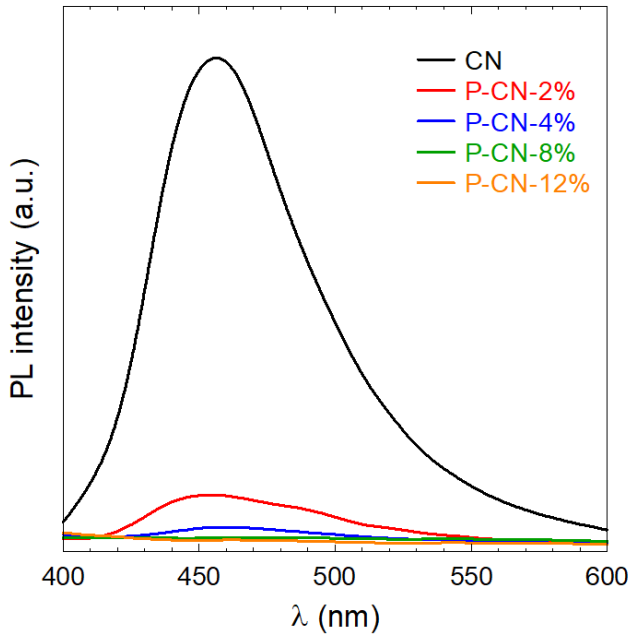

Fig. 5.8 *Photoluminescence spectra of P-CN samples.*

5.3.2. Photocatalytic production of cinnamaldehyde with the P-CN samples

The photocatalytic activity of P-CN samples was assessed for the reaction of oxidation of cinnamyl alcohol (CA) to cinnamaldehyde (CD). The temporal evolution of the normalized CA concentration and the yield of CD production are depicted in Fig. 5.9A. The pseudo-first order rate constant of CA abatement (k_{CA}) is available in Fig. 5.9B and Fig. 5.9C depicts the conversion after 5 h of reaction and the average selectivity to CD. The use of bare CN led to 37% of CA oxidation, with a selectivity of ~10%. The modification with P of the carbon nitride improved the photocatalytic oxidation of CA at low P doping dosage, i.e. P-CN-2%. However, at excessively high P doping (P-CN-12%) the kinetics of CA oxidation was worse than the non-doped sample, as the estimated k_{CA} and the conversion values at 5 h show. However, in terms of selectivity to CD, the presence of P improved the selectivity if compared to the bare CN in all the cases. It was observed a maximum selectivity with P-CN-4% (S_{CD}=49%). Table 5.2 summarizes the main kinetic parameters for all the tested samples. The quantum efficiency was calculated from the LVRPA estimation and the initial rate of cinnamyl alcohol abatement. The order of radiation uptake is, following the photocatalytic activity, P-CN-2% > P-CN-4% > CN > P-CN-8% > P-CN-12%. It corroborates the tendency observed for k_{CA}. Additionally, a test in the presence of visible radiation (>400 nm) instead of UVA (365 nm) was conducted. The sample P-CN-4% showed less activity under visible radiation. As shown in Table 5.2, the k_{CA} under visible illumination was only 39% of the achieved under UVA. The results indicate lower photocatalytic activity under visible radiation, which follows the absorptivity trend of P-CN-4%. However, due to the incorporation of P in the structure and the red-shifted absorption spectra, the samples performed certain activity under the visible region.

Table 5.2 *Kinetic parameters of the photocatalytic production of cinnamaldehyde with P-CN samples under UVA and visible radiation.*

Sample	$r_{CA,0}\cdot10^3$ (mM min^{-1})	$e^{\alpha,v}\cdot10^8$ (Einstein cm^{-3} s^{-1})	Q_E (%)	k_{CA} (h^{-1})	X_{CA} at 5 h (%)	S_{CD} (%)
UVA (365 nm)						
CN	1.383	1.620	0.142	0.083	36.9	9.8
P-CN-2%	2.950	1.944	0.253	0.177	59.6	22.0
P-CN-4%	2.500	2.025	0.206	0.150	53.0	49.2
P-CN-8%	1.300	2.349	0.092	0.078	36.3	35.3
P-CN-12%	0.450	2.268	0.033	0.027	19.8	20.2
Visible (>400 nm)						
P-CN-4%	0.985	-	-	0.059	25.5	16.1

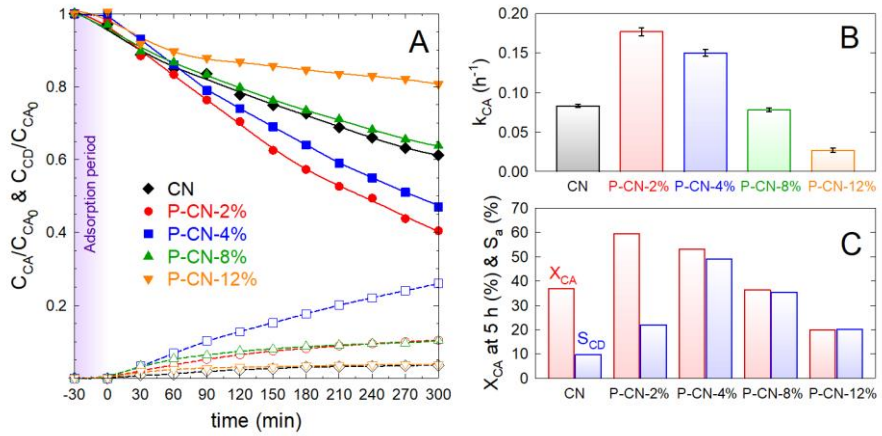

Fig. 5.9 *Photocatalytic oxidation of cinnamyl alcohol (CA) to cinnamaldehyde (CD). (A) Temporal evolution of the normalized concentration of CA and CD yield. (B) Pseudo-first order rate constant of CA abatement. (C) CA conversion at 5 h and average selectivity to CD. Experimental conditions: UVA radiation; V=350 mL; C_{CA}=1 mM; $C_{catalyst}$=0.5 g L^{-1}, T=20°C*

The use of organic solvents has been widely researched to raise the selectivity of the process [90], even to the detriment of the conversion of the parent alcohol. Acetonitrile is one of the most studied organic solvents since it raises the selectivity of cinnamaldehyde formation in the absence of water [91]. To compare the benefits of P doping over g-C_3N_4, the performance of the non-doped CN and the sample P-CN-4%, which displayed the highest CD yield, were further investigated in water-acetonitrile mixtures. Fig. 5.10 illustrates the conversion after 5 h of reaction and the average selectivity of CD formation for both catalysts at different water-acetonitrile proportions. It can be observed that an important decrease in the conversion is observed when adding acetonitrile. However, the reaction becomes more selective to CD

formation, probably due to the suppression of hydroxyl radical contribution which is more unselective than others such as superoxide. Moreover, when comparing the CN and P-CN-4% samples, it can be stated a lesser selectivity in the presence of acetonitrile for P-CN-4%. The presence of phosphate groups on the surface contributes to a higher surface-HO presence that might interact with CD during oxidation, which could explain the lesser selectivity achieved if compared to bare CN.

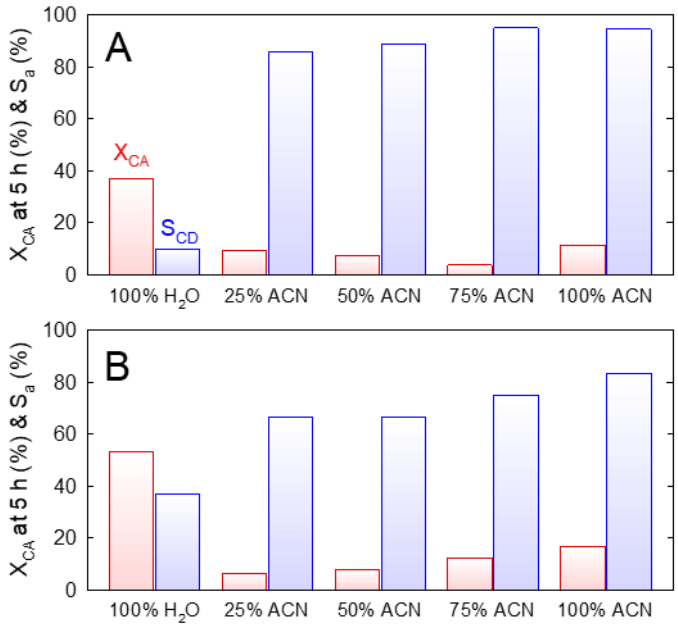

Fig. 5.10 *Conversion of cinnamyl alcohol (CA) and cinnamaldehyde (CD) selectivity in water-acetonitrile (ACN) mixtures with CN (A) and P-CN-4% (B) samples. Experimental conditions: UVA radiation; V=350 mL; C_{CA}=1 mM; $C_{catalyst}$=0.5 g L^{-1}, T=20ºC*

5.3.3. Photocatalytic mechanism and degradation pathway with P-CN-4%

The impact of the reactive oxidation species (ROS) involved in the photocatalytic oxidation of cinnamyl alcohol over P-CN-4% was tentatively studied by the addition of chemical radical scavengers [35], as shown in Fig. 5.11. It should be noted that the interaction of the chemical scavengers in the photocatalytic mechanism is not completely selective and should be analyzed with caution [36,37].

Firstly, the role played by the hydroxyl radical was assessed by adding to the solution tert-butyl alcohol (TBA), due to the high reactivity of TBA with HO• ($k_{TBA,HO•}$=6.2 × 10^8 M^{-1} s^{-1}) [92]. In the presence of TBA, the CA profile was slowed down, although the reaction was not completely stopped. The hydroxyl radical has been reported as an unselective oxidant species, and in the case of cinnamyl alcohol, the attack of HO to the C=C of the alkyl chain releases benzaldehyde or acetaldehyde as undesirable byproducts [93,94]. The role played by HO• in the degradation mechanism of P-CN-4% activation and CA oxidation was further analyzed by the use of 2-HO-TPA as an indirect molecule probe of HO• existence. It is well known that TPA can trap HO• selectively leading to the formation of the fluorescent 2-HO-TPA [38]. Fig. 5.11 depicts the temporal evolution of 2-OH-TPA during the photocatalytic transformation of TPA in the presence of P-CN-4%. As illustrated in the spectra recorded (Fig. 5.11C), the spectra are barely defined, being appreciated as an important signal-to-noise ratio that manifests the low production of HO•. This fact was further corroborated by the determination of the temporal evolution of the concentration of 2-OH-TPA, see Fig. 5.11D. From this figure, it is observed that a plateau is reached after 30-60 min. Noteworthy, the values obtained for the concentration of the generated 2-OH-TPA are below the limit of detection. This poor formation of the fluorescent 2-OH-TPA provides evidence of negligible production of HO, whose impact according to the scavengers' tests was suggested to be minimal. According to the reported band alignment for g-C_3N_4, the redox potential of the valence band does not display enough potential to trigger the oxidation of water molecules to HO• [14,95].

Secondly, the role played by the superoxide radical was assessed by adding -p-benzoquinone (p-BZQ), tiron, or removing the dissolved O_2 bubbling N_2 instead of air [96]. The use of p-BZQ is widely extended to check the role played by superoxide radicals in photocatalysis tests [35], due to the high reactivity ($k_{p\text{-}BZQ,O2•-}$=10^9 M^{-1} s^{-1} [97]). However, some authors have recently warned about the complexity of p-BZQ in aqueous photocatalytic media [36,37]. For instance, p-BZQ can trap electrons ($k_{p\text{-}BZQ,e-}$=1.35 × 10^9 M^{-1} s^{-1}[98]) leading to the formation of semiquinone radicals [37], it displays also a high reactivity with HO• ($k_{p\text{-}BZQ,HO•}$=6.6 × 10^9 M^{-1} s^{-1} [99]), p-BZQ is also photolyzed giving rise to extra $O_2^{•-}$ [100],

or being photo-activated to release single oxygen ($^1O_2$) [101]. To overcome these drawbacks, tiron, which is commonly used to test the presence of $O_2^{\bullet-}$ [36], was selected for additional analysis, although it also may react with $HO^\bullet$ ($k_{tiron}=10^9$ M^{-1} s^{-1} [102]). In the presence of p-BZQ, no significant alteration of the kinetics was observed if compared to the blank, and the selectivity was dramatically diminished; however, tiron did lead to a ~50% depletion of k_{CA} with no so huge affectation to the selectivity. Bearing in mind the lack of $HO^\bullet$ participation, the decrease in the presence of tiron may be taken as proof of $O_2^{\bullet-}$ participation. Additionally, a test under N_2 displacement of dissolved O_2 was conducted. It has been reported that an atmosphere of pure O_2 has led to boosted conversion but very similar selectivity if compared to air, Ar, or N_2 [103]. In this case, an abrupt decrease in the kinetics of CA oxidation was observed, which may suggest a high importance of $O_2^{\bullet-}$ in the oxidative process of CA. Nonetheless, it should be also considered that in the absence of any electron acceptor such as O_2, the recombination effect is potentiated, rising as conclusion an overrated participation of $O_2^{\bullet-}$. The results attained with tiron and N_2, cautiously considered, may provide evidence about the relevance of $O_2^{\bullet-}$ in the process if compared to other ROS.

Thirdly, the importance of the photo-generated holes was studied by adding oxalic acid [104] as oxalate anions can be easily oxidized by the holes to produce CO_2. Oxalate anion also can trap $HO^\bullet$; however, the kinetics is slow ($k_{Oxalate,HO^\bullet}= 1.5 \times 10^7$ M^{-1} s^{-1} [105]), and the production of $HO^\bullet$ has been discharged in P-CN-4%. In the presence of oxalic acid, the kinetic of CA oxidation was negatively influenced, suggesting the importance of photo-generated holes in the process. For further corroboration, EDTA was also tested as a hole scavenger. EDTA has been reported as a superior scavenger to oxalic acid due to its strong chelating effect and ability to directly fill electrons into the valance band [106]. The results attained with EDTA confirm the importance of the hole in the CA oxidation.

Finally, the plausible participation of singlet oxygen ($^1O_2$) was verified by a test adding L-Histidine (L-H). L-H has a great ability to react with $^1O_2$ and $HO^\bullet$ ($k_{L\text{-}H,HO^\bullet}= 1.5 \times 10^7$ M^{-1} s^{-1} [35]). As the production of $HO^\bullet$, the 60% decrease in k_{CA} may be attributed to the participation of $^1O_2$.

The mechanism of oxidation of cinnamyl alcohol involves the photogenerated holes by the formation of an intermediate organic

radical that could be further oxidized to the aldehyde by the holes [107] or by the superoxide radicals [96]. This mechanism would explain the results achieved in this work, in which the participation was tentatively identified as $h^+ > O_2^{\bullet-} \sim {}^1O_2$.

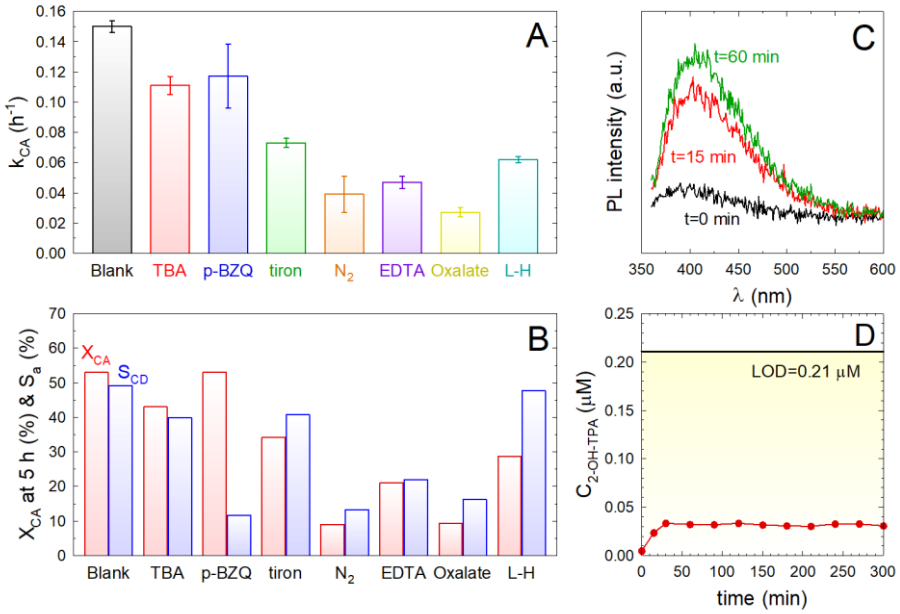

Fig. 5.11 *Photocatalytic oxidation of cinnamyl alcohol (CA) to cinnamaldehyde (CD). (A) The pseudo-first order rate constant of CA abatement with P-CN-4% in the presence of chemical scavengers (A) and the CA conversion at 5 h and average selectivity to CD (B). (Photoluminescence spectra of 2-OH-TPA (C) and temporal evolution of the concentration of 2-OH-TPA (D) during the photocatalytic transformation of TPA with P-CN-4%. Experimental conditions: UVA radiation; V=350 mL; C_{CA}=1 mM; $C_{catalyst}$=0.5 g L^{-1}; $C_{scavenger}$=10 mM; C_{TPA}=1 mM; T=20°C.*

A tentative proposal of the band alignment was carried out as an approach from the estimation of the valence band by XPS and the bandgap obtained from the Tauc plot of the absorption data of DRS-UV-visible [73,76,79]. Fig. 5.12A depicts the valence band edge obtained from XPS, leading to a slight shift to a higher potential value after P-doping, i.e. the redox potential of the holes are 1.10 and 1.26 V for CN and P-CN-4%, respectively. After considering the bandgap values, a scheme of the bands' placement is depicted in Fig. 5.12B, where it is stated the unfeasibility of formation of hydroxyl radical from the oxidation of water, redox of the pair $H_2O/HO^{\bullet}$, +2.31 V [108]. On the contrary, the formation of $O_2^{\bullet-}$ is favorable, redox $O_2/O_2^{\bullet-}$, -0.33 V [109]. A comparison between CN and P-CN-4% reveals that no substantial changes in the

band's alignment occur, so the better performance of P-CN-4% relies on the higher migration of charges due to the presence of P defects that minimize the recombination effect.

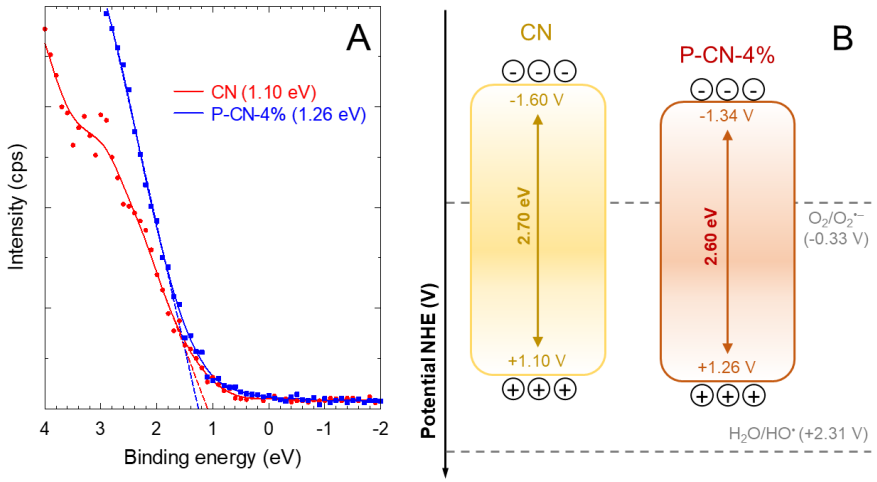

Fig. 5.12 *Determination of the valence band edge of CN and P-CN-4% by XPS (A) and bands alignment proposal (B).*

The products generated during the photocatalytic oxidation of cinnamyl alcohol were identified by liquid chromatography coupled to electrospray ionization under positive mode and mass spectrometry with a quadrupole time-of-flight, LC-ESI(+)-QTOF, using the photocatalyst with the best performance, i.e. P-CN-4%. Both, positive and negative ionization modes were tested, restricting the study under positive mode since cinnamyl alcohol and aldehyde were prone to it. Cinnamyl alcohol is an allyl alcohol, whose ionization under positive mode led to the loss of H_2O, $[M\text{-}H_2O]^+$=117.06054. The detected reaction byproducts and a plausible degradation pathway is depicted in Fig. 5.13. The aerobic oxidation of cinnamyl alcohol has been reported to occur spontaneously under the presence of oxygen and daylight radiation, appreciating the degradation after a long time though, i.e. 54 weeks [110]. Under these circumstances, the oxidation of CA can take place on the allyl alcohol group, leading to the formation of cinnamaldehyde (CD); alternatively, triggering an epoxy ring if the oxidation attack goes through the unsaturation of the allyl chain, generating the epoxy-cinnamyl alcohol (epoxy-CA). Both routes have been observed during the photocatalytic activation of P-CN-4%; nonetheless, the CD appeared in much more

intensity in the extracted ion chromatograms if compared to epoxy-CA, which suggests a great preference for the oxidation of the terminal alcohol, preserving the double bond of the chain. Studies of photocatalytic transformation of CA over TiO_2-based catalysts have concluded that the pathway route addresses the formation of CD and benzaldehyde as the main degradation byproducts [111,112]. Other catalytic oxidation systems involving the activation of hydrogen peroxide over catalysts based on iron or palladium as active species have described appreciable contribution of epoxide formation, either in the cinnamyl alcohol or aldehyde formulas [113]. Under the action of P-CN-4%, the further oxidation of CD led to the generation of cinnamic acid (CC), which appeared in similar intensity levels as CD, which is consistent with the other studies under the presence of oxygen [110–112]. The subsequent oxidation of CC led to the formation of phenylacetaldehyde [111], detected at long reaction times, i.e. 5 h. Alternatively, a $[M-H]^+$=167.0703 no reported previously was registered in this work, which according to in silico oxidation prediction tools [114], corresponds to hydroxylation of the allyl bond of cinnamic acid. However, these two byproducts produced from CC appeared at an intensity of one magnitude order below CC, which as the epoxy derivatives led to mass errors in ppm higher than the major compounds. No further oxidation to lower transformation products was detected, being the release of CD and CC, the most appreciable products detected in the photo-oxidation of CA.

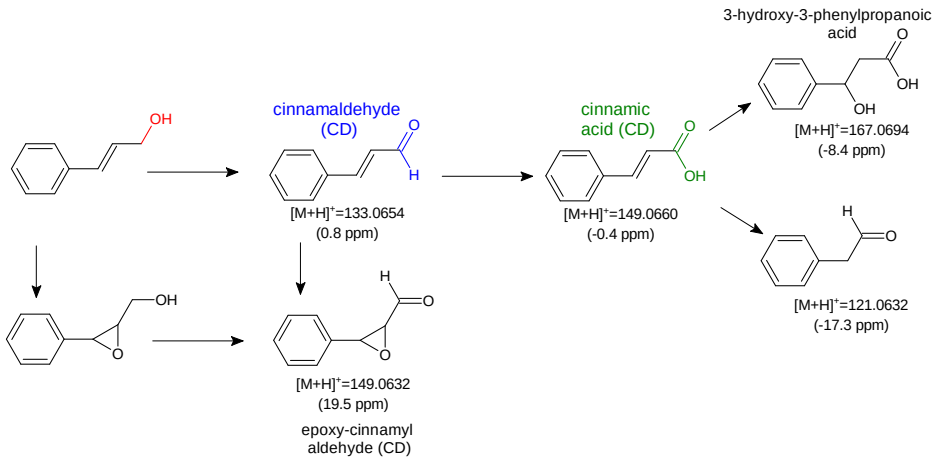

Fig. 5.13 *Proposed degradation mechanism of cinnamyl alcohol over P-CN-4%.*

5.4. CONCLUSIONS

The incorporation of P into graphitic carbon nitride with sodium polyphosphate in a two-step synthesis process has been successfully carried out. The crystalline structure suggested that P was incorporated in the external faces of the plates or the heptazine rings, attacking the layered structure. The FTIR analysis pointed out the decrease of vibration of the terminal $–NH_x$ groups and the appearance of a P-N bond anchoring of phosphate groups to N atoms. This fact was further confirmed by XPS analysis, deducing a plausible attack of phosphate to C positions, leading to the formation of terminal phosphate groups linked to N. The P is expected to be by C atoms in the graphitic structure at two points, i.e. bay and corner carbon, as NMR analysis suggested. Moreover, phosphate can also be linked to N atoms, i.e. at the edge or building a bridge. Regarding the optical properties, an intensive absorption enhancement in the UV and visible light regions was observed after P doping, and the band gap was narrowed as the P precursor amount was raised, from 2.7 (bare graphitic carbon) to 2.6 eV (sample doped with 4%). The photoluminescence properties of the doped samples showed a dramatic decrease in the PL peak. Doses over 4% of P were subjected to negligible PL response, providing evidence of efficient separation of charges due to the presence of defects in the structure after doping.

The P doping modified the photocatalytic activity of the oxidation reaction of cinnamyl alcohol (CA) to cinnamaldehyde (CD). Although the modification with P improved the photocatalytic oxidation of CA, it was only achieved at low P doping dosage, i.e. P-CN-2%, the selectivity to CD in the presence of P was improved if compared to the bare CN in all the cases, reaching a maximum of ~50% (P-CN-4%). The influence of the solvent was also studied by carrying out tests on acetonitrile. The presence of acetonitrile led to a rise of the selectivity to the detriment of lower conversion of the alcohol. The bare CN sample led to almost 100% of selectivity in acetonitrile while the P-CN-4% sample only led to 80%. Finally, the relative influence of the reactive oxygen species involved in the process of photocatalytic oxidation in water was studied. The mechanism of oxidation of cinnamyl alcohol involves the photogenerated holes by the formation of an intermediate organic radical that could be further oxidized to the aldehyde by the holes or by

the superoxide radicals, with a negligible contribution of the hydroxyl radicals. The analysis of the transformation products provides evidence of a preferential oxidation route of the alcohol group, triggering the oxidation to cinnamaldehyde and subsequent release of cinnamic acid.

REFERENCES

1. Cocchiara, J.; Letizia, C.S.; Lalko, J.; Lapczynski, A.; Api, A.M. Fragrance Material Review on Cinnamaldehyde. Food and Chemical Toxicology 2005, 43, 867–923, doi:10.1016/J.FCT.2004.09.014.
2. Friedman, M.; Kozukue, N.; Harden, L.A. Cinnamaldehyde Content in Foods Determined by Gas Chromatography-Mass Spectrometry. J Agric Food Chem 2000, 48, 5702–5709, doi:10.1021/JF000585G.
3. Franz, C.M.; Baser, K.H.C.; Hahn-Ramssl, I. Herbs and Aromatic Plants as Feed Additives: Aspects of Composition, Safety, and Registration Rules. In Feed Additives: Aromatic Plants and Herbs in Animal Nutrition and Health; Academic Press, 2020; pp. 35–56 ISBN 9780128147016.
4. Doyle, A.A.; Stephens, J.C. A Review of Cinnamaldehyde and Its Derivatives as Antibacterial Agents. Fitoterapia 2019, 139, 104405, doi:10.1016/J.FITOTE.2019.104405.
5. Lu, L.; Shu, C.; Chen, L.; Yang, Y.; Ma, S.; Zhu, K.; Shi, B. Insecticidal Activity and Mechanism of Cinnamaldehyde in C. Elegans. Fitoterapia 2020, 146, 104687, doi:10.1016/J.FITOTE.2020.104687.
6. Grunwaldt, J.D.; Keresszegi, C.; Mallat, T.; Baiker, A. In Situ EXAFS Study of Pd/Al2O3 during Aerobic Oxidation of Cinnamyl Alcohol in an Organic Solvent. J Catal 2003, 213, 291–295, doi:10.1016/S0021-9517(02)00083-0.
7. Mallat, T.; Bodnar, Z.; Hug, P.; Baiker, A. Selective Oxidation of Cinnamyl Alcohol to Cinnamaldehyde with Air over Bi-Pt/Alumina Catalysts. J Catal 1995, 153, 131–143, doi:10.1006/JCAT.1995.1115.
8. Frade, R.F.M.; Simão, D.; Afonso, C.A.M. Isolation of Cinnamaldehyde from Cinnamon. In Comprehensive Organic Chemistry Experiments for the Laboratory Classroom; The Royal Society of Chemistry, 2016; pp. 23–25.
9. Wang, R.; Wang, R.; Yang, B. Comparison of Volatile Compound of Cinnamon (Cinnamomum Cassia Presl) Bark Prepraed by Hydrodistillation and Headspace Solid Phase Microextraction. J Food Process Eng 2011, 34, 175–185, doi:10.1111/J.1745-4530.2008.00347.X.
10. Al-Bayati, F.A.; Mohammed, M.J. Isolation, Identification, and Purification of Cinnamaldehyde from Cinnamomum Zeylanicum

Bark Oil. An Antibacterial Study. Pharm Biol 2009, 47, 61–66, doi:10.1080/13880200802430607.

11. Modi, P.I.; Parikh, J.K.; Desai, M.A. Intensified Approach towards Isolation of Cinnamon Oil Using Microwave Radiation: Parametric, Optimization and Comparative Studies. Ind Crops Prod 2021, 173, 114088, doi:10.1016/J.INDCROP.2021.114088.
12. Modi, P.I.; Parikh, J.K.; Desai, M.A. Sonohydrodistillation: Innovative Approach for Isolation of Essential Oil from the Bark of Cinnamon. Ind Crops Prod 2019, 142, 111838, doi:10.1016/J.INDCROP.2019.111838.
13. Fan, Q.; Huang, F.; Zhou, L.; He, W.; Jiang, X.; Na, Z.; Gongpan, P.; Hu, H.; Song, Q. Development of a Strategy for a Quick Process for Separation of Volatile Compounds in Counter-Current Chromatography: Purification of Cinnamaldehyde from Cinnamomum Cassia by High Performance Counter-Current Chromatography. Prep Biochem Biotechnol 2021, 51, 1056–1059, doi:10.1080/10826068.2021.1894444.
14. Marcì, G.; García-López, E.I.; Palmisano, L. Polymeric Carbon Nitride (C3N4) as Heterogeneous Photocatalyst for Selective Oxidation of Alcohols to Aldehydes. Catal Today 2018, 315, 126–137, doi:10.1016/J.CATTOD.2018.03.038.
15. Chen, L.; Tang, J.; Song, L.N.; Chen, P.; He, J.; Au, C.T.; Yin, S.F. Heterogeneous Photocatalysis for Selective Oxidation of Alcohols and Hydrocarbons. Appl Catal B 2019, 242, 379–388, doi:10.1016/J.APCATB.2018.10.025.
16. Shen, Z.; Hu, Y.; Li, B.; Zou, Y.; Li, S.; Wilma Busser, G.; Wang, X.; Zhao, G.; Muhler, M. State-of-the-Art Progress in the Selective Photo-Oxidation of Alcohols. Journal of Energy Chemistry 2021, 62, 338–350, doi:10.1016/J.JECHEM.2021.03.033.
17. Xiong, L.; Tang, J. Strategies and Challenges on Selectivity of Photocatalytic Oxidation of Organic Substances. Adv Energy Mater 2021, 11, 2003216, doi:10.1002/AENM.202003216.
18. Hazra, S.; Malik, E.; Nair, A.; Tiwari, V.; Dolui, P.; Elias, A.J. Catalytic Oxidation of Alcohols and Amines to Value-Added Chemicals Using Water as the Solvent. Chem Asian J 2020, 15, 1916–1936, doi:10.1002/ASIA.202000299.
19. Wang, Y.; Wang, X.; Antonietti, M. Polymeric Graphitic Carbon Nitride as a Heterogeneous Organocatalyst: From Photochemistry to Multipurpose Catalysis to Sustainable Chemistry. Angewandte Chemie 2012, 51, 68–89, doi:10.1002/ANIE.201101182.

20. Zhang, W.; Bariotaki, A.; Smonou, I.; Hollmann, F. Visible-Light-Driven Photooxidation of Alcohols Using Surface-Doped Graphitic Carbon Nitride. Green Chemistry 2017, 19, 2096–2100, doi:10.1039/C7GC00539C.
21. Akhundi, A.; Badiei, A.; Ziarani, G.M.; Habibi-Yangjeh, A.; Muñoz-Batista, M.J.; Luque, R. Graphitic Carbon Nitride-Based Photocatalysts: Toward Efficient Organic Transformation for Value-Added Chemicals Production. Molecular Catalysis 2020, 488, 110902, doi:10.1016/J.MCAT.2020.110902.
22. Bellardita, M.; García-López, E.I.; Marcì, G.; Krivtsov, I.; García, J.R.; Palmisano, L. Selective Photocatalytic Oxidation of Aromatic Alcohols in Water by Using P-Doped g-C3N4. Appl Catal B 2018, 220, 222–233, doi:10.1016/J.APCATB.2017.08.033.
23. Bagherzade, A.; Nemati, F.; Nahzomi, H.T. Computational and Experimental Evidence of Pd Supported P-Doped Porous Graphitic Carbon Nitride as a Highly Efficient and Exceptionally Durable Photocatalyst for Boosted Visible-Light-Driven Benzyl Alcohol Oxidation. Journal of Physics and Chemistry of Solids 2021, 152, 109985, doi:10.1016/J.JPCS.2021.109985.
24. Cao, S.; Huang, Q.; Zhu, B.; Yu, J. Trace-Level Phosphorus and Sodium Co-Doping of g-C3N4 for Enhanced Photocatalytic H2 Production. J Power Sources 2017, 351, 151–159, doi:10.1016/J.JPOWSOUR.2017.03.089.
25. Altomare, A.; Corriero, N.; Cuocci, C.; Falcicchio, A.; Moliterni, A.; Rizzi, R. QUALX2.0: A Qualitative Phase Analysis Software Using the Freely Available Database POW_COD. J Appl Crystallogr 2015, 48, 598–603, doi:10.1107/S1600576715002319.
26. Pérez-Molina, Á.; Pastrana-Martínez, L.M.; Morales-Torres, S.; Maldonado-Hódar, F.J. Photodegradation of Cytostatic Drugs by G-C3N4: Synthesis, Properties and Performance Fitted by Selecting the Appropriate Precursor. Catal Today 2023, 418, 114068, doi:10.1016/J.CATTOD.2023.114068.
27. Makuła, P.; Pacia, M.; Macyk, W. How to Correctly Determine the Band Gap Energy of Modified Semiconductor Photocatalysts Based on UV-Vis Spectra. Journal of Physical Chemistry Letters 2018, 9, 6814–6817.
28. Landi, S.; Segundo, I.R.; Freitas, E.; Vasilevskiy, M.; Carneiro, J.; Tavares, C.J. Use and Misuse of the Kubelka-Munk Function to Obtain the Band Gap Energy from Diffuse Reflectance Measurements. Solid State Commun 2022, 341, 114573, doi:10.1016/J.SSC.2021.114573.

29. Solís, R.R.; Quintana, M.A.; Martín-Lara, M.Á.; Pérez, A.; Calero, M.; Muñoz-Batista, M.J. Boosted Activity of G-C3N4/UiO-66-NH2 Heterostructures for the Photocatalytic Degradation of Contaminants in Water. Int J Mol Sci 2022, 23, 12871, doi:10.3390/IJMS232112871/S1.
30. Serpone, N. Relative Photonic Efficiencies and Quantum Yields in Heterogeneous Photocatalysis. J Photochem Photobiol A Chem 1997, 104, 1–12, doi:10.1016/S1010-6030(96)04538-8.
31. Li Puma, G.; Brucato, A. Dimensionless Analysis of Slurry Photocatalytic Reactors Using Two-Flux and Six-Flux Radiation Absorption–Scattering Models. Catal Today 2007, 122, 78–90, doi:10.1016/J.CATTOD.2007.01.027.
32. Alfano, O.M.; Bahnemann, D.; Cassano, A.E.; Dillert, R.; Goslich, R. Photocatalysis in Water Environments Using Artificial and Solar Light. Catal Today 2000, 58, 199–230, doi:10.1016/S0920-5861(00)00252-2.
33. Muñoz-Batista, M.J.; Kubacka, A.; Fontelles-Carceller, O.; Tudela, D.; Fernández-García, M. Surface CuO, Bi2O3, and CeO2 Species Supported in TiO2-Anatase: Study of Interface Effects in Toluene Photodegradation Quantum Efficiency. ACS Appl Mater Interfaces 2016, 8, 13934–13945, doi:10.1021/ACSAMI.6B03081.
34. Quintana, M.A.; Solís, R.R.; Ángeles Martín-Lara, M.; Blázquez, G.; Mónica Calero, F.; Muñoz-Batista, M.J. Enhanced Boron Modified Graphitic Carbon Nitride for the Selective Photocatalytic Production of Benzaldehyde. Sep Purif Technol 2022, 298, 121613, doi:10.1016/J.SEPPUR.2022.121613.
35. Pelaez, M.; Falaras, P.; Likodimos, V.; O'Shea, K.; de la Cruz, A.A.; Dunlop, P.S.M.; Byrne, J.A.; Dionysiou, D.D. Use of Selected Scavengers for the Determination of NF-TiO2 Reactive Oxygen Species during the Degradation of Microcystin-LR under Visible Light Irradiation. J Mol Catal A Chem 2016, 425, 183–189, doi:10.1016/j.molcata.2016.09.035.
36. Rodríguez, E.M.; Márquez, G.; Tena, M.; Álvarez, P.M.; Beltrán, F.J. Determination of Main Species Involved in the First Steps of TiO2 Photocatalytic Degradation of Organics with the Use of Scavengers: The Case of Ofloxacin. Appl Catal B 2015, 178, 44–53, doi:10.1016/j.apcatb.2014.11.002.
37. Schneider, J.T.; Firak, D.S.; Ribeiro, R.R.; Peralta-Zamora, P. Use of Scavenger Agents in Heterogeneous Photocatalysis: Truths, Half-Truths, and Misinterpretations. Physical Chemistry Chemical Physics 2020, 22, 15723–15733, doi:10.1039/d0cp02411b.

38. Ishibashi, K.I.; Fujishima, A.; Watanabe, T.; Hashimoto, K. Detection of Active Oxidative Species in TiO2 Photocatalysis Using the Fluorescence Technique. Electrochem commun 2000, 2, 207–210, doi:10.1016/S1388-2481(00)00006-0.
39. Gómez-Avilés, A.; Solís, R.R.; García-Frutos, E.M.; Bedia, J.; Belver, C. Novel Isoreticular UiO-66-NH2 Frameworks by N-Cycloalkyl Functionalization of the 2-Aminoterephtalate Linker with Enhanced Solar Photocatalytic Degradation of Acetaminophen. Chemical Engineering Journal 2023, 461, 141889, doi:10.1016/J.CEJ.2023.141889.
40. Qamar, M.; Elsayed, R.B.; Alhooshani, K.R.; Ahmed, M.I.; Bahnemann, D.W. Chemoselective and Highly Efficient Conversion of Aromatic Alcohols into Aldehydes Photo-Catalyzed by Ag3PO4 in Aqueous Suspension under Simulated Sunlight. Catal Commun 2015, 58, 34–39, doi:10.1016/J.CATCOM.2014.08.025.
41. Fina, F.; Callear, S.K.; Carins, G.M.; Irvine, J.T.S. Structural Investigation of Graphitic Carbon Nitride via XRD and Neutron Diffraction. Chemistry of Materials 2015, 27, 2612–2618, doi:10.1021/ACS.CHEMMATER.5B00411.
42. Li, X.; Zhang, J.; Shen, L.; Ma, Y.; Lei, W.; Cui, Q.; Zou, G. Preparation and Characterization of Graphitic Carbon Nitride through Pyrolysis of Melamine. Appl Phys A Mater Sci Process 2009, 94, 387–392, doi:10.1007/S00339-008-4816-4.
43. Fei, Y.; Han, N.; Zhang, M.; Yang, F.; Yu, X.; Shi, L.; Khataee, A.; Zhang, W.; Tao, D.; Jiang, M. Facile Preparation of Visible Light-Sensitive Layered g-C3N4 for Photocatalytic Removal of Organic Pollutants. Chemosphere 2022, 307, 135718, doi:10.1016/J.CHEMOSPHERE.2022.135718.
44. Alwin, E.; Nowicki, W.; Wojcieszak, R.; Zieliński, M.; Pietrowski, M. Elucidating the Structure of the Graphitic Carbon Nitride Nanomaterials via X-Ray Photoelectron Spectroscopy and X-Ray Powder Diffraction Techniques. Dalton Transactions 2020, 49, 12805–12813, doi:10.1039/D0DT02325F.
45. Lan, Y.; Li, Z.; Li, D.; Yan, G.; Yang, Z.; Guo, S. Graphitic Carbon Nitride Synthesized at Different Temperatures for Enhanced Visible-Light Photodegradation of 2-Naphthol. Appl Surf Sci 2019, 467–468, 411–422, doi:10.1016/J.APSUSC.2018.10.152.
46. Bai, X.; Yan, S.; Wang, J.; Wang, L.; Jiang, W.; Wu, S.; Sun, C.; Zhu, Y. A Simple and Efficient Strategy for the Synthesis of a

Chemically Tailored G-C3N4 Material. J Mater Chem A Mater 2014, 2, 17521–17529, doi:10.1039/C4TA02781G.

47. Xing, W.; Liu, C.; Zhong, H.; Zhang, Y.; Zhang, T.; Cheng, C.; Han, J.; Wu, G.; Chen, G. Phosphate Group-Mediated Carriers Transfer and Energy Band over Carbon Nitride for Efficient Photocatalytic H2 Production and Removal of Rhodamine B. J Alloys Compd 2022, 895, 162772, doi:10.1016/J.JALLCOM.2021.162772.
48. Gibot, P.; Schnell, F.; Spitzer, D. Enhancement of the Graphitic Carbon Nitride Surface Properties from Calcium Salts as Templates. Microporous and Mesoporous Materials 2016, 219, 42–47, doi:10.1016/J.MICROMESO.2015.07.026.
49. Yan, X.; Yuan, P.; Meng, X.; Hu, R. Phosphorus Modified Graphitic Carbon Nitride Activated by Guanidine Phosphate Enables Fast, Efficient and Selective Immobilization of Aquatic Lead. J Mol Liq 2023, 375, 121339, doi:10.1016/J.MOLLIQ.2023.121339.
50. Kim, M.; Hwang, S.; Yu, J.S. Novel Ordered Nanoporous Graphitic C3N4 as a Support for Pt–Ru Anode Catalyst in Direct Methanol Fuel Cell. J Mater Chem 2007, 17, 1656–1659, doi:10.1039/B702213A.
51. Yang, Z.; Qi, C.; Yuan, P.; Hu, R.; Du, X.; Cheng, M. High-Efficiency Selective Removal of U(VI) by Phosphate-Functionalized Graphitic Carbon Nitride Activated Using Guanidine Phosphate. J Environ Chem Eng 2023, 11, 110272, doi:10.1016/J.JECE.2023.110272.
52. Wang, X.; Li, X.; Chen, W.; Wang, R.; Bian, W.; Choi, M.M.F. Phosphorus Doped Graphitic Carbon Nitride Nanosheets as Fluorescence Probe for the Detection of Baicalein. Spectrochim Acta A Mol Biomol Spectrosc 2018, 198, 1–6, doi:10.1016/J.SAA.2018.02.062.
53. Zhang, L.; Liu, Q.; Chai, Y.; Dai, W.L. Facile Construction of Phosphate Incorporated Graphitic Carbon Nitride with Mesoporous Structure and Superior Performance for H2 Production. Int J Hydrogen Energy 2018, 43, 5591–5602, doi:10.1016/J.IJHYDENE.2018.01.185.
54. Corbrjdge, D.E.C. Infra-Red Analysis of Phosphorus Compounds. Journal of Applied Chemistry 1956, 6, 456–465, doi:10.1002/JCTB.5010061007.
55. Puziy, A.M.; Poddubnaya, O.I.; Martínez-Alonso, A.; Suárez-García, F.; Tascón, J.M.D. Surface Chemistry of Phosphorus-Containing Carbons of Lignocellulosic Origin. Carbon N Y 2005, 43, 2857–2868, doi:10.1016/J.CARBON.2005.06.014.

56. Corbridge, D.E.C.; Lowe, E.J. The Infra-Red Spectra of Some Inorganic Phosphorus Compounds. J Chem Soc 1954, 493–502, doi:10.1039/JR9540000493.
57. Daasch, L.W.; Smith, D.C. Infrared Spectra of Phosphorus Compounds. Anal Chem 1951, 23, 853–868, doi:10.1021/AC60054A008/ASSET/AC60054A008.FP.PNG_V03.
58. Wen, Y.; Qu, D.; An, L.; Gao, X.; Jiang, W.; Wu, D.; Yang, D.; Sun, Z. Defective G-C3N4 Prepared by the NaBH4 Reduction for High-Performance H2 Production. ACS Sustain Chem Eng 2019, 7, 2343–2349, doi:10.1021/ACSSUSCHEMENG.8B05124.
59. Solís, R.R.; Quintana, M.A.; Blázquez, G.; Calero, M.; Muñoz-Batista, M.J. Ruthenium Deposited onto Graphitic Carbon Modified with Boron for the Intensified Photocatalytic Production of Benzaldehyde. Catal Today 2023, 423, 114266, doi:10.1016/J.CATTOD.2023.114266.
60. Su, J.; Zhao, Y.; Xi, J. Phosphorus-Doped Carbon Nitride as Powerful Electrocatalyst for High-Power Vanadium Flow Battery. Electrochim Acta 2018, 286, 22–28, doi:10.1016/J.ELECTACTA.2018.08.044.
61. Škuta, R.; Matějka, V.; Foniok, K.; Smýkalová, A.; Cvejn, D.; Gabor, R.; Kormunda, M.; Smetana, B.; Novák, V.; Praus, P. On P-Doping of Graphitic Carbon Nitride with Hexachlorotriphosphazene as a Source of Phosphorus. Appl Surf Sci 2021, 552, 149490, doi:10.1016/J.APSUSC.2021.149490.
62. Zhang, F.; Li, J.; Wang, H.; Li, Y.; Liu, Y.; Qian, Q.; Jin, X.; Wang, X.; Zhang, J.; Zhang, G. Realizing Synergistic Effect of Electronic Modulation and Nanostructure Engineering over Graphitic Carbon Nitride for Highly Efficient Visible-Light H2 Production Coupled with Benzyl Alcohol Oxidation. Appl Catal B 2020, 269, 118772, doi:10.1016/J.APCATB.2020.118772.
63. Dementjev, A.P.; De Graaf, A.; Van de Sanden, M.C.M.; Maslakov, K.I.; Naumkin, A. V.; Serov, A.A. X-Ray Photoelectron Spectroscopy Reference Data for Identification of the C3N4 Phase in Carbon–Nitrogen Films. Diam Relat Mater 2000, 9, 1904–1907, doi:10.1016/S0925-9635(00)00345-9.
64. Caudillo-Flores, U.; Rodríguez-Padrón, D.; Muñoz-Batista, M.J.; Kubacka, A.; Luque, R.; Fernández-García, M. Facile Synthesis of B/g-C3N4 Composite Materials for the Continuous-Flow Selective Photo-Production of Acetone. Green Chemistry 2020, 22, 4975–4984, doi:10.1039/D0GC01326A.

65. Xu, H.; Wu, Z.; Wang, Y.; Lin, C. Enhanced Visible-Light Photocatalytic Activity from Graphene-like Boron Nitride Anchored on Graphitic Carbon Nitride Sheets. J Mater Sci 2017, 52, 9477–9490, doi:10.1007/S10853-017-1167-6.
66. Duan, Y.; Wang, Y.; Gan, L.; Meng, J.; Feng, Y.; Wang, K.; Zhou, K.; Wang, C.; Han, X.; Zhou, X. Amorphous Carbon Nitride with Three Coordinate Nitrogen (N3C) Vacancies for Exceptional NOx Abatement in Visible Light. Adv Energy Mater 2021, 11, 2004001, doi:10.1002/AENM.202004001.
67. Wu, J.; Zheng, X.; Jin, C.; Tian, J.; Yang, R. Ternary Doping of Phosphorus, Nitrogen, and Sulfur into Porous Carbon for Enhancing Electrocatalytic Oxygen Reduction. Carbon N Y 2015, 92, 327–338, doi:10.1016/J.CARBON.2015.05.013.
68. Zhang, Y.; Mori, T.; Ye, J.; Antonietti, M. Phosphorus-Doped Carbon Nitride Solid: Enhanced Electrical Conductivity and Photocurrent Generation. J Am Chem Soc 2010, 132, 6294–6295, doi:10.1021/JA101749Y/SUPPL_FILE/JA101749Y_SI_002.PDF.
69. Zhu, Y.P.; Ren, T.Z.; Yuan, Z.Y. Mesoporous Phosphorus-Doped g-C3N4 Nanostructured Flowers with Superior Photocatalytic Hydrogen Evolution Performance. ACS Appl Mater Interfaces 2015, 7, 16850–16856, doi:10.1021/ACSAMI.5B04947.
70. Zhang, L.; Chen, X.; Guan, J.; Jiang, Y.; Hou, T.; Mu, X. Facile Synthesis of Phosphorus Doped Graphitic Carbon Nitride Polymers with Enhanced Visible-Light Photocatalytic Activity. Mater Res Bull 2013, 48, 3485–3491, doi:10.1016/J.MATERRESBULL.2013.05.040.
71. Guo, S.; Deng, Z.; Li, M.; Jiang, B.; Tian, C.; Pan, Q.; Fu, H. Phosphorus-Doped Carbon Nitride Tubes with a Layered Micro-Nanostructure for Enhanced Visible-Light Photocatalytic Hydrogen Evolution. Angewandte Chemie International Edition 2016, 55, 1830–1834, doi:10.1002/ANIE.201508505.
72. Li, J.; Qi, Y.; Mei, Y.; Ma, S.; Li, Q.; Xin, B.; Yao, T.; Wu, J. Construction of Phosphorus-Doped Carbon Nitride/Phosphorus and Sulfur Co-Doped Carbon Nitride Isotype Heterojunction and Their Enhanced Photoactivity. J Colloid Interface Sci 2020, 566, 495–504, doi:10.1016/J.JCIS.2020.01.102.
73. Huang, J.; Li, D.; Li, R.; Zhang, Q.; Chen, T.; Liu, H.; Liu, Y.; Lv, W.; Liu, G. An Efficient Metal-Free Phosphorus and Oxygen Co-Doped g-C3N4 Photocatalyst with Enhanced Visible Light Photocatalytic Activity for the Degradation of Fluoroquinolone

Antibiotics. Chemical Engineering Journal 2019, 374, 242–253, doi:10.1016/J.CEJ.2019.05.175.

74. Gaskell, K.J.; Sherwood, P.M.A. Sodium Phosphate Dodecahydrate (Na3PO4·12H2O) by XPS. Surface Science Spectra 2002, 9, 75–82, doi:10.1116/11.20030103.
75. Cai, B.; Kang, R.; Guo, D.; Feng, J.; Ma, T.; Pan, H. An Eco-Friendly Acidic Catalyst Phosphorus-Doped Graphitic Carbon Nitride for Efficient Conversion of Fructose to 5-Hydroxymethylfurfural. Renew Energy 2022, 199, 1629–1638, doi:10.1016/J.RENENE.2022.09.050.
76. Jang, D.; Lee, S.; Kwon, N.H.; Kim, T.; Park, S.; Jang, K.Y.; Yoon, E.; Choi, S.; Han, J.; Lee, T.W.; et al. Preparation of Carbon Nitride Nanotubes with P-Doping and Their Photocatalytic Properties for Hydrogen Evolution. Carbon N Y 2023, 208, 290–302, doi:10.1016/J.CARBON.2023.03.038.
77. Wang, S.; He, F.; Zhao, X.; Zhang, J.; Ao, Z.; Wu, H.; Yin, Y.; Shi, L.; Xu, X.; Zhao, C.; et al. Phosphorous Doped Carbon Nitride Nanobelts for Photodegradation of Emerging Contaminants and Hydrogen Evolution. Appl Catal B 2019, 257, 117931, doi:10.1016/J.APCATB.2019.117931.
78. Zhou, Y.; Zhang, L.; Liu, J.; Fan, X.; Wang, B.; Wang, M.; Ren, W.; Wang, J.; Li, M.; Shi, J. Brand New P-Doped g-C3N4: Enhanced Photocatalytic Activity for H2 Evolution and Rhodamine B Degradation under Visible Light. J Mater Chem A Mater 2015, 3, 3862–3867, doi:10.1039/C4TA05292G.
79. Sun, Y. jie; He, J. yan; Zhang, D.; Wang, X. jing; Zhao, J.; Liu, R. hong; Li, F. tang Simultaneous Construction of Dual-Site Phosphorus Modified g-C3N4 and Its Synergistic Mechanism for Enhanced Visible-Light Photocatalytic Hydrogen Evolution. Appl Surf Sci 2020, 517, 146192, doi:10.1016/J.APSUSC.2020.146192.
80. Ran, J.; Ma, T.Y.; Gao, G.; Du, X.W.; Qiao, S.Z. Porous P-Doped Graphitic Carbon Nitride Nanosheets for Synergistically Enhanced Visible-Light Photocatalytic H2 Production. Energy Environ Sci 2015, 8, 3708–3717, doi:10.1039/C5EE02650D.
81. Fang, H. Bin; Zhang, X.H.; Wu, J.; Li, N.; Zheng, Y.Z.; Tao, X. Fragmented Phosphorus-Doped Graphitic Carbon Nitride Nanoflakes with Broad Sub-Bandgap Absorption for Highly Efficient Visible-Light Photocatalytic Hydrogen Evolution. Appl Catal B 2018, 225, 397–405, doi:10.1016/J.APCATB.2017.11.080.

82. Yang, H.; Zhou, Y.; Wang, Y.; Hu, S.; Wang, B.; Liao, Q.; Li, H.; Bao, J.; Ge, G.; Jia, S. Three-Dimensional Flower-like Phosphorus-Doped g-C3N4 with a High Surface Area for Visible-Light Photocatalytic Hydrogen Evolution. J Mater Chem A Mater 2018, 6, 16485–16494, doi:10.1039/C8TA05723K.
83. Liu, L.L.; Chen, F.; Wu, J.H.; Li, W.W.; Chen, J.J.; Yu, H.Q. Fine Tuning of Phosphorus Active Sites on G-C3N4 Nanosheets for Enhanced Photocatalytic Decontamination. J Mater Chem A Mater 2021, 9, 10933–10944, doi:10.1039/D1TA01537K.
84. Li, H.; Zhang, N.; Zhao, F.; Liu, T.; Wang, Y. Facile Fabrication of a Novel Au/Phosphorus-Doped g-C3N4 Photocatalyst with Excellent Visible Light Photocatalytic Activity. Catalysts 2020, 10, 701, doi:10.3390/CATAL10060701.
85. Hu, S.; Ma, L.; You, J.; Li, F.; Fan, Z.; Lu, G.; Liu, D.; Gui, J. Enhanced Visible Light Photocatalytic Performance of G-C3N4 Photocatalysts Co-Doped with Iron and Phosphorus. Appl Surf Sci 2014, 311, 164–171, doi:10.1016/J.APSUSC.2014.05.036.
86. Ding, F.; Feng, Y.P. Structural and Electronic Properties of C3N4−nPn (N=0,1,2,3,4). Comput Mater Sci 2004, 30, 364–370, doi:10.1016/J.COMMATSCI.2004.02.032.
87. Sun, H.; Park, S.J. Phosphorus-Doped g-C3N4/SnS Nanocomposite for Efficient Photocatalytic Reduction of Aqueous Cr(VI) under Visible Light. Appl Surf Sci 2020, 531, 147325, doi:10.1016/J.APSUSC.2020.147325.
88. Guo, S.; Tang, Y.; Xie, Y.; Tian, C.; Feng, Q.; Zhou, W.; Jiang, B. P-Doped Tubular g-C3N4 with Surface Carbon Defects: Universal Synthesis and Enhanced Visible-Light Photocatalytic Hydrogen Production. Appl Catal B 2017, 218, 664–671, doi:10.1016/J.APCATB.2017.07.022.
89. Feng, J.; Zhang, D.; Zhou, H.; Pi, M.; Wang, X.; Chen, S. Coupling P Nanostructures with P-Doped g-C3N4 As Efficient Visible Light Photocatalysts for H2 Evolution and RhB Degradation. ACS Sustain Chem Eng 2018, 6, 6342–6349, doi:10.1021/ACSSUSCHEMENG.8B00140.
90. Hardacre, C.; Mullan, E.A.; Rooney, D.W.; Thompson, J.M. Use of a Rotating Disc Reactor to Investigate the Heterogeneously Catalysed Oxidation of Cinnamyl Alcohol in Toluene and Ionic Liquids. J Catal 2005, 232, 355–365, doi:10.1016/J.JCAT.2005.03.014.
91. Samiolo, L.; Valigi, M.; Gazzoli, D.; Amadelli, R. Photo-Electro Catalytic Oxidation of Aromatic Alcohols on Visible Light-

Absorbing Nitrogen-Doped TiO2. Electrochim Acta 2010, 55, 7788–7795, doi:10.1016/J.ELECTACTA.2009.09.044.

92. Alam, M.S.; Rao, B.S.M.; Janata, E. ·OH Reactions with Aliphatic Alcohols: Evaluation of Kinetics by Direct Optical Absorption Measurement. A Pulse Radiolysis Study. Radiation Physics and Chemistry 2003, 67, 723–728, doi:10.1016/S0969-806X(03)00310-4.
93. Bouleghlimat, E.; Bethell, D.; Davies, P.R. The Photocatalytic Destruction of Cinnamic Acid and Cinnamyl Alcohol: Mechanism and the Effect of Aqueous Ions. Chemosphere 2020, 251, 126469, doi:10.1016/J.CHEMOSPHERE.2020.126469.
94. Qamar, M.; Elsayed, R.B.; Alhooshani, K.R.; Ahmed, M.I.; Bahnemann, D.W. Chemoselective and Highly Efficient Conversion of Aromatic Alcohols into Aldehydes Photo-Catalyzed by Ag3PO4 in Aqueous Suspension under Simulated Sunlight. Catal Commun 2015, 58, 34–39, doi:10.1016/J.CATCOM.2014.08.025.
95. Srinivasu, K.; Modak, B.; Ghosh, S.K. Porous Graphitic Carbon Nitride: A Possible Metal-Free Photocatalyst for Water Splitting. Journal of Physical Chemistry C 2014, 118, 26479–26484, doi:10.1021/JP506538D/SUPPL_FILE/JP506538D_SI_001.PDF.
96. Wang, J.; Bian, Z.; Zhu, J.; Li, H. Ordered Mesoporous TiO2 with Exposed (001) Facets and Enhanced Activity in Photocatalytic Selective Oxidation of Alcohols. J Mater Chem A Mater 2012, 1, 1296–1302, doi:10.1039/C2TA00035K.
97. Bielski, B.H.J.; Cabelli, D.E.; Arudi, R.L.; Ross, A.B. Reactivity of HO2/O−2 Radicals in Aqueous Solution. J Phys Chem Ref Data 1985, 14, 1041–1100, doi:10.1063/1.555739.
98. Anbar, M.; Neta, P. A Compilation of Specific Bimolecular Rate Constants for the Reactions of Hydrated Electrons, Hydrogen Atoms and Hydroxyl Radicals with Inorganic and Organic Compounds in Aqueous Solution. Int J Appl Radiat Isot 1967, 18, 493–523, doi:10.1016/0020-708X(67)90115-9.
99. Nien Schuchmann, M.; Bothe, E.; von Sonntag, J.; von Sonntag, C. Reaction of OH Radicals with Benzoquinone in Aqueous Solutions. A Pulse Radiolysis Study. Journal of the Chemical Society, Perkin Transactions 2 1998, 791–796, doi:10.1039/A708772A.
100. Garg, S.; Rose, A.L.; Waite, T.D. Production of Reactive Oxygen Species on Photolysis of Dilute Aqueous Quinone Solutions.

Photochem Photobiol 2007, 83, 904–913, doi:10.1111/J.1751-1097.2007.00075.X.

101. Alegría, A.E.; Ferrer, A.; Santiago, G.; Sepúlveda, E.; Flores, W. Photochemistry of Water-Soluble Quinones. Production of the Hydroxyl Radical, Singlet Oxygen and the Superoxide Ion. J Photochem Photobiol A Chem 1999, 127, 57–65, doi:10.1016/S1010-6030(99)00138-0.
102. Bors, W.; Saran, M.; Michel, C. Pulse-Radiolytic Investigations of Catechols and Catecholamines II. Reactions of Tiron with Oxygen Radical Species. BBA - General Subjects 1979, 582, 537–542, doi:10.1016/0304-4165(79)90145-4.
103. Song, Y.; Wang, H.; Liu, G.; Wang, H.; Li, L.; Yu, Y.; Wu, L. Constructing Surface Synergistic Effect in Cu-Cu2O Hybrids and Monolayer H1.4Ti1.65O4·H2O Nanosheets for Selective Cinnamyl Alcohol Oxidation to Cinnamaldehyde. J Catal 2019, 370, 461–469, doi:10.1016/J.JCAT.2019.01.016.
104. Shah, B.R.; Patel, U.D. Mechanistic Aspects of Photocatalytic Degradation of Lindane by TiO2 in the Presence of Oxalic Acid and EDTA as Hole-Scavengers. J Environ Chem Eng 2021, 9, 105458, doi:10.1016/J.JECE.2021.105458.
105. Ershov, B.G.; Janata, E.; Alam, M.S.; Gordeev, A. V. A Pulse Radiolysis Study of the Reactions of the Hydrated Electron and Hydroxyl Radical with the Oxalate Ion in Neutral Aqueous Solution. High Energy Chemistry 2008, 42, 1–6, doi:10.1134/s0018143908010013.
106. Shah, B.R.; Patel, U.D. Mechanistic Aspects of Photocatalytic Degradation of Lindane by TiO2 in the Presence of Oxalic Acid and EDTA as Hole-Scavengers. J Environ Chem Eng 2021, 9, 105458, doi:10.1016/J.JECE.2021.105458.
107. Dai, X.; Xie, M.; Meng, S.; Fu, X.; Chen, S. Coupled Systems for Selective Oxidation of Aromatic Alcohols to Aldehydes and Reduction of Nitrobenzene into Aniline Using CdS/g-C3N4 Photocatalyst under Visible Light Irradiation. Appl Catal B 2014, 158–159, 382–390, doi:10.1016/J.APCATB.2014.04.035.
108. Koppenol, W.H.; Stanbury, D.M.; Bounds, P.L. Electrode Potentials of Partially Reduced Oxygen Species, from Dioxygen to Water. Free Radic Biol Med 2010, 49, 317–322, doi:10.1016/J.FREERADBIOMED.2010.04.011.
109. Wood, P.M. The Potential Diagram for Oxygen at PH 7. Biochemical Journal 1988, 253, 287–289, doi:10.1042/BJ2530287.

110. Niklasson, I.B.; Delaine, T.; Islam, M.N.; Karlsson, R.; Luthman, K.; Karlberg, A.T. Cinnamyl Alcohol Oxidizes Rapidly upon Air Exposure. Contact Dermatitis 2013, 68, 129–138, doi:10.1111/COD.12009.
111. Bouleghlimat, E.; Bethell, D.; Davies, P.R. The Photocatalytic Destruction of Cinnamic Acid and Cinnamyl Alcohol: Mechanism and the Effect of Aqueous Ions. Chemosphere 2020, 251, 126469, doi:10.1016/J.CHEMOSPHERE.2020.126469.
112. Wu, G.; Brett, G.L.; Cao, E.; Constantinou, A.; Ellis, P.; Kuhn, S.; Hutchings, G.J.; Bethell, D.; Gavriilidis, A. Oxidation of Cinnamyl Alcohol Using Bimetallic Au–Pd/TiO2 Catalysts: A Deactivation Study in a Continuous Flow Packed Bed Microreactor. Catal Sci Technol 2016, 6, 4749–4758, doi:10.1039/C6CY00232C.
113. Wang, Y.; Prinsen, P.; Mangin, F.; Yepez, A.; Pineda, A.; Rodríguez-Castellón, E.; Hasan Shah Gilani, M.R.; Xu, G.; Len, C.; Luque, R. Mechanistic Insights into the Microwave-Assisted Cinnamyl Alcohol Oxidation Using Supported Iron and Palladium Catalysts. Molecular Catalysis 2019, 474, 110409, doi:10.1016/J.MCAT.2019.110409.
114. Ellis, L.B.; Wackett, L.P. Use of the University of Minnesota Biocatalysis/Biodegradation Database for Study of Microbial Degradation. Microbial Informatics and Experimentation 2012 2:1 2012, 2, 1–10, doi:10.1186/2042-5783-2-1.

CHAPTER 6. PAPER FOUR

Sulfonic grafted graphitic-like carbon nitride for the improved photocatalytic production of benzaldehyde in water

Applied Surface Science 656 (2024) 159717

https://doi.org/10.1016/j.apsusc.2024.159717

M. Alejandra Quintana, Rafael R. Solís, Gabriel Blázquez,

Mónica Calero, Mario J. Muñoz-Batista

Abstract

This work reports the modification of graphitic carbon nitride (CN) through sulfonation (SCN) as an enhanced strategy for photocatalytic activity during the oxidation of benzyl alcohol to benzaldehyde. CN was prepared from melamine and functionalized with -SO_3H groups using different doses of chlorosulfonic acid. The textural, structural, morphological, chemical, and optical properties of the prepared samples were characterized by diverse techniques. The increase in the doping dose produced, a decrease in surface area, a blue-shifted absorption edge under irradiation, and a decrease in the recombination charges. The -SO_3H improved the kinetics of benzyl alcohol oxidation (BA) in aqueous solution and raised the selectivity to benzaldehyde (BD). An optimum dosage of precursor led to an SCN sample with the highest removal rate and selectivity. This optimized sample was selected for the study of the reactive oxidant species involved during the photocatalytic process, suggesting that the species with the highest contribution during BA oxidation was the superoxide radical, especially in terms of selectivity for the aldehyde formation. This work examples the modification of carbon nitride to enhance the production of an aldehyde with interest in the industry under a sustainable scheme that involves the transformation of light into chemical energy in water.

Keywords: photocatalysis, sulfonated carbon nitride, benzaldehyde

6.1. INTRODUCTION

At the industrial scale, the synthesis of benzaldehyde has been carried out from the hydrolysis of benzyl chloride or the oxidation of toluene [1]. There are other technologically feasible routes already used in the past, such as the oxidation of benzyl alcohol, the reduction of benzoyl chloride, and the reaction of carbon monoxide and benzene. However, their low rentability makes them no longer industrially useful. Currently, the oxidation of toluene with air is the most popular process worldwide. Nonetheless, high temperatures and pressures are required, and low yields of aldehyde are produced due to the large formation of by-products [2]. This is the main reason that aims at the research of alternative processes that can overcome the current drawbacks of benzyl alcohol oxidation [3].

The synthesis of benzaldehyde from the oxidation of precursors such as benzyl alcohol by photocatalysis has acquired importance due to the sustainability and green aspect of the technology. Among all the photocatalysts used to date, in which TiO_2 outstands due to the high activity, abundance, and low cost, graphitic carbon nitride has emerged as a non-metallic semiconductor with a lower bandgap compared to TiO_2, i.e. 2.7 vs 3.2 eV [4]. Graphitic carbon nitride is a free-meal semiconductor that displays interesting properties for photocatalytic selective synthesis of organic compounds [5], concretely a high activity for the oxidation of alcohols to aldehydes [6]. The photo-oxidation of benzyl alcohols by carbon nitride with the competitive conversion of the alcohol and high selectivity to the aldehyde relies on the use of organic solvents (acetonitrile, trifluorotoluene), high temperatures (60-150°C) and O_2 pressure up to 8 bar [7–9]. Diverse strategies are currently under research to improve the activity of g-C_3N_4, promoting a competitive activity under milder conditions of pressure and temperature without the need to use toxic and expensive organic solvents [10]. For instance, by raising the mesoporosity of g-C_3N_4 [11]. The doping with no metals such as sulfur has provided evidence of improvements concerning bare g-C_3N_4 in the photocatalytic production of H_2 or photocatalytic reduction of CO_2, due to the modification of the optical and/or electrical properties [12].

The doping of C_3N_4 with sulfur has been carried out with diverse precursors, thiourea the most popular [13–15]. However, the amount of sulfur cannot be controlled unless it is mixed with urea [16]. The amount of S doping has been controlled in diverse synthesis methods depending on the sulfur precursor used. For instance, trithiocyanuric acid mixed with dicyandiamide at different ratios, followed by further thermal treatment, led to control of the S amount inserted in the polymeric structure [17]. Also sublimed sulfur mixed with C_3N_4 and thermal treatment has been successfully used to dope the structure [18,19]. Sulfonation is a functionalization strategy that confers amphoteric properties to carbon nitride. The incorporation of -SO_3H groups display Brønsted acid sites to the already present Brønsted base of the terminal amine groups [20]. The presence of both acid and base groups has been demonstrated interesting properties in certain reactions. Sulfonated graphitic carbon was first reported as a high-active and low-cost organo-sulfonated heterogeneous acid catalyst for the synthesis of biodiesel in 2016 [21], enabling to conduct the reaction at milder temperature conditions. The functionalization with sulfonic acid has been also proven effective in certain organic synthesis routes such as the Knoevenagel condensation [20]. Furthermore, this sulfonation strategy has shown effectiveness in the conversion of biomass-derived saccharides into 5-hydroxymethylfurfural, a precursor in the obtention of biodiesel and other fuels [22]. Besides, the use of sulfonic groups in carbon nitride has been tested in the catalytic synthesis of heterocycles in molecules with added value in the pharmaceutical industry [23]. Although these works have greatly demonstrated the activity of the material after sulfonation, they have been used as heterogeneous catalysts at mild conditions, not taking advantage of the semiconductor character of carbon nitride under a photocatalysis scheme. Few works have tackled the sulfonation of graphitic carbon nitride for photocatalytic purposes. Recently work has assessed the effect of the presence of the sulfonic groups in carbon nitride using sulfamic acid as a precursor for the photocatalytic production of H_2 [24]. The presence of sulfonic acid groups has been claimed to create an inductive effect that enhances the charge transfer dynamics and inhibits their recombination. The sulfonic tailoring of g-C_3N_4 has been also tested for the photocatalytic reduction of Cr (VI) [25], using sulfuric acid in a two-pot step synthesis. The presence of sulfonic groups resulted in beneficial to the charge-

separation ability triggering more charge carrier density. Similarly, the modification with sulfanilic acid led to similar results when using the sulfonic-modified material for the photocatalytic reduction of Cr (VI) [26], as the presence of -SO_3H groups raised the capacity for separating photo-generated carriers and increased the transport efficiency, supporting consequently the photocatalytic reaction.

This work reports a study of the benefits of sulfonic functionalization of graphitic carbon nitride with application to selective organic synthesis of benzyl alcohol to benzaldehyde in aqueous media, without the use of any organic solvent. Different sulfonated dosages were tested aiming at the optimization of the precursor incorporated. The textural, structural, chemical, morphological, and optical properties of the sulfonated g-C_3N_4 (SCN) were analyzed by N_2 physisorption, XRD, FTIR, XPS, elemental analysis, STEM, DRS-UV-visible and photoluminescence. The photocatalytic activity was tested for the selective oxidation of benzyl alcohol to benzaldehyde under UVA (365 nm) irradiation. The SCN samples displayed better activity and selectivity if compared to the bare carbon nitride sample. The plausible mechanism of the photocatalytic process was assessed with the optimum SCN sample, leading to a similar contribution of superoxide radicals, hydroxyl radicals, and photogenerated holes.

6.2. EXPERIMENTAL SECTION

6.2.1. Materials and catalyst preparation

All the reagents used were analytical grade and used as received. Ultrapure water (18.2 MΩ·cm) from a Direct-Q®-UV device (Millipore®) was used for the preparation of all the solutions. The acetonitrile and trifluoroacetic acid used for the chromatographic analysis was HPLC grade.

The graphitic carbon nitride (g-C_3N_4), named CN, was prepared from the polymerization of melamine [27]. Melamine (>99%) was submitted to thermal treatment under static air at 500 °C for 1 h, with a heating rate of 10 °C min^{-1}. The resulting yellowish solid material was crushed in a mortar.

The sulfonated graphitic carbon nitride (g-S-C_3N_4), denoted as SCN was prepared by adapting a previously reported recipe [21,22]. A scheme of the synthesis process is depicted in Fig. 6.1. The sulfonic acid groups were placed in the CN structure by using chlorosulfonic acid (99%) as the sulfur precursor. Briefly, 2 g of CN was suspended in 20 mL of dichloromethane (99%) in a beaker under vigorous stirring. Then, a certain volume of chlorosulfonic acid (x=0.5-15 mL) was dropwise added to the above suspension and further stirred for 3 h until a homogeneous paste was obtained. The resulting paste was washed with 20 mL of methanol (99%) four times. The washed solid was recovered by centrifugation and dried at 80 ºC. The resulting light yellowish powder was ground in a mortar.

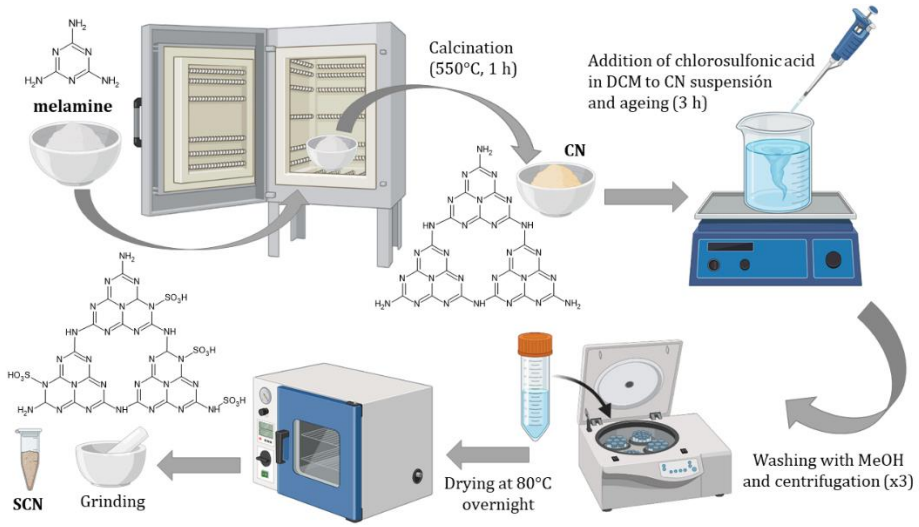

Fig. 6.1 *Schematic representation of the synthesis of the sulfonated carbon nitride*

6.2.2. Characterization of the catalysts

The crystalline properties of the samples were studied by X-Ray Diffraction (XRD) in a Bruker D8 Discover instrument equipped with a Pilatus 3R 100K-A detector, using Cu Kα radiation (1.5406 Å). The diffractograms were recorded within a 2θ range of 5–65° at a rate of 0.034° min^{-1}. The freeware QualX® [28] was used to process the diffractograms and obtain the crystallite size ($L_{crystal}$) and the interlayer spacing (d_{layer}). The relation $L_{crystal}/d_{layer}$ was used as a rough approximation of the number of layers estimation [29]. The structural properties were further assessed by Fourier Transform InfraRed (FTIR)

Spectroscopy in a device model Spectrum 65 from Perkin-Elmer monitoring the absorbance within 550-4000 cm^{-1}. The textural properties were studied by adsorption-desorption isotherms with N_2 at 77 K carried out in a Sync 200 device from 3P Instruments©. Firstly, samples were outgassed under a vacuum at 150 ºC for 12 h. The specific surface area was calculated by the Brunauer-Emmett-Teller method (S_{BET}), and the total specific pore volume (V_T) was obtained from the N_2 uptake at p/p_0~0.99. The Barrett, Joyner, and Halenda method (BJH) was applied to analyze the average (4V/A) and most frequent (dV/dD) mesopore diameter. The morphology and elemental composition of the nanoparticles were studied by Scanning Transmission Electron Microscopy (STEM) in a Thermo Scientific™ Talos™ F200X (200 kV) equipped with Energy Dispersive Spectroscopy (EDS). The elemental composition was analyzed in a TrueSpec® Micro CHNS analyzer from Leco instruments. The chemical environment in the surface was studied by X-ray Photoelectron Spectroscopy (XPS), in a Kratos AXIS UltraDLD device working with an X-ray source from Al Kα. The XPS spectra were referenced to the C1s peak of adventitious carbon at 284.6 eV. The software XPSpeak 4.1® was used for the deconvolution of the peaks, considering a Shirley background correction. The optical properties were evaluated through Diffuse Reflectance Spectroscopy (DRS) and photoluminescence. The DRS-UV-visible spectra were acquired in a Varian Cary 5E device equipped with a praying mantis accessory. The absorbance and reflectance spectra were registered within 200-2000 nm. The reflectance was used to determine the Kubelka-Munk Function, $F(R_\infty)$, and the bandgap was estimated from the Tauc plot method, considering indirect electron transitions. The photoluminescence was measured by fluorescence spectrometry in a Varian Cary Eclipse fluorometer using 365 nm as the excitation wavelength.

6.2.3. Photocatalytic production of benzaldehyde

The photocatalytic activity of the prepared materials was tested in the oxidative reaction of benzyl alcohol to benzaldehyde. The experiments were conducted in a discontinuous annular photoreactor, already described in the literature [30]. In this system the aqueous solution of benzyl alcohol, initially at 0.5 mM, with the photocatalyst in the slurry was continuously pumped from an auxiliary tank, kept at a constant temperature of 20 ºC with a cooling system, to the annular space of a

cylindrical borosilicate glass reactor. In the center, two UVA lamps were located (Sylvania® F11W T5 BL368 lamp, emitting at 365 nm, 9 W each). Air was bubbled into the auxiliary tank to ensure dissolved O_2. Before the irradiation, an adsorption step of 30 min was carried out. The temporal evolution of the concentration of benzyl alcohol (BA) and benzaldehyde (BD) was monitored by extracting samples. The samples were filtered (syringe filters, Millipore Millex-GV PVDF, 0.45 µm) to remove the photocatalyst.

The reactive oxidative species involved in the photocatalytic process were tentatively assessed by the addition of chemical scavengers [31,32]. The influence of superoxide radical was evaluated by replacing the air bubbling with N_2, with the addition of p-benzoquinone (p-BZQ, 1 mM), or disodium 4,5-dihydroxybenzene-1,3-disulfonate (tiron, 1 mM). The impact of hydroxyl radicals on the BA degradation was evaluated with the addition of tert-butyl alcohol (TBA, 10 mM). The photo-generated hole contribution was eliminated with the addition of oxalic acid (10 mM).

The concentration of BA and BD was determined by High-Pressure Liquid Chromatography (HPLC) in an Alliance e2695 HPLC device from Waters™ coupled to a 2998 photodiode array with UV-visible detection. The chromatographic analysis was carried out with a Zorbax Bonus-RP column (4.6×150 mm, 5 µm). An isocratic method of acetonitrile (A) and acidified water with 0.1% (vol.) of trifluoroacetic acid (B) was pumped at a rate of 1 mL min^{-1} and A: B ratio of 30:70. The quantification was conducted at 215 and 248 nm for the BA and BD, respectively. The limit of detection (LOD) was 10.0 µM for BA and 2.2 µM for BD. The limit of quantification (LOQ) was 33.0 µM for BA and 7.4 µM for BD.

The presence of short-chain organic acids as final oxidation products was analyzed by HPLC using a CoreGel 87H3 column (7.8×300 mm) under isocratic pumping of acidified water solution (4 mM H_2SO_4) at 1 mL min^{-1} and detection at 210 nm.

The pseudo-first order rate constant of BA abatement (k_{BA}) was calculated as a mere tool for comparison purposes. Moreover, the temporal evolution of the selectivity to benzaldehyde (S_{BD}) was determined and the average value in the reaction interval was calculated as follows:

$$S_{BD} = \frac{\int S(t)dt}{(t-0)} \tag{6.1}$$

The quantum efficiency (Q_E) of BA degradation was determined according to the IUPAC recommended procedure [33–35], which defines the Q_E as the proportion of the number of molecules reacting (r_{BA}) with the number of photons that interact with the catalyst, i.e. the photon absorption rate ($e^{\alpha,\nu}$) [36].

$$Q_E = \frac{r_{BA_0}}{e^{\alpha,\nu}} = \frac{k_{BA}C_{BA_0}}{e^{\alpha,\nu}}\left(\frac{\text{mol m}^{-3}\,\text{s}^{-1}}{\text{Einstein m}^{-3}\,\text{s}^{-1}}\right) \tag{6.2}$$

where $r_{BA,0}$ is the initial reaction rate. The quantification of the photon absorption rate ($e^{\alpha,\nu}$), and the radiative transfer equation (RTE) was completed taking the geometry of the used photoreactor into account [30]. Previously, the estimation of the optical properties of the catalytic suspensions was required. A detailed description of the mathematical procedure for the estimation of the optical properties and photon rate estimations is provided in previous works [30,37]. Fig. 6.2 illustrates the variation of the Local Volumetric Rate of Photon Absorption (LVRPA) with the radial and longitudinal coordinates of the annular space of the photoreactor of the different samples.

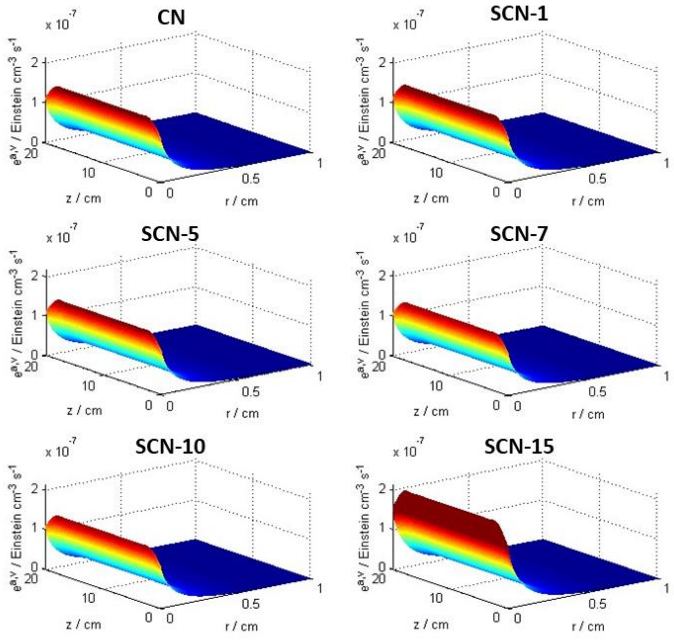

Fig. 6.2 *Local volumetric rate of photon absorption (LVRPA, $e^{\alpha,\nu}$) of SCN samples.*

Using a similar procedure extensively described in previous contributions [38], an analysis of the optical properties of the samples under reaction conditions was carried out based on the spectral absorption coefficient, the spectral scattering coefficient, and the scattering phase [30,37]. The comparison between the aforementioned optical coefficients of the samples reveals highly similar profiles, with the most noticeable variations observed for the estimated absorption coefficient of the sample SCN-15., which is in line with the results obtained from UV-vis spectroscopy, which will be further discussed. The modelling allows calculating the average volumetric rate of photon absorption around 1.58×10^{-8} Einstein cm^{-3} s^{-1} ($\pm0.1\times10^{-8}$) for samples CN, SCN-1, SCN-5, SCN-7, and SCN-10, while the observable was increased by a factor of 1.4 for the sample with the highest concentration of S (SCN-15). Regarding the LVRPA geometric profiles, an expected pattern according to the reactor geometry was obtained [30,37]. Maximum local values of photon absorption were obtained at the radial coordinate (r = 0), associated with the nearest zone of the irradiation source. Such values are progressively decreasing as the evaluated point moves away from the illumination source. Axial coordinate (z) describes a common edge effect usually reported for fluorescent lamps. Nevertheless, considering that catalytic measurements are conducted under vigorous and constant agitation, the quantum yields of the samples were determined using the average value of the photon rate throughout the entire reactor volume.

6.3. RESULTS AND DISCUSSION

6.3.1. Characterization of the sulfonated carbon nitride

The changes in the crystalline structure during the sulfonation of graphitic carbon nitride were assessed by the XRD technique. Fig. 6.3A illustrates the changes in the diffractograms when raising the sulfonation degree. The XRD pattern reported for graphitic carbon nitride includes two well-defined peaks [39]. The most intensive regarding the (002) plane is due to the aromatic interaction of π-π^* electrons between layers located at 27.4°. A second peak, much less intense, appears at 13.1° corresponding to the (100), ascribed to the intralayer spacing of the tri-s-triazine units. The bare CN samples also described a weak peak at

low intensity centered at 17.5°, which can be understood as the plane that appears as a consequence of the diffraction plane of the repeating motifs of the s-triazine unit of the aromatic system [29,40,41]. The bare CN sample, prepared from the polymerization of melamine, describes the (002) and (100) planes with a good definition which provides evidence of a successful formation of graphitic heptazine units. The sulfonation of the surface of CN led to considerable changes in the XRD patterns. The sulfonic group insertion creates surface defects that generate lattice stress and decrease the crystallinity of the CN structure [24]. At a low dose of sulfonation, the intensity of the (002) peak decreases. The rise of the sulfonation degree promotes a gradual decrease of the interlayer peak [20] as visible in SCN1 and SCN5 samples, which provides evidence of a chemical delamination effect due to the chemical attack of chlorosulfonic acid [42–44]. When raising the dose, the (002) peak was poorly defined, it appeared broadened and shifted about 0.8° to a lower diffraction angle. This moving of the peak to lower values provides evidence of a plausible agglomeration effect [45]. Also, other peaks regarding S-based organic compounds appear to detriment the pattern of the g-C_3N_4 structure, suggesting considerable destruction of the polymeric structure, as reported previously when doping with high chlorosulfonic dosage [21]. Concerning the crystallite size, an increase was registered at a high doping level, raising the size from 5.77 nm in bare CN to 12-13 nm in the highest dosages. The presence of functional groups may act as a platform to increase the crystal size as reported in other functionalization strategies [46].

The structural changes due to the sulfonation of graphitic carbon nitride were studied by FTIR, see Fig. 6.3B. CN displays a graphite-like sp^2-bonded structure with a very characteristic fingerprint in the FTIR spectrum [47]. The insertion of sulfur generated considerable changes in the FTIR spectra due to a change in the electronic environment after sulfonation [48], especially appreciable at the highest chlorosulfonic acid ratio. Either CN or SCN samples showed the presence of a wide band within 3000-3500 cm^{-1}, which is ascribed mainly to the vibration of N-H bonds in -NH_2 and -NH- terminal groups [49,50] and water molecules. Additionally, the presence of sulfonic groups also may lead to the contribution of this peak [23], which is slightly visible in the SCN with the highest S proportion. There was no presence of a peak at 2360 cm^{-1} in none of the samples, which provides evidence of a lack of terminal nitrile

groups [51]. The peak at 801 cm^{-1}, completely defined in the CN sample, appears as a consequence of out-of-plane vibration [50,52], and is partially decreased as the CN is treated with a higher amount of chlorosulfonic acid. Moreover, this peak is shifted to a lower wavelength in the SCN samples, as reported in the literature and linked to the presence of sulfonated groups [20,22]. The CN sample defines a group of peaks within 900-1800 cm^{-1} as a consequence of the vibration of the bonds of the tri-s-triazine rings. The well-defined peaks located at 1620, 1530, and 1390 cm^{-1} are assigned to the aromatic C-N stretching vibration [50,53]. Remarkably, the peak at 1620 cm^{-1} defined in the untreated CN increases to a high extent as the amount of chlorosulfonic acid is raised. This fact can be attributable to the presence of C=O groups due to an oxidation effect of chlorosulfonic acid [54]. By the same token, the sulfur functionalization was also evidenced by the definition of two new peaks in the SCN samples at ca. 1150 and 1069 cm^{-1}, being the latest better defined, especially in the SCN-10 sample. The peak resulting in C-S vibration that appears at 980 cm^{-1} [55] was only slightly observable in the SCN-10 sample. These two vibration peaks are ascribed, respectively, to asymmetric and symmetric vibration of S=O if sulfonic groups [20,56,57]. The presence of a peak at roughly 1410 cm^{-1} has been reported in the literature due to SO_2 vibration in the sulfonic group; however, due to the overlapping with original CN bands, this peak was not well observed [56]. Furthermore, the peaks that appear at 1310 and 1230 cm^{-1}, which are ascribed to the respective stretching vibrations of C-N-(C)-C or C-NH-C bonds [50], are also altered with the insertion of sulfur in the structure, being almost erased at the highest chlorosulfonic dosage. Finally, at low wavenumber, some bands appear as a result of the presence of sulfonic groups. A peak located in 575 cm^{-1} is attributed to the bending vibration of -S=O [25,44,58]. Furthermore, a new peak emerged in the SCN samples with the highest S content, located at 785 cm^{-1} near the out-of-plane vibration of the triazine ring, which is related to the C-N-S structure in the surface sulfamic acid [25,44,58].

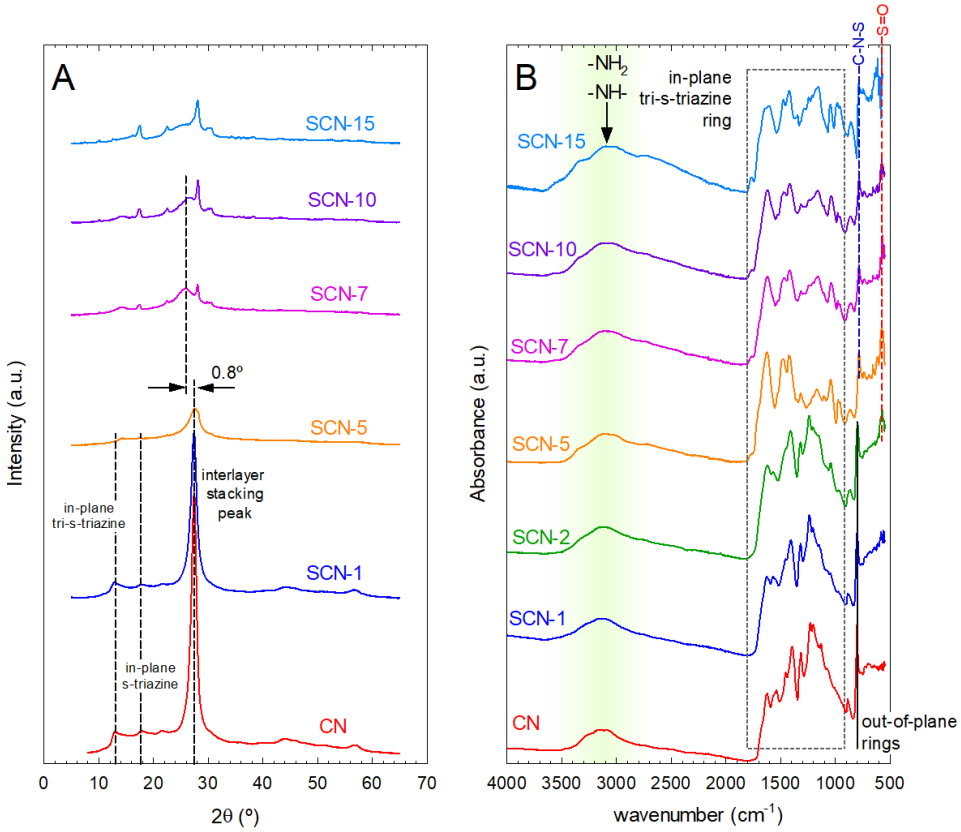

Fig. 6.3 *XRD diffractograms (A) and FTIR spectra (B) of SCN samples*

The textural properties are summarized in Table 6.1 Crystal, textural, and optical properties of the SCN samples The BET area of the unmodified CN led to 9.1 m^2 g^{-1}. The treatment with chlorosulfonic acid led to a decrease in the surface area, i.e. the sample treated with the highest acid dose displayed the lowest value, i.e. below 1 m^2 g^{-1}. The results of XRD suggest a delamination effect; however, the formation of ionic surface groups may promote the formation of electric interaction, which entails a higher agglomeration of the graphitic sheets as reported in the literature [21].

Table 6.1 *Crystal, textural, and optical properties of the SCN samples*

Sample	$L_{crystal}$ (nm)	d_{Layer} (Å)	n	S_{BET} ($m^2\ g^{-1}$)	V_T ($cm^3\ g^{-1}$)	$D_{average}$ (nm)	$D_{frequent}$ (nm)	E_{BG} (eV)
CN	5.77	3.250	18	9.1	0.050	30.4	3.5	2.7
SCN-0.5	-	-	-	10.4	0.052	29.2	3.5	-
SCN-1	5.34	3.252	16	9.2	0.046	29.9	2.6	2.9
SCN-1.5	-	-	-	9.0	0.043	26.7	3.1	-
SCN-2	-	-	-	6.4	0.032	37.9	2.6	-
SCN-5	12.50	3.177	39	4.7	0.017	22.4	3.1	2.8
SCN-7	13.36	3.171	42	2.1	0.009	21.5	3.5	2.8
SCN-10	13.36	3.177	42	0.9	0.004	24.1	3.5	2.8
SCN-15	13.36	3.180	42	0.7	0.003	18.2	3.5	2.7

$L_{crystal}$: crystallite size obtained from (002) peak with Scherrer's equation; d_{layer}: interlayer spacing obtained from (002) peak; n: number of layers; S_{BET}: total specific surface area by BET method; V_T: total pore volume; $D_{average}$ and $D_{frequent}$: average and most frequent pore diameter by BJH method, respectively; E_{BG}: bandgap by Tauc plot method.

The chemical composition of the samples was determined by elemental analysis, leading to the proportion of N, C, H, and S. The ratio N/C, shown in Table 6.2, C was kept after chlorosulfonic acid addition. Pertaining to the amount of sulfur fixed during the synthesis process, it seems that there is an optimum of S incorporation within samples SCN-7 and SCN-10, a higher addition of chlorosulfonic acid may lead to reaction due to its acid character and contribute to the destruction of the structure rather than the grafting of terminal –SO_3H.

Table 6.2 *Elemental analysis of the SCN samples (wt. %)*

Sample	N	C	H	S	N/C
CN	60.8	35.1	1.8	-	1.73
SCN-5	42.4	24.8	3.2	6.5	1.70
SCN-7	40.9	22.8	3.1	9.1	1.79
SCN-10	39.3	23.9	3.2	9.1	1.64
SCN-15	43.6	24.9	3.0	5.5	1.75

The chemical composition of the SCN-7 surface was studied by the XPS technique, see Fig. 6.4. The high-resolution XPS spectra in the C_{1s}

region defined the three typical peaks reported in g-C_3N_4 structures [59], i.e. the peaks in sp^2 N = C-N (288.6 eV), sp^3 C-C/C-N (285.8 eV), and sp^2 C-C/C = C (284.5 eV) bonds [37,60]. Additionally, due to the modification with S, an intermediate peak centered at 287.5 eV was successfully included in the deconvolution, representative of C-S bonds [55,61,62]. If the relative importance of each contribution is compared in bare CN and sulfonated SCN-7, an important decrease of the sp^2 N-C=N is depicted after modification with chlorosulfonic acid. The high resolution of N_{1s} spectra was deconvoluted in the contributions N–C=N (N_2C, 397.8 eV), C_3–N (N_3C, 399.3 eV), and N-SO_3H (400.3 eV) [58]. The contribution of –NH_x bonds of terminal amine groups, found at ca. 401 eV [63] for CN was displaced to lower values, suggesting the presence of N-SO_3H bonds. The high resolution of O_{1s} in SCN-7 revealed the presence of mainly two contributions, i.e. 531.7 and 530.2 eV. The lowest value can be attributed to –SO_3H groups while the highest is linked to residual N═C–O/C═O/–OH groups [55]. The unmodified sample, i.e. CN, displayed a much lower oxygen proportion than the SCN-7, with a very different pattern, in which a deconvoluted peak at 533.2 eV [64], attributable to C-O, was outlined as the major contribution. The region of S_{2p} was deconvoluted in two contributions located at 167.1 and 168.3 eV. The peaks defined over 168 eV are sulfonate or sulfate species [65]. The deconvoluted peak centered at 168.3 eV, accounting for 40% of the whole S_{2p} peak, can be attributed to sulfonic groups [66,67] appearing after the linkage to terminal –NH_x groups as N-SO_3H [44,58,68]. The peak located at 167.1 eV, whose contribution was 60% of all the S_{2p} peak, can be attributed to sulfoxide bonds, C–S(═O)–C, whose XPS peaks are reported within 166-168 eV [55,69,70]. This contribution is consistent with the C-S bond detected in the C 1s spectrum. It should be noted that the carbons in the resulting C–S(═O)–C group would still be aromatic. The presence of sulfoxide suggests the doping of the S atom in the heptazine unit by the replacement of N. As this exchange is not isoelectronic, the oxidation of C-S-C moieties to a sulfoxide C–S(═O)–C is expected [55], keeping the aromaticity of the ring. No peaks at ca. 164 eV of thiol -SH groups [66] or sulfide C-S-C at ca. 161 eV [71] were observed. A quantification analysis in SCN-7 led to a 7.03% (wt.) of S.

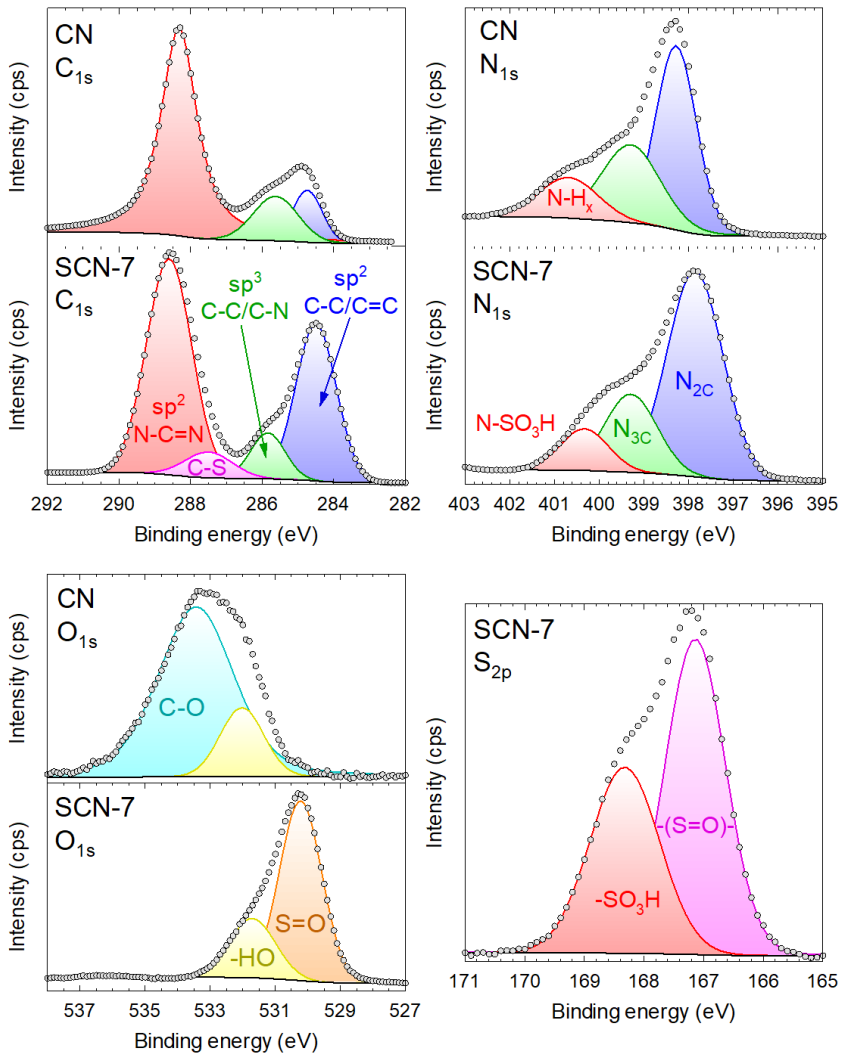

Fig. 6.4 *High-resolution XPS spectra of C_{1s}, N_{1s}, O_{1s}, and S_{2p} of bare CN and SCN-7*

Fig. 6.5 illustrates some of the selected STEM micrographs obtained from some selected samples. The particles displayed irregular shapes of thin plates of different sizes, but over 500 nm. The bare CN particles displayed more opaqueness than the samples modified with chlorosulfonic acid whose sheets seem to be more transparent to the TEM images. Furthermore, the particles of those samples modified with the acid, especially at high proportions, i.e. SCN-7 and SCN-10, depicted certain breakage of the sheets leading to smaller fragments

that appeared agglomerated in bigger formations. This evidence may provide additional support to the effect of delamination already deduced from XRD. The presence of sulfur was confirmed by EDS analysis in the samples treated with the acid. As can be seen from the elemental mapping, sulfur appears homogeneously in the particle, demonstrating the successful sulfur insertion in the polymeric structure.

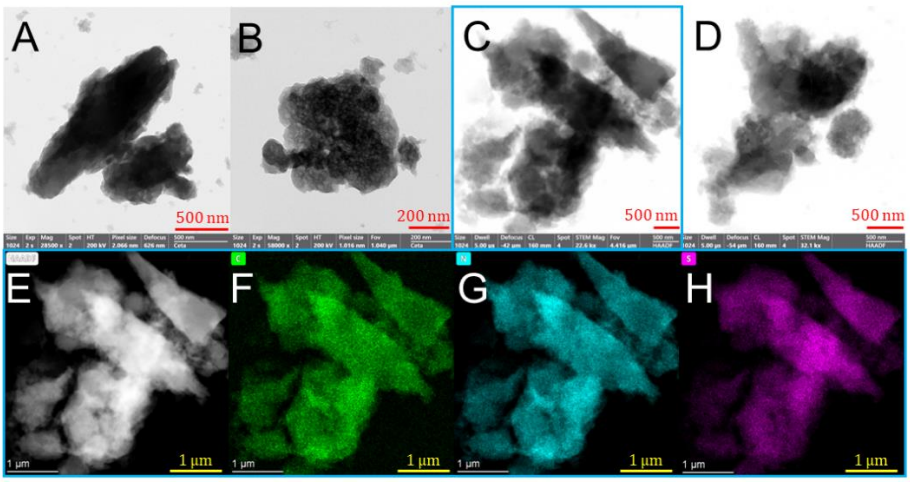

Fig. 6.5 *STEM micrographs of bare CN (A), SCN-2 (B), SCN-7 (C), SCN-10 (D), HAADF of SCN-7 (E), and EDS mapping in SCN-7 of carbon (F), nitrogen (G), and sulfur (H).*

The changes of sulfur incorporation onto the optical properties of CN were analyzed by DRS-UV-visible spectrophotometry. The absorbance spectra are depicted in Fig. 6.6A and the estimation of the bandgap energy by the Tauc plot method is illustrated in Fig. 6.6B, values shown in Table 6.1. The bare CN sample displayed a sharp decay of absorption spectra within 400-500 nm. The sulfonated samples showed higher absorption in the visible region, i.e. over 500 nm, than the bare graphitic carbon nitride. Regarding the bandgap, the non-modified CN displayed a bandgap value of approximately 2.7 eV, which means that the photocatalyst can be photoexcited with radiation up to 459 nm. It has been reported that if sulfur is incorporated in the aromatic heterocycles of the carbon nitride structure, as the electronegativity of S is lower than that of N, the extra valence electrons brought by S are donated to the system, occupying a part of the conduction band, resulting in a decrease in the band gap width of sulfur-doped carbon nitride [72]. However, this was not the case for the sulfonated SCN samples. When S is

incorporated in the terminal groups as -SO_3H functional groups, as carried out in this work, a blue-shift of the absorption edge takes place, slightly enlarging the bandgap value 0.1-0.2 eV depending on the chlorosulfonic doping dose, which means that the maximum wavelength of excitation is 427-443 nm. This slight blue shift shown after sulfonation of g-C_3N_4 has been reported as the result of the electron-withdrawing ability of the -SO_3H present on the surface [44]. The blue-shift of absorbance spectra has been also reported in mesoporous and exfoliated g-C_3N_4 samples [73,74], sulfur g-C_3N_4 prepared from thiourea [75,76], sulfonated g-C_3N_4 [44], g-C_3N_4 doped with elemental S using as precursor H_2S [77], or using ammonium sulfate [78] or thiourea followed by post-treatment oxidation [79].

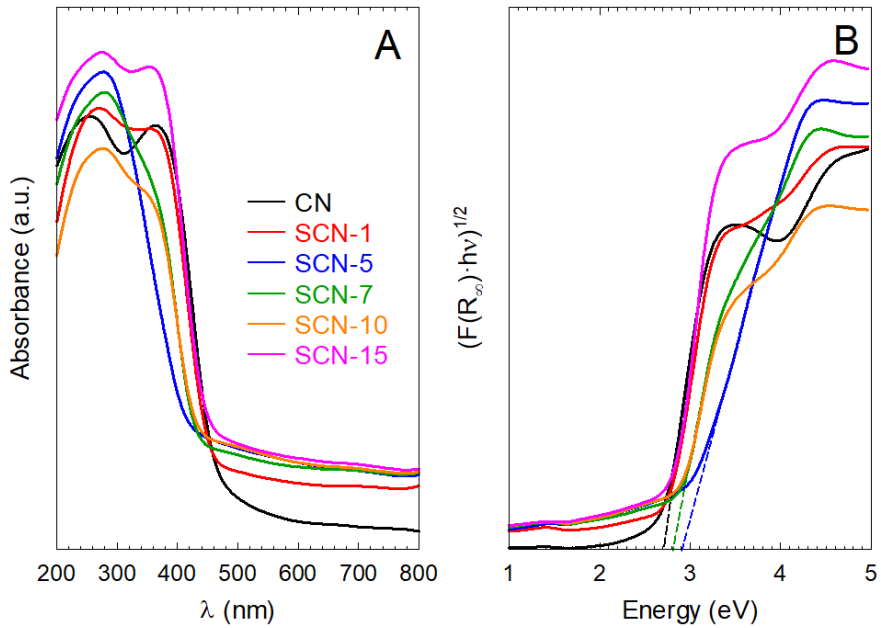

Fig. 6.6 *Absorption DRS-UV–visible spectra (A) and Tauc plot method for the bandgap determination (B) of SCN samples.*

The photoluminescence (PL) properties of a semiconductor are derived from the emitted radiation after the recombination of photogenerated charges. Therefore, the PL analysis can provide evidence about the efficiency of charge carrier trapping, transfer, and separation. A high PL signal is related to a high rate of charge carrier recombination; while a low PL peak is ascribed to a high separation of charges [13]. As shown

in Fig. 6.7 Photoluminescence spectra of SCN samples., the PL peak registered at 460 nm for the bare CN can be ascribed to the recombination of the hole-electron pair, being the wavelength value consistent with the bandgap energy. The presence of sulfonic groups in the polymeric tris-s-triazine structure of carbon nitride creates defects that potentiate the charge separation after irradiation, decreasing therefore the PL peak registered as the S precursor amount is increased [14,18,19,80]. Concretely, it has been reported that the negative inductive effect of sulfonic acid groups enhances the charge transfer dynamics and effectively inhibits the recombination effect [24]. Moreover, it is observed that the absorption edges are shifted toward longer wavelength values with the highest -SO_3H dose. This blue shift is in accordance with the slightly lower bandgap values stimulated by the DRS-UV-visible spectra, as observed in other previous works [44]. Similar materials such as nitrogen and sulfur-doped quantum carbon dots have been reported as strong blue shifts in the PL, with a maximum peak located at 400-425 nm [81]. The maximum PL spectra of SCN were located at 420-440 nm very close to the values of wavelength attributed to their bandgap values.

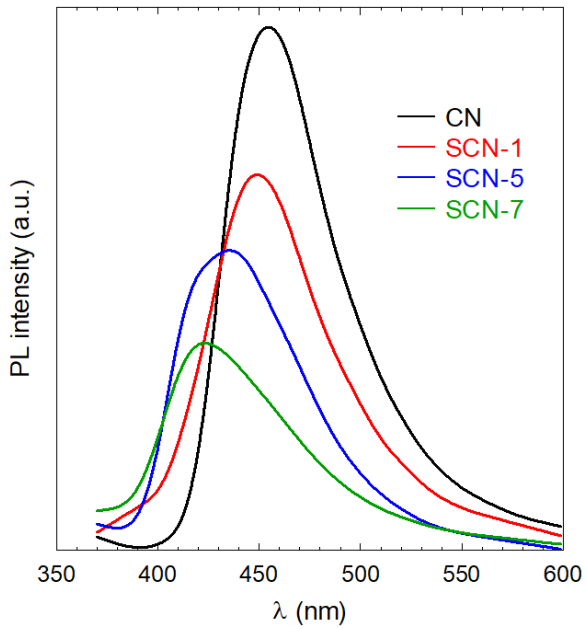

Fig. 6.7 *Photoluminescence spectra of SCN samples.*

6.3.2. Photocatalytic oxidation of benzyl alcohol to benzaldehyde

The photocatalytic activity of the sulfur-modified samples was assessed and applied to the selective oxidation of benzyl alcohol (BA) to benzaldehyde (BD). Fig. 6.8A depicts the temporal evolution of the normalized concentration of benzyl alcohol and the production of benzaldehyde. A previous adsorption stage of 30 min was conducted, with no appreciable adsorption of BA over the samples. The unmodified CN displayed poor activity with a BA conversion at 3 h of X_{BA}=14.6% and low selectivity, i.e. S_{BD}=32.5%. It should be highlighted the mild conditions and the aqueous media in which the reaction was tested. Higher conversion and selectivity have been reported for graphitic carbon nitride; however, the use of organic solvents, such as acetonitrile, and extreme conditions of O_2 pressure and temperature are required [7,8]. The low conversion registered in water for CN as reported in the literature, is roughly 10% at room temperature [10]. The modification of the graphitic carbon nitride structure with chlorosulfonic acid gave an improvement in the oxidation of BA. Thus, as sulfur was incorporated into the structure, the conversion of BA was enhanced, improving the reaction rate and the conversion of BA, see Table 6.3. Noteworthy, there is a gradual increase in the reaction rate until the sample SCN-7, reaches a maximum, as depicted in Fig. 6.8B. The increase of -SO_3H groups considerably raised the activity reaching a maximum to decrease with higher amounts. The presence of sulfonic groups enhanced the separation of the photogenerated charges according to the PL results, which may be attributed as the main reason that explains the best photo-activity of the SCN samples compared to the CN blank. Regarding the selectivity to the production of benzaldehyde, the 32.5% performed by the pristine CN was improved, displaying the SCN samples a selectivity within 40-55%, reaching a maximum value with the SCN-7 sample. These results are competitive compared to the reported in the literature if it is taken into account the use of water instead of organic solvent as the reaction media [82].

An analysis of the short-chain organic acids in the solution after the reaction suggested the formation of oxalic and acetic acid, which provides evidence of the breakage of the aromatic ring, and the lack of complete selectivity towards the aldehyde.

The quantum yield of some selected samples at the beginning of the reaction is provided in Table 6.3. This parameter entails the local volume photon absorption rate (LVRPA, $e^{\alpha,v}$) and the photocatalytic activity, quantifying the percentage of the irradiated photons that are transformed into chemical energy, leading to the formation of the aldehyde. Although the LVRPA values of the samples are within the same order of magnitude, due to the different photocatalytic activity achieved during the oxidation of BA to BD, the Q_E values are in accordance with the photocatalytic activity. As shown, the sample SCN-7 shows the highest radiation uptake efficiency with Q_E=0.124%, followed closely by SCN-10, with Q_E=0.117%, explaining, therefore, the optimum doping dosage of sulfonic groups.

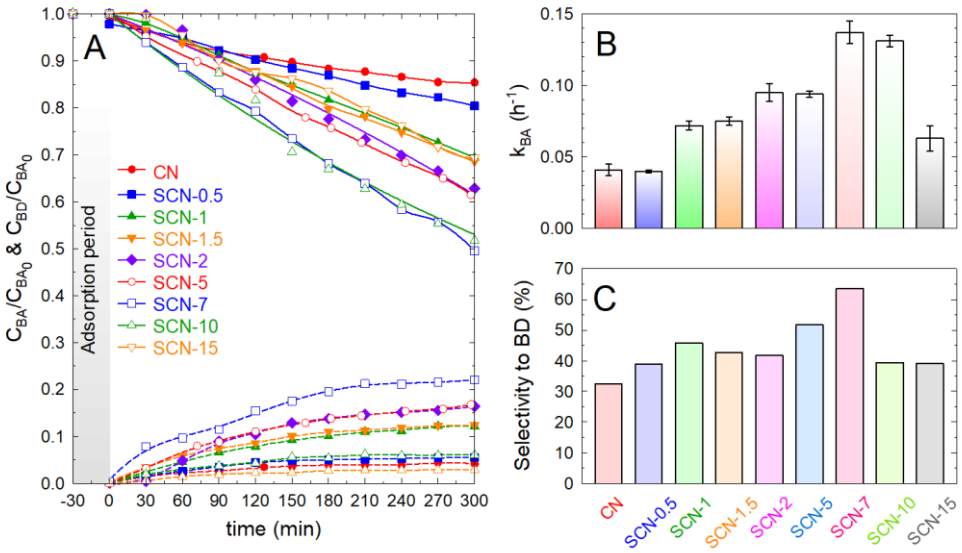

Fig. 6.8 *Photocatalytic production of benzaldehyde with SCN samples. Temporal normalized concentration of benzyl alcohol and benzaldehyde (A), pseudo-first order rate constant of benzyl alcohol abatement, k_{BA} (B); and, average selectivity to benzaldehyde (C). Experimental conditions: V= 350 mL, T=20ºC, $C_{BA,0}$= 0.5 mM; C_{CAT}=0.5 g L^{-1}.*

Table 6.3 *Kinetic parameters of the photocatalytic production of benzaldehyde with SCN samples*

Sample	$r_{BA,0}\cdot10^3$ (mM min^{-1})	$e^{a.v.}\cdot10^8$ (Einstein cm^{-3} s^{-1})	Q_E (%)	k_{BA} (h^{-1})	X_{BA} at 3 h (%)	S_{BD} (%)
CN	0.34	1.620	0.035	0.041	14.6	32.5
SCN-0.5	0.33	-	-	0.040	19.6	38.9
SCN-1	0.60	1.652	0.061	0.072	32.6	45.8
SCN-1.5	0.63	-	-	0.075	32.6	42.6
SCN-2	0.79	-	-	0.095	40.6	41.8
SCN-5	0.78	1.588	0.082	0.094	39.5	51.7
SCN-7	1.14	1.539	0.124	0.137	53.0	63.6
SCN-10	1.09	1.549	0.117	0.131	48.3	39.4
SCN-15	0.53	2.219	0.039	0.063	30.6	39.2

Comparison to similar graphitic carbon nitride-based materials should be seized with caution due to the prevalence of many variables in the process [83], such as light intensity, photoreactor configuration, catalyst preparation, etc. Nonetheless, as diverse as they may be, the comparison of the conversion and selectivity with other reported studies in aqueous solution, illustrated in Table 6.4, clearly states that the SCN-7 photocatalyst displays quite competitive activity concerning the conversion of BA and the selectivity of BD.

Table 6.4 *Reported characteristics of photocatalytic oxidation of benzyl alcohol to benzaldehyde in the literature and the results obtained in this present work under aqueous conditions.*

Material	Radiation Source	Initial BA (mM)	Reaction time (h)	X_{BA} (%)	S_{BD} (%)	Ref.
g-C_3N_4	UV LED (392 nm)	1.5	4	30	90	[84]
Ru-g-C_3N_4	UV LED (390 nm)	1.5	4	73	72	[6]
rGO- g-C_3N_4	UV LED (390 nm)	1.5	4	63	87	[83]
B-g-C_3N_4	UVA (365 nm)	0.7	5	29	36	[37]
Ru-B-g-C_3N_4	UVA (365 nm)	0.5	5	40	70	[63]
g-C_3N_4	UVA (365 nm)	0.5	5	15	32	This study
g-C_3N_4-SO_3H	UVA (365 nm)	0.5	5	53	64	

The mechanism of the photocatalytic performance over SCN-7 was studied by chemical scavenger tests [32,85,86]. The relative influence

of the reactive oxidant species was assessed by adding para-benzoquinone (p-BZQ), tiron or replacing the air bubbling with N_2 in the case of superoxide radical; adding tert-butyl alcohol (TBA) for the influence of hydroxyl radical; or in the presence of oxalic acid (OA) for the evaluation of the importance of the photogenerated holes. The results are illustrated in Fig. 6.9. The $O_2^{\bullet-}$ is generated after the reduction of dissolved O_2 that is adsorbed onto the surface of the photocatalyst by the photogenerated electrons after irradiation. The use of p-BZQ is extensively used as a probe of $O_2^{\bullet-}$ contribution [32] due to the great activity of this substance towards $O_2^{\bullet-}$ ($k_{p\text{-}BZQ,O2^{\bullet-}}=1\times10^9\ M^{-1}\ s^{-1}$ [87]). The k_{BA} was considerably reduced in the presence of p-BZQ compared to the blank test, i.e. from 0.136 to 0.048 min^{-1}, which could be interpreted as a strong impact of $O_2^{\bullet-}$ on the overall degradation mechanism. The selectivity decreased to an extent, i.e. 64% to 43%. These values may suggest a low contribution of $O_2^{\bullet-}$; however, the use of p-BZQ should be taken with caution [88] since p-BZQ can also trap $HO^{\bullet}$ with even higher reactivity ($k_{p\text{-}BZQ,HO^{\bullet}}=6.6\times10^9\ M^{-1}\ s^{-1}$ [89]) and be photolyzed [90,91]. The photo-reduction of quinones such as p-BZQ in aqueous systems triggers the formation of $HO^{\bullet}$ and semiquinone radicals, contributing to a misinterpretation of the results [92]. Based on these reasons, the use of alternative superoxide scavengers was considered. Tiron has been reported in the literature for studies of cell aging. The kinetics of tiron and $O_2^{\bullet-}$ has been estimated as $k_{tiron,O2^{\bullet-}}=5.0\times10^8\ M^{-1}\ s^{-1}$ [93]. Although tiron also reacts with $HO^{\bullet}$ ([94]), it shows higher stability toward photolysis degradation. In the presence of tiron, the oxidation of BA was considerably inhibited, leading to a $k=0.020\ h^{-1}$. Noteworthy, no formation of BD was registered. As tiron scavenged the formation of superoxide radicals, and no BD was registered, the slight decrease of BA may be attributable to other oxidative pathways such as the opening ring, which was suggested by the presence of small amounts of short-chain organic acids. Alternatively, an inert gas bubbling such as N_2 was used as an alternative to assess the real contribution of $O_2^{\bullet-}$ [82]. After the replacement of dissolved O_2 by N_2, the depletion of BA described a lower pseudo-first order rate constant, i.e. 0.071 min^{-1}. Interestingly, the selectivity of BD formation was also dramatically decreased to a poor 1%. These results suggest that the contribution of the superoxide seems to display an important role, especially in terms of the selectivity of

oxidation of the alcohol to the aldehyde, but as the BA oxidation was not inhibited, additional routes should not be discharged. The contribution of $HO^{\bullet}$ was studied by the addition of TBA, with high reactivity, i.e. second-order rate constant $k_{TBA,HO^{\bullet}} = 6.2 \times 10^8$ M^{-1} s^{-1} [95]. The addition of TBA also denoted an impact in terms of inhibition since the rate constant decreased to 0.047 min^{-1}, which represents only a third of the blank test. Regarding selectivity, a value of S_{BD}=41% was monitored in the presence of TBA, which is lower than the blank test, but the formation of BD was not completely hindered. $HO^{\bullet}$ affects the BA degradation but not the selectivity of BD production. Finally, a test adding OA was carried out [96] to assess the impact of photogenerated holes. The oxalate anion is adsorbed in the surface of the photocatalysts and oxidized by the photogenerated holes, releasing the formation of CO_2 with the previous formation of the radical $CO_2^{\bullet-}$ [97]. The oxalate anions can also react with $HO^{\bullet}$; however, the kinetics is slow enough to discharge an important contribution of this reaction, $k_{OA,HO^{\bullet}} = 1.5 \times 10^7$ M^{-1} s^{-1} [98]. According to Fig. 6.9, the presence of OA accelerated the degradation of OA, increasing the k_{BA} value over 8 times. This fact suggests the action of OA as a sacrificial agent of the photogenerated holes [37]. The photocatalytic decomposition of oxalate may take place with the transfer of electrons from this compound to the valence band of the photocatalyst, generating more $O_2^{\bullet-}$ [92]. Also, the $CO_2^{\bullet-}$ may be involved in the accelerated degradation of BA. To summarize, in overall terms, $O_2^{\bullet-}$ displayed a strong impact, especially in the selectivity of the reaction in which its presence results in positive. The role of $HO^{\bullet}$ affected BA oxidation, but not to the selectivity as $O_2^{\bullet-}$ did.

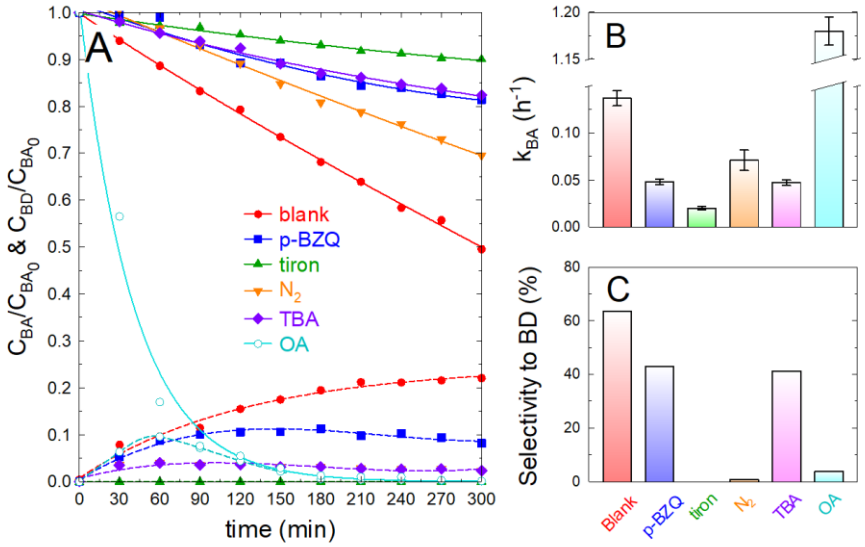

Fig. 6.9 *Influence of radical scavengers on the photocatalytic production of benzaldehyde with SCN-7 sample. Temporal normalized concentration of benzyl alcohol and benzaldehyde (A pseudo-first order rate constant of benzyl alcohol abatement, k_{BA} (B); and, average selectivity to benzaldehyde (C). Experimental conditions: V= 350 mL, T=20ºC, $C_{BA},0$= 0.5 mM; C_{CAT}=0.5 g L^{-1}; $C_{scavenger}$= 1 mM (p-BQZ, tiron), 10 mM (TBA, OA).*

6.4. CONCLUSIONS

The modification of carbon nitride with surface sulfonic groups results in a positive strategy to improve the activity of bare g-C_3N_4. The action of chlorosulfonic acid over g-C_3N_4 promotes the delamination of the material, according to the decrease of the characteristic interlayer peak of XRD of g-C_3N_4. The N_2 isotherms provided a decrease in the surface area, promoted by the acid delamination and electrostatic interaction of the functionalized sheets. The majority presence of -SO_3H groups on the surface was confirmed by FTIR and XPS analysis. XPS confirmed the presence of -SO_3H groups, attached to terminal N atoms. Moreover, the formation of carbon sulfoxide, C–S(=O)–C is suggested. Regarding the optical properties, a blue-shift behavior in the radiation absorption was observed, also confirmed by a shift in the photoluminescence spectra. The intensity of the photoluminescence peaks of sulfonated samples was lower than the bare g-C_3N_4 sample, which indicates an enhanced separation of the photo-generated charges, decreasing, therefore, the recombination effect. The enhanced separation of charges impacted positively on the photocatalytic activity of

benzaldehyde oxidation in water solution, also affected by the delamination effect which aids a better harvesting of light. An optimum dose of -SO_3H was observed for a higher benzaldehyde oxidation rate and benzaldehyde selectivity. The mechanism of benzaldehyde oxidation was studied by the use of chemical scavengers, concluding that superoxide radical displayed an important contribution to de oxidation of benzyl alcohol, higher than the action of hydroxyl radicals. In terms of selectivity, the presence of superoxide results is essential to aim the reaction to benzaldehyde formation.

REFERENCES

1. Andrade, M.A.; Martins, L.M.D.R.S. Selective Styrene Oxidation to Benzaldehyde over Recently Developed Heterogeneous Catalysts. Molecules 2021, 26, 1680, doi:10.3390/MOLECULES26061680.
2. Satrio, J.A.B.; Doraiswamy, L.K. Production of Benzaldehyde: A Case Study in a Possible Industrial Application of Phase-Transfer Catalysis. Chemical Engineering Journal 2001, 82, 43–56, doi:10.1016/S1385-8947(00)00351-X.
3. Ghahremani, M.; Ciriminna, R.; Pandarus, V.; Scurria, A.; La Parola, V.; Giordano, F.; Avellone, G.; Béland, F.; Karimi, B.; Pagliaro, M. Green and Direct Synthesis of Benzaldehyde and Benzyl Benzoate in One Pot. ACS Sustain Chem Eng 2018, 6, 15441–15446, doi:10.1021/ACSSUSCHEMENG.8B03893.
4. Ismael, M. A Review on Graphitic Carbon Nitride (g-C3N4) Based Nanocomposites: Synthesis, Categories, and Their Application in Photocatalysis. J Alloys Compd 2020, 846, 156446, doi:10.1016/J.JALLCOM.2020.156446.
5. Wang, X.; Blechert, S.; Antonietti, M. Polymeric Graphitic Carbon Nitride for Heterogeneous Photocatalysis. ACS Catal 2012, 2, 1596–1606, doi:10.1021/CS300240X.
6. Lima, M.J.; Tavares, P.B.; Silva, A.M.T.; Silva, C.G.; Faria, J.L. Selective Photocatalytic Oxidation of Benzyl Alcohol to Benzaldehyde by Using Metal-Loaded g-C3N4 Photocatalysts. Catal Today 2017, 287, 70–77, doi:10.1016/J.CATTOD.2016.11.023.
7. Su, F.; Mathew, S.C.; Lipner, G.; Fu, X.; Antonietti, M.; Blechert, S.; Wang, X. Mpg-C3N4-Catalyzed Selective Oxidation of Alcohols Using O2 and Visible Light. J Am Chem Soc 2010, 132, 16299–16301, doi:10.1021/JA102866P.
8. Chen, Y.; Zhang, J.; Wang, X. Molecular and Textural Engineering of Conjugated Carbon Nitride Catalysts for Selective Oxidation of Alcohols with Visible Light. Chem Sci 2013, 4, 3244–3248, doi:10.1039/C3SC51203G.
9. Zhang, L.; Liu, D.; Guan, J.; Chen, X.; Guo, X.; Zhao, F.; Hou, T.; Mu, X. Metal-Free g-C3N4 Photocatalyst by Sulfuric Acid Activation for Selective Aerobic Oxidation of Benzyl Alcohol under

Visible Light. Mater Res Bull 2014, 59, 84–92, doi:10.1016/J.MATERRESBULL.2014.06.021.

10. Long, B.; Ding, Z.; Wang, X. Carbon Nitride for the Selective Oxidation of Aromatic Alcohols in Water under Visible Light. ChemSusChem 2013, 6, 2074–2078, doi:10.1002/CSSC.201300360.
11. Savateev, A.; Ghosh, I.; König, B.; Antonietti, M. Photoredox Catalytic Organic Transformations Using Heterogeneous Carbon Nitrides. Angewandte Chemie International Edition 2018, 57, 15936–15947, doi:10.1002/ANIE.201802472.
12. Zhou, L.; Zhang, H.; Sun, H.; Liu, S.; Tade, M.O.; Wang, S.; Jin, W. Recent Advances in Non-Metal Modification of Graphitic Carbon Nitride for Photocatalysis: A Historic Review. Catal Sci Technol 2016, 6, 7002–7023, doi:10.1039/C6CY01195K.
13. Ge, L.; Han, C.; Xiao, X.; Guo, L.; Li, Y. Enhanced Visible Light Photocatalytic Hydrogen Evolution of Sulfur-Doped Polymeric g-C3N4 Photocatalysts. Mater Res Bull 2013, 48, 3919–3925, doi:10.1016/J.MATERRESBULL.2013.06.002.
14. Wang, K.; Li, Q.; Liu, B.; Cheng, B.; Ho, W.; Yu, J. Sulfur-Doped g-C3N4 with Enhanced Photocatalytic CO2-Reduction Performance. Appl Catal B 2015, 176–177, 44–52, doi:10.1016/J.APCATB.2015.03.045.
15. Hong, J.; Xia, X.; Wang, Y.; Xu, R. Mesoporous Carbon Nitride with in Situ Sulfur Doping for Enhanced Photocatalytic Hydrogen Evolution from Water under Visible Light. J Mater Chem 2012, 22, 15006–15012, doi:10.1039/C2JM32053C.
16. An, T.D.; Phuc, N. Van; Tri, N.N.; Phu, H.T.; Hung, N.P.; VO, V. Sulfur-Doped g-C3N4 with Enhanced Visible-Light Photocatalytic Activity. Applied Mechanics and Materials 2019, 889, 43–50, doi:10.4028/WWW.SCIENTIFIC.NET/AMM.889.43.
17. Guan, K.; Li, J.; Lei, W.; Wang, H.; Tong, Z.; Jia, Q.; Zhang, H.; Zhang, S. Synthesis of Sulfur Doped G-C3N4 with Enhanced Photocatalytic Activity in Molten Salt. Journal of Materiomics 2021, 7, 1131–1142, doi:10.1016/J.JMAT.2021.01.008.
18. Feng, C.; Tang, L.; Deng, Y.; Wang, J.; Liu, Y.; Ouyang, X.; Yang, H.; Yu, J.; Wang, J. A Novel Sulfur-Assisted Annealing Method of g-C3N4 Nanosheet Compensates for the Loss of Light Absorption with Further Promoted Charge Transfer for Photocatalytic

Production of H2 and H2O2. Appl Catal B 2021, 281, 119539, doi:10.1016/J.APCATB.2020.119539.

19. Jiang, J.; Xiong, Z.; Wang, H.; Liao, G.; Bai, S.; Zou, J.; Wu, P.; Zhang, P.; Li, X. Sulfur-Doped g-C3N4/g-C3N4 Isotype Step-Scheme Heterojunction for Photocatalytic H2 Evolution. J Mater Sci Technol 2022, 118, 15–24, doi:10.1016/J.JMST.2021.12.018.
20. Choudhary, P.; Sen, A.; Kumar, A.; Dhingra, S.; Nagaraja, C.M.; Krishnan, V. Sulfonic Acid Functionalized Graphitic Carbon Nitride as Solid Acid–Base Bifunctional Catalyst for Knoevenagel Condensation and Multicomponent Tandem Reactions. Mater Chem Front 2021, 5, 6265–6278, doi:10.1039/D1QM00650A.
21. Baig, R.B.N.; Verma, S.; Nadagouda, M.N.; Varma, R.S. Room Temperature Synthesis of Biodiesel Using Sulfonated Graphitic Carbon Nitride. Scientific Reports 2016 6:1 2016, 6, 1–6, doi:10.1038/srep39387.
22. Chhabra, T.; Bahuguna, A.; Dhankhar, S.S.; Nagaraja, C.M.; Krishnan, V. Sulfonated Graphitic Carbon Nitride as a Highly Selective and Efficient Heterogeneous Catalyst for the Conversion of Biomass-Derived Saccharides to 5-Hydroxymethylfurfural in Green Solvents. Green Chemistry 2019, 21, 6012–6026, doi:10.1039/C9GC02120E.
23. Edrisi, M.; Azizi, N. Sulfonic Acid-Functionalized Graphitic Carbon Nitride Composite: A Novel and Reusable Catalyst for the One-Pot Synthesis of Polysubstituted Pyridine in Water under Sonication. Journal of the Iranian Chemical Society 2019 17:4 2019, 17, 901–910, doi:10.1007/S13738-019-01820-1.
24. Zhang, M.; Li, Y.; Chang, W.; Zhu, W.; Zhang, L.; Jin, R.; Xing, Y. Negative Inductive Effect Enhances Charge Transfer Driving in Sulfonic Acid Functionalized Graphitic Carbon Nitride with Efficient Visible-Light Photocatalytic Performance. Chinese Journal of Catalysis 2022, 43, 526–535, doi:10.1016/S1872-2067(21)63872-X.
25. Meng, Q.; Cai, Y.; Cong, B.; Xing, W.; Chen, G. Enhanced Carriers Separation Efficiency in G-C3N4 Modified with Sulfonic Groups for Efficient Photocatalytic Cr(VI) Reduction. Mater Res Bull 2020, 122, 110681, doi:10.1016/J.MATERRESBULL.2019.110681.
26. Masoumi Sangani, M.M.; Shahin, M.S.; Yavari, M.A.; Faghihinezhad, M.; Baghdadi, M. Tailoring Photocatalytic Activity

of Graphitic Carbon Nitride Using Sulfanilic Acid and Incorporating in Chitosan Beads: Cr(VI) Removal from Aqueous Solutions. Journal of Industrial and Engineering Chemistry 2024, 130, 412–424, doi:10.1016/J.JIEC.2023.09.047.

27. Praus, P.; Smýkalová, A.; Foniok, K.; Matějka, V.; Kormunda, M.; Smetana, B.; Cvejn, D. The Presence and Effect of Oxygen in Graphitic Carbon Nitride Synthetized in Air and Nitrogen Atmosphere. Appl Surf Sci 2020, 529, 147086, doi:10.1016/J.APSUSC.2020.147086.
28. Altomare, A.; Corriero, N.; Cuocci, C.; Falcicchio, A.; Moliterni, A.; Rizzi, R. QUALX2.0: A Qualitative Phase Analysis Software Using the Freely Available Database POW_COD. J Appl Crystallogr 2015, 48, 598–603, doi:10.1107/S1600576715002319.
29. Pérez-Molina, Á.; Pastrana-Martínez, L.M.; Morales-Torres, S.; Maldonado-Hódar, F.J. Photodegradation of Cytostatic Drugs by G-C3N4: Synthesis, Properties and Performance Fitted by Selecting the Appropriate Precursor. Catal Today 2023, 418, 114068, doi:10.1016/J.CATTOD.2023.114068.
30. Solís, R.R.; Quintana, M.A.; Martín-Lara, M.Á.; Pérez, A.; Calero, M.; Muñoz-Batista, M.J. Boosted Activity of G-C3N4/UiO-66-NH2 Heterostructures for the Photocatalytic Degradation of Contaminants in Water. Int J Mol Sci 2022, 23, 12871, doi:10.3390/IJMS232112871/S1.
31. Pelaez, M.; de la Cruz, A.A.; O'Shea, K.; Falaras, P.; Dionysiou, D.D. Effects of Water Parameters on the Degradation of Microcystin-LR under Visible Light-Activated TiO2 Photocatalyst. Water Res 2011, 45, 3787–3796, doi:10.1016/J.WATRES.2011.04.036.
32. Pelaez, M.; Falaras, P.; Likodimos, V.; O'Shea, K.; de la Cruz, A.A.; Dunlop, P.S.M.; Byrne, J.A.; Dionysiou, D.D. Use of Selected Scavengers for the Determination of NF-TiO2 Reactive Oxygen Species during the Degradation of Microcystin-LR under Visible Light Irradiation. J Mol Catal A Chem 2016, 425, 183–189, doi:10.1016/j.molcata.2016.09.035.
33. Serpone, N. Relative Photonic Efficiencies and Quantum Yields in Heterogeneous Photocatalysis. J Photochem Photobiol A Chem 1997, 104, 1–12, doi:10.1016/S1010-6030(96)04538-8.

34. Li Puma, G.; Brucato, A. Dimensionless Analysis of Slurry Photocatalytic Reactors Using Two-Flux and Six-Flux Radiation Absorption–Scattering Models. Catal Today 2007, 122, 78–90, doi:10.1016/J.CATTOD.2007.01.027.
35. Alfano, O.M.; Bahnemann, D.; Cassano, A.E.; Dillert, R.; Goslich, R. Photocatalysis in Water Environments Using Artificial and Solar Light. Catal Today 2000, 58, 199–230, doi:10.1016/S0920-5861(00)00252-2.
36. Muñoz-Batista, M.J.; Kubacka, A.; Fontelles-Carceller, O.; Tudela, D.; Fernández-García, M. Surface CuO, Bi2O3, and CeO2 Species Supported in TiO2-Anatase: Study of Interface Effects in Toluene Photodegradation Quantum Efficiency. ACS Appl Mater Interfaces 2016, 8, 13934–13945, doi:10.1021/ACSAMI.6B03081.
37. Quintana, M.A.; Solís, R.R.; Ángeles Martín-Lara, M.; Blázquez, G.; Mónica Calero, F.; Muñoz-Batista, M.J. Enhanced Boron Modified Graphitic Carbon Nitride for the Selective Photocatalytic Production of Benzaldehyde. Sep Purif Technol 2022, 298, 121613, doi:10.1016/J.SEPPUR.2022.121613.
38. Muñoz-Batista, M.J.; Ballari, M.M.; Kubacka, A.; Alfano, O.M.; Fernández-García, M. Braiding Kinetics and Spectroscopy in Photo-Catalysis: The Spectro-Kinetic Approach. Chem Soc Rev 2019, 48, 637–682, doi:10.1039/c8cs00108a.
39. Fina, F.; Callear, S.K.; Carins, G.M.; Irvine, J.T.S. Structural Investigation of Graphitic Carbon Nitride via XRD and Neutron Diffraction. Chemistry of Materials 2015, 27, 2612–2618, doi:10.1021/ACS.CHEMMATER.5B00411.
40. Jiménez-Calvo, P.; Marchal, C.; Cottineau, T.; Caps, V.; Keller, V. Influence of the Gas Atmosphere during the Synthesis of G-C3N4 for Enhanced Photocatalytic H2 Production from Water on Au/g-C3N4 Composites. J Mater Chem A Mater 2019, 7, 14849–14863, doi:10.1039/C9TA01734H.
41. Gao, J.; Zhou, Y.; Li, Z.; Yan, S.; Wang, N.; Zou, Z. High-Yield Synthesis of Millimetre-Long, Semiconducting Carbon Nitride Nanotubes with Intense Photoluminescence Emission and Reproducible Photoconductivity. Nanoscale 2012, 4, 3687–3692, doi:10.1039/C2NR30777D.
42. Qiu, P.; Chen, H.; Xu, C.; Zhou, N.; Jiang, F.; Wang, X.; Fu, Y. Fabrication of an Exfoliated Graphitic Carbon Nitride as a Highly

Active Visible Light Photocatalyst. J Mater Chem A Mater 2015, 3, 24237–24244, doi:10.1039/C5TA08406G.

43. Bai, X.; Yan, S.; Wang, J.; Wang, L.; Jiang, W.; Wu, S.; Sun, C.; Zhu, Y. A Simple and Efficient Strategy for the Synthesis of a Chemically Tailored G-C3N4 Material. J Mater Chem A Mater 2014, 2, 17521–17529, doi:10.1039/C4TA02781G.
44. Venkatesvaran, H.; Balu, S.; Chowdhury, A.; Chen, S.W.; Yang, T.C.K. Photo–Redox Properties of –SO3H Functionalized Metal-Free g-C3N4 and Its Application in the Photooxidation of Sunset Yellow FCF and Photoreduction of Cr (VI). Catalysts 2022, 12, 751, doi:10.3390/CATAL12070751/S1.
45. Xing, W.; Liu, C.; Zhong, H.; Zhang, Y.; Zhang, T.; Cheng, C.; Han, J.; Wu, G.; Chen, G. Phosphate Group-Mediated Carriers Transfer and Energy Band over Carbon Nitride for Efficient Photocatalytic H2 Production and Removal of Rhodamine B. J Alloys Compd 2022, 895, 162772, doi:10.1016/J.JALLCOM.2021.162772.
46. Ghosh, S.; Ramaprabhu, S. High-Pressure Investigation of Ionic Functionalized Graphitic Carbon Nitride Nanostructures for CO2 Capture. Journal of CO2 Utilization 2017, 21, 89–99, doi:10.1016/J.JCOU.2017.06.022.
47. Miller, T.S.; Jorge, A.B.; Suter, T.M.; Sella, A.; Corà, F.; McMillan, P.F. Carbon Nitrides: Synthesis and Characterization of a New Class of Functional Materials. Physical Chemistry Chemical Physics 2017, 19, 15613–15638, doi:10.1039/C7CP02711G.
48. Verma, S.; Baig, R.B.N.; Nadagouda, M.N.; Len, C.; Varma, R.S. Sustainable Pathway to Furanics from Biomass via Heterogeneous Organo-Catalysis. Green Chemistry 2017, 19, 164–168, doi:10.1039/C6GC02551J.
49. Ding, Z.; Chen, X.; Antonietti, M.; Wang, X. Synthesis of Transition Metal-Modified Carbon Nitride Polymers for Selective Hydrocarbon Oxidation. ChemSusChem 2011, 4, 274–281, doi:10.1002/CSSC.201000149.
50. Li, X.; Zhang, J.; Shen, L.; Ma, Y.; Lei, W.; Cui, Q.; Zou, G. Preparation and Characterization of Graphitic Carbon Nitride through Pyrolysis of Melamine. Appl Phys A Mater Sci Process 2009, 94, 387–392, doi:10.1007/S00339-008-4816-4.

51. Wei, J.; Hing, P.; Mo, Z.Q. TEM, XPS and FTIR Characterization of Sputtered Carbon Nitride Films. Surface and Interface Analysis 1999, 28, 208–211.
52. Zhao, D.; Dong, C.-L.; Wang, B.; Chen, C.; Huang, Y.-C.; Diao, Z.; Li, S.; Guo, L.; Shen, S.; Zhao, D.; et al. Synergy of Dopants and Defects in Graphitic Carbon Nitride with Exceptionally Modulated Band Structures for Efficient Photocatalytic Oxygen Evolution. Advanced Materials 2019, 31, 1903545, doi:10.1002/ADMA.201903545.
53. Kim, M.; Hwang, S.; Yu, J.S. Novel Ordered Nanoporous Graphitic C3N4 as a Support for Pt–Ru Anode Catalyst in Direct Methanol Fuel Cell. J Mater Chem 2007, 17, 1656–1659, doi:10.1039/B702213A.
54. Mohammadi, M.; Garmarudi, A.B.; Khanmohammadi, M.; Rouchi, M.B. Infrared Spectrometric Evaluation of Carbon Nanotube Sulfonation. Fullerenes, Nanotubes and Carbon Nanostructures 2016, 24, 219–224, doi:10.1080/1536383X.2015.1125341.
55. Kumar, P.; Shayesteh Zeraati, A.; Roy, S.; Miller, K.A.; Wang, A.; Alemany, L.B.; Al-Attas, T.A.; Trivedi, D.; Ajayan, P.M.; Hu, J.; et al. Metal-Free Sulfonate/Sulfate-Functionalized Carbon Nitride for Direct Conversion of Glucose to Levulinic Acid. ACS Sustain Chem Eng 2022, 10, 6230–6243, doi:10.1021/ACSSUSCHEMENG.2C00309.
56. Douzandegi Fard, M.A.; Ghafuri, H.; Rashidizadeh, A. Sulfonated Highly Ordered Mesoporous Graphitic Carbon Nitride as a Super Active Heterogeneous Solid Acid Catalyst for Biginelli Reaction. Microporous and Mesoporous Materials 2019, 274, 83–93, doi:10.1016/J.MICROMESO.2018.07.030.
57. Velayutham, P.; Sahu, A.K. Graphitic Carbon Nitride Nanosheets - Nafion as a Methanol Barrier Hybrid Membrane for Direct Methanol Fuel Cells. Journal of Physical Chemistry C 2018, 122, 21735–21744, doi:10.1021/ACS.JPCC.8B06042.
58. Balu, S.; Chen, Y.L.; Juang, R.C.; Yang, T.C.K.; Juan, J.C. Morphology-Controlled Synthesis of α–Fe2O3 Nanocrystals Impregnated on g-C3N4–SO3H with Ultrafast Charge Separation for Photoreduction of Cr (VI) Under Visible Light. Environmental Pollution 2020, 267, 115491, doi:10.1016/J.ENVPOL.2020.115491.

59. Alwin, E.; Nowicki, W.; Wojcieszak, R.; Zieliński, M.; Pietrowski, M. Elucidating the Structure of the Graphitic Carbon Nitride Nanomaterials via X-Ray Photoelectron Spectroscopy and X-Ray Powder Diffraction Techniques. Dalton Transactions 2020, 49, 12805–12813, doi:10.1039/D0DT02325F.
60. Wen, Y.; Qu, D.; An, L.; Gao, X.; Jiang, W.; Wu, D.; Yang, D.; Sun, Z. Defective G-C3N4 Prepared by the NaBH4 Reduction for High-Performance H2 Production. ACS Sustain Chem Eng 2019, 7, 2343–2349, doi:10.1021/ACSSUSCHEMENG.8B05124.
61. Abdul Razzaq, A.; Yao, Y.; Shah, R.; Qi, P.; Miao, L.; Chen, M.; Zhao, X.; Peng, Y.; Deng, Z. High-Performance Lithium Sulfur Batteries Enabled by a Synergy between Sulfur and Carbon Nanotubes. Energy Storage Mater 2019, 16, 194–202, doi:10.1016/J.ENSM.2018.05.006.
62. Li, G.; Sun, J.; Hou, W.; Jiang, S.; Huang, Y.; Geng, J. Three-Dimensional Porous Carbon Composites Containing High Sulfur Nanoparticle Content for High-Performance Lithium–Sulfur Batteries. Nat Commun 2016, 7, 1–10, doi:10.1038/ncomms10601.
63. Solís, R.R.; Quintana, M.A.; Blázquez, G.; Calero, M.; Muñoz-Batista, M.J. Ruthenium Deposited onto Graphitic Carbon Modified with Boron for the Intensified Photocatalytic Production of Benzaldehyde. Catal Today 2023, 423, 114266, doi:10.1016/J.CATTOD.2023.114266.
64. Ahammad, A.J.S.; Odhikari, N.; Shah, S.S.; Hasan, M.M.; Islam, T.; Pal, P.R.; Ahmed Qasem, M.A.; Aziz, M.A. Porous Tal Palm Carbon Nanosheets: Preparation, Characterization and Application for the Simultaneous Determination of Dopamine and Uric Acid. Nanoscale Adv 2019, 1, 613–626, doi:10.1039/C8NA00090E.
65. González, M.D.; Salagre, P.; Taboada, E.; Llorca, J.; Molins, E.; Cesteros, Y. Sulfonic Acid-Functionalized Aerogels as High Resistant to Deactivation Catalysts for the Etherification of Glycerol with Isobutene. Appl Catal B 2013, 136–137, 287–293, doi:10.1016/J.APCATB.2013.02.018.
66. Russo, P.A.; Antunes, M.M.; Neves, P.; Wiper, P. V.; Fazio, E.; Neri, F.; Barreca, F.; Mafra, L.; Pillinger, M.; Pinna, N.; et al. Solid Acids with SO3H Groups and Tunable Surface Properties:

Versatile Catalysts for Biomass Conversion. J Mater Chem A Mater 2014, 2, 11813–11824, doi:10.1039/C4TA02320J.

67. Dandia, A.; Saini, P.; Kumar, K.; Sethi, M.; Rathore, K.S.; Meena, M.L.; Parewa, V. Synergetic Effect of Functionalized Graphitic Carbon Nitride Catalyst and Ultrasound in Aqueous Medium: An Efficient and Sustainable Synthesis of 1,3,5-Trisubstituted Hexahydro-1,3,5-Triazines. Current Research in Green and Sustainable Chemistry 2021, 4, 100170, doi:10.1016/J.CRGSC.2021.100170.
68. Dandia, A.; Mahawar, D.K.; Saini, P.; Saini, S.; Gupta, S.L.; Rathore, K.S.; Parewa, V. Site-Specific Role of Bifunctional Graphitic Carbon Nitride Catalyst for the Sustainable Synthesis of 3,3-Spirocyclic Oxindoles in Aqueous Media. RSC Adv 2021, 11, 28452–28465, doi:10.1039/D1RA03881H.
69. Siow, K.S.; Britcher, L.; Kumar, S.; Griesser, H.J. XPS Study of Sulfur and Phosphorus Compounds with Different Oxidation States. Sains Malays 2018, 47, 1913–1922, doi:10.17576/JSM-2018-4708-33.
70. Seredych, M.; Wu, C.T.; Brender, P.; Ania, C.O.; Vix-Guterl, C.; Bandosz, T.J. Role of Phosphorus in Carbon Matrix in Desulfurization of Diesel Fuel Using Adsorption Process. Fuel 2012, 92, 318–326, doi:10.1016/J.FUEL.2011.08.007.
71. Fantauzzi, M.; Elsener, B.; Atzei, D.; Rigoldi, A.; Rossi, A. Exploiting XPS for the Identification of Sulfides and Polysulfides. RSC Adv 2015, 5, 75953–75963, doi:10.1039/C5RA14915K.
72. Zuo, M.; Li, X.; Liang, Y.; Zhao, F.; Sun, H.; Liu, C.; Gong, X.; Qin, P.; Wang, H.; Wu, Z.; et al. Modification of Sulfur Doped Carbon Nitride and Its Application in Photocatalysis. Sep Purif Technol 2023, 308, 122875, doi:10.1016/J.SEPPUR.2022.122875.
73. Rana, A.G.; Tasbihi, M.; Schwarze, M.; Minceva, M. Efficient Advanced Oxidation Process (AOP) for Photocatalytic Contaminant Degradation Using Exfoliated Metal-Free Graphitic Carbon Nitride and Visible Light-Emitting Diodes. Catalysts 2021, 11, 662, doi:10.3390/CATAL11060662.
74. YunYang; Lei, W.; Xu, Y.; Zhou, T.; Xia, M.; Hao, Q. Determination of Trace Uric Acid in Serum Using Porous Graphitic Carbon Nitride (g-C3N4) as a Fluorescent Probe. Microchimica Acta 2018, 185, 1–9, doi:10.1007/S00604-017-2533-4.

75. Feng, X.; Chen, H.; Jiang, F.; Wang, X. Enhanced Visible-Light Photocatalytic Nitrogen Fixation over Semicrystalline Graphitic Carbon Nitride: Oxygen and Sulfur Co-Doping for Crystal and Electronic Structure Modulation. J Colloid Interface Sci 2018, 509, 298–306, doi:10.1016/J.JCIS.2017.09.026.
76. Jourshabani, M.; Shariatinia, Z.; Badiei, A. Controllable Synthesis of Mesoporous Sulfur-Doped Carbon Nitride Materials for Enhanced Visible Light Photocatalytic Degradation. Langmuir 2017, 33, 7062–7078, doi:10.1021/ACS.LANGMUIR.7B01767.
77. Liu, G.; Niu, P.; Sun, C.; Smith, S.C.; Chen, Z.; Lu, G.Q.; Cheng, H.M. Unique Electronic Structure Induced High Photoreactivity of Sulfur-Doped Graphitic C3N4. J Am Chem Soc 2010, 132, 11642–11648, doi:10.1021/JA103798K.
78. Lv, H.; Huang, Y.; Koodali, R.T.; Liu, G.; Zeng, Y.; Meng, Q.; Yuan, M. Synthesis of Sulfur-Doped 2D Graphitic Carbon Nitride Nanosheets for Efficient Photocatalytic Degradation of Phenol and Hydrogen Evolution. ACS Appl Mater Interfaces 2020, 12, 12656–12667, doi:10.1021/ACSAMI.9B19057.
79. Khedr, T.M.; El-Sheikh, S.M.; Endo-Kimura, M.; Wang, K.; Ohtani, B.; Kowalska, E. Development of Sulfur-Doped Graphitic Carbon Nitride for Hydrogen Evolution under Visible-Light Irradiation. Nanomaterials 2023, 13, 62, doi:10.3390/NANO13010062.
80. Ke, L.; Li, P.; Wu, X.; Jiang, S.; Luo, M.; Liu, Y.; Le, Z.; Sun, C.; Song, S. Graphene-like Sulfur-Doped g-C3N4 for Photocatalytic Reduction Elimination of UO22+ under Visible Light. Appl Catal B 2017, 205, 319–326, doi:10.1016/J.APCATB.2016.12.043.
81. Ding, H.; Wei, J.S.; Xiong, H.M. Nitrogen and Sulfur Co-Doped Carbon Dots with Strong Blue Luminescence. Nanoscale 2014, 6, 13817–13823, doi:10.1039/C4NR04267K.
82. Qiu, C.; Wang, S.; Zuo, J.; Zhang, B. Photocatalytic CO2 Reduction Coupled with Alcohol Oxidation over Porous Carbon Nitride. Catalysts 2022, 12, 672, doi:10.3390/CATAL12060672.
83. Lima, M.J.; Pastrana-Martínez, L.M.; Sampaio, M.J.; Dražić, G.; Silva, A.M.T.; Faria, J.L.; Silva, C.G. Selective Production of Benzaldehyde Using Metal-Free Reduced Graphene Oxide/Carbon Nitride Hybrid Photocatalysts. ChemistrySelect 2018, 3, 8070–8081, doi:10.1002/SLCT.201800962.

84. Lima, M.J.; Silva, A.M.T.; Silva, C.G.; Faria, J.L. Graphitic Carbon Nitride Modified by Thermal, Chemical and Mechanical Processes as Metal-Free Photocatalyst for the Selective Synthesis of Benzaldehyde from Benzyl Alcohol. J Catal 2017, 353, 44–53, doi:10.1016/J.JCAT.2017.06.030.
85. Rodríguez, E.M.; Márquez, G.; Tena, M.; Álvarez, P.M.; Beltrán, F.J. Determination of Main Species Involved in the First Steps of TiO2 Photocatalytic Degradation of Organics with the Use of Scavengers: The Case of Ofloxacin. Appl Catal B 2015, 178, 44–53, doi:10.1016/j.apcatb.2014.11.002.
86. Rivas, J.; Solis, R.R.; Gimeno, O.; Sagasti, J. Photocatalytic Elimination of Aqueous 2-Methyl-4-Chlorophenoxyacetic Acid in the Presence of Commercial and Nitrogen-Doped TiO2. International Journal of Environmental Science and Technology 2015, 12, 513–526, doi:10.1007/s13762-013-0452-4.
87. Bielski, B.H.J.; Cabelli, D.E.; Arudi, R.L.; Ross, A.B. Reactivity of HO2/O−2 Radicals in Aqueous Solution. J Phys Chem Ref Data 1985, 14, 1041–1100, doi:10.1063/1.555739.
88. Rodríguez, E.M.; Rey, A.; Mena, E.; Beltrán, F.J. Application of Solar Photocatalytic Ozonation in Water Treatment Using Supported TiO2. Appl Catal B 2019, 254, 237–245, doi:10.1016/J.APCATB.2019.04.095.
89. Nien Schuchmann, M.; Bothe, E.; von Sonntag, J.; von Sonntag, C. Reaction of OH Radicals with Benzoquinone in Aqueous Solutions. A Pulse Radiolysis Study. Journal of the Chemical Society, Perkin Transactions 2 1998, 791–796, doi:10.1039/A708772A.
90. Von Sonntag, J.; Mvula, E.; Hildenbrand, K.; Von Sonntag, C. Photohydroxylation of 1,4-Benzoquinone in Aqueous Solution Revisited. Chemistry – A European Journal 2004, 10, 440–451, doi:10.1002/CHEM.200305136.
91. Ononye, A.I.; McIntosh, A.R.; Bolton, J.R. Mechanism of the Photochemistry of P-Benzoquinone in Aqueous Solutions. 1. Spin Trapping and Flash Photolysis Electron Paramagnetic Resonance Studies. Journal of Physical Chemistry 1986, 90, 6266–6270, doi:10.1021/J100281A039.
92. Schneider, J.T.; Firak, D.S.; Ribeiro, R.R.; Peralta-Zamora, P. Use of Scavenger Agents in Heterogeneous Photocatalysis: Truths,

Half-Truths, and Misinterpretations. Physical Chemistry Chemical Physics 2020, 22, 15723–15733, doi:10.1039/d0cp02411b.

93. Greenstock, C.L.; Miller, R.W. The Oxidation of Tiron by Superoxide Anion. Kinetics of the Reaction in Aqueous Solution and in Chloroplasts. Biochim Biophys Acta 1975, 396, 11–16, doi:10.1016/0005-2728(75)90184-X.
94. Bors, W.; Saran, M.; Michel, C. Pulse-Radiolytic Investigations of Catechols and Catecholamines II. Reactions of Tiron with Oxygen Radical Species. BBA - General Subjects 1979, 582, 537–542, doi:10.1016/0304-4165(79)90145-4.
95. Alam, M.S.; Rao, B.S.M.; Janata, E. ·OH Reactions with Aliphatic Alcohols: Evaluation of Kinetics by Direct Optical Absorption Measurement. A Pulse Radiolysis Study. Radiation Physics and Chemistry 2003, 67, 723–728, doi:10.1016/S0969-806X(03)00310-4.
96. Shah, B.R.; Patel, U.D. Mechanistic Aspects of Photocatalytic Degradation of Lindane by TiO2 in the Presence of Oxalic Acid and EDTA as Hole-Scavengers. J Environ Chem Eng 2021, 9, 105458, doi:10.1016/J.JECE.2021.105458.
97. Babu, P.; Mohanty, S.; Naik, B.; Parida, K. Synergistic Effects of Boron and Sulfur Co-Doping into Graphitic Carbon Nitride Framework for Enhanced Photocatalytic Activity in Visible Light Driven Hydrogen Generation. Applied Energy Materials 2018, 1, 5936–5947, doi:10.1021/acsaem.8b00956.
98. Ershov, B.G.; Janata, E.; Alam, M.S.; Gordeev, A. V. A Pulse Radiolysis Study of the Reactions of the Hydrated Electron and Hydroxyl Radical with the Oxalate Ion in Neutral Aqueous Solution. High Energy Chemistry 2008, 42, 1–6, doi:10.1134/s0018143908010013.

CHAPTER 7. PAPER FIVE

Sodium thiosulfate modified graphitic carbon nitride for enhancing the photocatalytic production of aldehydes

Sustainable Materials and Technologies

https://doi.org/10.1016/j.susmat.2024.e01123

M. Alejandra Quintana, Julia Aguirre, M. Ángeles Martín-Lara,

Mónica Calero, Mario J. Muñoz-Batista, Rafael R. Solís

Abstract

The oxidation of alcohols to aldehydes is one of the most relevant reactions in organic chemistry. The currently implemented methods based on expensive noble metallic catalysts, toxic solvents, and high temperature and pressure conditions have released the seek for softer and cheaper alternatives such as photocatalysis. In this sense, graphitic carbon nitride has been modified with sodium thiosulfate as a source of S and Na^+ incorporation in the structure, aimed at enhancing the photocatalytic performance on the photocatalytic oxidation of alcohols to aldehydes, cinnamaldehyde, benzaldehyde, and vanillin in aqueous solution. Three g-C_3N_4 samples synthesized from different precursors, i.e. melamine, thiourea, and urea, were treated with sodium thiosulfate. Urea led to the g-C_3N_4 with the highest mesoporosity (surface area, 69 m^2 g^{-1}) and photocatalytic activity. The modification with 5% (wt.) of $Na_2S_2O_3$ enhanced the pseudo-first order rate constant of cinnamyl alcohol oxidation from 0.265 h^{-1} (bare sample) to 0.792 h^{-1} ($Na_2S_2O_3$-modified). The characterization of the material suggests a better charge separation of the photogenerated charges after S and Na^+ incorporation in the structure, minimizing the recombination rate of photogenerated charges. The optimum photocatalyst, tested in aqueous solution, was most selective in the production of benzaldehyde (selectivity, >100%) > cinnamaldehyde (>23%) > vanillin (~5%). The selectivity was considerably boosted under acetonitrile as the solvent medium, raising the 23% recorded in water to 51% in pure acetonitrile. The degradation

mechanism suggests a strong influence of the photogenerated holes and the superoxide radical, the latter being more selective in the oxidation of the alcohol.

Keywords: graphitic carbon nitride, thiosulfate, photocatalytic oxidation, aldehydes, selectivity

7.1. INTRODUCTION

The production of ketones, aldehydes, and carboxylic acids from the oxidation of alcohols is one of the paramount reactions in industrial organic chemistry [1,2]. Cinnamaldehyde has uncountable applications in the food industry [3] and recently its pharmacological activity has been valued [4,5]. Benzaldehyde is a raw material with ample applications in the fields of medicine, chemical industry, printing, and dyeing [6]. Vanillin has traditionally been used in the food industry as an additive due to its flavor and antimicrobial activity [7]. In addition, the role played by vanillin in the cosmetics and perfumes area is relevant [8]. Moreover, it has been stated as an emerging intermediate in the synthesis of pharmaceutical products [9] or even a therapeutic molecule [10].

The oxidation of aromatic alcohols to aldehydes has been implemented using traditional oxidants such as ozone, peroxides, or halides, or under catalytic scenarios considering metal oxides, noble metals, and metal-free catalysts. Nevertheless, the required operation conditions under high temperature and pressure raise the cost and complexity. In this sense, photocatalysis emerges as a green novel technology to promote certain synthetic pathways that selectively trigger the formation of some added-value chemicals [11,12]. From all the tested photocatalysts to date, TiO_2 stands out by far [13]. However, some free-metals photocatalysts are acquiring relevance such as the graphitic carbon nitride (g-C_3N_4) [14], an organocatalyst with semiconductor properties featured by polymeric melon laminates with a bandgap of 2.7 eV, i.e. photo-activation up to 460 nm [15]. g-C_3N_4 is prepared from the thermal polymerization of nitrogen-enriched precursors. However, the resultant g-C_3N_4 may display excessive aggregation of laminates that result in limited surface area, reactive sites, and limited visible light harvesting, both negative for the photocatalytic application [16]. This drawback can be alleviated by selecting an adequate precursor [17]. The use of sodium thiosulfate as a sulfur-containing precursor has been widely implemented in sulfur doping of carbon-based materials. Sodium thiosulfate decomposes under thermal treatment, triggering the release of sulfur species that react with the carbon nitride structure [18]. Nonetheless, the use of

thiosulfate in graphitic carbon nitride is quite limited. It has been used as a sulfur precursor to generate the deposition of elemental sulfur nanoparticles after modification with citric and ascorbic acid [19], enlarging the radiation absorption in the visible region, and improving the reduction of Cr^{6+} to Cr^{3+}. In other work, the carbon nitride has been modified under an aqueous solution of $Na_2S_2O_3$, aimed at creating some nitrogen vacancies and acting as potential reactive sites. Hence, the presence of these irregularities in the structure modulates the formation of $HO^{\bullet}$ in the photocatalytic degradation of fluoroquinolones [20].

Based on the lack of information on the use of thiosulfate as a plausible modifier of g-C_3N_4, this work aims to study this strategy for the enhancement of the photocatalytic properties of g-C_3N_4 oriented to enhance the photocatalytic transformation of alcohols to aldehydes in aqueous solution. The influence of three different g-C_3N_4 precursors, i.e. melamine, thiourea, and urea, has been selected to prepare the bare g-C_3N_4 formula. In a second step, a $Na_2S_2O_3$ modification of the g-C_3N_4 samples obtained has been studied, urea being the most convenient and the one that largest boosted the kinetics of the oxidation of cinnamyl alcohol after thiosulfate modification. The ratio thiosulfate: g-C_3N_4 has been explored in the range of 1-10%, with an optimum value centered at 5%. The optimum sample was also tested in acetonitrile and water with other alcohols such as benzyl alcohol and vanillyl alcohol.

7.2. EXPERIMENTAL SECTION

7.2.1. Materials and synthesis of S-modified g-C_3N_4

All the chemicals were acquired from Merck®, analytical grade at least, and were used as received. For chromatographic analysis, acetonitrile of HPLC grade was used. The solutions were made with ultrapure water from a Direct-Q®-UV purification system (18.2 MΩ cm, Millipore®).

The synthesis of graphitic carbon nitride (CN) was conducted by thermal polymerization of different precursors (>99%), i.e. melamine, urea, and thiourea, by setting a certain amount in a covered ceramic crucible at 550 °C (heating rate, 10 °C min^{-1}) for 2 h. The resulting materials were labeled as CNx where ‘x’ stands for the precursor used, i.e. melamine (CNm), urea (CNu), and thiourea (CNt). The sulfur-

modification of these carbon nitride materials (SCNx) was carried out in a second stage, as depicted in Fig. 7.1. Then, $Na_2S_2O_3$ (1-10% wt. to the CN amount) was mixed with the CNx and ground in a mortar. The resulting mixture was then thermally treated under N_2 atmosphere (100 mL min^{-1}) at 550 °C (heating rate, 10 °C min^{-1}) for 2 h. The obtained solid was crushed and labeled as SCNx-y% where 'y' stands for the S doping percentage (wt.%).

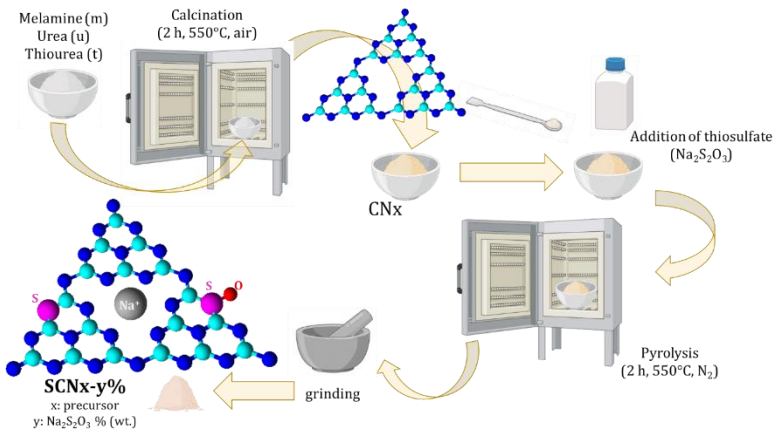

Fig. 7.1 *Synthesis process of the thiosulfate-modified g-C3N4 samples.*

7.2.2. Characterization of the S-modified g-C_3N_4 samples

The thermal behavior of the precursors during the polymerization to g-C_3N_4 was analyzed using a thermobalance STA 6000 from Perkin Elmer®. The sample was heated from room temperature to 850 ° C (heating rate, 20 °C min^{-1}) under N_2 flow (20 mL min^{-1}).

The crystal properties were analyzed by X-ray diffraction (XRD). The diffractometer used was a Bruker D8 Discover, coupled to a Pilatus 3R 100 K-A detector, working with Cu Kα radiation (1.5406 Å). The diffractograms were registered in the 2θ range of 5–65° (monitoring rate, 0.034° min^{-1}). The crystallite size ($L_{crystal}$) and the interlayer spacing (d_{layer}) were calculated with the help of the freeware QualX® to process the data [21]. The relation $L_{crystal}/d_{layer}$ was considered as a tentative approach to quantify the number of layers [22]. The structural properties were further evaluated by Fourier Transform InfraRed (FTIR) Spectroscopy, conducted in a Perkin Elmer FTIR device, model

Spectrum 65. The FTIR spectra were recorded in the interval 550–4000 cm^{-1}. Adsorption-desorption isotherms with N_2 at 77 K were conducted to assess the textural properties. The samples were firstly degassed under vacuum at 110 ºC, in a prep J4 station from 3P Instruments©. Next, the isotherms were obtained in a Sync 200 physisorption device of 3P Instruments©. The total specific surface area was obtained by the standardized Brunauer-Emmett-Teller method (S_{BET}), and the N_2 uptake at $p/p_0 \sim 0.99$ was referenced for calculating the total specific pore volume (V_T).

The elemental composition was determined in a Flash 2000 device of CHNS analyzer from ThermoScientific™. The surface chemical environment was assessed by X-ray Photoelectron Spectroscopy (XPS). The device used was a Kratos AXIS UltraDLD, operating with an X-ray source from Al Kα. The recorded spectra were referenced to the C_{1s} peak of adventitious carbon at 284.6 eV. The data was processed with the aid of the software XPSpeak 4.1®, and a Shirley background correction was applied as background.

The morphological properties were examined through Scan Transmission Electron Microscopy (STEM) in a Thermo Fisher Scientific TALOS F200X G2device (20-200kV) equipped with High-Angle Annular Dark Field (HAADF) detection and Electron Disperse X-Ray (EDX) analysis (Brucker X-flash 6T-30).

The optical properties were evaluated by the Diffuse Reflectance Spectroscopy (DRS) and photoluminescence (PL) techniques. For the DRS-UV-visible analysis, a Varian Cary 5E spectrophotometer was used. The absorbance and reflectance spectra were monitored at 200–2000 nm. From the reflectance signal, the function Kubelka-Munk Function, $F(R\infty)$ was calculated, and the bandgap was estimated by the Tauc plot method, applying indirect electron transitions. The PL spectra were monitored in a Varian Cary Eclipse fluorimeter, setting an excitation wavelength of 365 nm.

7.2.3. Photocatalytic production of aldehydes

The photocatalytic behavior of the prepared samples was assessed in the selective oxidation of cinnamyl alcohol (CA) to cinnamaldehyde (CD). However, other selected alcohols such as benzyl alcohol (BA) and vanillin alcohol (VA) were also oxidized to their respective aldehydes (BD, benzaldehyde; VD, vanillin). The photocatalytic experiments were

conducted in a jacketed cylindrical photoreactor, in whose center two UVA (365 nm, 9 W each) lamps were placed. The lamps were placed in the central space of the photoreactor. The reacting slurry solution (catalyst dose, 0.5 g L^{-1}) was pumped through the annular space. The temperature was controlled at 20 ºC with the help of an auxiliary tank containing the alcohol solution (1 mM), which was pumped to the annular space of the photoreactor. Specific details of the setup's scheme and dimensions can be checked in previous works [23,24]. To ensure the presence of dissolved O_2, air was supplied in the auxiliary tank. Before starting the photocatalytic assay, an adsorption period was conducted in the darkness to ensure the adsorption equilibrium. Next, the lamps were switched on, and samples were withdrawn and filtered (Millex PVDF, 0.45 µm) before analysis.

The influence of the oxidative species was evaluated by adding chemical scavengers that suppress certain reactive routes during the oxidation of the alcohol to the aldehyde [25,26]. The role played by the superoxide radical was tentatively analyzed by exchanging air with N_2 bubbling, or the presence of specific inhibitors such as p-benzoquinone (1 mM) or disodium 4,5-dihydroxybenzene-1,3-disulfonate (tiron, 1 mM). The addition of tert-butyl alcohol (TBA, 10 mM) was considered to remove the action of the hydroxyl radicals. Additionally, the formation of hydroxyl radicals was detected by an indirect probe method based on the presence of 2-hydroxy-terephthalic acid (2-HO-TPA) [27,28]. The non-fluorescent terephthalic acid (TPA) displays a strong ability to trap $HO^{\bullet}$, leading to the formation of the fluorescent 2-HO-TPA. A test in the presence of TPA (1 mM) was carried out to potentially probe or discharge the formation of $HO^{\bullet}$. The presence of 2-HO-TPA was analyzed in a Varian Cary fluorescence spectrometer. The excitation wavelength for 2-HO-TPA analysis was set at 315 nm and the emission spectra were recorded at 360–600 nm, defining a maximum peak at roughly 420 nm. The 2-HO-TPA concentration was determined from the peak area with standard solutions in the range 0.5-5 µM. From the calibration curve, a value of 0.21 µM was calculated for the limit of detection. Finally, the action of the photo-generated holes was scavenged with oxalic acid (1 mM) or ethylenediaminetetraacetic acid (EDTA, 1 mM).

High-Pressure Liquid Chromatography (HPLC) technique was used for quantifying the concentration of the alcohols and the aldehydes. The

HPLC device was an Alliance 2695 HPLC from Waters™, with a 2998 photodiode array detector. A Zorbas Bonus-RP column (5 µm, 4.6 ×150 mm) was used. The pumped mobile phase (1 mL min^{-1}) was a mixture of 40% (v/v) acetonitrile and 60% (v/v) ultrapure water acidified with 0.1% (v/v) of trifluoroacetic acid. The wavelength selected for quantification was 240 nm for CA, 331 nm for CD, 215 nm for BA, 248 nm for BD, 280 nm for VA, and 248 nm for VD.

The temporal reduction of the alcohol concentration was adjusted to a pseudo-first order kinetics. Hence, the calculated pseudo-first order rate constant (k) was compared among the photocatalytic tests. The selectivity of the aldehyde's formation was calculated from the aldehyde and alcohol temporal profiles, and an average value (S) was estimated for comparison purposes.

7.3. RESULTS

7.3.1. Characterization of the S-modified g-C3N4 samples

The thermal behavior of the three selected precursors during their polymerization was evaluated with thermogravimetric analysis under an N_2 atmosphere. The TGA profiles are depicted in Fig. 7.2The N_2 pyrolysis of melamine depicts a large mass loss between 300-400 ºC. Firstly, a rapid deamination of melamine takes place and condensates into melem (2,5,8-triamino-tri-s-triazine) and other polymeric derivatives [29]. Over 500 ºC, melem is transformed into g-C_3N_4 accompanied by a gradual further weight loss as depicted in the TGA of melamine. The TGA profile obtained in the case of thiourea can be divided into three stages. It has been stated that thiourea isomerizes to NH_4SCN in the range 140-180 ºC [30], being the proportion thiourea: NH_4SCN roughly 1:3 [31]. Next, the first largest mass loss takes place (76-78%). In this step the mix of thiourea and NH_4SCN undergoes pyrolysis reactions, leaving the formation of guanidinium thiocyanate and the release of H_2S and NH_2CN [31]. Next, the guanidinium thiocyanate decomposes into melamine and melem at 260-300 ºC releasing NH_3 and CS_2 [32]. Finally, from 350 to 450 ºC, the decomposition of g-C_3N_4 is deduced [33]. The TGA plot shows three steps for the case of urea. The first loss, appreciated at 160-250 ºC, is attributed to vaporization and decomposition into ammonia, cyanic acid, and CO_2 [34]. These gases

then react with urea to produce biuret [35]. The second major loss, starting at 230-360 ºC, is linked to the degradation of biuret to produce cyanuric acid and ammelide [36], one of the precursors of the tri-s-heptazine aromatic rings of g-C_3N_4. The final mass loss takes place gradually between 360-450 ºC. In this stage, residual cyanuric acid and ammelide continue their decomposition to produce ammeline, which triggers melamine formation. The formation of stable tri-s-triazine rings and their polymerization takes place at over 390 ºC, leading to the formation of the g-C_3N_4 [37]. The final structure of g-C_3N_4 is determined mainly by the reaction produced above 350 °C. The heating rate has been stated as crucial for developing porous structures. Thus, a high heating rate (15 ºC min^{-1}) has been demonstrated to scaffold a porous structure, with a high surface area, a complete g-C_3N_4 skeleton, and more amino groups [37], as is the case of the TGA curves of Fig. 7.2(heating rate, 20ºC min^{-1}). Temperatures higher than 700 ºC promote the complete degradation of the polymeric material. Based on the results achieved by the TGA analysis of the three precursors, it can be concluded that the formation of the g-C_3N_4 occurs by the rearrangement of melamine into melon units, even when using precursors such as thiourea and urea. Temperatures over 500 ºC provide optimal conditions for defining the g-C_3N_4 structure, albeit inferior to 700 ºC. For this reason, a standard value of 550 ºC was set as the temperature for synthesizing the CNx samples. Also, from the results achieved in the TGA, it is appreciated that the production yield was CNt > CNm > CNu.

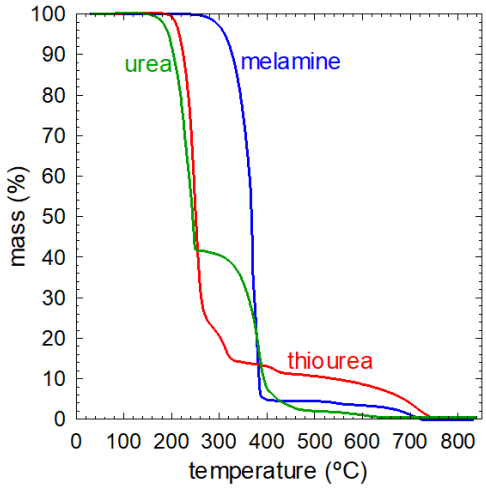

Fig. 7.2 *Thermogravimetric analysis of the g-C_3N_4 precursors under N_2 atmosphere.*

The XRD technique was conducted to assess the crystallinity of the prepared g-C_3N_4 with the three g-C_3N_4 precursors and their following modification with thiosulfate. Fig. 7.3A illustrates the diffractograms of the CNx before and after modification with 5% $Na_2S_2O_3$. The samples displayed the typical feather of g-C_3N_4 with two peaks attributed to the graphite structure and the tri-s-triazine units [38]. The most intense peak at approx. 27.4º appears from the piling aromatic units, being the result of the (002) crystal face, interplanar distance of the conjugated units of roughly 0.325 nm. The second peak, much less intense, is the result of the ordered tri-s-triazine units in the sheets. This peak was categorized as the (001) diffraction plane, attributed to the intraplanar distance. In this case, the precursor nature influenced the location of this peak, and therefore the d-value, being in the case of CNm 0.68 nm (13.1°), CNt 0.66 nm (13.4°), and CNu 0.68 nm (13.0°). This distance was, in all the cases, smaller than expected in the tri-s-triazine unit, reported as 0.73 nm [39]. This variation can be explained based on a small curvature in the planar structure. The modification with Na_2SO_3 contributed to the decrease of the crystalline peaks, especially the (002) stacking layer. Also, additional peaks were defined. Although an attempt to identify the nature of these peaks was conducted no clear components were found. The most intense peak, i.e. (002), was selected for the crystal size calculation, and the number of layers was calculated [22], see Table 7.1. The results suggest that the $Na_2S_2O_3$ modification led to a decrease in the crystal size, except for the CNt. The sample CNt led to the lowest number of layers, i.e. 19. The CN prepared with melamine described roughly 29 layers and urea led to 24. After treatment with $Na_2S_2O_3$, there was a stable decrease with the concentration defined as 19 layers in the case of CNu. Additionally, peaks at low intensity were registered. Although an attempt to identify the nature of these peaks was conducted, no clear components were found. These peaks are hypothesized to appear as the consequence of Na presence in the structure, as corroborated by XPS. However, the complexity of their interaction with the polymeric structure did not provide any match to the known registered inorganic compounds in the XRD database even in the sample with the best definition of these peaks, i.e. SCNu-10%. This lack of coincidence evidences the complexity of the interaction of the impurities with the structure, discharging any simpler known Na-related inorganic compound. The doping of g-C_3N_4 with Na^+ has been reported

to be combined with the in-plane N atoms in an ionic bond [40], which increases the electron density of the planar CN, with potential boosted separation of the charge carriers upon irradiation [40,41]. The available works dealing with Na-modification with NaOH did not report any appearance of impurities as here with the sample SCNu-10%, probably due to the low concentration of Na if compared to this sample (10%) [42,43].

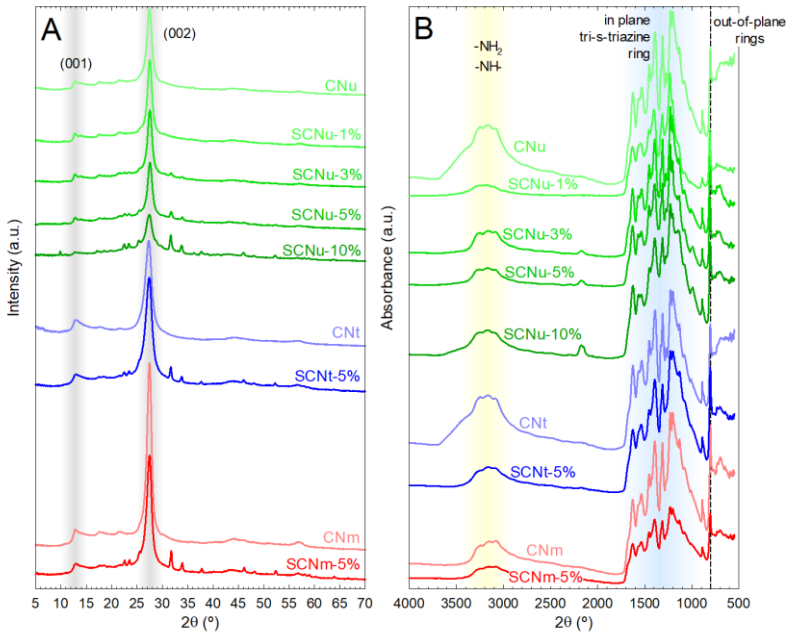

Fig. 7.3 *XRD diffractograms (A) and FTIR spectra (B) of the CNx and SCNx-y% samples.*

The structural properties of the g-C_3N_4 skeleton were evaluated by FTIR analysis. The FTIR fingerprints of the CN materials are depicted in Fig. 7.3B and the corresponding modified counterparts with $Na_2S_2O_3$. The three CN samples described the typical fingerprint of this graphite-like sp^2-bonded structure [44]. A broad peak placed 3000-3400 cm^{-1}, is mainly attributed to N-H vibration in the terminal -NH_2 and -NH- [45,46]. Remarkably, the presence of terminal nitrile groups was discharged since there was a complete lack of any peak centered on 2360 cm^{-1} [47]. All the samples described an intensive peak located at 800 cm^{-1}, described due to the vibration among the planes [46,48]. The presence of tri-s-triazine rings describes a particular fingerprint in the range 900-

1800 cm^{-1}. The most important are those located at 1620, 1530, and 1390 cm^{-1}, described by the stretching vibration of the C-N rings [46,49]. The three precursors led to very similar FTIR spectra. CNu and CNt described the highest contribution of the terminal -NH_2/-NH- groups. In contrast, melamine described the highest peak at 800 cm^{-1}, e.g. the out-of-plane interaction, consistent with the highest peak related to the interplanar layers in the XRD diffractogram. The modification with $Na_2S_2O_3$ implied a certain loss in the definition of the peaks, especially impacted on SCNm-5%. Interestingly, as the dose of $Na_2S_2O_3$ increased in SCNu, concretely over 3%, a peak centered at 2160 cm^{-1} augmented its intensity. This peak can be attributed to a thiocyanate (S-C≡N) or isothiocyanate (S=C=N) stretching, evidence of sulfur incorporation in the structure by replacing N positions [50,51]. This peak was not registered in the SCNm-5% and SCNt-5%. The sample prepared from urea denoted sensitivity for a better reaction with $Na_2S_2O_3$ than the others.

Table 7.1 *Crystal, textural, and optical properties of the CNx and SCNx-y% samples.*

Sample	$L_{crystal}$ (nm)	n layers	S_{BET} (m^2 g^{-1})	V_T (cm^3 g^{-1})	E_{BG} (eV)
CNm	8.5	29	12.5	0.061	2.60
SCNm-5%	7.8	24	12.8	0.061	2.60
CNt	6.3	19	18.9	0.097	2.64
SCNt-5%	6.3	19	16.7	0.079	2.66
CNu	7.7	24	69.5	0.318	2.85
SCNu-1%	7.6	23	69.5	0.288	2.85
SCNu-3%	7.0	22	66.9	0.284	2.85
SCNu-5%	6.8	21	64.4	0.214	2.75
SCNu-10%	6.2	19	40.0	0.177	2.80

Physisorption analysis was conducted to analyze the textural properties of the samples. Fig. 7.4 illustrates the N_2 adsorption-desorption isotherms. All the isotherms can be interpreted, according to the IUPAC classification, with Type II, characteristic of nonporous materials with a large contribution of macropores. The knee is not quite sharp, as it appears at low N_2 uptake in all the samples. This means a significant overlapping of the monolayer, promoting the multilayer formation [52]. Furthermore, the hysteresis loop, attributable to Type H3 according to IUPAC's classification, is commonly observed in aggregated plate-like particles, such as the case of graphitic carbon nitride materials, but also if the pore distribution is predominantly made

of macropores which are not filled with pore condensate [52]. The precursor influenced the BET area of the resulting carbon nitride, being CNm (12.5 m^2 g^{-1}) < CNt (18.9 m^2 g^{-1}) < CNu (69.5 m^2 g^{-1}). The total pore volume describes a similar trend. The modification with thiosulfate implied a decrease in the area, as shown in Table 7.1. Generally, carbon nitride prepared displays low surface area [22], unless a physical or chemical modification is carried out to boost the porosity [53,54]. Regarding the nature of the precursor, the presence of heteroatoms, such as oxygen and sulfur like the respective cases of urea and thiourea, favored the formation of noticeable porosity because of the released volatiles, i.e. CO_2 and CS_2, during the thermal rearrangement of melon units into heptazine units. For this reason, thiourea [55] and urea [56] lead to less crystalline and more porous carbon nitrides. The modification with thiosulfate of the CNm and CNt samples barely defined any substantial change in the surface area when modified at a dose of 5%. However, in the samples prepared with urea, a slight decrease is appreciated at low thiosulfate dosages (1-5%), until a considerable area decrease was registered at the highest dose (10%), i.e. 69.5 m^2 g^{-1} (CNu) versus 40.0 m^2 g^{-1} (SCNu-5%). This considerable decrease may be attributed to a smoothing effect after the reaction on the surface and/or an agglomeration effect during the second thermal treatment.

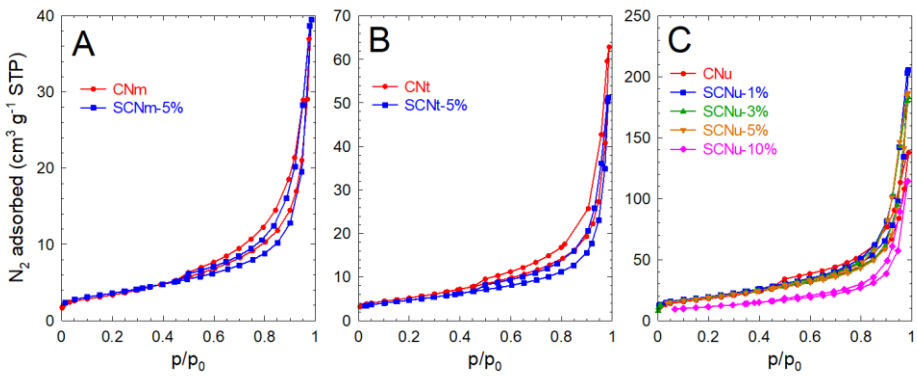

Fig. 7.4 *N_2 adsorption-desorption isotherms at 77 K of the CNx and SCNx-y% samples prepared from melamine (A), thiourea (B), and urea (C).*

The composition at the bulk was analyzed by elemental analysis and at the surface level by XPS analysis, see results in Table 7.2. A detailed analysis of the high-resolution spectra of the CNx and SCNx-5%

samples is depicted in Fig. 7.5. The C_{1s} peak is frequently deconvoluted in sp^2 N=C-N (287.9 eV), sp^3 C-C/C-N (285.2 eV), and sp^2 C-C/C=C (284.4 eV) contributions [57]. These three contributions were described in all the CNx samples, and an extra contribution in 289-290 eV was observed in the CNm and CNt, probably because of carboxyl, lactone, and ester groups [58]. The modification with thiosulfate did not substantially alter the C_{1s} deconvolution pattern, with a slight increase of the sp^2 C-C/C=C by the loss of sp^3 C-C/C-N. Also, the peak centered at 289-290 eV of oxygenated groups (carboxyl, lactone, and ester) disappeared after treatment probably due to the reducing character of $Na_2S_2O_3$. The N_{1s} region was deconvoluted as the result of three contributions related to N–C=N (N_2C, 398.4 eV), C_3–N (N_3C, 399.9 eV), and terminal N–H_x (401.0 eV) bonds [57,59–61]. The three precursors led to CN materials with the N–C=N outstands. In CNm, the terminal N–H_x follows in importance to the sp^2 nitrogen, while the CNt the sp^3 N is the second in importance. The sample CNu displayed a good equilibrium between sp^3-N and terminal N–H_x. The modification with thiosulfate assisted in the equilibration of these minor contributions. Regarding the region of S_{2p}, the thiosulfate samples displayed two contributions, one located at 162-164 eV that could be attributed to C-S-C environment [62], and the other placed at 168 eV that can be attributed to C-SO_2- binding [63,64]. The samples SCNm-5% and SCNu-5% displayed more contribution of the C-SO_2- than the C-S-C group, while thiourea as precursor had more preference for the C-S-C bonds. According to the surface quantification by XPS, the S content was the highest in the sample SCNu-5%, e.g. 2.4%. The thiosulfate modification with the other two precursors led to barely half of the S content. If these results are compared to the elemental analysis, see Table 7.2, it is appreciated that the three SCNx-5% samples led to a similar S content of 2.1-2.6%. The sample SCNu-5% displayed a uniform distribution of S among all the samples where the SCNm-5% and SCNt-5% have the sulfur concentrated in the core rather than on the surface compared to the bulk composition by elemental analysis. The presence of Na^+ cation was confirmed, as depicted in the Na_{1s} spectrum of Fig. 7.5. A peak centered at 1070.5 eV evidences the presence of Na^+ [43], as reported in previous works focused on incorporating Na^+ and N defects in the graphitic carbon nitride structure

[65]. The quantified amount of Na in the SCNx-5% samples, available in Table 7.2, varied from 0.3 to 1.6% depending on the precursor used.

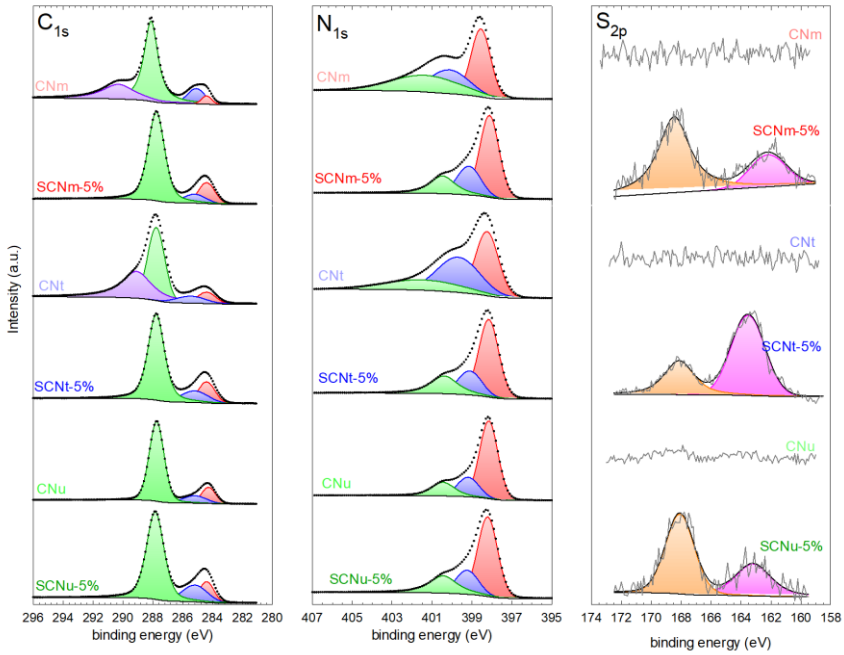

Fig. 7.5 *High-resolution XPS spectra of C_{1s} (left), N_{1s} (middle), S_{2p} (top-right), and Na_{1s} (bottom-right) of the CNx and SCNx-y% samples.*

Table 7.2 *Surface composition by XPS and elemental analysis of the CNx and SCNx-y% samples.*

	Elemental analysis (wt.%)				XPS (wt.%)					
Sample	**C**	**N**	**H**	**S**	**C**	**N**	**O**	**S**	**Na**	**VB_{XPS} (eV)**
CNm	35.2	63.9	1.9	-	42.5	54.6	2.9	-	-	2.1
SCNm-5%	32.8	58.9	1.7	2.4	42.7	51.5	4.5	1.0	0.3	2.0
CNt	34.9	62.8	2.0	-	41.0	56.4	2.6	-	-	2.0
SCNt-5%	34.2	57.6	1.8	2.1	42.9	50.0	5.1	1.3	0.7	2.0
CNu	29.9	53.2	1.8	-	42.8	54.0	3.2	-	-	2.0
SCNu-5%	31.5	55.5	1.5	2.6	42.3	48.5	5.2	2.4	1.6	2.2

The morphology of CNu and SCNu-5%, the precursor and thiosulfate-modified with the best photocatalytic active, was examined by the TEM microscopy, leading to the micrographs summarized in Fig. 7.6 The CNu imaging was characterized by the presence of randomly curved films. These films appeared as wrinkled clusters of over 1 μm,

creating cavities as observed in Fig. 7.6A_1, supporting the textural mesoporosity deduced from N_2 isotherms. The use of urea is expected to develop a porous material due to the release of CO_2 during its polymerization, providing porous structures composed of pressed sheets with irregular roughness [66–69]. The treatment with thiosulfate led to particles of smaller size, up to roughly 500 nm in which the roughness is considerably softened. The presence of sulfur and sodium in the SCNu-5% was confirmed by EDS mapping although the intensity at which detected was low, due to the low concentration as the quantification by XPS suggested.

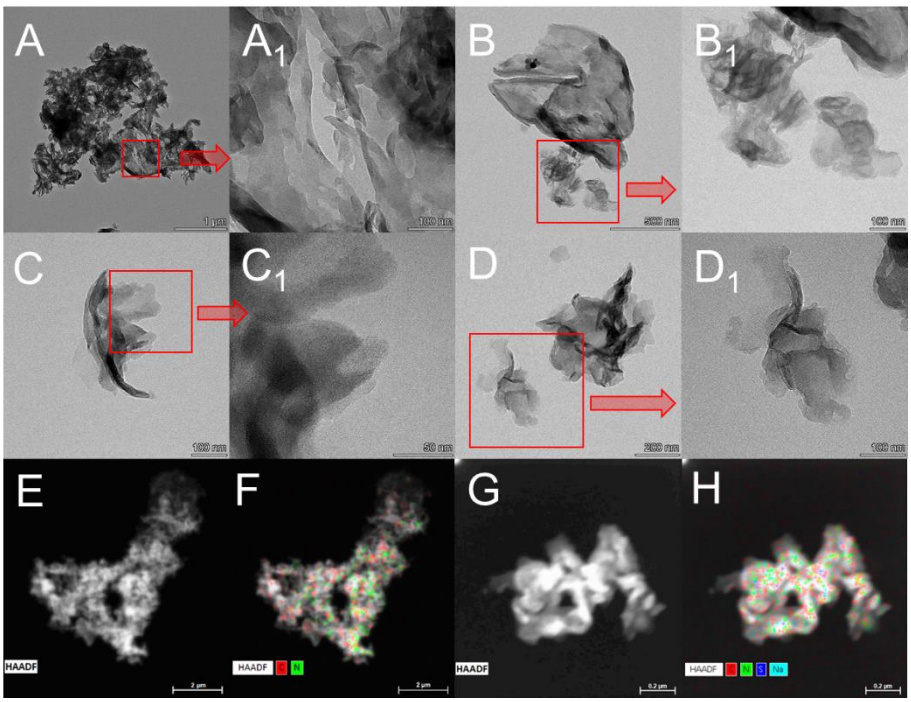

Fig. 7.6 *TEM pictures of CNu (A and B) and SCNu-5% (C and D). HAADF and element mapping of CNu (E and F) and SCNu-5% (G and H).*

The DRS-UV-visible characterization was conducted to evaluate the optical properties. The absorption spectra are portrayed in Fig. 7.7A, and the bandgap calculation (Table 7.1) is depicted in Fig. 7.7B. All the CN photocatalysts performed a strong absorption ability in the visible range, the result of the π-π* electronic transition of the conjugated planes. The lowest absorption of CNu may be the result of the presence

of less condensed melem or melon oligomers, a fact corroborated by the lower crystalline structure in this case [70]. This effect impacted the bandgap of the three precursors, i.e. CNm (2.60 eV) ~ CNt (2.66 eV) < CNu (2.85 eV). Poor crystallinity of g-C_3N_4 has been reported to promote an enlargement of the π-π * piling distance, which embraces a wider bandgap and more charge recombination [71], both detrimental for a photocatalytic application. The modification of thiosulfate enlarged the harvesting of radiation in the visible range; therefore, decreasing the bandgap values, which was more appreciable in the case of the largest bandgap CN, i.e. CNu.

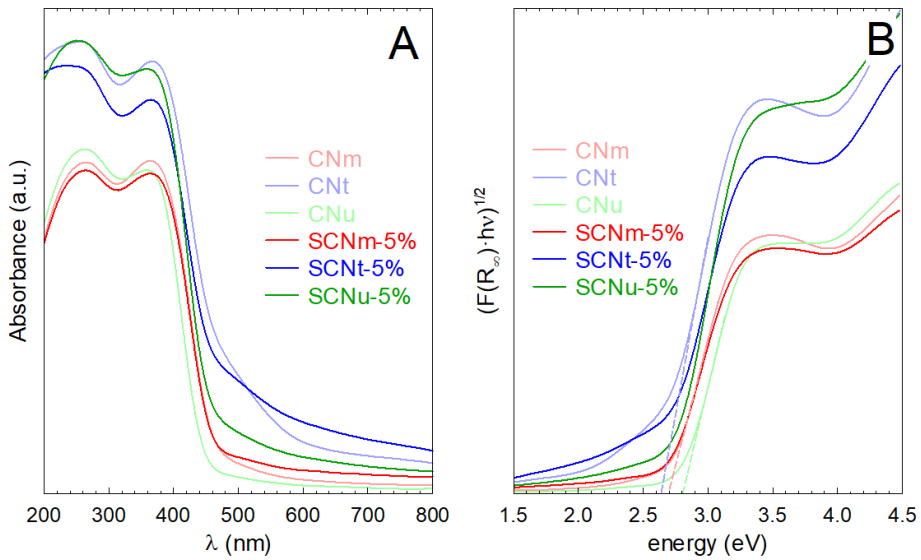

Fig. 7.7 *DRS-UV-visible spectra (A) and Tauc's plot for the bandgap estimation (B) of the CNx and SCNx-5% samples.*

7.3.2. Photocatalytic activity in the production of aldehydes

The photocatalytic production of aldehydes with the different graphitic carbon nitride prepared from the different precursors' formulas was first evaluated with the oxidation of cinnamyl alcohol (CA) to cinnamaldehyde (CD). Fig. 7.8 depicts the time course of the CA concentration and the related pseudo-first order rate constant (k_{CA}). As illustrated, CA was not photolyzed under the source of irradiation used, i.e. UVA of 365 nm. The different precursors lead to g-C_3N_4 with different

efficiency in the oxidation of CA. The melamine was the least active g-C_3N_4, k_{CA}=0.086 h^{-1}. The CNt and CNu improved the results achieved with melamine, leading to similar activity, k_{CA}=0.241±0.019 h^{-1} for CNt and k_{CA}=0.265±0.004 h^{-1} for CNu. The photocatalytic oxidation reactions are triggered on the surface of the semiconductor after irradiation. Both textural and optical properties define the activity of the material. The optical properties of CNm, CNt, and CNu in terms of bandgap or photoluminescence response (see Fig. 7.8C) cannot solely explain why CNu is the most photoactive. In this case, it seems that the surface area, much higher in the CNu sample, is the key factor.

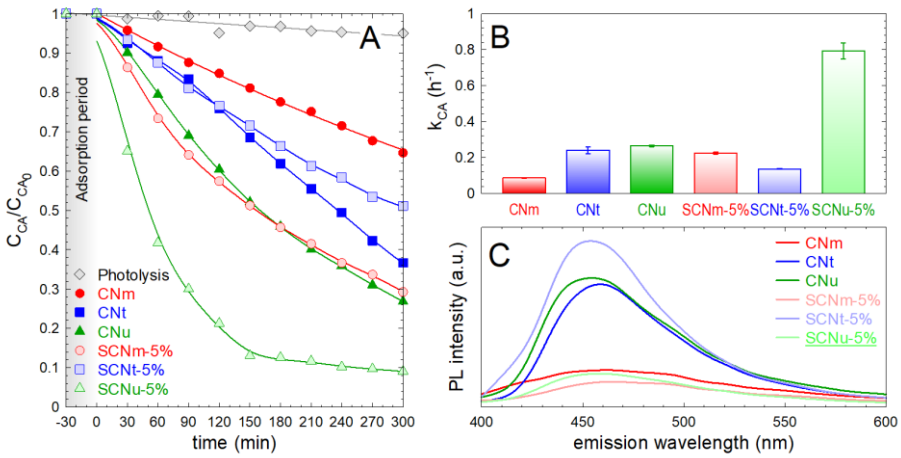

Fig. 7.8 *Photocatalytic oxidation of cinnamyl alcohol with CNx and SCNx-5% samples. (A) Temporal evolution of the normalized concentration of CA. (B) Pseudo-first order rate constant of CA abatement. (C) Photoluminescence spectra of CNx and SCNx-5% samples. Experimental conditions: UVA radiation; V= 350 mL; C_{CA}= 1 mM; $C_{catalyst}$= 0.5 g^{-1}, T = 20 ºC.*

The modification with thiosulfate of the CNx samples led to different behavior depending on the precursor. Regarding melamine, the photocatalytic activity of CNm-5% was improved concerning the bare CNm, although the increase in the k_{CA} was limited, from 0.086±0.003 to 0.224±0.005 h^{-1}. In the case of thiourea, the modification with thiosulfate led to a detrimental effect, negatively affecting the oxidation kinetics of CA, 0.241±0.019 to 0.136±0.003 h^{-1}. The modification with 5% of NaS_2O_3 did not substantially change the surface area of the CNx samples. Therefore, the differences in photocatalytic activity may rely on the optical properties. According to the photoluminescence of the samples, see Fig. 7.8C, the PL peak of thiourea was increased after the thiosulfate treatment, leading to a poorer separation of charges. The

analysis by photoluminescence has been linked to the electronic behavior of a semiconductor after irradiation. Hence, after excitation, the electron-hole pair recombination leads to the emission of a photon of energy equal to the bandgap energy. Therefore, a low-intensity PL peak can be associated with a lower recombination effect, undesirable for efficient radiation harvesting [72]. The incorporation of sulfur and Na^+ contributed to imperfections that minimized the electronic recombination after excitation [40,42,43], leading to enhanced photocatalytic activity. The photocatalytic activity described by CNt and SCNt-5% is under the response registered by PL. The CNu modification, i.e. SCNu-5%, led to the best improvement compared to the rest of the used precursors. In this case, the k_{CA} was remarkably augmented from 0.265±0.004 to 0.792±0.044 h^{-1}, which means 3 times folded. The PL intensity of the SCNu-5% was considerably lower than the counterpart CNu; therefore, the modification with thiourea improved the charge separation rate, minimizing the recombination effect that positively impacts the activity performance. As the modification of CNu led to the best result, the proportion of thiourea was assessed for this sample.

Fig. 7.9 depicts the effect of the thiosulfate ratio during the modification of CNu. As illustrated, it is observed that the proportion of thiosulfate reaches an optimum value for the kinetics of CA oxidation, located at 5%. The k_{CA} values matched the behavior of the PL peak, being the activity inverse to the intensity of the emission peak, CNu-5% (0.792±0.044 h^{-1}) > CNu-10% (0.682±0.044 h^{-1}) > CNu-3% (0.615±0.040 h^{-1}) > CNu-1% (0.341±0.012 h^{-1}) > CNu (0.265±0.004 h^{-1}). Therefore, the modification with thiosulfate could be ascribed to the minimization of the recombination effect by the definition of imperfections on the surface, despite the case of SCNu-10% in which a decrease of the surface area, and therefore the active reacting sites were observed.

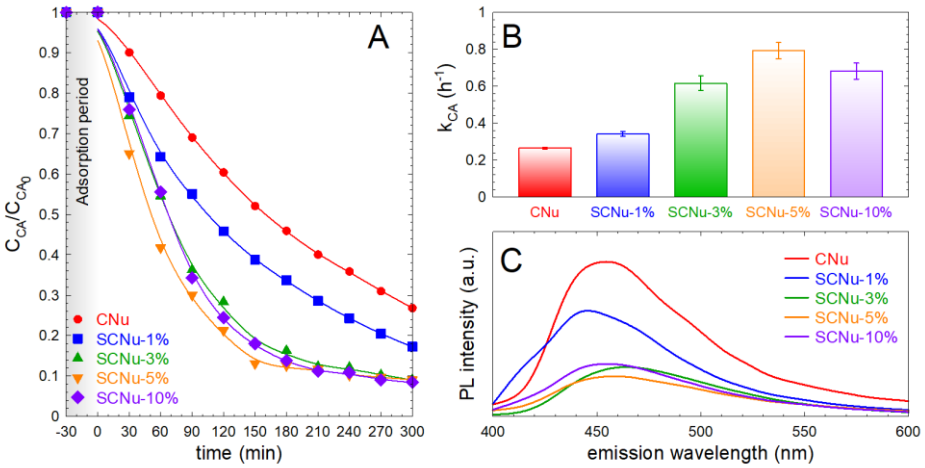

Fig. 7.9 *Photocatalytic oxidation of cinnamyl alcohol with SCNu-y% samples. (A) Temporal evolution of the normalized concentration of CA. (B) Pseudo-first order rate constant of CA abatement. (C) Photoluminescence spectra of SCNu-y% samples. Experimental conditions: UVA radiation; V= 350 mL; C_{CA}= 1 mM; $C_{catalyst}$= 0.5 g^{-1}, T = 20 ºC.*

Based on the greater photocatalytic performance during CA oxidation, the sample SCNu-5% was selected for further study. Fig. 7.10 portrays the average selectivity during the 5 h of CA oxidation to CD. The selectivity of the SCNu-5% sample was ~20% whereas the non-modified CNu achieved 13%. More interestingly, not only did the nature of the solvent impact kinetics but also the selectivity. In the presence of acetonitrile (ACN), the sample SCNu-5% led to a reduction of the k_{CA} to 0.140±0.007 h^{-1}. However, selectivity was boosted to 51% in the presence of acetonitrile. The use of a water-ACN mixture at 50:50 described intermediate k_{CA} and selectivity values. In the presence of water, cinnamyl alcohol displays great reactivity. The aldehyde formation passes through a hydration step to form a geminal diol in the presence of water, which then dehydrogenates to trigger the corresponding acid, making the transient aldehyde formed undetected in the reaction medium [1]. In the specific case of cinnamaldehyde, the hydration and further oxidation to form cinnamic acid have been reported as important [1]. This fact explains why the selectivity of CA decays in the presence of water if compared to organic solvents such as acetonitrile or toluene [73]. Moreover, the presence of organic solvent also promotes a higher solubility of O_2 if compared to water [74]. The lack of water and the higher dissolved O_2 may lead to a better generation of superoxide

radicals and photogenerated holes, positively impacting the selectivity to the aldehyde [23].

The effectiveness of the SCNu-5% sample in water was also tested in the oxidation of other aromatic alcohols, such as benzyl and vanillyl alcohol, generating their respective aldehydes. Fig. 7.10C depicts the time course of each alcohol and its aldehyde. In the case of benzyl alcohol (BA), it is observed that the reactivity is lower than the observed for cinnamyl alcohol, k_{CA}=0.792±0.044 vs k_{BA}=0.236±0.007 h^{-1}. Nonetheless, the oxidation was exclusively oriented to the production of benzaldehyde, leading to a selectivity of 100%. In the case of the oxidation of vanillyl alcohol (VA), it was not the case. This alcohol was the least reactive to the SCNu-5% sample, k_{VA}=0.088±0.003 h^{-1}, with a poor selectivity to vanillin (VD), only 5%.

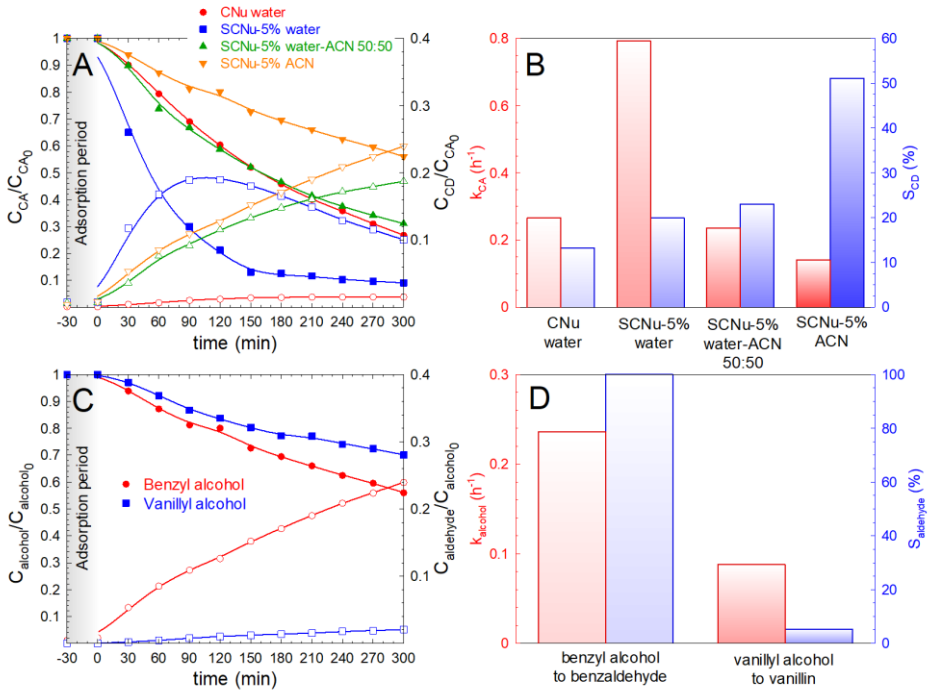

Fig. 7.10 *Temporal evolution of CA and CD (empty symbols) during the photocatalytic oxidation with SCNu-5% in water, acetonitrile (ACN), and 50:50 mixtures (A). Pseudo-first order rate constant of CA oxidation and average selectivity to CD (B). Temporal evolution of benzyl alcohol, vanillyl alcohol, and their respective aldehydes (empty symbols) during the photocatalytic oxidation with SCNu-5% in water (C). Pseudo-first order rate constant of benzyl and vanillyl alcohol oxidation and their average selectivity to their respective*

aldehydes (D). Experimental conditions: UVA radiation; V= 350 mL; $C_{alcohol}$= 1 mM; $C_{catalyst}$= 0.5 g^{-1}, T = 20 ºC.

The impact of the different Reactive Oxidative Species (ROS) involved in the oxidation of cinnamyl alcohol has been elucidated by adding to the reaction medium different chemical scavengers that inhibit certain species associated with a higher affinity towards them [75–77].Fig. 7.11A shows the temporal evolution of CA concentration in the presence of inhibitors. The influence of superoxide radical ($O_2^{\bullet-}$), generated after adsorbed O_2 is reduced by the photogenerated electrons of the conduction band was evaluated by exchanging the air bubbling with N_2, with the addition of chemical scavengers such as p-benzoquinone (p-BZQ) or tiron [23,78]. In the presence of N_2, the k_{CA} was reduced, as illustrated in Fig. 7.11B, which proves the importance of $O_2^{\bullet-}$ in the overall oxidative mechanism. However, the absence of O_2 may contribute to a higher recombination effect since the photogenerated electrons are not consumed. A test with p-BZQ was conducted. The kinetics was considerably decelerated, i.e. k_{CA} was 30% of the blank test. Although this fact would mean considerable participation of $O_2^{\bullet-}$, the results must be interpreted with caution due to the complex chemistry of p-BZQ which may lead to alternative side-chain reactions [76], such as reaction with $HO^{\bullet}$, formation of semiquinone radicals [25], or photolysis that produces extra $O_2^{\bullet-}$ [79] or $^1O_2$ [80]. For this reason, tiron was also assessed as an alternative scavenger [76]. In the presence of tiron, the k_{CA} value was not substantially altered as observed with p-BZQ.

The role played by the $HO^{\bullet}$ was evaluated in the presence of tert-butyl alcohol (TBA), due to its high affinity [81]. In the test with TBA, the CA oxidation kinetic was barely altered; therefore, the influence of $HO^{\bullet}$ must be discharged. To further confirm the lack of $HO^{\bullet}$, a probe test of 2-hydroxy-terephthalic acid (2-HO-TPA) from the reaction of terephthalic acid (TPA) with $HO^{\bullet}$ was conducted [27]. According to the considerable signal-to-noise ratio of the fluorescent spectra registered for 2-HO-TPA with the temporal evolution (Fig. 7.11C), the amount of 2-HO-TPA could be predicted as negligible. The quantification led to the temporal profile of 2-HO-TPA depicted in Fig. 7.11D, whose values were all below the limit of detection of the method, stimulated as 0.21 μM, a value much

lower than the detected in photocatalytic processes with a predominant role of the $HO^{\bullet}$ route [28,82].

The plausible contribution of the photogenerated holes to the oxidative mechanism was assessed by two traditional hole-scavengers, the oxalate anion [83] and ethylenediaminetetraacetic acid (EDTA) [83,84]. The addition of oxalate anion decelerated the kinetics of CA oxidation while EDTA kept it like the blank test. Interestingly, selectivity was raised in both cases, which may be proof of a more selective oxidation process in the absence of the photogenerated holes. It should be considered that the presence of these substances positively contributes to the kinetics of the process in some cases since it favors the insertion of extra photogenerated electrons to the conduction band as the holes are consumed. The faster and greater removal in the presence of EDTA compared to oxalate has been confirmed as superior due to the hole consumption by EDTA [83]. Therefore, it seems that the presence of holes contributes to the degradation process, negatively affecting the selectivity of the process if compared to the superoxide radical. Finally, the contribution of single oxygen was evaluated by adding L-histidine (L-H) to the aqueous medium [26]. Nonetheless, the addition of L-H did not modify the kinetics of the process.

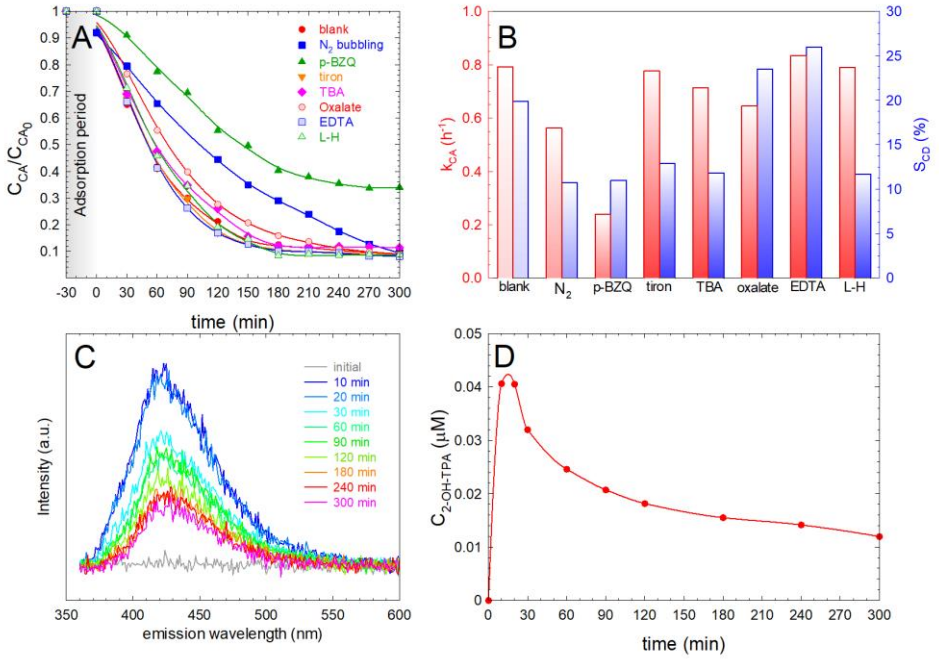

Fig. 7.11 *Photocatalytic oxidation of cinnamyl alcohol (CA) to cinnamaldehyde (CD). The pseudo-first order rate constant of CA abatement with SCNu-5% in the presence of chemical scavengers (A) and the CA conversion at 5 h and average selectivity to CD (B). Photoluminescence spectra of 2-OH-TPA (C) and the temporal evolution of the concentration of 2-OH-TPA (D) during the photocatalytic transformation of TPA with SCNu-5%. Experimental conditions: UVA radiation; V= 350 mL; $C_{CA,0}$= 1 mM; CSCNu-5%= 0.5 g L^{-1}; $C_{scavenger}$= 1 mM; $C_{TPA,0}$= 1 mM; T = 20 ºC.*

A plausible mechanism of photo-activation with the band alignment for CNu and SCN-5% is proposed in Fig. 7.12. The valence band energy level was tentatively estimated from the energy edge of XPS (VB_{XPS}) at low energy values, see Fig. 7.12A. The Fermi level is above the estimated VB_{XPS} value [85,86]. Furthermore, the band edge positions of the valence band (E_{VB}) can be calculated as follows [87,88]:

$$E_{VB} = \Delta E - E_{vac} + W_S \quad (7.1)$$

where ΔE stands for the difference between the E_F level and the VB maximum value, E_{vac} is the energy of free electrons in the hydrogen scale (4.5 eV), and W_S means the work function. The work function W_S can be considered 4.0 eV for g-C_3N_4 materials [89].

Table 7.2 shows all the XPS edge values for the CNx and SCNx-5% samples. All the CNx materials display very similar energy edges in their

XPS spectra, around +2.0 eV, i.e. their E_{VB} is +1.5 eV. However, concerning the values of the SCNx-5%, it was only the sample prepared with urea the precursor that performed an enlargement of the value, concretely the XPS valence band was +2.2 eV, i.e. the E_{VB} = +1.70 eV. This shifted value after thiosulfate medication implies a higher oxidative potential of the holes of the modified photocatalyst. From the estimated E_{VB}, the conduction band energy (E_{CB}) was determined by subtracting the bandgap energy from the E_{VB}, leading to E_{CB} = -1.35 eV for CNu and E_{CB} = -1.05 eV for SCNu-5%. The value obtained in this work for CNu is within the range of values reported in the literature [90]. A scheme of the band's alignment is portrayed in Fig. 7.12B. for CNu and SCNu-5%. According to this band placement, it is stated the unfeasibility of the formation of $HO^{\bullet}$, since the redox of the pair $H_2O/HO^{\bullet}$ is + 2.31 V [91]. Conversely, the production of the $O_2^{\bullet-}$ is favored, with redox potential $O_2/O_2^{\bullet-}$, -0.33 V [92]. The contrast of the band's energy before and after modification with thiosulfate led to an increase in the redox potential of the photogenerated holes. This fact and the enhanced migration of charges from the photoluminescence emission spectra can be attributed as the main reasons for the boosted photocatalytic activity difference after thiosulfate modification.

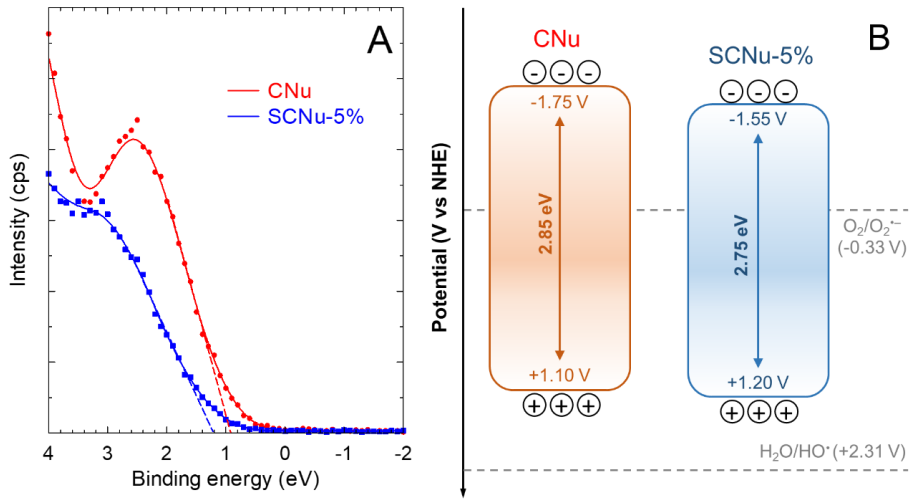

Fig. 7.12 *Determination of the valence band edge of CNu and SCNu-5% by XPS (A) and their band's alignment proposal (B).*

The sample with the optimum activity, i.e. SCNu-5%, was submitted to sequential recycling and reusing tests to examine the material's

stability. Fig. 7.13A depicts the cinnamyl alcohol evolution during four consecutive experiments in water and Fig. 7.13B illustrates the pseudo-first order rate constant calculated from each one. As illustrated, no significant loss of activity was observed. The time-course curves were completely overlapped among them, with an insignificant deviation at the beginning of the assay. The alcohol conversion over 180 min was the same in all the runs. Besides, the pseudo-first order rate constant was kept stable with a minimal decrease, i.e. 0.792 h^{-1} (1st run), 0.763 h^{-1} (2nd run), 0.693 h^{-1} (3rd run), and 0.677 h^{-1} (4th run), which evidences the great stability of the material. The material recovered from the last run was characterized by FTIR. As shown in Fig. 7.13C, the characteristic absorbance footprint of the material was maintained, discharging structural changes after its use.

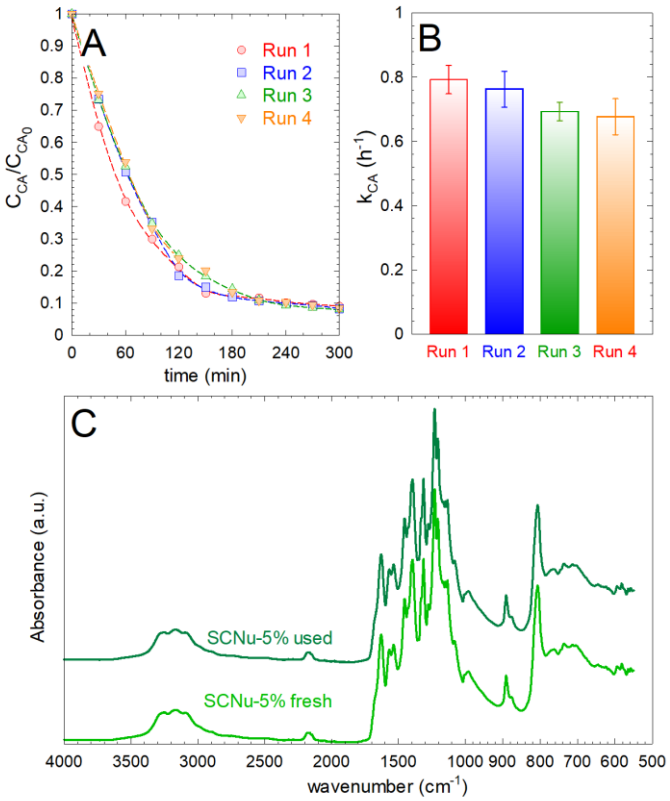

Fig. 7.13 *Stability tests of SCNu-5% sample. (A) Time-course of the CA normalized concentration. (B) Pseudo-first order rate constant of CA abatement. (C) FTIR spectra before and after use. Experimental conditions: UVA radiation; V= 350 mL; C_{CA}= 1 mM; $C_{catalyst}$= 0.5 g^{-1}, T = 20 ºC.*

7.4. CONCLUSIONS

Photocatalytic reactions provide a new platform for synthesizing added-value organic compounds such as aldehydes from the oxidation of their alcohols. Hence, the reaction of alcohol oxidation under ambient temperature and pressure conditions, water as a solvent instead of the traditional expensive and toxic organic solvents, and a metal-free cheaper catalyst such as graphitic carbon nitride has been examined.

The nature of the nitrogen carbonaceous precursor strongly impacts the crystalline and textural properties of graphitic carbon nitride formulas, leading to the use of melamine for a more crystalline and less porous g-C_3N_4, due to the important gases released during the pyrolysis process of thiourea and, especially urea, which leaves imperfections in the structure. In the case of thiourea, and remarkably urea, the synthesized g-C_3N_4 was less crystalline and more porous. This aspect is essential in photocatalytic performance, with the g-C_3N_4 prepared with thiourea and urea being the most active. The oxidation rate constant of cinnamyl alcohol was 0.086±0.003 h^{-1} for the material prepared with melamine, 0.241±0.019 h^{-1} with thiourea, and 0.265±0.004 h^{-1} with urea (initial alcohol concentration, 1 mM). The modification with sodium thiosulfate incorporated enhanced the photocatalytic activity, in the g-C_3N_4 prepared from melamine and urea, being the latter considerable, i.e. the pseudo-first order rate constant of cinnamyl alcohol oxidation k_{CA}=0.792±0.044 h^{-1}. This improvement was ascribed to the better separation of charges and reduction of the recombination effect as suggested by the photoluminescence characterization, originated by the creation of imperfections on the carbon nitride base, raising the oxygen content and incorporating S as thiocyanate/isothiocyanate, C-S-C, and C-SO_2 bonds. The selectivity to cinnamyl alcohol of the thiosulfate sample prepared with urea was enhanced from 13% (bare g-C_3N_4) to 23% in aqueous solution. This value was further boosted by replacing the aqueous media with acetonitrile, increasing it to 51%. This sample demonstrated higher effectiveness in oxidizing benzyl alcohol to benzaldehyde, i.e. 100% selectivity. The study of the mechanism of the reacting species involved in the process suggested the importance of superoxide radicals and holes, the former being more selective. The hydroxyl radical impact was negligible due to insufficient energy for the oxidation of water molecules.

REFERENCES

1. Besson, M.; Gallezot, P. Selective Oxidation of Alcohols and Aldehydes on Metal Catalysts. *Catal Today* 2000, *57*, 127–141, doi:10.1016/S0920-5861(99)00315-6.
2. Romano, D.; Villa, R.; Molinari, F. Preparative Biotransformations: Oxidation of Alcohols. *ChemCatChem* 2012, *4*, 739–749, doi:10.1002/CCTC.201200042.
3. Muhoza, B.; Qi, B.; Harindintwali, J.D.; Koko, M.Y.F.; Zhang, S.; Li, Y. Encapsulation of Cinnamaldehyde: An Insight on Delivery Systems and Food Applications. *Crit Rev Food Sci Nutr* 2023, *63*, 2521–2543, doi:10.1080/10408398.2021.1977236.
4. Guo, J.; Yan, S.; Jiang, X.; Su, Z.; Zhang, F.; Xie, J.; Hao, E.; Yao, C. Advances in Pharmacological Effects and Mechanism of Action of Cinnamaldehyde. *Front Pharmacol* 2024, *15*, 1365949, doi:10.3389/FPHAR.2024.1365949.
5. Doyle, A.A.; Stephens, J.C. A Review of Cinnamaldehyde and Its Derivatives as Antibacterial Agents. *Fitoterapia* 2019, *139*, 104405, doi:10.1016/J.FITOTE.2019.104405.
6. Zhou, Z.; Xie, Y.N.; Zhu, W.; Zhao, H.; Yang, N.; Zhao, G. Selective Photoelectrocatalytic Tuning of Benzyl Alcohol to Benzaldehyde for Enhanced Hydrogen Production. *Appl Catal B* 2021, *286*, 119868, doi:10.1016/J.APCATB.2020.119868.
7. Martău, G.A.; Călinoiu, L.F.; Vodnar, D.C. Bio-Vanillin: Towards a Sustainable Industrial Production. *Trends Food Sci Technol* 2021, *109*, 579–592, doi:10.1016/J.TIFS.2021.01.059.
8. Upadhyay, S.K.; Singh, S.P. Plants as Source of Essential Oils and Perfumery Applications. In *Bioprospecting of Plant Biodiversity for Industrial Molecules*; John Wiley & Sons, Ltd, 2021; Vol. 13, pp. 261–292 ISBN 9781119718017.
9. Liaqat, F.; Xu, L.; Khazi, M.I.; Ali, S.; Rahman, M.U.; Zhu, D. Extraction, Purification, and Applications of Vanillin: A Review of Recent Advances and Challenges. *Ind Crops Prod* 2023, *204*, 117372, doi:10.1016/J.INDCROP.2023.117372.
10. Arya, S.S.; Rookes, J.E.; Cahill, D.M.; Lenka, S.K. Vanillin: A Review on the Therapeutic Prospects of a Popular Flavouring Molecule. *Advances in Traditional Medicine* 2021, *21*, 1–17, doi:10.1007/S13596-020-00531-W.

11. Marcì, G.; García-López, E.I.; Palmisano, L. Polymeric Carbon Nitride (C_3N_4) as Heterogeneous Photocatalyst for Selective Oxidation of Alcohols to Aldehydes. *Catal Today* 2018, *315*, 126–137, doi:10.1016/J.CATTOD.2018.03.038.
12. Ciriminna, R.; Fidalgo, A.; Meneguzzo, F.; Parrino, F.; Ilharco, L.M.; Pagliaro, M. Vanillin: The Case for Greener Production Driven by Sustainability Megatrend. *ChemistryOpen* 2019, *8*, 660–667, doi:10.1002/OPEN.201900083.
13. Luong, G.K.T.; Ku, Y. Selective Oxidation of Benzyl Alcohol in the Aqueous Phase by TiO_2-Based Photocatalysts: A Review. *Chem Eng Technol* 2021, *44*, 2178–2190, doi:10.1002/CEAT.202100321.
14. Su, F.; Mathew, S.C.; Lipner, G.; Fu, X.; Antonietti, M.; Blechert, S.; Wang, X. Mpg-C_3N_4-Catalyzed Selective Oxidation of Alcohols Using O_2 and Visible Light. *J Am Chem Soc* 2010, *132*, 16299–16301, doi:10.1021/JA102866P.
15. Priyanga, G.S.; Pransu, G.; Sampath, S. A Comprehensive Overview of the Graphitic-Carbon Nitride Computational Approach: From Basic Properties to a Wide Range of Applications. *Chemical Physics Impact* 2024, *8*, 100408, doi:10.1016/J.CHPHI.2023.100408.
16. Panthi, G.; Park, M. Graphitic Carbon Nitride/Zinc Oxide-Based Z-Scheme and S-Scheme Heterojunction Photocatalysts for the Photodegradation of Organic Pollutants. *Int J Mol Sci* 2023, *24*, 15021, doi:10.3390/IJMS241915021.
17. Kumar, S.; Battula, V.R.; Kailasam, K. Single Molecular Precursors for C_xN_y Materials- Blending of Carbon and Nitrogen beyond g-C_3N_4. *Carbon N Y* 2021, *183*, 332–354, doi:10.1016/J.CARBON.2021.07.025.
18. Mohammad, A.; Chandra, P.; Khan, M.E.; Choi, C.H.; Yoon, T. Sulfur-Doped Graphitic Carbon Nitride: Tailored Nanostructures for Photocatalytic, Sensing, and Energy Storage Applications. *Adv Colloid Interface Sci* 2023, *322*, 103048, doi:10.1016/J.CIS.2023.103048.
19. Bankole, O.M.; Olorunsola, T.D.; Ogunlaja, A.S. Photocatalytic Decontamination of Toxic Hexavalent Chromium in Water over Graphitic Carbon Nitride Supported Sulfur Nanoparticles. *J*

Photochem Photobiol A Chem 2021, *405*, 112934, doi:10.1016/J.JPHOTOCHEM.2020.112934.

20. Zhong, J.; Ni, T.; Huang, J.; Li, D.; Tan, C.; Liu, Y.; Chen, P.; Wen, C.; Liu, H.; Wang, Z.; et al. Directional Utilization Disorder Charge via In-Plane Driving Force of Functionalized Graphite Carbon Nitride for the Robust Photocatalytic Degradation of Fluoroquinolone. *Chemical Engineering Journal* 2022, *442*, 135943, doi:10.1016/J.CEJ.2022.135943.
21. Altomare, A.; Corriero, N.; Cuocci, C.; Falcicchio, A.; Moliterni, A.; Rizzi, R. QUALX2.0: A Qualitative Phase Analysis Software Using the Freely Available Database POW_COD. *J Appl Crystallogr* 2015, *48*, 598–603, doi:10.1107/S1600576715002319.
22. Pérez-Molina, Á.; Pastrana-Martínez, L.M.; Morales-Torres, S.; Maldonado-Hódar, F.J. Photodegradation of Cytostatic Drugs by G-C_3N_4: Synthesis, Properties and Performance Fitted by Selecting the Appropriate Precursor. *Catal Today* 2023, *418*, 114068, doi:10.1016/J.CATTOD.2023.114068.
23. Quintana, M.A.; Picón, A.; Martín-Lara, M.Á.; Calero, M.; Muñoz-Batista, M.J.; Solís, R.R. Towards the Photocatalytic Production of Cinnamaldehyde with Phosphorous-Tailored Graphitic-like Carbon Nitride. *Appl Catal A Gen* 2024, *674*, 119607, doi:10.1016/J.APCATA.2024.119607.
24. Solís, R.R.; Quintana, M.A.; Martín-Lara, M.Á.; Pérez, A.; Calero, M.; Muñoz-Batista, M.J. Boosted Activity of G-C_3N_4/UiO-66-NH_2 Heterostructures for the Photocatalytic Degradation of Contaminants in Water. *Int J Mol Sci* 2022, *23*, 12871, doi:10.3390/IJMS232112871/S1.
25. Schneider, J.T.; Firak, D.S.; Ribeiro, R.R.; Peralta-Zamora, P. Use of Scavenger Agents in Heterogeneous Photocatalysis: Truths, Half-Truths, and Misinterpretations. *Physical Chemistry Chemical Physics* 2020, *22*, 15723–15733, doi:10.1039/d0cp02411b.
26. Pelaez, M.; Falaras, P.; Likodimos, V.; O'Shea, K.; de la Cruz, A.A.; Dunlop, P.S.M.; Byrne, J.A.; Dionysiou, D.D. Use of Selected Scavengers for the Determination of NF-TiO_2 Reactive Oxygen Species during the Degradation of Microcystin-LR under

Visible Light Irradiation. *J Mol Catal A Chem* 2016, *425*, 183–189, doi:10.1016/j.molcata.2016.09.035.

27. Ishibashi, K.I.; Fujishima, A.; Watanabe, T.; Hashimoto, K. Detection of Active Oxidative Species in TiO_2 Photocatalysis Using the Fluorescence Technique. *Electrochem commun* 2000, *2*, 207–210, doi:10.1016/S1388-2481(00)00006-0.
28. Gómez-Avilés, A.; Solís, R.R.; García-Frutos, E.M.; Bedia, J.; Belver, C. Novel Isoreticular UiO-66-NH_2 Frameworks by N-Cycloalkyl Functionalization of the 2-Aminoterephtalate Linker with Enhanced Solar Photocatalytic Degradation of Acetaminophen. *Chemical Engineering Journal* 2023, *461*, 141889, doi:10.1016/J.CEJ.2023.141889.
29. Papailias, I.; Giannakopoulou, T.; Todorova, N.; Demotikali, D.; Vaimakis, T.; Trapalis, C. Effect of Processing Temperature on Structure and Photocatalytic Properties of G-C_3N_4. *Appl Surf Sci* 2015, *358*, 278–286, doi:10.1016/J.APSUSC.2015.08.097.
30. Dai, C.; Zhang, H.; Li, R.; Zou, H. Synthesis and Characterization of Thiourea. *Polish Journal of Chemical Technology* 2019, *21*, 35–39, doi:10.2478/PJCT-2019-0027.
31. Timchenko, V.P.; Novozhilov, A.L.; Slepysheva, O.A. Kinetics of Thermal Decomposition of Thiourea. *Russ J Gen Chem* 2004, *74*, 1046–1050, doi:10.1023/B:RUGC.0000045862.69442.AA.
32. Madarász, J.; Pokol, G. Comparative Evolved Gas Analyses on Thermal Degradation of Thiourea by Coupled TG-FTIR and TG/DTA-MS Instruments. *J Therm Anal Calorim* 2007, *88*, 329–336, doi:10.1007/S10973-006-8058-4.
33. Zhang, S.; Li, G.; Wang, H.; Li, C.; Li, T.; Zhang, Y. Study on the Pyrolysis of Ammonium Thiocyanate and Its Product Formation Characteristics in H_2. *J Anal Appl Pyrolysis* 2018, *134*, 427–438, doi:10.1016/J.JAAP.2018.07.009.
34. Rahmanian, N.; Naderi, S.; Supuk, E.; Abbas, R.; Hassanpour, A. Urea Finishing Process: Prilling Versus Granulation. *Procedia Eng* 2015, *102*, 174–181, doi:10.1016/J.PROENG.2015.01.122.
35. Krum, K.; Patil, R.; Christensen, H.; Hashemi, H.; Wang, Z.; Li, S.; Glarborg, P.; Wu, H. Kinetic Modeling of Urea Decomposition and Byproduct Formation. *Chem Eng Sci* 2021, *230*, 116138, doi:10.1016/J.CES.2020.116138.

36. Schaber, P.M.; Colson, J.; Higgins, S.; Thielen, D.; Anspach, B.; Brauer, J. Thermal Decomposition (Pyrolysis) of Urea in an Open Reaction Vessel. *Thermochim Acta* 2004, *424*, 131–142, doi:10.1016/J.TCA.2004.05.018.
37. Yang, W.; Jia, L.; Wu, P.; Zhai, H.; He, J.; Liu, C.; Jiang, W. Effect of Thermal Program on Structure–Activity Relationship of g-C_3N_4 Prepared by Urea Pyrolysis and Its Application for Controllable Production of g-C_3N_4. *J Solid State Chem* 2021, *304*, 122545, doi:10.1016/J.JSSC.2021.122545.
38. Fina, F.; Callear, S.K.; Carins, G.M.; Irvine, J.T.S. Structural Investigation of Graphitic Carbon Nitride via XRD and Neutron Diffraction. *Chemistry of Materials* 2015, *27*, 2612–2618, doi:10.1021/ACS.CHEMMATER.5B00411.
39. Xin, G.; Meng, Y. Pyrolysis Synthesized G-C_3N_4 for Photocatalytic Degradation of Methylene Blue. *J Chem* 2013, *2013*, 187912, doi:10.1155/2013/187912.
40. Liu, X.; Ma, R.; Zhuang, L.; Hu, B.; Chen, J.; Liu, X.; Wang, X. Recent Developments of Doped G-C_3N_4 Photocatalysts for the Degradation of Organic Pollutants. *Crit Rev Environ Sci Technol* 2021, *51*, 751–790, doi:10.1080/10643389.2020.1734433.
41. Habarugira, F.N.; Yao, D.; Miao, W.; Chu, C.; Chen, Z.; Mao, S. Synergy of Sodium Doping and Nitrogen Defects in Carbon Nitride for Promoted Photocatalytic Synthesis of Hydrogen Peroxide. *Chinese Chemical Letters* 2024, *35*, 109886, doi:10.1016/J.CCLET.2024.109886.
42. Zhang, J.; Hu, S.; Wang, Y. A Convenient Method to Prepare a Novel Alkali Metal Sodium Doped Carbon Nitride Photocatalyst with a Tunable Band Structure. *RSC Adv* 2014, *4*, 62912–62919, doi:10.1039/C4RA11377B.
43. Jigyasa; Pratibha; Rajput, J.K. Alkali Metal (Na/ K) Doped Graphitic Carbon Nitride (g-C_3N_4) for Highly Selective and Sensitive Electrochemical Sensing of Nitrite in Water and Food Samples. *Journal of Electroanalytical Chemistry* 2020, *878*, 114605, doi:10.1016/J.JELECHEM.2020.114605.
44. Miller, T.S.; Jorge, A.B.; Suter, T.M.; Sella, A.; Corà, F.; McMillan, P.F. Carbon Nitrides: Synthesis and Characterization of a New Class of Functional Materials. *Physical Chemistry Chemical Physics* 2017, *19*, 15613–15638, doi:10.1039/C7CP02711G.

45. Ding, Z.; Chen, X.; Antonietti, M.; Wang, X. Synthesis of Transition Metal-Modified Carbon Nitride Polymers for Selective Hydrocarbon Oxidation. *ChemSusChem* 2011, *4*, 274–281, doi:10.1002/CSSC.201000149.
46. Li, X.; Zhang, J.; Shen, L.; Ma, Y.; Lei, W.; Cui, Q.; Zou, G. Preparation and Characterization of Graphitic Carbon Nitride through Pyrolysis of Melamine. *Appl Phys A Mater Sci Process* 2009, *94*, 387–392, doi:10.1007/S00339-008-4816-4.
47. Wei, J.; Hing, P.; Mo, Z.Q. TEM, XPS and FTIR Characterization of Sputtered Carbon Nitride Films. *Surface and Interface Analysis* 1999, *28*, 208–211.
48. Zhao, D.; Dong, C.-L.; Wang, B.; Chen, C.; Huang, Y.-C.; Diao, Z.; Li, S.; Guo, L.; Shen, S.; Zhao, D.; et al. Synergy of Dopants and Defects in Graphitic Carbon Nitride with Exceptionally Modulated Band Structures for Efficient Photocatalytic Oxygen Evolution. *Advanced Materials* 2019, *31*, 1903545, doi:10.1002/ADMA.201903545.
49. Kim, M.; Hwang, S.; Yu, J.S. Novel Ordered Nanoporous Graphitic C_3N_4 as a Support for Pt–Ru Anode Catalyst in Direct Methanol Fuel Cell. *J Mater Chem* 2007, *17*, 1656–1659, doi:10.1039/B702213A.
50. Lieber, E.; Rao, C.N.R.; Ramachandran, J. The Infrared Spectra of Organic Thiocyanates and Isothiocyanates. *Spectrochimica Acta* 1959, *13*, 296–299, doi:10.1016/0371-1951(59)80030-8.
51. Bertini, I.; Sabatini, A. Infrared Spectra of Substituted Thiocyanate Complexes. The Effect of the Substituent on Bond Type. II. *Inorg Chem* 1966, *5*, 1025–1028, doi:10.1021/IC50040A017.
52. Thommes, M.; Kaneko, K.; Neimark, A. V.; Olivier, J.P.; Rodríguez-Reinoso, F.; Rouquerol, J.; Sing, K.S.W.W. Physisorption of Gases, with Special Reference to the Evaluation of Surface Area and Pore Size Distribution (IUPAC Technical Report). *Pure and Applied Chemistry* 2015, *87*, 1051–1069.
53. Kong, L.; Wang, J.; Mu, X.; Li, R.; Li, X.; Fan, X.; Song, P.; Ma, F.; Sun, M. Porous Size Dependent G-C_3N_4 for Efficient Photocatalysts: Regulation Synthesizes and Physical

Mechanism. *Mater Today Energy* 2019, *13*, 11–21, doi:10.1016/J.MTENER.2019.04.011.

54. Stefa, S.; Zografaki, M.; Dimitropoulos, M.; Paterakis, G.; Galiotis, C.; Sangeetha, P.; Kiriakidis, G.; Konsolakis, M.; Binas, V. High Surface Area G-C_3N_4 Nanosheets as Superior Solar-Light Photocatalyst for the Degradation of Parabens. *Appl Phys A Mater Sci Process* 2023, *129*, 1–12, doi:10.1007/S00339-023-07032-Y.
55. Pattanayak, D.S.; Pal, D.; Thakur, C. The Influence of Various Precursors on Solar-Light-Driven g-C_3N_4 Synthesis and Its Effect on Photocatalytic Tetracycline Hydrochloride (TCH) Degradation. *Inorg Chem Commun* 2024, *162*, 112201, doi:10.1016/J.INOCHE.2024.112201.
56. Fernandes, E.; Mazierski, P.; Klimczuk, T.; Zaleska-Medynska, A.; Martins, R.C.; Gomes, J. G-C_3N_4 for Photocatalytic Degradation of Parabens: Precursors Influence, the Radiation Source and Simultaneous Ozonation Evaluation. *Catalysts* 2023, *13*, 789, doi:10.3390/CATAL13050789.
57. Wen, Y.; Qu, D.; An, L.; Gao, X.; Jiang, W.; Wu, D.; Yang, D.; Sun, Z. Defective G-C_3N_4 Prepared by the $NaBH_4$ Reduction for High-Performance H_2 Production. *ACS Sustain Chem Eng* 2019, *7*, 2343–2349, doi:10.1021/ACSSUSCHEMENG.8B05124.
58. Smith, M.; Scudiero, L.; Espinal, J.; McEwen, J.S.; Garcia-Perez, M. Improving the Deconvolution and Interpretation of XPS Spectra from Chars by Ab Initio Calculations. *Carbon N Y* 2016, *110*, 155–171, doi:10.1016/J.CARBON.2016.09.012.
59. Xu, H.; Wu, Z.; Wang, Y.; Lin, C. Enhanced Visible-Light Photocatalytic Activity from Graphene-like Boron Nitride Anchored on Graphitic Carbon Nitride Sheets. *J Mater Sci* 2017, *52*, 9477–9490, doi:10.1007/S10853-017-1167-6.
60. Wang, X.; Liu, B.; Xiao, X.; Wang, S.; Huang, W. Boron Dopant Simultaneously Achieving Nanostructure Control and Electronic Structure Tuning of Graphitic Carbon Nitride with Enhanced Photocatalytic Activity. *J Mater Chem C Mater* 2021, *9*, 14876–14884, doi:10.1039/D1TC04142H.
61. Caudillo-Flores, U.; Rodríguez-Padrón, D.; Muñoz-Batista, M.J.; Kubacka, A.; Luque, R.; Fernández-García, M. Facile Synthesis of B/g-C_3N_4 Composite Materials for the Continuous-Flow

Selective Photo-Production of Acetone. *Green Chemistry* 2020, *22*, 4975–4984, doi:10.1039/D0GC01326A.

62. Pettifer, Z.E.; Quinton, J.S.; Harmer, S.L. Reconstruction of Pyrrhotite Fracture Surfaces. *Miner Eng* 2022, *184*, 107666, doi:10.1016/J.MINENG.2022.107666.
63. Terlingen, J.G.A.; Feijen, J.; Hoffman, A.S. Immobilization of Surface Active Compounds on Polymer Supports Using Glow Discharge Processes: 1. Sodium Dodecyl Sulfate on Poly(Propylene). *J Colloid Interface Sci* 1993, *155*, 55–65, doi:10.1006/JCIS.1993.1009.
64. Gardella, J.; Ferguson, S.A.; Chin, R.L. Π* ← π Shakeup Satellites for the Analysis of Structure and Bonding in Aromatic Polymers by X-Ray Photoelectron Spectroscopy. *Appl Spectrosc* 1986, *40*, 224–232, doi:10.1366/0003702864509565.
65. Wang, K.L.; Li, Y.; Sun, T.; Mao, F.; Wu, J.K.; Xue, B. Fabrication of Na, Cl Co-Doped Graphitic Carbon Nitride with Enhanced Photocatalytic Activity for Degradation of Dyes and Antibiotics. *Journal of Materials Science: Materials in Electronics* 2019, *30*, 4446–4454, doi:10.1007/S10854-019-00733-2.
66. Liu, J.; Zhang, T.; Wang, Z.; Dawson, G.; Chen, W. Simple Pyrolysis of Urea into Graphitic Carbon Nitride with Recyclable Adsorption and Photocatalytic Activity. *J Mater Chem* 2011, *21*, 14398–14401, doi:10.1039/C1JM12620B.
67. Chidhambaram, N.; Ravichandran, K. Single Step Transformation of Urea into Metal-Free g-C_3N_4 Nanoflakes for Visible Light Photocatalytic Applications. *Mater Lett* 2017, *207*, 44–48, doi:10.1016/J.MATLET.2017.07.040.
68. Panneri, S.; Ganguly, P.; Nair, B.N.; Mohamed, A.A.P.; Warrier, K.G.K.; Hareesh, U.N.S. Role of Precursors on the Photophysical Properties of Carbon Nitride and Its Application for Antibiotic Degradation. *Environmental Science and Pollution Research* 2017, *24*, 8609–8618, doi:10.1007/S11356-017-8538-Z.
69. Sun, K.; Shen, J.; Liu, Q.; Tang, H.; Zhang, M.; Zulfiqar, S.; Lei, C. Synergistic Effect of Co(II)-Hole and Pt-Electron Cocatalysts for Enhanced Photocatalytic Hydrogen Evolution Performance of P-Doped g-C_3N_4. *Chinese Journal of Catalysis* 2020, *41*, 72–81, doi:10.1016/S1872-2067(19)63430-3.

70. Pérez-Molina, Á.; Pastrana-Martínez, L.M.; Pérez-Poyatos, L.T.; Morales-Torres, S.; Maldonado-Hódar, F.J. One-Pot Thermal Synthesis of g-C_3N_4/ZnO Composites for the Degradation of 5-Fluoruracil Cytostatic Drug under UV-LED Irradiation. *Nanomaterials* 2022, *12*, 340, doi:10.3390/NANO12030340.
71. Cui, Y.; Zhang, J.; Zhang, G.; Huang, J.; Liu, P.; Antonietti, M.; Wang, X. Synthesis of Bulk and Nanoporous Carbon Nitride Polymers from Ammonium Thiocyanate for Photocatalytic Hydrogen Evolution. *J Mater Chem* 2011, *21*, 13032–13039, doi:10.1039/C1JM11961C.
72. Sun, H.; Park, S.J. Phosphorus-Doped g-C_3N_4/SnS Nanocomposite for Efficient Photocatalytic Reduction of Aqueous Cr(VI) under Visible Light. *Appl Surf Sci* 2020, *531*, 147325, doi:10.1016/J.APSUSC.2020.147325.
73. Waffel, D.; Alkan, B.; Fu, Q.; Chen, Y.T.; Schmidt, S.; Schulz, C.; Wiggers, H.; Muhler, M.; Peng, B. Towards Mechanistic Understanding of Liquid-Phase Cinnamyl Alcohol Oxidation with Tert-Butyl Hydroperoxide over Noble-Metal-Free $LaCo_{1-x}Fe_xO_3$ Perovskites. *Chempluschem* 2019, *84*, 1155–1163, doi:10.1002/CPLU.201900429.
74. Dvoranová, D.; Barbieriková, Z.; Brezová, V. Radical Intermediates in Photoinduced Reactions on TiO₂ (An EPR Spin Trapping Study). *Molecules* 2014, *19*, 17279–17304, doi:10.3390/MOLECULES191117279.
75. Rivas, J.; Solis, R.R.; Gimeno, O.; Sagasti, J. Photocatalytic Elimination of Aqueous 2-Methyl-4-Chlorophenoxyacetic Acid in the Presence of Commercial and Nitrogen-Doped TiO2. *International Journal of Environmental Science and Technology* 2015, *12*, 513–526, doi:10.1007/s13762-013-0452-4.
76. Rodríguez, E.M.; Márquez, G.; Tena, M.; Álvarez, P.M.; Beltrán, F.J. Determination of Main Species Involved in the First Steps of TiO_2 Photocatalytic Degradation of Organics with the Use of Scavengers: The Case of Ofloxacin. *Appl Catal B* 2015, *178*, 44–53, doi:10.1016/j.apcatb.2014.11.002.
77. Zheng, P.; Pan, Z.; Li, H.; Bai, B.; Guan, W. Effect of Different Type of Scavengers on the Photocatalytic Removal of Copper and Cyanide in the Presence of TiO2@yeast Hybrids. *Journal of*

Materials Science: Materials in Electronics 2015, *26*, 6399–6410, doi:10.1007/S10854-015-3229-3/FIGURES/9.

78. Wang, J.; Bian, Z.; Zhu, J.; Li, H. Ordered Mesoporous TiO_2 with Exposed (001) Facets and Enhanced Activity in Photocatalytic Selective Oxidation of Alcohols. *J Mater Chem A Mater* 2012, *1*, 1296–1302, doi:10.1039/C2TA00035K.
79. Garg, S.; Rose, A.L.; Waite, T.D. Production of Reactive Oxygen Species on Photolysis of Dilute Aqueous Quinone Solutions. *Photochem Photobiol* 2007, *83*, 904–913, doi:10.1111/J.1751-1097.2007.00075.X.
80. Alegría, A.E.; Ferrer, A.; Santiago, G.; Sepúlveda, E.; Flores, W. Photochemistry of Water-Soluble Quinones. Production of the Hydroxyl Radical, Singlet Oxygen and the Superoxide Ion. *J Photochem Photobiol A Chem* 1999, *127*, 57–65, doi:10.1016/S1010-6030(99)00138-0.
81. Alam, M.S.; Rao, B.S.M.; Janata, E. ·OH Reactions with Aliphatic Alcohols: Evaluation of Kinetics by Direct Optical Absorption Measurement. A Pulse Radiolysis Study. *Radiation Physics and Chemistry* 2003, *67*, 723–728, doi:10.1016/S0969-806X(03)00310-4.
82. Silva, L.L.S.; Abdelraheem, W.; Nadagouda, M.N.; Rocco, A.M.; Dionysiou, D.D.; Fonseca, F. V.; Borges, C.P. Novel Microwave-Driven Synthesis of Hydrophilic Polyvinylidene Fluoride/Polyacrylic Acid (PVDF/PAA) Membranes and Decoration with Nano Zero-Valent-Iron (NZVI) for Water Treatment Applications. *J Memb Sci* 2021, *620*, 118817, doi:10.1016/J.MEMSCI.2020.118817.
83. Shah, B.R.; Patel, U.D. Mechanistic Aspects of Photocatalytic Degradation of Lindane by TiO2 in the Presence of Oxalic Acid and EDTA as Hole-Scavengers. *J Environ Chem Eng* 2021, *9*, 105458, doi:10.1016/J.JECE.2021.105458.
84. Madona, J.; Sridevi, C.; Velraj, G.; Wu, J.; Torsykbayeva, B.; Aimbetova, E.; Hosseini-Bandegharaei, A. Boosting Solar-Driven Photocatalytic Degradation of Organic Contaminants and Bacterial Deactivation Using Marigold- like Cu_2O Decorated g-C_3N_4 Nanocomposite. *J Mol Liq* 2024, *403*, 124870, doi:10.1016/J.MOLLIQ.2024.124870.

85. Bian, C.; Wang, Y.; Yi, Y.; Shao, S.; Sun, P.; Xiao, Y.; Wang, W.; Dong, X. Enhanced Photocatalytic Activity of S-Doped Graphitic Carbon Nitride Hollow Microspheres: Synergistic Effect, High-Concentration Antibiotic Elimination and Antibacterial Behavior. *J Colloid Interface Sci* 2023, *643*, 256–266, doi:10.1016/J.JCIS.2023.04.034.
86. Shao, S.; Liu, X.; Wang, R.; He, Y.; Bian, C.; Sun, P.; Dong, X. Morphologic and Microstructural Modulation of Graphitic Carbon Nitride through EDTA-2Na Mediated Supramolecular Self-Assembly Route: Enhanced Visible-Light-Driven Photocatalytic Activity for Antibiotic Degradation. *Appl Surf Sci* 2024, *669*, 160501, doi:10.1016/J.APSUSC.2024.160501.
87. Chen, W.; Chen, Z.; Liu, T.; Jia, Z.; Liu, X. Fabrication of Highly Visible Light Sensitive Graphite-like C_3N_4 Hybridized with $Zn_{0.28}Cd_{0.72}S$ Heterojunctions Photocatalyst for Degradation of Organic Pollutants. *J Environ Chem Eng* 2014, *2*, 1889–1897, doi:10.1016/J.JECE.2014.07.019.
88. Cao, J.; Nie, W.; Huang, L.; Ding, Y.; Lv, K.; Tang, H. Photocatalytic Activation of Sulfite by Nitrogen Vacancy Modified Graphitic Carbon Nitride for Efficient Degradation of Carbamazepine. *Appl Catal B* 2019, *241*, 18–27, doi:10.1016/J.APCATB.2018.09.007.
89. Yang, F.; Lublow, M.; Orthmann, S.; Merschjann, C.; Tyborski, T.; Rusu, M.; Kubala, S.; Thomas, A.; Arrigo, R.; Hävecker, M.; et al. Metal-Free Photocatalytic Graphitic Carbon Nitride on p-Type Chalcopyrite as a Composite Photocathode for Light-Induced Hydrogen Evolution. *ChemSusChem* 2012, *5*, 1227–1232, doi:10.1002/CSSC.201100691.
90. Gao, T.; Zhao, D.; Yuan, S.; Zheng, M.; Pu, X.; Tang, L.; Lei, Z. Energy Band Engineering of Graphitic Carbon Nitride for Photocatalytic Hydrogen Peroxide Production. *Carbon Energy* 2024, e596, doi:10.1002/CEY2.596.
91. Koppenol, W.H.; Stanbury, D.M.; Bounds, P.L. Electrode Potentials of Partially Reduced Oxygen Species, from Dioxygen to Water. *Free Radic Biol Med* 2010, *49*, 317–322, doi:10.1016/J.FREERADBIOMED.2010.04.011.

92. Wood, P.M. The Potential Diagram for Oxygen at PH 7. *Biochemical Journal* 1988, *253*, 287–289, doi:10.1042/BJ2530287.

CHAPTER 8. CONCLUSIONS

In this doctoral thesis, the effective preparation of graphite carbon nitride catalysts doped with heteroatoms B, Ru, P, and S has been achieved. Catalytic systems were designed from different precursors and dopant proportions. These materials were obtained through simple synthesis methods such as impregnation and carbonization, notable for reducing the use of complex equipment, toxic substances, energy consumption, and waste generation.

The synthesized materials promoted the selective oxidation of alcohols for the production of industrially relevant aldehydes. Additionally, an environmentally friendly reaction system was established, as the use of solvents or chemical intermediates was reduced in all cases, air was used as the oxidizing agent, which in turn favored the generation of some reactive species useful in the oxidation process, and ambient pressure and temperature conditions were employed. After conducting the catalytic evaluation, it was determined that the materials were effective, and generally, the effect of the dopant agent boosted the attainment of better oxidation kinetics, selectivity, and conversion compared to the non-modified catalyst.

Through complete characterization of the materials, a significant improvement in the catalytic properties was observed. Furthermore, various characterization techniques provided evidence and a better understanding of the obtained results during the catalytic evaluation. This tool was demonstrated to be essential in precisely selecting the optimal catalyst in each catalytic series. Moreover, studying the matter-light interaction allowed for an in-depth understanding of the interaction between the light source and the system, enabling precise determination of the number of photons effectively interacting to produce an electron-hole pair, fundamental species in the studied reaction

Boron doping was carried out using two different precursors, elemental boron and sodium borohydride, both showing better photocatalytic activity compared to the catalytic base. In this series of catalysts, g-C_3N_4 modified with $NaBH_4$ (NaBCN) was designated the optimal catalyst, achieving a selectivity of 36%, compared to 12% in the absence of boron, and obtaining a maximum quantum efficiency of

0.15%. Additionally, the catalytic properties of NaBCN were improved significantly, presenting a bandgap of 2.28 eV, which allows the sample to be activated with lower energy radiation. This sample also showed a lower photoluminescence peak intensity, indicating lower recombination of photogenerated charges, resulting in better selectivity. NaBCN also proved to be a stable catalyst after use, maintaining the original structure of graphite carbon nitride, representing a significant advantage in terms of catalyst reuse, and aligning with green chemistry principles.

The study of boron doping and ruthenium nanoparticle deposition was conducted by varying the proportion of ruthenium. Catalytic activity results revealed that, although the NaBCN-4Ru catalyst achieved higher oxidation kinetics, its selectivity was significantly lower. Therefore, the NaBCN-1Ru catalyst was selected as optimal in terms of selectivity. Furthermore, NaBCN-1Ru enhanced its reaction kinetics and selectivity by approximately five and two times, respectively, compared to the catalytic support. It was also determined that the predominant reactive oxidizing species during the reaction were photogenerated holes, followed by the superoxide radical, allowing for highly selective product formation. Finally, it was observed that the average photo-absorption rate values were quite similar, so the quantum efficiency would be defined by the initial reaction rate, with NaBCN-1Ru being the sample with the third-best quantum efficiency.

Graphite carbon nitride doping with different proportions of P was successfully performed. Using these materials for the oxidation of cinnamyl alcohol (CA) to cinnamaldehyde (CD) showed an improvement in catalytic activity, especially with low doping percentages, demonstrated by the increase in oxidation kinetics and conversion. Selective synthesis of CD was achieved, reaching selectivity of up to 49% in the optimal sample P-CN-4%, compared to 10% in g-C_3N_4. Characterization results determined that phosphorus incorporation occurred in the internal positions of the tris-triazine rings, where partial substitution of C atoms by P atoms took place. This was confirmed through the determination of the number of layers and the ^{13}C NMR spectrum, indicating that P doping promoted the reduction of bay sites, suggesting the exchange of C atoms for P atoms in the internal positions of the tris-triazine rings.

Furthermore, the modification of graphite carbon nitride through sulfonation proved to be an efficient strategy to improve benzaldehyde production. It was found that both the oxidation kinetics and selectivity improved in the materials as the degree of sulfonation increased, reaching its maximum value in the optimal sample (60%); beyond this point, these values tend to decrease. The selectivity of the optimum sample was possibly improved due to its ability to separate photogenerated charges, as evidenced by photoluminescence peaks. Additionally, superoxide radicals, which are the main species acting during the reaction, contribute to better selectivity due to their moderate oxidative potential, helping to control possible over-oxidation and the generation of undesired by-products. The optimal sample achieved the highest radiation absorption efficiency, reaching a quantum efficiency of 0.124%. Diverse characterization techniques revealed that the insertion of the sulfonic group creates surface defects that generate lattice strain, chemical delamination, and a decrease in surface area due to the attack of chlorosulfonic acid.

On the other hand, the nature of the carbon nitride precursor has great relevance within the catalytic activity for the generation of aldehydes. From melamine, a more crystalline but less porous material was obtained. On the contrary, when using thiourea and urea as precursors, it was shown that the resulting material was less crystalline but more porous, which favored better reaction rates caused by the creation of more active sites, especially in the case of urea. The modification of the urea-derived g-C_3N_4 (S-CNu) with different proportions of sodium thiosulfate improved the reaction kinetics, optical properties, absorption in the visible light range and reduced the charge recombination effect, with the S-CNu5% sample being chosen as the optimal one. The study of the reaction mechanism suggests that both superoxide radicals and photogenerated holes are the species that actively intervene during the oxidation of alcohols, leading to more selective reactions.

Upon completing the activities established at the beginning of the research, catalytic systems with improved properties have been obtained, particularly useful in the aldehyde synthesis process. Additionally, this work aims to foster greater interest in this research

field, hoping that these advances can eventually be implemented at an industrial level in the future.